HYDROGEN SPILLOVER AND ADSORPTION ON NANOPOROUS CARBON-BASED MATERIALS FOR STORAGE APPLICATIONS

by

Anthony J. Lachawiec Jr.

A dissertation submitted in partial fulfillment
of the requirements for the degree of
Doctor of Philosophy
(Chemical Engineering)
in The University of Michigan
2009

Doctoral Committee:

Professor Ralph T. Yang, Chair
Professor Erdogan Gulari
Professor Xiaoqing Pan
Professor Robert M. Ziff

Acknowledgements

I would like to extend sincere thanks to those who have supported me during the journey to complete this dissertation. I owe gratitude…

…to God, for without You I am nothing and can achieve nothing.

…to Mom and Dad, you have been an inspiration and model parents. I aspire to follow your example. You will forever be in my heart, no matter how many miles separate us.

…to the rest of my family for their support and encouragement throughout the years.

…to Dr. Ralph Yang, my advisor, for constantly challenging me and supplying the environment for me to grow as a researcher and teacher.

…to my committee members for providing guidance.

…to the members of the Yang research group throughout my time at the University of Michigan: Arturo Hernandez-Maldonado, Ambal Jayaraman, Gongshin Qi, Dennis Crespo Matos, Yingwei Li, Lifeng Wang, Yuhe Wang, Tommy DiRaimondo, and Hao Chen for their friendship, fruitful discussions, and bringing me to a deeper understanding of cultures from their various home countries.

…to the administrative staff in the Department of Chemical Engineering for showing patience and efficiency.

…and to my friends in Ann Arbor and elsewhere who made the bad times good and the good times better.

And now, on with the show!

Table of Contents

Acknowledgements ii
List of Figures vii
List of Tables xi
Abstract xiii
Chapter
1 Introduction 1
1.1 Motivation for On-Board Hydrogen Storage 1
1.2 Overview of Hydrogen Storage Techniques 4
1.2.1 Compressed Gas 4
1.2.2 Cryogenic Liquid 5
1.2.3 Absorption by Intermetallic Compounds 7
1.2.4 Adsorption to Solids 9
1.3 A Brief History of Spillover Research 13
1.4 Objectives and Structure of This Dissertation 15
1.5 Literature Cited 16
2 Synthesis and Characterization of Carbon-Based Nanomaterials 21
2.1 Introduction to Nanostructured Carbon-Based Adsorbents 21
2.2 Adsorbents for Spillover 23
2.3 Receptor Synthesis 25
2.3.1 Templated Carbon (TC) Procedure 26
2.3.2 Single-Walled Nanotube (SWNT) Procedure 28
2.3.3 Graphite Nanofiber (GNF) Procedure 30
2.3.4 Sol-Gel Mesoporous Carbon Procedure 32
2.4 Synthesis of Source-Receptor Composites 33

2.4.1 Primary Spillover: Direct Doping of Receptor 33
2.4.2 Secondary Spillover: Bridging Primary Source to Receptor 36
2.4.3 Limited Spillover: Primary Source/Receptor Physical Mixture 39
2.5 Characterization of Adsorbents 40
2.5.1 Surface Area and Pore Size Distribution 40
2.5.1.1 Receptor BET SA and PSD 41
2.5.1.2 Composites BET SA and PSD 52
2.5.2 Metal Dispersion and Particle Size 62
2.5.3 Imaging and Surface Analysis 66
2.6 Conclusions 68
2.7 Literature Cited 68
3 Hydrogen Adsorption Measurement: Apparatus and Techniques 73
3.1 Overview of Measurement Methods 73
3.1.1 Gravimetric Techniques 74
3.1.2 Volumetric Techniques 75
3.2 Design of a High-Pressure Volumetric Apparatus 77
3.2.1 Equipment Specification and Details 78
3.2.2 Experimental Procedure 82
3.2.3 Data Analysis Method 85
3.2.4 Heuristic to Correct for Helium Adsorption 87
3.2.5 Error Propagation for Adsorbed Amount 90
3.3 Validation of Apparatus and Method 91
3.3.1 Standard Materials 91
3.3.2 Results of Validation Study 92
3.3.3 Helium Adsorption Correction to Free Space Measurement 99
3.3.4 Effect of Manifold Temperature Variation 99
3.3.5 Calculation of Diffusion Time Constant from Kinetic Data 102
3.4 Conclusions 105
3.5 Literature Cited 106
4 Hydrogen Adsorption Properties of Carbon-Based Materials 111
4.1 Parameters Obtained from Volumetric Adsorption Measurement 111

4.1.1 Adsorbed Amount 111
4.1.2 Isosteric Heat of Adsorption 113
4.1.3 Diffusion Time Constant 114
4.2 Results for Receptors 117
4.3 Results for Primary Spillover Adsorbents 122
4.4 Results for Secondary Spillover Adsorbents 131
4.5 Application of Spillover Isotherm Model and - ΔH_{ads} 136
4.6 Kinetic Results and Diffusion Time Constant ($D_{s,e}/R_s^2$) 141
4.7 Conclusions 147
4.8 Literature Cited 149
5 Isotope Tracer Evaluation of Hydrogen Spillover 153
5.1 Introduction to Hydrogen Isotopic Exchange 153
5.1.1 Hydrogen/Deuterium Exchange Reaction 153
5.1.2 Mass Spectral Methods in Hydrogen Spillover Research 154
5.1.3 Mechanistic Observations of Spillover 155
5.2 Experimental Methods for Temperature Programmed Desorption 157
5.2.1 TPD Apparatus 157
5.2.2 Samples for Studying the Spillover Mechanism 159
5.2.3 Rate Measurements to Determine the Dose Time Scale 160
5.2.4 Sequential Dosing Procedure 161
5.2.5 Deuterium Hydride Equilibration Procedure 165
5.3 Sequential Dosing Results 166
5.4 Deuterium Hydride Equilibration Results 173
5.5 Recombination Phenomenon on Desorption 176
5.6 Conclusions 183
5.7 Literature Cited 184
6 Conclusions and Future Work 188
6.1 Conclusions and Key Findings of This Research 188
6.2 Proposed Future Studies 190
6.2.1 Enhancement of Spillover Adsorbent Properties 190
6.2.2 Additional Characterization of Spillover 191

6.2.3 Novel Applications of Spillover Adsorbents 191
6.3 Literature Cited 192

List of Figures

Figure

2.1 Oxygen Functionalities on Carbon Layer Edges 23
2.2 Primary and Secondary Spillover from Source (M) to Receptor 25
2.3 TGA Result, Glucose Melting and Decomposition 38
2.4 Templated Carbon (TC), N_2 Isotherm, 77 K 42
2.5 Templated Carbon (TC), BET Plot With Statistics 42
2.6 Templated Carbon (TC), Pore Size Distribution 43
2.7 Templated Carbon (TC), Cumulative Pore Volume 43
2.8 Single Walled Nanotubes (SWNTs), N_2 Isotherm, 77 K 44
2.9 Single Walled Nanotubes (SWNTs), BET Plot With Statistics 44
2.10 Single Walled Nanotubes (SWNTs), Pore Size Distribution 45
2.11 Single Walled Nanotubes (SWNTs), Cumulative Pore Volume 45
2.12 Graphite Nanofibers (GNFs), N_2 Isotherm, 77 K 46
2.13 Graphite Nanofibers (GNFs), BET Plot With Statistics 46
2.14 Graphite Nanofibers (GNFs), Pore Size Distribution 47
2.15 Graphite Nanofibers (GNFs), Cumulative Pore Volume 47
2.16 Sol-Gel Carbon (SGC), N_2 Isotherm, 77 K 48
2.17 Sol-Gel Carbon (SGC), BET Plot With Statistics 48
2.18 Sol-Gel Carbon (SGC), Pore Size Distribution 49
2.19 Sol-Gel Carbon (SGC), Cumulative Pore Volume 49
2.20 AX-21, N_2 Isotherm, 77 K 50
2.21 AX-21, BET Plot With Statistics 50
2.22 AX-21, Pore Size Distribution 51
2.23 AX-21, Cumulative Pore Volume 51

2.24 6 wt% Pt/TC, N_2 Isotherm, 77 K 53
2.25 6 wt% Pt/TC, BET Plot With Statistics 53
2.26 6 wt% Pt/TC, Pore Size Distribution 54
2.27 6 wt% Pt/TC, Cumulative Pore Volume 54
2.28 AX-21/PdC/Bridge (8:1:1), N_2 Isotherm, 77 K 55
2.29 AX-21/PdC/Bridge (8:1:1), BET Plot With Statistics 55
2.30 AX-21/PdC/Bridge (8:1:1), Pore Size Distribution 56
2.31 AX-21/PdC/Bridge (8:1:1), Cumulative Pore Volume 56
2.32 5 wt% Pd/SGC, N_2 Isotherm, 77 K 57
2.33 5 wt% Pd/SGC, BET Plot With Statistics 57
2.34 5 wt% Pd/SGC, Pore Size Distribution 58
2.35 5 wt% Pd/SGC, Cumulative Pore Volume 58
2.36 5 wt% Ni/SGC, N_2 Isotherm, 77 K 59
2.37 5 wt% Ni/SGC, BET Plot With Statistics 59
2.38 5 wt% Ni/SGC, Pore Size Distribution 60
2.39 5 wt% Ni/SGC, Cumulative Pore Volume 60
2.40 Metal Dispersion of 5 wt% PdC (Strem) Using H_2 Chemisorption 63
2.41 Metal Dispersion of 6 wt% Pt/TC Using CO Titration 64
2.42 XRD Results for 6 wt% Pt/TC 65
2.43 TEM Images of 6 wt% Pt/TC 66
2.44 SEM Images of 5 wt% PdC and AX-21 67
2.45 SEM Images of AX-21/PdC/Bridge (8:1:1) and AX-21/PdC (9:1) 67
3.1 Schematic of High-Pressure Volumetric Adsorption Apparatus 79
3.2 Calibration of Pressure Transducer Low Range 81
3.3 Henry's Law Constant and Heat of Adsorption for Helium 89
3.4 AX-21 Repeatability for Variable Pressure Steps 93
3.5 Agreement Between High Pressure and Low Pressure Measurements 94
3.6 Hydrogen Absorption by $LaNi_5$ Using the High Pressure System 96
3.7 Hydrogen Adsorption on Graphite Powder 97
3.8 Hydrogen Adsorption on 5A Zeolite 98
3.9 Hydrogen Adsorption on SWNTs 98

3.10 Helium Adsorption Influence on Isotherm Accuracy 100
3.11 Temperature and Pressure Accuracy at Equilibrium 101
3.12 Kinetics of Hydrogen Adsorption on AX-21 104
4.1 Schematic of Spillover Geometry 116
4.2 H_2 Adsorption Capacity and Enthalpy for GNF Below 100 kPa 118
4.3 H_2 Adsorption Capacity for GNF at 298 K to 10 MPa 119
4.4 H_2 Adsorption Capacity and Enthalpy for SWNT Below 100 kPa 119
4.5 H_2 Adsorption Capacity and Enthalpy for SGC Below 100 kPa 120
4.6 H_2 Adsorption Capacity and Enthalpy for AX-21 Below 100 kPa 120
4.7 H_2 Adsorption Capacity and Enthalpy for TC Below 100 kPa 121
4.8 H_2 Adsorption Capacity for TC at 298 K to 10MPa 121
4.9 H_2 Adsorption Capacity for 6 wt% Pt/GNF at 298 K to 10MPa 123
4.10 H_2 Adsorption Capacity for 5 wt% Pd/SGC at 298 K Below 100 kPa 124
4.11 H_2 Adsorption Capacity for 5 wt% Ni/SGC at 298 K Below 100 kPa 126
4.12 H_2 Adsorption Capacity for 6 wt% Pt/AX-21 at 298 K to 10 MPa 126
4.13 H_2 Adsorption Capacity for 6 wt% Pt/TC at 298 K to 10 MPa 127
4.14 H_2 Adsorption Capacity for 1.5 wt% Pt/TC at 298 K to 10 MPa 128
4.15 H_2 Adsorption Capacity for Ni/TC and Pd/TC at 298 K Below 100 kPa 129
4.16 H_2 Adsorption Capacity for SWNT Secondary Receptor at 298 K 132
4.17 H_2 Adsorption Capacity for AX-21 Secondary Receptor at 298 K 134
4.18 H_2 Adsorption Capacity for Variable Bridge Proportion, AX-21 Receptor .. 135
4.19 H_2 Adsorption on Platinum Black at 298 K 137
4.20 H_2 Isotherms and Spillover Model, 6 wt% Pt/TC 138
4.21 H_2 Enthalpy of Adsorption, 6 wt% Pt/TC 139
4.22 H_2 Isotherms and Spillover Model, AX-21/PdC/Bridge (8:1:1) 140
4.23 H_2 Enthalpy of Adsorption, AX-21/PtC/Bridge (8:1:1) 141
4.24 Fick's Law Diffusion Model for Adsorption, 6 wt% Pt/TC 143
4.25 Fick's Law Diffusion Model for Desorption, 6 wt% Pt/TC 143
4.26 Diffusion Time Constants for Spillover of H, 6 wt% Pt/TC 144
4.27 Fick's Law Diffusion Model for Adsorption, AX-21/PtC/Bridge 145
4.28 Fick's Law Diffusion Model for Desorption, AX-21/PtC/Bridge 145

4.29 Diffusion Time Constants for Spillover of H, AX-21/PtC/Bridge 146
5.1 TPD Manifold and Sample Cell 157
5.2 Rate of Adsorption of H_2 and D_2 on 6 wt% Pt/TC, 0.4 bar and 298 K 161
5.3 TPD Result for Sequential D_2/H_2 Dose, Empty Chamber 164
5.4 TPD Result for Sequential D_2/H_2 Dose, TC 164
5.5 TPD Result for Sequential D_2/H_2 Dose, Platinum Black 165
5.6 TPD Result for Sequential H_2/D_2 Dose, 6 wt% Pt/TC at 298 K 167
5.7 Schematic of Hydrogen Spillover Patterns for H_2/D_2 Dose 167
5.8 TPD Result for Sequential D_2/H_2 Dose, 6 wt% Pt/TC at 298 K 169
5.9 Schematic of Hydrogen Spillover Patterns for D_2/H_2 Dose 169
5.10 TPD Result for Dual H_2 Doses, 6 wt% Pt/TC at 298 K 171
5.11 TPD Result for Sequential D_2/H_2 Dose, IRMOF-8/PtC/Bridge at 298 K 172
5.12 TPD Result for HD Equilibration on 6 wt% Pt/TC at 298 K 173
5.13 TPD Result for HD Equilibration on IRMOF-8/PtC/Bridge at 298 K 175
5.14 Step Desorption for HD Equilibration on 6 wt% Pt/TC at 298 K 177
5.15 Step Desorption for HD Equilibration on 6 wt% Pt/TC at 273 K 177
5.16 Step Desorption for HD Equilibration on IRMOF-8/PtC/Bridge at 298 K ... 178
5.17 Step Desorption for HD Equilibration on IRMOF-8/PtC/Bridge at 273 K ... 178
5.18 Deuterium Adsorption Isotherm for 6 wt% Pt/TC at 298 K..... 180
5.19 Diffusion Time Constant for Deuterium on 6 wt% Pt/TC..... 180
5.20 Recombination Time Constant for H_2 and D_2 on 6 wt% Pt/TC at 298 K..... 182
5.21 Recombination Time Constant for Hydrogen: Adsorbent Comparison 182

List of Tables

Table		
1.1	Key U.S. DOE On-Board Hydrogen Storage Targets for 2010	2
1.2	Properties of Several Transportation Fuel Options	3
1.3	Selected Metal Hydride Capacities and Enthalpies of Absorption	8
1.4	Properties of Selected Common Adsorbents	10
1.5	Components of the Adsorbent-Adsorbate Interaction Potential	11
2.1	Materials for Production of Templated Carbon	26
2.2	Materials for Production of SWNT Catalyst	28
2.3	Materials for Production of GNF Catalyst	30
2.4	Materials for Production of Sol-Gel Carbon	32
2.5	Materials Prepared to Study Primary Spillover	35
2.6	Materials Prepared to Study Secondary Spillover	39
2.7	Summary of Receptor BET SA and PSD Results	52
2.8	Summary of Composites BET SA and PSD Results	61
3.1	Nomenclature for High-Pressure Volumetric Apparatus Schematic	79
3.2	Henry's Law Constants for Nanostructured Adsorbents at 298 K	89
3.3	Uncertainty in Measured Variables for Adsorption Apparatus	90
3.4	Materials Studied to Demonstrate Instrument Accuracy	95
3.5	Variation of Amount Adsorbed for Manifold Temperature Fluctuation	102
3.6	Values of the Diffusion Time Constant for AX-21	104
4.1	Hydrogen Adsorption Characteristics of Receptors	118
4.2	Primary Spillover of Hydrogen on Composite Adsorbents at 298 K	130
4.3	Spillover Isotherm Partition Coefficients for 6 wt% Pt/TC	137
4.4	Spillover Isotherm Partition Coefficients for AX-21/PtC/Bridge (8:1:1)	140

5.1 Equilibrium Constant for $H_2 + D_2 \leftrightarrow 2HD$ 154
5.2 Nomenclature for TPD Apparatus 157
5.3 Bond Energies for Species Containing Hydrogen and Deuterium 174

Abstract

Interest in hydrogen as an alternative fuel has grown recently due, in part, to increasing global energy demands and environmental concerns. A challenge for commercialization of hydrogen fuel cells is storage of an adequate quantity of hydrogen on-board to match the range of current internal combustion power plants. Among several options, storage by adsorption is attractive because it has the potential to lower the overall system pressure for an equivalent amount of hydrogen, yielding a safer operating condition. In addition, adsorption is kinetically favorable compared to the absorption phenomena employed by most high capacity intermetallics.

Enhanced capacity spillover adsorbents have been synthesized using ultrasound assisted solution impregnation and bridge building techniques between common catalytic materials and novel nanostructured carbons. The impregnation method generates a metal dispersion of nearly 40% on nanoporous carbons. Bridge-building techniques can be applied with varied receptors to quickly augment spillover behavior of new materials. Capacity enhancements of up to 70% over molecular hydrogen physisorption on carbons have been realized at 10 MPa and 298 K.

A highly accurate, volumetric adsorption apparatus has been constructed and validated as a cost-effective means of high throughput screening for hydrogen spillover adsorbents at ambient temperature. Kinetic data can be collected for adsorption and

desorption to facilitate comparison of the rates for both processes. This capability has directly led to the theory of different forward and reverse spillover mechanisms.

Isotopic tracer studies have been developed to evaluate forward and reverse spillover on carbon-based nanomaterials. A sequential dosing procedure has proven that hydrogen spillover proceeds at ambient temperature and follows a radial diffusion mechanism from the source particle with a diffusion coefficient on the order of 10^{-15} cm^2/s. Equilibrium dosing procedures, building upon kinetic results obtained with volumetric techniques, have pointed toward a mechanism for desorption whereby a portion of the adsorbed species recombine before reaching the source particle. Using kinetic results, a maximum reachable distance of 800 Å has been calculated for spillover on bridged composite nanostructured carbons. This information is a key parameter for optimizing the dispersion of metal nanoparticles on new materials to enhance capacity and improve kinetic response.

Chapter 1

Introduction

1.1 Motivation for On-Board Hydrogen Storage

Increasing global energy demands, limited fossil fuel reserves and production capacities, geopolitical conflicts, and efforts to reduce greenhouse gas emissions have motivated research efforts into alternative transportation fuels. Among the many candidates, hydrogen for use in fuel cells has been the subject of intense focus for the past two decades. Although there is some debate on the role hydrogen and fuel cells will play in the transportation sector,[1.1] the transition of the global energy supply from the current infrastructure to a renewable one will likely include hydrogen as part of the amalgam. While much of the hydrogen used today is generated from steam reforming of hydrocarbons and produces carbon dioxide as a byproduct, hydrogen production from novel sources such as solar, wind, or biological processes presents the opportunity of a clean, environmentally friendly energy cycle for transportation. The final embodiment of hydrogen supply for a mass production fuel cell vehicle is yet unknown, however, storage techniques have been employed in the initial demonstration technologies as on-board reforming continues to evolve. Even if a move is made to on demand hydrogen generation, one can presume that a reservoir of stored hydrogen will be needed to bridge situations such as startup or high-energy demand. Storage of hydrogen, therefore,

becomes a key enabling technology for fuel cell-powered vehicles and more broadly, the hydrogen economy.

There are many excellent resources that treat fuel cell technology in detail;[1.2-1.5] thus, the background discussion focuses on-board hydrogen storage needs in the context of its supply to the anode of a fuel cell. The U.S. Department of Energy (DOE) has established a comprehensive set of targets for on-board hydrogen storage and delivery.[1.6] Major features addressed by these targets are the capacity, kinetics, and economics of such a system. Many of the target parameters are adjusted over a prescribed timeline from 2007-2015 to reflect the presumed maturation of storage materials and processes. Some critical targets for the year 2010 are listed in Table 1.1.[1.6]

Table 1.1 Key U.S. DOE On-Board Hydrogen Storage Targets for 2010

Parameter	**Target**
Gravimetric Capacity (system)	2.0 kWh/kg (0.06 kg H_2/kg system)
Volumetric Capacity (system)	1.5 kWh/L (0.045 kg H_2/L system)
Operating Ambient Temperature	- 30 / 50 °C
Delivery Temperature Range	- 40 / 85 °C
Cycle Life	1000 cycles
Delivery Pressure Range	4 / 100 atm (abs)
System Charge Rate	1.67 kg/min
Minimum Full Flow Rate	0.02 (g/s)/kW
Transient Response (10 - 90%, 90 – 0%)	0.75 s
Fuel Purity	99.99 % H_2 (dry basis)
Fuel Cost	$2 - $3 / gal gasoline equivalent at pump

The capacity requirements for hydrogen storage draw a basis from the assumption that a fuel cell vehicle should have a range comparable to current state-of-the-art vehicles. This range is 400 km (250 mi), on average, for a gasoline-powered internal combustion engine (ICE) vehicle.[1.7] The Carnot limit of a combustion engine operating within material constraints reaches a maximum of 40% efficiency but in practice is close to 30%.[1.4,1.8,1.9] The efficiency of a fuel cell, which is based on an electron transfer process, can reach a maximum of 60 to 80%, depending on the operating temperature.[1.4] As a result of this gain, a smaller mass of hydrogen (4 kg) is required for an equivalent range despite its lower volumetric energy density (also known as the higher heating value or HHV) compared to gasoline.[1.10, 1.11] As Table 1.2 shows, the hydrogen content of octane (representing gasoline) is 16 wt%, which gives an example of the storage efficiency for an on-board reforming option.[1.12]

Table 1.2 Properties of Several Transportation Fuel Options

	T (K)	**Density (kg/m^3)**	**H_2 Content (wt%)**	**Gravimetric HHV (MJ/kg)**	**Volumetric HHV (MJ/m^3)**
H_2 (g)	293	0.0887	100	142.0	12.7
CH_4 (g)	293	0.707	25	55.6	40
C_8H_{18} (l)[a]	298	698	16	47.9	33,430
$C_{12}H_{23}$ (l)[b]	298	850	14	44.8	38,080
C_2H_5OH (l)	298	789	13	29.7	23,430
H_2 (l)	20	70	100	142.0	9,930

Note: All properties are reported at atmospheric pressure.
(a) Octane, representative of gasoline, (b) Diesel, average formula

Kinetic requirements are based on the operation and refueling of a fuel cell vehicle. The flow rate of hydrogen to the anode must be sufficient to sustain operation at the maximum speed of the vehicle (80 mph), operation at 55 mph on a 6.5% grade for 20 min,[1.13] and acceleration from a standstill to 60 mph in 10 s or less. The refueling of a hydrogen storage system should occur in a reasonable amount of time, considering that a typical trip to refuel a gasoline-powered vehicle involves roughly three minutes of pumping time. The target maintains this time parameter while achieving a mass flow rate that is one order of magnitude less than a gasoline pump.

1.2 Overview of Hydrogen Storage Techniques

Hydrogen storage can be accomplished by various techniques.[1.14] Some of the more common options are compression as a gas, condensation as a liquid, absorption chemically by a solid, or adsorption physically to a solid. These methods will be reviewed in the succeeding subsections.

1.2.1 Compressed Gas

One of the simplest techniques to store a quantity of hydrogen is by compression. The amount stored depends on a balance between the size of the container and the maximum allowable system pressure from a safety perspective. The current state-of-the art compressed gas container from Quantum Technologies, Inc. is rated for a maximum storage pressure of 70 MPa (10,000 psi). The science behind this vessel, known as TriShield™ technology, uses aerospace-grade carbon fiber reinforcement to achieve the 2.35 safety factor required by current regulations.[1.15] While the container meets many of

the DOE targets, the high cost of carbon fiber reinforcement is motivating research for lower pressure alternatives.

The energy input required to compress hydrogen reduces its efficiency as a fuel. The work of adiabatic compression provides an estimate of this input since isothermal compression is not practical on a production scale. The adiabatic compression work is given by the following equation[1.16]

$$W = \left(\frac{\gamma}{\gamma - 1}\right) P_i V_i \left[\left(\frac{P_f}{P_i}\right)^{(\gamma-1)/\gamma} - 1\right] \tag{1.1}$$

where γ is the ratio of specific heat capacity, V is the specific volume, and the subscripts represent initial (i) and final (f) conditions. As seen in the DOE targets (Table 1.1), hydrogen for delivery to a fuel cell must be of suitable purity to prevent poisoning of the electrode catalysts. Note that the target is on a dry basis and vendor process specifications typically include water as one of the impurities. Pressure swing adsorption (PSA) is most commonly used to produce high purity hydrogen (99.999+%) from the effluent of steam reforming processes.[1.17] If one considers that hydrogen from the PSA purification process of a methanol steam-reforming plant is delivered at approximately 1.2 MPa (160 psig),[1.18, 1.19] the work of isothermal compression required to fill a cylinder to 70 MPa is approximately 8.6 MJ/kg, or 6% of the hydrogen HHV.

1.2.2 Cryogenic Liquid

Storage of hydrogen as a liquid is a lighter and more compact alternative to the compressed gas variant. Liquid hydrogen has a high density at low pressure, which reduces the size of the vessel required for an equivalent amount of fuel. Containers for

liquid hydrogen storage are frequently aluminum-lined and composite-wrapped with multi-layer vacuum superinsulation that reduces heat leak to the liquid.[1.20,1.21] Tanks must still be designed as pressure vessels and contain a substantial vapor space to prevent overpressurization as the liquid warms to the critical point due to heat leak. Energy intrusion is a significant concern for liquid hydrogen storage, as it causes vaporization and loss of hydrogen fuel even during idle periods.[1.22] The tank must be maintained below its burst pressure by venting some gas. A compact tank containing gas phase hydrogen at atmospheric pressure and 300 K would only allow for 0.4 km (0.25 mi) emergency driving range. This could potentially strand an unsuspecting driver upon rapid vaporization of the final amounts of liquid phase after extended inoperative periods.

A variant on liquid hydrogen storage at atmospheric pressure is a pressurized liquid storage system. Lawrence Livermore National Laboratory (LLNL) has developed a vessel that is capable of storing liquid hydrogen at 240 atm and 20 K.[1.20] The system has been demonstrated to vent less hydrogen relative to a low pressure one and contains enough residual hydrogen at 240 atm and 300 K to operate a fuel cell for nearly 97 km (60 mi). This option has shown flexibility to accept liquid or compressed hydrogen, thus increasing its applicability for production-scale vehicles.

As in the compression of hydrogen, the energy balance for its liquefaction must be considered to evaluate its effectiveness as a fuel. In order to produce liquid hydrogen, a substantial energy input is required due to its low normal boiling point (20.4 K). Sensible heat removal to cool hydrogen from ambient temperature to the boiling point dominates the energy requirement. The enthalpy change associated with sensible heat can be calculated from the enthalpy of gaseous hydrogen at these two temperatures.

$$\Delta h_{sh} = h_{g,20.4\ K} - h_{g,300\ K} \quad (1.2)$$

The enthalpies at these conditions are $h_{g,\ 20.4\ K}$ = 0.29 MJ/kg and $h_{g,\ 300\ K}$ = 4.23 MJ/kg, which yields $\Delta h_{sh} \cong$ - 3.94 MJ/kg.[1.23] The latent heat of vaporization at the normal boiling point of hydrogen is Δh_{vap} = 0.44 MJ/kg,[1.24] which is one-tenth of the overall theoretical energy required for liquefaction. The actual process for liquid hydrogen production operates at a Carnot efficiency of < 10% and varies with plant throughput.[1.12] A theoretical minimum energy demand of approximately 40 MJ/kg exists for large scale plants. This is 28% of the HHV of hydrogen.

1.2.3 Absorption by Intermetallic Compounds

Intermetallic compounds are well known for their hydrogen absorption capacities. They are often used as calibration or validation materials for volumetric or gravimetric sorption techniques. In practical application, the compounds would likely be deployed in powder or pellet form in a pressure vessel to lower the storage pressure for a given quantity of hydrogen. Table 1.1 lists some of the common metal composites along with their absorption capacities as well as some recently discovered high-capacity materials. Note that the reported capacity is a function of pressure and temperature, which can vary widely for each material.

The pressure-concentration behavior can influence the effectiveness of a material in a proposed storage system and often forms the basis for selection. Despite their relatively high storage capacities, metal hydrides have not seen widespread practical use because they often require a steep energy input to extract the absorbed hydrogen. Formation energies are often in the range of 13-58 MJ/kg, as Table 1.3 shows. An

additional consideration for practical application is the kinetic response of the materials, which is often quite slow. Equilibration time is often on the order of several hours for both absorption and release of stored hydrogen. Some intermetallic compounds are also quite sensitive to gas phase impurities, demonstrating reduced capacity, slower kinetics or both.[1.30]

There is promise for some intermetallics as composites or dopants with other materials that demonstrate improved kinetics and require less rigorous conditions to recover the stored hydrogen.[1.31-1.33] Transition metals that form hydrides are among several sources for hydrogen atoms that can spill over and adsorb to a receptor.[1.34-1.36] An overview of his phenomenon will be presented in subsection 1.3.

Table 1.3 Selected Metal Hydride Capacities and Enthalpies of Absorption

Metal	**Hydride**	**Capacity (wt%)**	**P_{eq}, T**	**$-\Delta H_f$ (MJ/kg-H_2)**
Pd	$PdH_{0.6}$	0.56	0.002 MPa, 298 K	20.5
Mg	MgH_2	7.6	0.19 MPa, 573 K	37.7
Ti	TiH_2	4.0	0.09 MPa, 909 K	62.8
V	VH_2	2.1	0.37 MPa, 313 K	29.3
FeTi	$FeTiH_2$	1.89	0.5 MPa, 303 K	14.0
$LaNi_5$	$LaNi_5H_6$	1.37	0.2 MPa, 298 K	15.5
Mg_2Ni	Mg_2NiH_4	3.59	0.1 MPa, 555 K	32.5
NaAl	$NaAlH_4$	8.0	9 MPa, 403 K	56.5
$Ti_{0.9}Al_{0.06}V_{0.04}$	$Ti_{0.9}Al_{0.06}V_{0.04}H_2$	3.8	0.1 MPa, 300 K	NR

P-C-T Data from References (1.25 - 1.27), ΔH_f adapted from References (1.26, 1.28, 1.29).

1.2.4 Adsorption to Solids

Adsorption is defined as the enrichment or depletion (desorption) of one or more components in an interfacial layer.[1.36] It can be classified as physical or chemical in nature. Physical adsorption is caused by intermolecular (van der Waals) forces and does not involve a significant change in the electronic orbital patterns of the interacting species.[1.25] Chemical adsorption involves chemical bond formation between the adsorbate and adsorbent surface and is an inherently stronger interaction. It is distinct from absorption in that it describes the interaction of a species on a solid surface rather than the penetration of that species into a solid mass.

Storage by adsorption is attractive for reasons similar to absorption because it has the potential to lower the overall system pressure for an equivalent amount of hydrogen, thus presenting a safer and commercially applicable alternative to compression or liquefaction. Adsorption offers additional benefits to absorption because the forces involved, particularly in physical adsorption, are weak enough to allow for near complete reversibility of adsorbed species at moderate temperatures and pressures. Since the adsorbate does not penetrate the solid lattice, the kinetics of charging and discharging are much faster than absorption by intermetallic compounds.

For high capacity, an adsorbent must provide significant area to accommodate adsorbate species on its surface. Adsorbents are frequently characterized with two well-known parameters that reflect their capacity, Brunauer-Emmett-Teller Surface Area (BET SA) and pore volume (PV).[1.37] The pore volume is further divided into micropore (< 20 Å) and mesopore volumes. Large micropore volumes contribute to high surface areas and increased interaction energy between the adsorbent and adsorbate. The pore dimension is

also critical to determining the strength of interaction. A solid will have a range of pore sizes based on its synthesis technique. The optimal pore size distribution (PSD) allows for maximum interaction (capacity) and facile transport (kinetics) based on the dimensions of the adsorbate. The PSD often forms the basis of the selection of an adsorbent for a targeted application. Table 1.4 lists several common adsorbents and their characteristic parameters.

Table 1.4 Properties of Selected Common Adsorbents

Adsorbent	BET SA (m^2/g)	Pore Volume		PSD Peak (Å)
		Total (mL[STP]/g)	Micro (mL[STP]/g)	
Activated Alumina[1.25]	325	0.2	0.1	> 20
5A Zeolite[1.38]	550	0.24	0.18	4.3
LD Silica Gel[1.25]	700	0.42	0.2	24
LiLSX Zeolite[1.39]	717	0.57	0.40	8.1
PCB Carbon[1.40]	1018	0.69	0.37	15
Maxsorb Carbon[1.41]	3100	1.75	1.5	10

The enthalpy of adsorption ($-\Delta H_{ads}$) is a measure of the strength of the interaction between the adsorbate and adsorbent, an analogy to the hydride formation enthalpy in Table 1.3. Near ambient temperature, $-\Delta H_{ads}$, is approximately equal to the adsorbent-adsorbate interaction potential, ϕ_{ads}. The interaction potential can be broken into contributions from dispersion energy (ϕ_D), close-range repulsion energy (ϕ_R), induction energy (ϕ_{Ind}), energy of interaction between and electric field and permanent dipole ($\phi_{F\mu}$), and interaction between a field gradient and a quadrupole ($\phi_{\dot{F}Q}$). Equations for the

calculation of these parameters are readily available in the literature and are summarized in Table 1.5.[1.42] The distance between the centers of the interacting pair, r, appears in all equations.

Table 1.5 Components of the Adsorbent-Adsorbate Interaction Potential

Interaction	Symbol	Equation	
Dispersion	ϕ_D	$-\frac{A}{r^6},\ A=\frac{6mc^2\alpha_1\alpha_2}{(\alpha_1/\chi_1+\alpha_2/\chi_2)}$	(1.3)
Close-Range Repulsion	ϕ_R	$\frac{B}{r^{12}},\ B=-\frac{Ar_0^6}{2}$	(1.4)
Field of Ion & Induced Dipole (Induction)	ϕ_{Ind}	$-\frac{\alpha q^2}{2r^4(4\pi\varepsilon_o)^2}$	(1.5)
Field of Ion & Permanent Dipole	$\phi_{F\mu}$	$-\frac{q\mu\cos\theta}{r^2(4\pi\varepsilon_o)}$	(1.6)
Field Gradient & Quadrupole	$\phi_{\dot{F}Q}$	$-\frac{Qq(3\cos^2\theta-1)}{4r^3(4\pi\varepsilon_o)}$	(1.7)

Constants: m = mass of electron, c = speed of light, α = polarizability, χ = magnetic susceptibility, q = electronic charge of ion on surface, ε_o = permittivity of vacuum, μ permanent dipole moment, θ = angle between field direction/gradient and axis of dipole/linear quadrupole, Q = linear quadrupole moment.

The hydrogen molecule does not have a permanent dipole moment, however, it has a significant quadrupole moment (+2.2 x 10^{-40} C m^2).[1.43] Forces of importance for the hydrogen-adsorbent interaction are ϕ_D, ϕ_R, ϕ_{Ind}, and $\phi_{\dot{F}Q}$. Calculation of the interaction potential for a given ion-hydrogen molecule tends to over predict the enthalpy of adsorption measured experimentally. This is because, in practice, ions in a zeolite structure are shielded from direct interaction with the molecule due to site configuration.[1.44] Although interaction potentials cannot be predicted exactly, trends have

been verified experimentally for low silica type X zeolites exchanged with cations Li^+, Na^+, and K^+.[1.39] The maximum capacity for physisorption of molecular hydrogen was 0.6 wt% at 298 K and 10 MPa for Li-LSX. This was nearly five times the adsorption capacity measured for 5A zeolite at 298 K and 5 MPa.[1.45, 1.46] Zeolites, while proving fully reversible due to lower interaction energies compared to metal hydrides, cannot achieve the hydrogen capacity required at moderate conditions for on-board storage application.

The adsorption of hydrogen to nanostructured carbon materials has been studied for over two decades.[1.47-1.49] Particular motivation was provided by the discovery of the interesting behavior of single-walled nanotubes (SWNTs).[1.47] Active carbon surfaces present enhanced interactions for adsorbing species due to oxygen functional groups that impart acidic or basic character.[1.25,1.50] These groups increase induction and field gradient-quadrupole interactions significantly compared to a clean graphitic carbon surface. It is possible to tune the carbon surface by simple wet chemical or gaseous treatments to achieve distributions of functional groups and pore size distributions. Active carbons with tuned distributions, investigated at cryogenic temperatures (77 K) and atmospheric pressure, have demonstrated hydrogen capacity of up to 3 wt% due to physisorption.[1.51] The capacity of active carbon and nanostructured carbons (SWNTs) is less than 1 wt% at ambient temperature and up to 10 MPa when storage is by physisorption of hydrogen molecules.[1.52]

The physisorption of molecular hydrogen on nanostructured carbons does not yield adequate capacity for on-board applications. If hydrogen could be stored atomically on a carbon-based material and maintain full reversibility, the adsorbent would have a theoretical capacity of 7.7 wt% for a 1:1 carbon-hydrogen interaction. This is equal to the

theoretical capacity calculated from filling 1.1 mL[STP]/g of pores with liquid hydrogen. Active carbons possess such high pore volumes and new carbons have been synthesized with pore volumes close to 2.0 mL[STP]/g.[1.41] Smaller radii of hydrogen atoms provide opportunity for increased interaction potential. Capacity enhancements for transition metal doped SWNTs have been reported in the literature and attributed to atomic hydrogen spillover.[1.36,1.53] Thus, there is promise for reversible, atomic storage of hydrogen on carbon-based adsorbents through the phenomenon of spillover.

1.3 A Brief History of Spillover Research

The phenomenon of spillover has been studied for nearly a half century. Numerous reviews have been published on the process for transition metal sources supported on adsorbents, or receptors.[1.54-1.56] Spillover is defined as the transport of an active adsorbed species from one phase onto another phase where it does not directly adsorb or form the species at the prevailing condition.[1.57] Once the transport occurs, the species may adsorb to the second phase or react either with adsorbed gases on the second phase or directly with it, thus serving to activate it. The first indirect proof of spillover was observed for hydrogenation of ethylene to ethane over platinum supported on silica (Pt/SiO_2) and alumina (Pt/Al_2O_3).[1.58] The conversions were higher for the platinum containing catalysts for temperatures of 373 K and 426 K. Khoobiar provided the first experimental proof of spillover at room temperature when the formation of tungsten bronzes (H_xWO_3) were documented for physical mixtures of tungsten oxide and platinum supported alumina (Pt/Al_2O_3).[1.59] Such bronzes were not formed upon room temperature exposure of hydrogen absent Pt/Al_2O_3. Following this study, spillover was verified by

uptake measurements at room temperature for Pt/SiO_2 and Pd/SiO_2[1.60] and researchers developed a mechanistic understanding of the bronze formation phenomenon.[1.61] The rate of hydrogen spillover from transition metal sources onto metal oxide receptors generally increases as temperature is increased and for the Pt/Al_2O_3 system, temperatures above 523 K are needed to show appreciable rates.[1.62]

Spillover of hydrogen with systems of transition metals doped on active carbons was studied primarily at elevated temperatures. These are conditions where most of the materials find application as supported catalysts. A mechanism was postulated for diffusion from platinum centers on active carbon (Pt/C) and the diffusion time constant (D/R^2) was calculated for 663 K (5×10^{-2} s^{-1}) and 573 K (3×10^{-4} s^{-1}).[1.63] These values were several orders of magnitude greater compared with those found on metal oxide supports.[1.57] The amount and rate of hydrogen spillover at 623 K was enhanced by carbon bridges formed during the doping process between the metal source and the support.[1.64] This behavior was verified at room temperature for a system with carbon bridges built with perylene precursor between platinum black and a ceria-exchanged Y zeolite support.[1.65,1.66]

Interest in spillover on nanostructured carbons at room temperature was driven by the observation that physical mixtures of Pt/C and Vulcan® XC72 active carbon (BET SA = 250 m^2/g) were found to exhibit spillover at 298 K when measured for hydrogen uptake and benzene hydrogenation activity.[1.67] Inelastic neutron scattering studies with physically mixed Pt/C and Ru/C fuel cell catalysts and Vulcan® active carbon have repeatedly demonstrated hydrogen spillover at room temperature.[1.68-1.70] The capacity of these systems are constrained by the structure of the active carbon support. Thus, tuning

the pore size distribution and surface of the support, increasing the support surface area, and improving the metal-support interaction via bridges or doping technique, could lead to an adsorbent with increased hydrogen capacity and facile kinetics that would be applicable for on-board storage application.

1.4 Objectives and Structure of This Dissertation

This dissertation has three main objectives: (1) synthesis and characterization of transition metal doped high surface area nanostructured carbons for hydrogen spillover and storage, (2) accurate measurement of hydrogen adsorption and spillover isotherms near ambient temperature, and (3) identification of the mechanism and kinetics of hydrogen spillover on carbon-based nanomaterials with isotopic tracers to provide routes for optimization of spillover adsorbents.

The chapters of this dissertation outline the background, experimental design, results, and analysis used to meet the objectives. The current chapter has provided an overview of the motivation for hydrogen storage research, current state-of-the art storage options, and briefly reviewed the phenomenon of spillover. Chapter 2 discusses the synthesis and characterization of carbon-based nanomaterials used in the study. Chapter 3 describes the use of volumetric techniques to measure hydrogen spillover and adsorption. Special consideration is given to apparatus design and calibration. Chapter 4 reviews the capacity of synthesized materials and provides kinetic analysis of selected primary and secondary spillover adsorbents. Chapter 5 provides details of the use of isotope tracers, namely deuterium and deuterium hydride, in sequential and equilibration dosing experiments to determine the mechanism for hydrogen spillover on carbon-based

nanomaterials. Chapter 6 presents a summary of the key findings, conclusions, and proposes future work to enhance and optimize the materials for on-board hydrogen storage application.

1.5 Literature Cited

[1.1] Demirdöven, N.; Deutch, J. *Science* **2004,** *305* (Aug 13), 974.

[1.2] O'Hayre, R.; Cha, S.-W.; Colella, W.; Prinz, F. B. *Fuel Cell Fundamentals*; Wiley & Sons: New York, 2005.

[1.3] EG&G Technical Services, Inc. *Fuel Cell Handbook*, 7th ed.; Report DOE/NETL-2004/1179; U.S. Department of Energy, National Energy Technology Laboratory: Morgantown, WV, 2004.

[1.4] Larminie, J.; Dicks, A. *Fuel Cell Systems Explained*, 2nd ed.; Wiley & Sons: New York, 2003; pp 170-172.

[1.5] Appleby, A. J.; Foulkes, F. R. *Fuel Cell Handbook*; Van Nostrand Reinhold: New York, 1989.

[1.6] Satyapal, S.; Petrovic, J.; Read, C.; Thomas, G.; Ordaz, G. *Catal. Today* **2007,** *120*, 246.

[1.7] Delucchi, M. A. *Hydrogen Fuel Cell Vehicles*; UCD-ITS-RR-92-14; Institute of Transportation Studies, University of California, Davis: Davis, CA, Sep 1992.

[1.8] Ferguson, C. R.; Kirkpatrick, A. T. Introduction to Internal Combustion Engines. In *Internal Combustion Engines: Applied Thermosciences*, 2nd ed.; Wiley & Sons: New York, 2001; pp 1-27.

[1.9] Plint, M.; Martyr, A. Thermal Efficiency and Measurement of Heat Losses – Ideal Standard Cycles. In *Engine Testing Theory and Practice*, 2nd ed.; Butterworth-Heinemann: Woburn, MA, 1999; pp 200-214.

[1.10] Schlapbach, L.; Züttel, A. *Nature* **2001,** *414*, 353.

[1.11] Schlapbach, L. *MRS Bull.* **2002,** *27*, 675.

[1.12] Eliasson, B.; Bossel, U.; Taylor, G. *The Future of the Hydrogen Economy: Bright or Bleak?* Report E02; European Fuel Cell Forum: Oberrohrdorf, Switzerland, Feb 26 2005.

[1.13] Ahluwalia, R. K.; Wang, X.; Rousseau, A. *J. Power Sources* **2005,** *152*, 233.

[1.14] Züttel, A. *Mater. Today* **2003,** *6* (9), 24.

[1.15] Dubno, W. *Low Cost, High Efficiency, High Pressure Hydrogen Storage*; 2007 Annual Progress Report for the DOE Hydrogen Program; U.S. Department of Energy: Washington, DC, 2007; p 608.

[1.16] Smith, J. M.; Van Ness, H. C. *Introduction to Chemical Engineering Thermodynamics*, 3rd ed.; McGraw-Hill: New York, 1975; p 472.

[1.17] Miller, G. Q.; Stöcker, J. *Selection of a Hydrogen Separation Process*; Report 3111; UOP LLC.; Des Plaines, IL, 1999.

[1.18] Yang, R. T. *Gas Separation by Adsorption Processes*; Imperial College Press: London, 1997; pp 255-258.

[1.19] Stöcker, J.; Whysall, M.; Miller, G. Q. *30 Years of PSA Technology for Hydrogen Purification*; Report 2818; UOP LLC.: Des Plaines, IL, 1998.

[1.20] Aceves, S. M.; Berry, G. D.; Martinez-Frias, J.; Espinosa-Loza, F. *Int. J. Hydrogen Energy* **2006,** *31*, 2274.

[1.21] Aceves, S. M.; Berry, G. D. *J Energy Res. Technol.* **1998,** *120*, 137.

[1.22] Wolf, J. *MRS Bull.* **2002,** *27*, 684.

[1.23] Liley, P. E.; Thomson, G. H.; Friend, D. G.; Daubert, T. E.; Buck, E. Section 2: Physical and Chemical Data. In *Perry's Chemical Engineers' Handbook*, 7th ed.; McGraw-Hill: New York, 1997; p 244-245.

[1.24] McCarty, R. D. In *Hydrogen: Its Technology and Implications, Hydrogen Properties*; Cox, K. E., Williamson, K. D., Eds.; CRC Press: Cleveland, 1975; Vol. 3, pp 25-26.

[1.25] Yang, R. T. *Adsorbents: Fundamentals and Applications*; Wiley & Sons: New York, 2005; p 307.

[1.26] Sastri, M. V. C. Introduction to Metal Hydrides: Basic Chemistry and Thermodynamics of Their Formation. In *Metal Hydrides: Fundamentals and Applications*; Sastri, M. V. C., Viswanathan, B., Srinivasa Murthy, S., Eds.; Springer-Verlag: New York, 1988; pp 1-21.

[1.27] Blackburn, J. L.; Parilla, P. A.; Gennett, T.; Hurst, K. E.; Dillon, A. C.; Heben, M. J. *J. Alloys Compd.* **2008,** *454*, 483.

[1.28] Smith, M. B.; Bass, Jr., G. E. *J. Chem. Eng. Data* **1963,** *8*, 342.

[1.29] Jensen, J. O.; Vestbø, A. P.; Li, Q.; Bjerrum, N. J. *J. Alloys Compd.* **2007,** *446-447*, 723.

[1.30] Schweppe, F.; Martin, M.; Fromm, E. *J. Alloys Compd.* **1997,** *253-254*, 511.

[1.31] Gross, K. J.; Thomas, G. J.; Jensen, C. M. *J. Alloys Compd.* **2002,** *330-332*, 683.

[1.32] Zaluski, L.; Zaluska, A.; Tessier, P.; Ström-Olsen, J. O.; Schulz, R. *J. Alloys Compd.* **1995,** *217*, 295.

[1.33] Wu, T.-I.; Wu, J.-K. *Mater. Chem. Phys.* **2003,** *80*, 150.

[1.34] Lachawiec, Jr., A. J.; Qi, G.; Yang, R. T. *Langmuir* **2005,** *21*, 11418.

[1.35] Haluska, M.; Hirscher, M.; Becher, M.; Dettlaff-Weglikowska, U.; Chen, X.; Roth, S. *Mater. Sci. Eng., B* **2004,** *108*, 130.

[1.36] Becher, M.; Haluska, M.; Hirscher, M.; Quintel, A.; Skakalova, V.; Dettlaff-Weglikovska, U.; Chen, X.; Hulman, M.; Choi, Y.; Roth, S.; Meregalli, V.; Parrinello, M.; Ströbel, R.; Jörissen, L.; Kappes, M. M.; Fink, J.; Züttel, A.; Stepanek, I.; Bernier, P. *C. R. Phys.* **2003,** *4*, 1055.

[1.37] Gregg, S. J.; Sing, K. S. W. *Adsorption, Surface Area and Porosity*, 2nd ed.; Academic Press: London, 1982.

[1.38] Díaz, E.; Ordóñez, S.; Vega, A.; Coca, J. *Thermochim. Acta* **2005,** *434*, 9.

[1.39] Li, Y.; Yang, R. T. *J. Phys. Chem. B* **2006,** *110*, 17175.

[1.40] Bashkova, S.; Bagreev, A.; Bandosz, T. J. *Catal. Today* **2005,** *99*, 323.

[1.41] Otowa, T.; Tanibata, R.; Itoh, M. *Gas. Sep. Purif.* **1993,** *7*, 241.

[1.42] Yang, R. T. Nanostructured Adsorbents. In *Nanostructured Materials*; Ying, J., Ed.; Advances in Chemical Engineering; Academic Press: New York, 2001; Vol. 27, p 79-124.

[1.43] Prausnitz, J. M.; Lichtenthaler, R. N.; Gomes de Azevedo, E. *Molecular Thermodynamics of Fluid-Phase Equilibria*, 3rd ed.; Prentice-Hall: New York, 1999; p 65.

[1.44] Kang, L.; Deng, W.; Han, K.; Zhang, T.; Liu, Z. *Int. J. Hydrogen Energy* **2008,** *33*, 105.

[1.45] Nam, G. M.; Jeong, B. M.; Kang, S. H.; Lee, B. K.; Choi, D. K. *J. Chem. Eng. Data* **2005,** *50*, 72.

[1.46] Chen, Y. D.; Ritter, J. A.; Yang, R. T. *Chem. Eng. Sci.* **1990,** *45*, 2877.

[1.47] Dillon, A. C.; Jones, K. M.; Bekkedahl, T. A.; Kiang, C. H.; Bethune, D. S.; Heben, M. J. *Nature* **1997,** *386*, 377.

[1.48] Noh, J. S.; Agarwal, R. K.; Schwarz, J. A. *Int. J. Hydrogen Energy* **1987,** *12*, 693.

[1.49] Panella, B.; Hirscher, M.; Roth, S. *Carbon* **2005,** *43*, 2209.

[1.50] Bansal, R. C.; Goyal, M. *Activated Carbon Adsorption*; CRC Press: Boca Raton, FL, 2005.

[1.51] Nijkamp, M. G.; Raaymakers, J. E. M. J.; van Dillen, A. J.; de Jong, K. P. *Appl. Phys. A* **2001,** *72*, 619.

[1.52] Hirscher, M.; Becher, M.; Haluska, M.; von Zeppelin, F.; Chen, X.; Dettlaff-Weglikowska, U.; Roth, S. *J. Alloys Compd.* **2003,** *356-357*, 433.

[1.53] Lueking, A. D.; Yang, R. T. *Appl. Catal., A* **2004,** *265*, 259.

[1.54] Wang, L.; Yang, R. T. *Energy Environ. Sci.* **2008,** *1*, 268.

[1.55] Conner, Jr.; W. C.; Falconer, J. L. *Chem. Rev.* **1995,** *95*, 759.

[1.56] Bond, G. C. *Stud. Surf. Sci. Catal.* **1983,** *17*, 1.

[1.57] Conner, Jr.; W. C. Spillover of Hydrogen. In *Hydrogen Effects in Catalysis: Fundamentals and Practical Applications*; Paál, Z., Menon, P. G., Eds.; Marcel Dekker, Inc.: New York, 1988; Vol. 31, p 311-346.

[1.58] Sinfelt, J. H.; Lucchesi, P. J. *J. Am. Chem. Soc.* **1963,** *85*, 3365.

[1.59] Khoobiar, S. *J. Phys. Chem.* **1964,** *68*, 411.

[1.60] Boudart, M.; Vannice, M. A.; Benson, J. E. *Z. Phys. Chem. Neue Fol.* **1969,** *64* (S), 171.

[1.61] Levy, R. B.; Boudart, M. *J. Catal.* **1974,** *32*, 304.

[1.62] Kramer, R.; Andre, M. *J. Catal.* **1979,** *58*, 287.

[1.63] Robell, A. J.; Ballou, E. V.; Boudart, M. *J. Phys. Chem.* **1964,** *68*, 2748.

[1.64] Boudart, M.; Aldag, A. W.; Vannice, M. A. *J. Catal.* **1970,** *18*, 46.

[1.65] Neikam, W. C.; Vannice, M. A. *J. Catal.* **1972,** *27*, 207.

[1.66] Vannice, M. A.; Neikam, W. C. *J. Catal.* **1971,** *20*, 260.

[1.67] Srinivas, S. T.; Rao, P. K. *J. Catal.* **1994,** *148*, 470.

[1.68] Ramirez-Cuesta, A. J.; Mitchell, P. C. H.; Parker, S. F.; Tomkinson, J.; Thompsett, D. *Stud. Surf. Sci. Catal.* **2001,** *138*, 55.

[1.69] Mitchell, P. C. H.; Ramirez-Cuesta, A. J.; Parker, S. F.; Tomkinson, J. *J. Mol. Struct.* **2003,** *651-653*, 781.

[1.70] Mitchell, P. C. H.; Ramirez-Cuesta, A. J.; Parker, S. F.; Tomkinson, J.; Thompsett, D. *J. Phys. Chem. B* **2003,** *107*, 6838.

Chapter 2

Synthesis and Characterization of Carbon-Based Nanomaterials

2.1 Introduction to Nanostructured Carbon-Based Adsorbents

Carbon-based adsorbents are the most widely used materials in the gas separation, purification, and catalysis field, outselling molecular sieve zeolites by one order of magnitude.[2.1] The most common carbon materials for industrial use have been classified as active (or activated) carbons, owing to the procedures used to 'activate' or modify the structure of the adsorbent for a specific application. Indeed, it is the facility to tailor the adsorbent that supports its broad range of applications.

All active carbons originate from organic sources but the final structural form is governed by the synthesis route and post-synthesis treatments.[2.2,2.3] Source materials have been wood, coals, petroleum coke, coconut shell, and fruit nuts, among others.[2.4] Such materials are carbonized at temperatures up to 773 K to remove volatiles. The product is activated by gaseous or chemical techniques to develop porosity and increase surface area. Gas phase methods are performed in oxygen, carbon dioxide, or steam at temperatures up to 1273 K. The gas phase and temperature impact the pore structure of the final product. Oxygen is an aggressive activation species, gasifying carbon at a rate five orders of magnitude greater relative to carbon dioxide or steam. The latter molecules are used more frequently for mild activation and development of a uniform pore

structure. Chemical methods often involve the addition of inorganic species in solution, which subsequently act on the precursor materials prior to or during carbonization. An activation technique commonly known to those skilled in the art is the use of potassium hydroxide (KOH) in solid form during carbonization.[2.5-2.8] The process develops an extensive microporous structure that contributes to high surface areas (3000 m^2/g), leading to the classification of 'superactivated' carbons. A commercial product based on this technique, developed as AX-21 and commercially marketed as MAXSORB, has found wide applications in the adsorption community and is one of the hydrogen spillover receptors in this work.[2.9-2.10]

The microcrystalline structure of active carbon forms during the carbonization step. Although similar to the graphite lattice, the interlayer spacing is larger (3.4 – 3.5 Å) and the layers are disordered due to heteroatoms (oxygen or hydrogen) and defects.[2.3] These heteroatoms and defects may be exploited with various post-production treatments to further tune the surface for a particular application. Liquid or gas phase treatments are used to increase or decrease the type and number of oxygen functional groups present on the edges of the carbon layer planes. Some of these groups are shown in Figure 2.1. Oxidizing treatments yield groups of acidic character, as in (a) through (e). Basic or inert annealing treatments tend to remove oxygen functionalities, forming the basic groups of (f) and (g). In the liquid phase, an acidic surface exhibits enhanced cation exchange properties, while a basic surface demonstrates superior anion exchange capacity. This is important for doping transition metals, as most procedures use incipient wetness with a metal salt in solution.

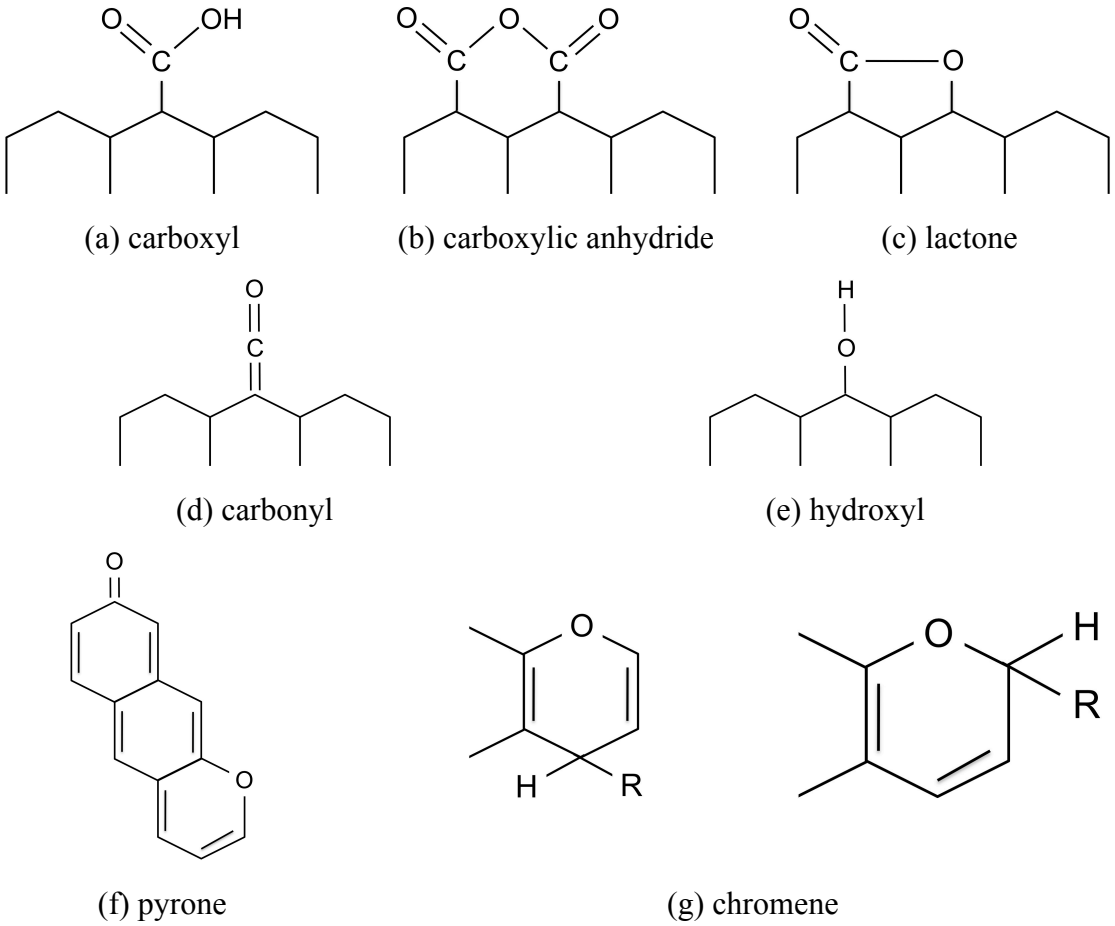

Figure 2.1 Oxygen Functionalities on Carbon Layer Edges

2.2 Adsorbents for Spillover

The nanostructured carbon-based adsorbents used in this work are a subset of the broader classification of active carbons. They consist of a composite of two or more materials comprising a spillover source and a spillover receptor. Several features characterize an effective spillover source. It should be capable of dissociating hydrogen molecules near ambient conditions. It must be well dispersed on a carbon-based substrate so that it exposes maximum metal surface while not obstructing receptor pores. It must have a strong interaction with the receptor to provide facile pathways for atomic hydrogen diffusion and to prevent sintering or agglomeration during pretreatment or

regeneration. Although edge functionalities on graphite sheets have demonstrated dissociative capacity,[2.12] the most frequently employed spillover sources are nanoscale transition metal particles.

Spillover receptors should have ample capacity for hydrogen atoms. This makes carbon-based materials attractive and discounts classical adsorbents such as molecular sieves, alumina, and silica based on the capacities observed for molecular hydrogen at ambient conditions. Although hydrogen physisorption capacities of active carbons are typically < 0.6 wt% at ambient temperature,[2.13] storage of hydrogen as atoms yields a maximum theoretical capacity of nearly 8 wt% (H/C = 1). Carbon-based materials provide tractable routes for synthesis of hydrogen adsorbents since their surfaces may be readily tuned for high metal dispersion and discrete pore size distributions. Despite the dissociative mechanism being common to both spillover on carbon-based adsorbents and metal hydrides, hydrogen atoms are not incorporated (absorbed) into the carbon structure; thus, kinetic behavior of these adsorbents is more favorable.

Spillover is a transport process that relies on diffusion of hydrogen atoms across a chemical potential gradient. A physical pathway for hydrogen atoms to 'hop' on the surface promotes the process.[2.14] One way to provide this pathway is to create a strong source-receptor interaction by the selection of doping technique. An alternative is to create a physical bridge between the two components. Both techniques were studied in this work. Some precedent for bridge building exists. The formation of coke bridges during reduction of active carbon composites was implicated in spillover at 623 K.[2.15] Introduction of a bridge precursor was used to generate catalysts for dehydrogenation reactions at similar temperatures.[2.16] The bridge building process opens new avenues for

composites because the method can be used to couple existing commercial catalysts to newly developed receptors. Figure 2.2 depicts such a situation in which a transition metal (M) supported on active carbon serves as the primary receptor. Such materials are readily available as commercial catalysts. A bridge has been formed between this material and a nanostructured secondary receptor designed with consideration for hydrogen storage. In this situation, there are two corresponding phases of hydrogen spillover – primary and secondary. The synthesis of materials according to this method will be discussed in succeeding sections.

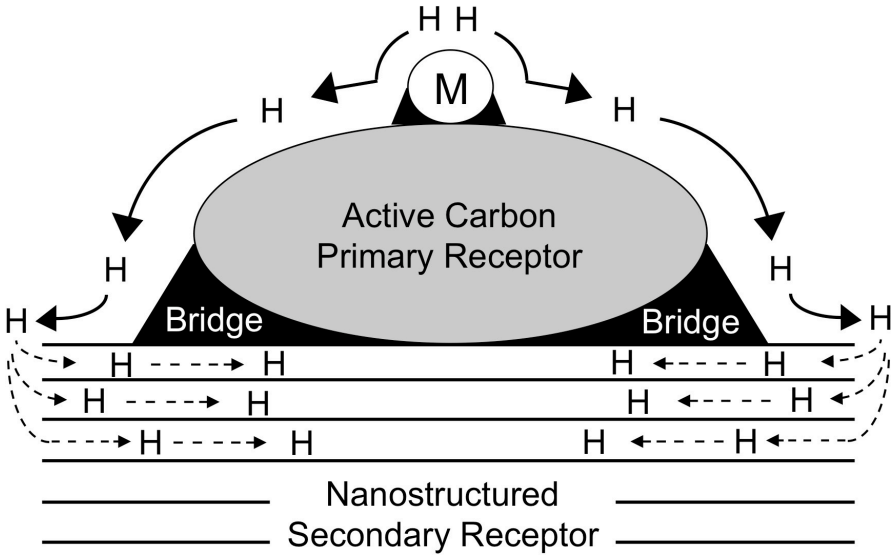

Figure 2.2 Primary and Secondary Spillover from Source (M) to Receptor

2.3 Receptor Synthesis

All synthesis and analytical characterization gases were ultra-high purity (99.999%) and purified at point-of-use using molecular sieve 3A zeolite adsorbent beds. All reagents were analytical grade or better, as specified for a particular synthesis.

2.3.1 Templated Carbon (TC) Procedure

Carbons formed from zeolite templates have the benefits of active carbons, such as functionalized surfaces, microporosity, and large surface areas, with structural regularity imparted by the zeolite.[2.17-2.19] The synthesis procedure generally followed the work of Ma et al.[2.20-2.22] The materials and amounts per gram of final product yield are shown in Table 2.1.

Table 2.1 Materials for Production of Templated Carbon

Material	Chemical Formula	CAS Number	Amount (per g carbon)
Ammonium Y Zeolite	$0.21Na_2O \cdot 0.79(NH_4)_2O \cdot Al_2O_3 \cdot 5.1SiO_2 \cdot yH_2O$	1318-02-1	5 g
Furfuryl Alcohol	$C_5H_6O_2$	98-00-0	20 mL
Mesitylene	$C_6H_3(CH_3)_3$	108-67-8	5 mL

Synthesis of templated carbon began with ammonium Y zeolite (Zeolyst International, CBV 300) as the pattern material. Y zeolite has a skeletal structure identical naturally occurring faujasite, with an aperture size of 7.4 Å.[2.21] The powder was dehydrated at 423 K under rough vacuum (0.013 mbar) for 6 h in a Pyrex® Erlenmeyer flask fitted with an addition funnel. This temperature was suitable to remove most of the water of hydration but leave a significant amount of ammonium ions in the structure.[2.23] After the zeolite was cooled to room temperature under vacuum, furfuryl alcohol was added while slowly stirring. The zeolite changed color from white to amber and there was excess liquid in the flask. The mixture was stirred under a nitrogen atmosphere, maintained by trickle purge, for 8 h. The suspension was filtered to remove excess

furfuryl alcohol and rinsed three times with mesitylene. The filtrand was dried in air at room temperature for 24 h, resulting in a gray-green solid.

The impregnated zeolite was treated in flowing nitrogen (100 mL(STP)/min) in a horizontal quartz furnace. Two sequential temperature programs were employed to dehydrate the solid (5 K/min to 353 K, hold 24 h) and to polymerize furfuryl alcohol (5 K/min to 423 K, hold 8 h). After this treatment, the solid turned a tan color, indicative of polymerization products.

The tan solid was transferred to a vertical quartz reactor for carbonization and chemical vapor deposition (CVD) of carbon. The material was heated in flowing nitrogen (100 sccm) to 973 K (5 K/min) to carbonize the polymerization products. The temperature was held at 973 K for 4 h and the gas was changed to 2% propylene in nitrogen (240 mL(STP)/min). The flow rate was chosen to match the space velocity used by Ma et al.[2.20] for a 2.54 cm diameter tube. A final annealing step was performed in nitrogen (5 K/min to 1173 K, hold 3 h). The material was cooled to room temperature (5 K/min) under nitrogen flow (100 mL(STP)/min) and the product was a black powder.

The zeolite-carbon composite was given two treatments to remove the zeolite template. It was first treated with 48% hydrofluoric acid (9 mL/g-composite) in a polypropylene beaker. There was a significant release of heat when HF was added to the beaker. The solution was stirred for 3 h at room temperature and rinsed with deionized water in a filtration funnel. The product collected on a filter paper (0.5 μm pore size) was transferred to a Pyrex® Erlenmeyer flask. It underwent a second treatment with concentrated 37% hydrochloric acid (19 mL/g-composite) to remove remaining zeolite template. The solution was heated to 333 K and stirred under reflux for 3 h. After cooling

to room temperature, the solution was filtered with deionized water until the rinses were pH neutral. The templated carbon was dried in air at 393 K for 24 h, resulting in a fine black powder.

2.3.2 Single-Walled Nanotube (SWNT) Procedure

Synthesis of SWNT was performed following the procedure of Cassell et al.[2.24] The process involved catalyst synthesis, chemical vapor deposition (CVD) to form the nanotubes, and purification to remove the catalyst.

Table 2.2 Materials for Production of SWNT Catalyst

Material	Chemical Formula	CAS Number	Amount (per g catalyst)
Alumina (fumed)	Al_2O_3	1344-28-1	1 g
Iron (III) Sulfate Hydrate	$Fe_2(SO_4)_3 \cdot xH_2O$	15244-10-7	120 mg
Ammonium Molybdate	$(NH_4)_6Mo_7O_{24} \cdot 4H_2O$	12054-85-2	18 mg
Water	H_2O	7732-18-5	70 mL

Alumina (AEROXIDE® Alu C, Degussa/Evonik Industries) was suspended in deionized water. The metal hydrates were ground into fine powder with an agate mortar and pestle. The solid hydrates were added to the suspended alumina; first ammonium molybdate followed by iron (III) sulfate and mixed using a magnetic stirrer and Teflon® coated stir bar for 30 min. The solution was sonicated for 30 min to ensure full solids dissolution and mixing. The solution was returned to the stirrer and heated at 343 K with an air purge to aid evaporation. When a paste formed, the mixture was removed from the

stirrer and dried overnight in an oven at 373 K. The dry solid was removed from the beaker and ground into a fine orange powder using an agate mortar and pestle.

The catalyst (100 mg) was loaded into a vertical quartz tube reactor and suspended on a quartz frit. A thermocouple was placed above the frit inside the tube for accurate temperature measurement. The catalyst was calcined in flowing air (115 mL(STP)/min) at 773 K for 1 h. The gas was switched to helium (100 mL(STP)/min) and the catalyst was heated to 1223 K (5 K/min). Upon reaching 1223 K, the gas phase was changed to a 10% methane/helium mixture (400 mL(STP)/min) and chemical vapor deposition was performed for 45 min. The hydrocarbon was diluted to limit amorphous carbon formation. The material was cooled to room temperature (5 K/min) in flowing helium (100 mL(STP)/min). The product was a black powder comprising a mixture of catalyst and nanotubes.

The nanotube-catalyst composite was subjected to three acid treatments to fully remove catalyst particles and amorphous carbon. The first acid treatment was performed in a polypropylene test tube by mixing the solid product with 48% hydrofluoric acid (50 mL/g-composite). This treatment released significant heat and the tube was allowed to cool to room temperature before placing it on a shaker table for 24 h. The well-mixed suspension of nanotubes was filtered through 0.5 μm paper and rinsed with deionized water until the rinses were pH neutral. The product was dried overnight at 373 K. The second acid treatment was performed in a Pyrex® Erlenmeyer flask using 4 M nitric acid (50 mL/g-nanotubes). Treatment in nitric acid was performed three times at 348 K under reflux for 1 h with deionized water rinses between each. The final acid treatment was performed in a Pyrex® Erlenmeyer flask with concentrated sulfuric acid (50 mL/g-

nanotubes). The treatment was performed once at 348 K for 30 min. Both nitric and sulfuric acid treatments selectively attacked amorphous carbon, increasing the purity of SWNTs. After washing with deionized water until the rinses were pH neutral, the SWNTs were dried in a 373 K oven. Yield was 25% of the catalyst-nanotube composite.

2.3.3 Graphite Nanofiber (GNF) Procedure

Synthesis of catalyst and chemical vapor deposition followed the procedure of Kim et al.[2.25] The catalyst was bimetallic and its composition was 8:2 Ni/Cu. Table 2.3 lists the compounds and amounts required for synthesis of this material.

Table 2.3 Materials for Production of GNF Catalyst

Material	Chemical Formula	CAS Number	Amount (per g catalyst)
Nickel(II) Nitrate Hexahydrate	$Ni(NO_3)_2 \cdot 6H_2O$	13478-00-7	3.9 g
Copper(II) Nitrate Hemipentahydrate	$Cu(NO_3)_2 \cdot 2.5H_2O$	19004-19-4	0.78 g
Ammonium Bicarbonate	NH_4HCO_3	1066-33-7	2.9 g
Water	H_2O	7732-18-5	25 mL

Catalyst synthesis by precipitation began with the dissolution of the nitrates in water and dilution to correspond to 5 g nickel or copper oxide per 100 mL of solution. As the solution was rapidly stirred at room temperature, ammonium bicarbonate was added until a permanent turbidity formed. Immediately after the turbidity was established, excess ammonium bicarbonate (2.2 moles/mole metal ion) was added and the solution

was stirred for 15 min as carbon dioxide was evolved from the mixture. The precipitation reactions in this step were

$$\mathrm{Ni(NO_3)_2 \cdot 6H_2O(s) + 2NH_4HCO_3(s) \rightarrow NiCO_3(s) + 2NH_3(l) + 2HNO_3(l) + 7H_2O(l) + CO_2(g)} \quad (2.1)$$

$$\mathrm{Cu(NO_3)_2 \cdot 3H_2O(s) + 2NH_4HCO_3(s) \rightarrow CuCO_3(s) + 2NH_3(l) + 2HNO_3(l) + 4H_2O(l) + CO_2(g)} \quad (2.2)$$

The precipitate was allowed to settle overnight in a covered flask. Hot deionized water was used to wash the precipitate until the washings were colorless, indicating the absence of ammonium or nitrate ions. After decanting the final washing, the liquid in the precipitate was evaporated over a steam bath until the solid was of putty-like consistency. The solid was dried for 24 h in an oven at 383 K. The dried solid was ground to a fine powder using an agate mortar and pestle and calcined in a muffle furnace at 673 K for 4 h. The calcination process converted the carbonates to metal oxide form.

$$\mathrm{NiCO_3(s) \xrightarrow{\Delta,air} NiO(s) + CO_2(g)} \quad (2.3)$$

$$\mathrm{CuCO_3(s) \xrightarrow{\Delta,air} CuO(s) + CO_2(g)} \quad (2.4)$$

The catalyst (50 mg) was transferred to a quartz boat and inserted into a horizontal quartz reactor for reduction and chemical vapor deposition (CVD) growth of nanofibers. It was reduced in flowing hydrogen (100 mL(STP)/min) at 773 K for 20 h. In order to prepare for CVD, the gas phase was changed to 10% hydrogen in helium and the temperature was increased to 873 K at 2.5 K/min. CVD was performed at 873 K with a 4:1 ethylene/hydrogen mixture at a total flow rate of 100 mL(STP)/min for 1.5 h. After nanofiber synthesis, the reactor was cooled to room temperature in flowing helium (100 mL(STP)/min. Yield was typically 3.5 g raw GNF per g-catalyst.

The raw nanofibers were purified by stirring in a solution of 1 M HCl (25 mL/g raw GNF) at room temperature for 24 h. This facilitated the removal of catalyst particles while maintaining the nanostructure integrity.[2.26] The product was filtered and washed with deionized water until the rinses were pH neutral. The purified GNFs were dried overnight in an oven at 373 K prior to characterization.

2.3.4 Sol-Gel Mesoporous Carbon (SGC) Procedure

The sol-gel carbonization procedure produces a material with a distribution of mesopores. The micropore volume is small and does not contribute significantly to the surface area available for adsorption. This type of material often finds application in catalytic processes involving large hydrocarbon molecules.[2.27] For this study, the sol-gel carbon provides a useful comparison of hydrogen adsorption behavior in different pore networks. The synthesis process also provides the opportunity to incorporate transition metal species directly into the carbon structure.[2.28]

Table 2.4 Materials for Production of Sol-Gel Carbon

Material	Chemical Formula	CAS Number	Amount (per g carbon)
Tetraethyl Orthosilicate	$Si(OC_2H_5)_4$	78-10-4	8.5 mL
Hydrochloric Acid	HCl	7647-01-0	0.046 mL
Ethanol	C_2H_5OH	64-17-5	13.5 mL
Water	H_2O	7732-18-5	11.9 mL
Sucrose	$C_{12}H_{22}O_{11}$	57-50-1	3.5 g

The synthesis procedure followed the method of Hu et al.,[2.28] omitting transition metal salt addition to generate pure mesoporous carbon. Tetraethyl orthosilicate (TEOS),

ethanol, deionized water and hydrochloric acid were mixed together while heating to 333 K. The solution was stirred for 4 h while maintaining this temperature. Sucrose dissolved in deionized water (0.45 g sucrose/mL) was added and this solution was stirred for 1 h. After cooling to room temperature, the material was dried in air for 2 days. The resulting nanocomposite was broken into small pieces for carbonization.

Carbonization was performed in a horizontal quartz tube reactor under 100 mL(STP)/min helium. The temperature was raised to 1173 K at 2.5 K/min and held for 4 h. The inverse temperature program was used to cool the reactor to room temperature. A coarse black powder resulted from the carbonization reaction. The silica template was removed by treating the powder with 48% hydrofluoric acid (1.5 mL/g nanocomposite) at while stirring at room temperature for 6 h. The solution was filtered and the mesoporous carbon product was rinsed ten times with deionized water. The carbon was dried in an oven at 373 K overnight before characterization studies. Yield was 30% of the carbonized gel.

2.4 Synthesis of Source-Receptor Composites

2.4.1 Primary Spillover: Direct Doping of Receptor

Nanostructured carbon receptors were doped with transition metals to promote primary spillover. The doping procedure involved solution impregnation of a selected metal salt. Catalyst doping is usually performed in aqueous solution; however, carbon is generally hydrophobic without applying special treatments. The Young-Dupré equation relates the work of adhesion to fluid surface tension and contact angle.[2.29]

$$W_a = \gamma_{LV}(1+\cos\theta) \tag{2.5}$$

At room temperature, the surface tension of water is 72.0 mN/m and that of acetone is 22.7 mN/m.[2.30] The contact angle is approximately 82° for water and 45° for acetone on graphite or carbon nanostructures.[2.31,2.32] The work of adhesion for water and acetone on carbon nanofibers is calculated as 82 mN/m and 39 mN/m, respectively. A lower value for adhesion work indicates that less energy must be overcome for the liquid to spread. As this calculation indicates, acetone is predicted to spread more easily on carbon nanofibers - a result that has been confirmed by observations in this work and by others.[2.33,2.34] This result supports the choice of acetone as the solvent for doping carbon.

The doping method was similar to that used by Joo et al. to generate high dispersions of platinum nanoparticles on nanostructured carbon.[2.35] The procedure began by suspending the desired carbon receptor in acetone (HPLC grade) at a ratio of 100 mL/g receptor and stirring for 20 min. Hexachloroplatinic acid hydrate ($H_2PtCl_6 \cdot 6H_2O$, Aldrich 398322) was dissolved in acetone at a ratio of 60 mL/g salt. The amount of metal salt required was determined by the desired final metal content of the composite, considering that platinum was only 37.5 wt% of the dopant. A typical batch was 200 mg of carbon receptor, which was doped to a final platinum content of 6 wt%. This required 34 mg of metal salt to deliver 12.8 mg of platinum. The solution of acetone and metal salt was added drop wise to the carbon receptor-acetone mixture while moderately stirring. The mixture was transferred to a water bath where it was treated with ultrasound for 1 h. Ultrasound enhanced doping has been shown to promote spillover through increased source-receptor interaction and metal dispersion.[2.36-2.38] The procedure was modified slightly from that followed by Li et al.[2.37] to allow for sonication of the slurry in a polyethylene bag. This step was performed to decrease sonic wave attenuation that occurs

using laboratory glassware[2.39] and subsequently improve metal-support interaction. After sonication, the mixture was stirred at room temperature for 24 h. Acetone was evaporated and the sample was dried in an oven at 333 K for 8 h.

The doped carbon material was degassed and reduced prior to characterization and hydrogen capacity measurements. The sample was placed in a quartz boat and inserted into a horizontal quartz reactor for treatment. It was degassed in flowing helium (100 mL[STP]/min) at 393 K for 2 h. The gas phase was switched to flowing hydrogen (120 mL[STP]/min) while the temperature was raised to 573 K (1 K/min) and held for 3 h. The sample was cooled in hydrogen and purged with helium to prepare for transfer to storage or analytical instruments. Table 2.5 lists the adsorbents prepared in this manner for this work.

Table 2.5 Materials Prepared to Study Primary Spillover

Receptor	Source	Metal Salt	Short Name
Templated Carbon	Platinum	$H_2PtCl_6 \cdot 6H_2O$[a]	6 wt% Pt/TC
Templated Carbon	Platinum	$H_2PtCl_6 \cdot 6H_2O$	1.5 wt% Pt/TC
Templated Carbon	Platinum	$H_2Pt(OH)_6$[b]	6 wt% Pt/TC
Templated Carbon	Nickel	$NiCl_2$[c]	6 wt% Ni/TC
Templated Carbon	Palladium	$PdCl_2$[d]	6 wt% Pd/TC
AX-21	Platinum	$H_2PtCl_6 \cdot 6H_2O$	6 wt% Pt/AX-21
Graphite Nanofibers	Platinum	$H_2PtCl_6 \cdot 6H_2O$	6 wt% Pt/GNF
Sol-Gel Carbon	Palladium	$Pd(NH_3)_2(NO_2)_2$ (aq)[e]	5 wt% Pd/SGC
Sol-Gel Carbon	Nickel	$Ni(NO_3)_2 \cdot 6H_2O$[f]	5 wt% Ni/SGC

(a) hexachloroplatinic acid (Aldrich 398322); (b) hydrogen hexahydroxyplatinate(IV) (Aldrich 334472); (c) nickel(II) chloride (Aldrich 339350); (d) palladium(II) chloride (Adrich 323373); (e) diamminepalladium(II) nitrite, 5% solution (Strem 46-0329); (f) nickel(II) nitrate hexahydrate (Aldrich 203874)

Sol-gel carbon composites were prepared to study primary spillover from sources that were included in the receptor synthesis procedure, rather than doped after synthesis. The procedure followed that outlined in Section 2.3.4 with the appropriate amount of metal salt incorporated during addition of sucrose solution.[2.28] Such materials synthesized for study are noted in Table 2.5.

2.4.2 Secondary Spillover: Bridging Primary Source to Receptor

There were two bridged spillover sources used in this work: 5 wt% Pt/Active Carbon (Strem Chemicals, Inc., 78-1600) and 5 wt% Pd/Active Carbon (Strem Chemicals, Inc., 46-1890). These were selected because they are readily available and well characterized commercial catalysts.

D-Glucose ($C_6H_{12}O_6$) was used as the bridge precursor. Glucose was selected because it has a relatively low melting point (~ 423 K) and easily carbonizes at a temperature that does not sinter metal supported catalysts or destroy structure in nanostructured receptors. Glucose and other simple sugars (e.g. sucrose) have been used to generate active carbon adsorbents.[2.40,2.41] In principle, alternative precursors may be used with modification to the temperature program required for bridge building.[2.42] The theoretical carbonization reaction is

$$C_6H_{12}O_6(s) \xrightarrow{\Delta} 6C(s) + 6H_2O(g) \qquad (2.6)$$

The yield of carbon from the decomposition of glucose should theoretically be 0.4 g/g-glucose. Since there are additional reactions and dewatering that may occur during heating, an experiment was conducted to determine the actual carbon yield. The amount of glucose precursor was adjusted according to the results of the preliminary

carbonization experiment. Glucose melting and decomposition was carried out using at Shimadzu Thermogravimetric Analyzer (TGA-50) in flowing helium (100 mL(STP)/min). The glucose sample (20 mg) was suspended in a quartz pan and heated to 453 K (at 1 K/min) where it was held for 1 h. The sample was heated from 453 K to 673 K (at 1 K/min) where it was held for 6 h to carbonize the material. The sample was cooled to room temperature at 1 K/min. The results of the TGA experiment are shown in Figure 2.3. When the glucose is heated and maintained at 453 K, it loses 13 wt%. Some dewatering and decomposition reactions occur at these conditions.[2.43,2.44] The temperature program to 673 K results in a net loss of 86.5 wt% of sample as carbonization occurs, compared to a theoretical loss of only 60 wt%. Similar results were obtained for a larger (1 g) sample in a horizontal quartz reactor. The actual carbon yield of 0.135 g/g-glucose (34% of the theoretical value) was used in all calculations for required bridge precursor amounts.

Carbon formed from the glucose precursor does not contribute significant surface area (< 2 m^2/g),[2.45,2.46] thus, it is critical to position this bridge only where necessary to facilitate spillover but not block pores. The melting step of the program was selected so that liquid glucose wicks into the interstices between the secondary receptor and source prior to carbonization. At room temperature, the surface tension reported for corn or glucose syrup is similar to water and the corn syrup contact angle is 63°, which is less than water.[2.47,2.48] As the temperature is increased, the surface tension of most liquids decreases according to the Eötvös theory.[2.49] On this basis, the wetting characteristics of glucose are predicted to be better than those of water at room temperature.

Production of secondary spillover adsorbents for this study began with grinding of a mixture of the receptor, bridge precursor, and source using an agate mortar and pestle for 30 min.[2.50] The proportion of receptor-bridges-source was fixed at 8:1:1 based on hydrogen spillover results of Srinivas and Rao for physical mixtures of Pt/C source catalysts and active carbon receptors.[2.51] The glucose added to the mixture was adjusted given the lower actual conversion of bridge precursor compared to theory. In addition, the as-received source catalysts were degassed and experienced 9.5 wt% loss. Since the mixture was formed with the as-received catalyst, the amount was adjusted for the desired proportionality in the final product. Table 2.6 shows the amounts of each raw material used for the desired adsorbents.

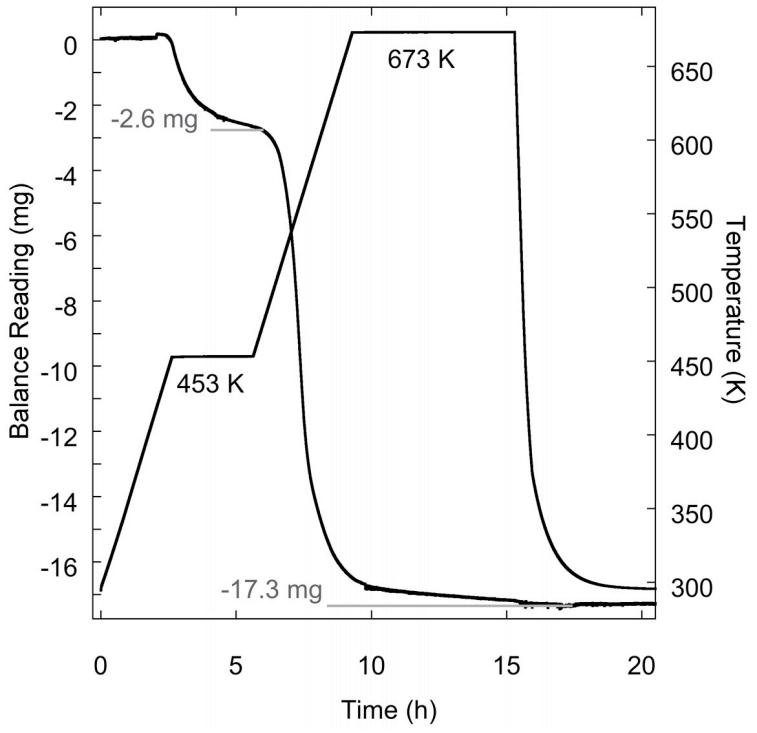

Figure 2.3 TGA Result, Glucose Melting and Decomposition

The ground mixture was transferred to a quartz boat and inserted in a horizontal quartz reactor. The temperature program was nearly identical to the preliminary melting and carbonization test on glucose. The gas phase was flowing helium at 100 mL[STP]/min. The temperature was increased to 453 K (at 1 K/min) and held for 3 h to ensure complete melting. In the carbonization step, the temperature was increased to 673 K (at 1 K/min) and held for 6 h. The material was cooled to room temperature in flowing helium. All samples were degassed and reduced according to the same procedure outlined in Section 2.4.1. The samples were stored in a dessicator for later characterization and hydrogen adsorption measurements.

Table 2.6 Materials Prepared to Study Secondary Spillover

Material	**Receptor**	**Source**	**Precursor**
	g raw material/g desired product		
AX-21/PtC/Bridge (8:1:1)	0.825	0.111	0.741
AX-21/PdC/Bridge (8:1:1)	0.825	0.111	0.741
AX-21/PdC/Bridge (8.6:1:0.4)	0.825	0.111	0.250
SWNT/PdC/Bridge (8:1:1)	0.808	0.111	0.741

2.4.3 Limited Spillover: Primary Source/Receptor Physical Mixture

The effect of bridges on spillover was ascertained with the analysis of physical mixtures of the primary source and receptors without bridges. The components were ground together with an agate mortar and pestle for 30 min to produce the physical mixtures. The proportion of receptor to source was fixed at 9:1 to ensure consistency of the source amount for comparison with bridged samples. This also allowed comparison of the systems studied here with some published results on physical mixtures in the

literature.[2.50] The ground mixtures were transferred to a quartz boat, which was inserted into a horizontal quartz reactor, and subjected to the degassing and reduction treatment as noted above. The samples were stored in a dessicator for later characterization and hydrogen adsorption measurements.

2.5 Characterization of Adsorbents

The adsorbents used in this study were characterized with many common techniques. The physical properties measured for all adsorbents were BET surface area, pore size distribution, and pore volume (total and micropore). Composite adsorbents demonstrating enhanced capacity due to hydrogen spillover were further characterized for metal dispersion (chemisorption/CO titration), metal particle size (X-ray diffraction), and imaged with scanning (SEM) and transmission electron microscopy (TEM).

2.5.1 Surface Area and Pore Size Distribution

A Micromeritics® Accelerated Surface Area and Porosimetry (ASAP) 2010 instrument was used to measure nitrogen adsorption isotherms at 77 K for calculation of BET surface area, total and micropore volumes, and pore size distribution.[2.52]

BET estimates are ubiquitous in the adsorption community for adsorbent characterization. While there are known accuracy issues associated with applying the method to ultrahigh surface area, microporous materials,[2.53-2.55] it has recently been shown that carefully examining the reduced data can provide reasonable estimates of accessible area for comparison purposes.[2.56] The revised method limits BET calculations

to P/P_o (P_o = 0.99 bar, N_2 saturation pressure) data collected below 0.15, compared to the traditional 0.30 value for this parameter.[2.52]

Pore size distributions (PSDs) and micropore volumes are computed from nitrogen adsorption isotherms at 77 K using density functional theory (DFT). This is a standard method in adsorption and is accomplished readily with software in the ASAP 2010 package. The method has advantages over other PSD estimation techniques in that it covers three orders of magnitude of pore sizes (4.0 to 4000 Å).[2.57] Other methods, such as Horvath-Kawazoe (HK)[2.58] or Barrett-Joyner-Halenda (BJH)[2.59] techniques are only accurate for micropores and mesopores, respectively, and must be pieced together for complete PSDs. Results of DFT calculations are continuous and remove this step. Total pore volumes are computed using the well known Gurvitsch rule at the relative pressure yielding the maximum adsorbed amount.[2.3,2.52] This allows calculation of the total pore volume (TPV) from the following equation

$$\mathrm{TPV(mL/g)} = \frac{Q_{ads}(\mathrm{mL[STP]/g})}{22414\,\mathrm{mL[STP]/mol}} \cdot \left(\frac{28\,\mathrm{g/mol}}{\rho_{N2,liq}(\mathrm{g/mL})} \right) \tag{2.6}$$

where Q_{ads} is the maximum adsorbed amount and $\rho_{N2,\,liq}$ is the density of liquid nitrogen at saturation pressure.

2.5.1.1 Receptor BET SA and PSD

Nitrogen adsorption isotherms, BET SA reduction plots, PSDs, and cumulative pore volume plots are presented for five receptors: TC, SWNTs, GNFs, SGC, and AX-21. These results are shown sequentially in Figures 2.4 through 2.23. BET SA statistics are provided on the respective plots. Table 2.7 summarizes the results.

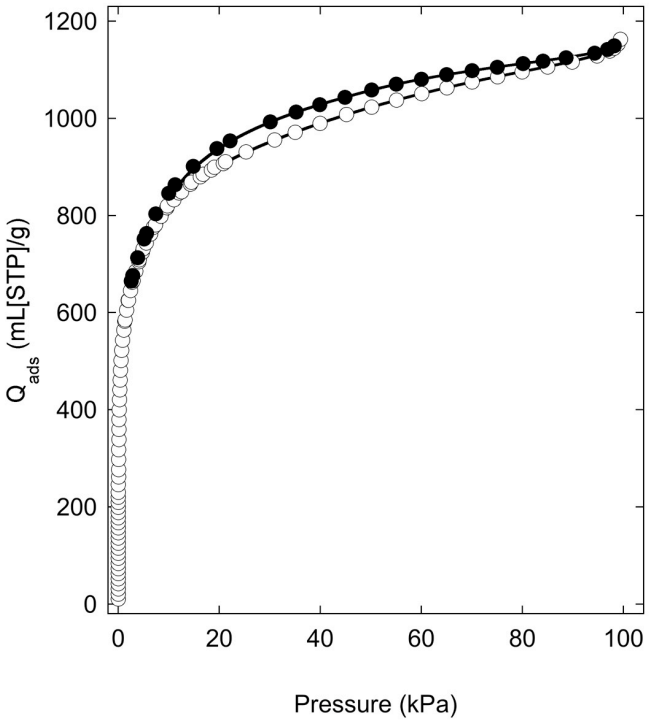

Figure 2.4 Templated Carbon (TC), N_2 Isotherm, 77 K

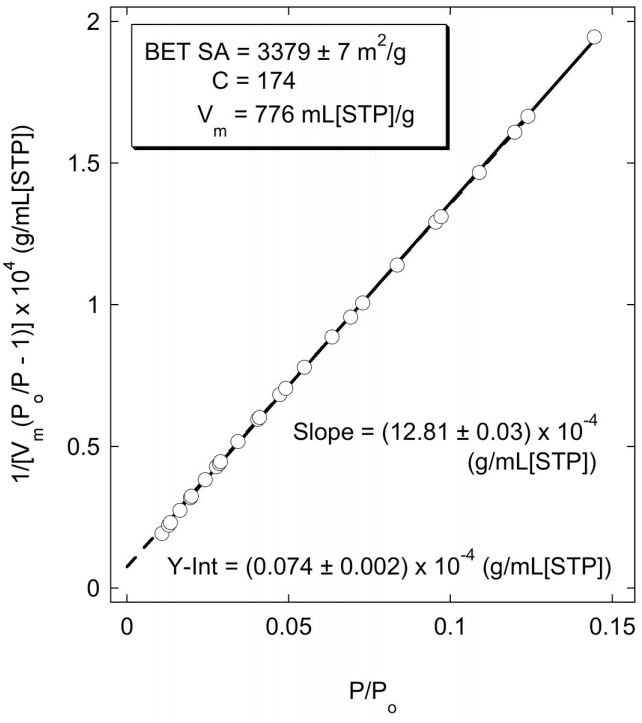

Figure 2.5 Templated Carbon (TC), BET Plot With Statistics

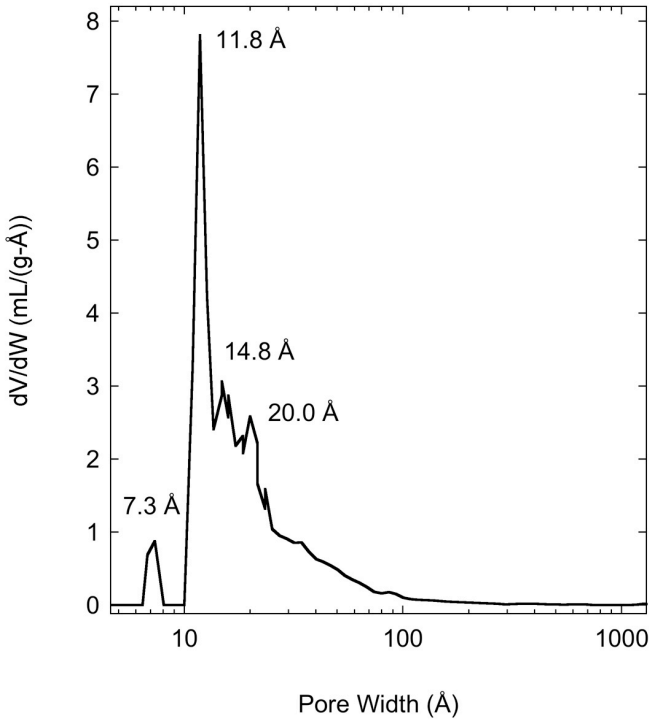

Figure 2.6 Templated Carbon (TC), Pore Size Distribution

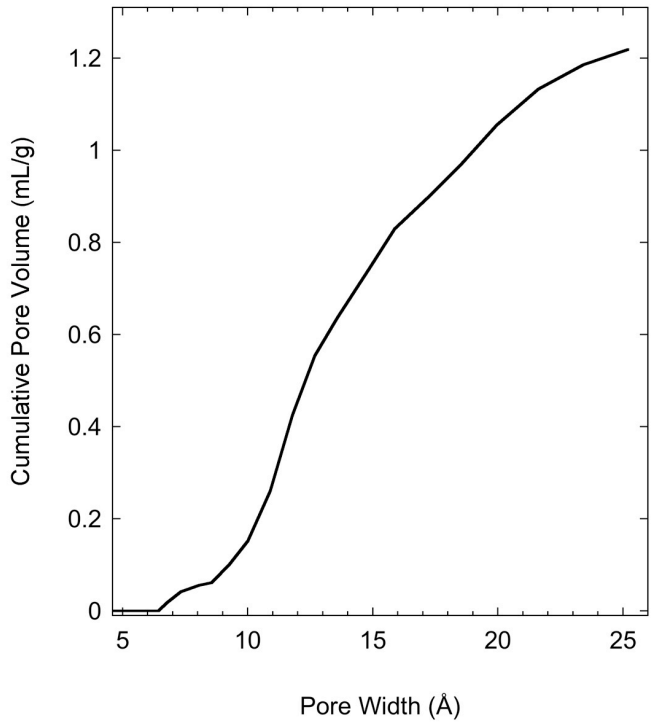

Figure 2.7 Templated Carbon (TC), Cumulative Pore Volume

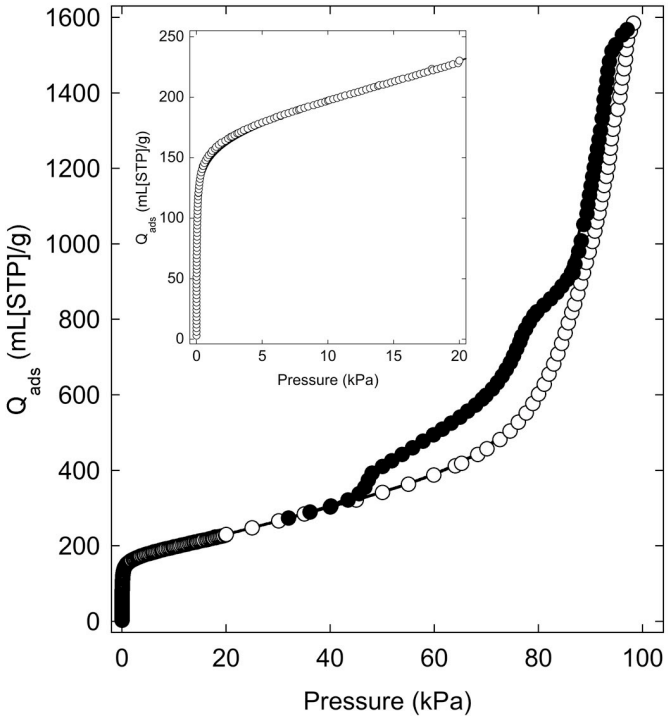

Figure 2.8 Single Walled Nanotubes (SWNTs), N_2 Isotherm, 77 K

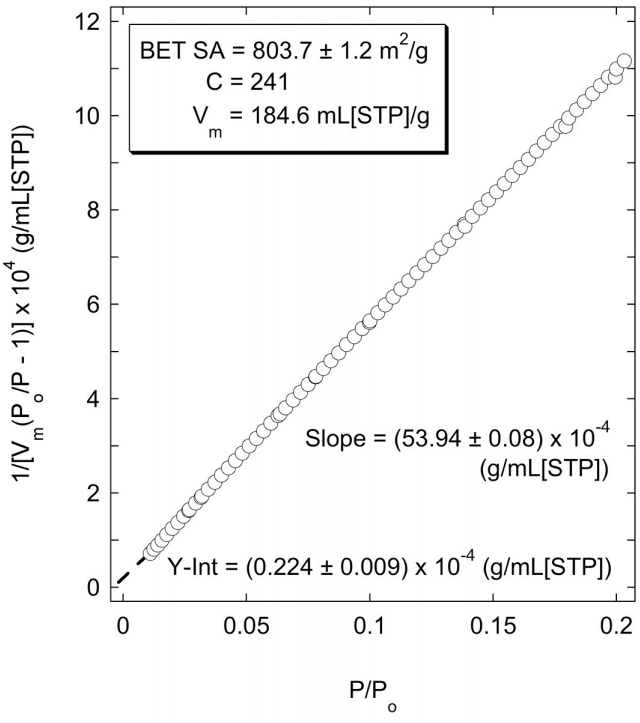

Figure 2.9 Single Walled Nanotubes (SWNTs), BET Plot With Statistics

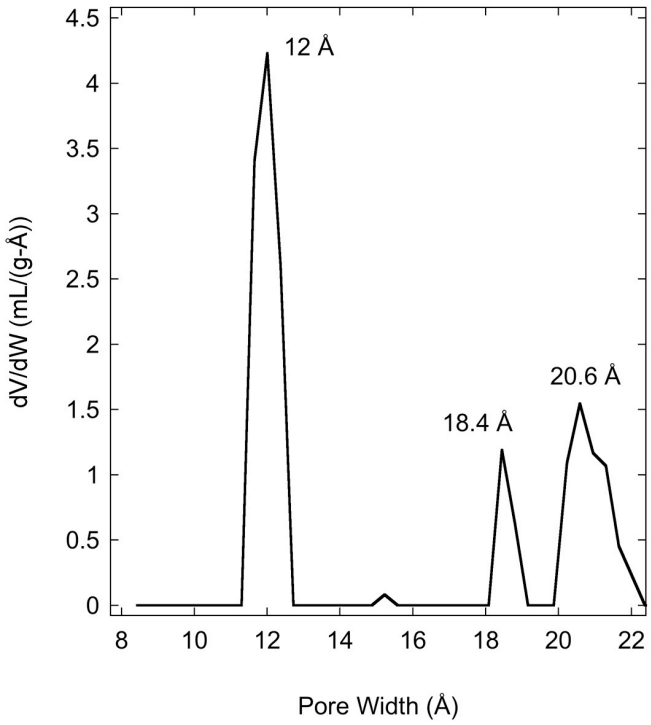

Figure 2.10 Single Walled Nanotubes (SWNTs), Pore Size Distribution

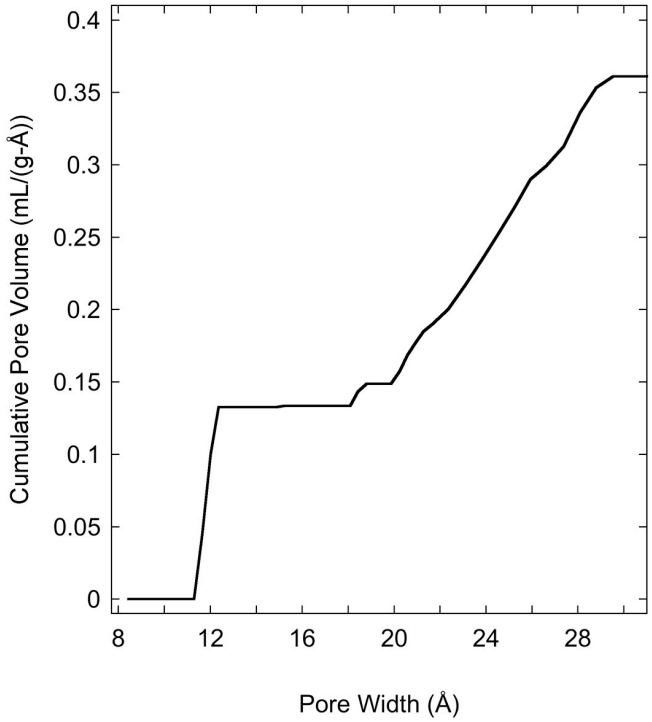

Figure 2.11 Single Walled Nanotubes (SWNTs), Cumulative Pore Volume

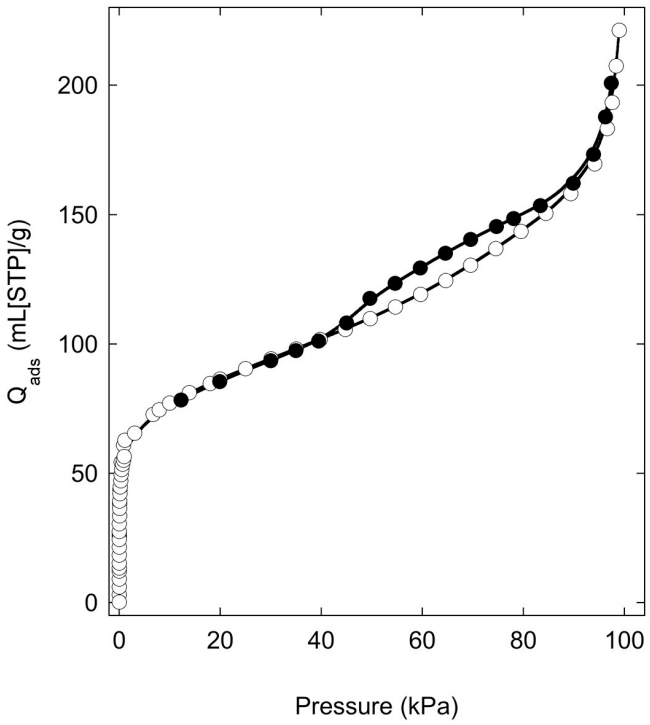

Figure 2.12 Graphite Nanofibers (GNFs), N_2 Isotherm, 77 K

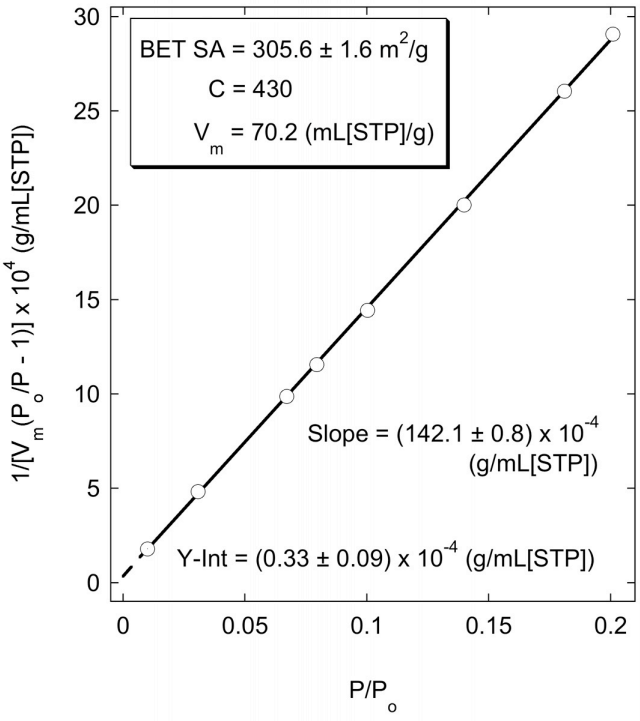

Figure 2.13 Graphite Nanofibers (GNFs), BET Plot With Statistics

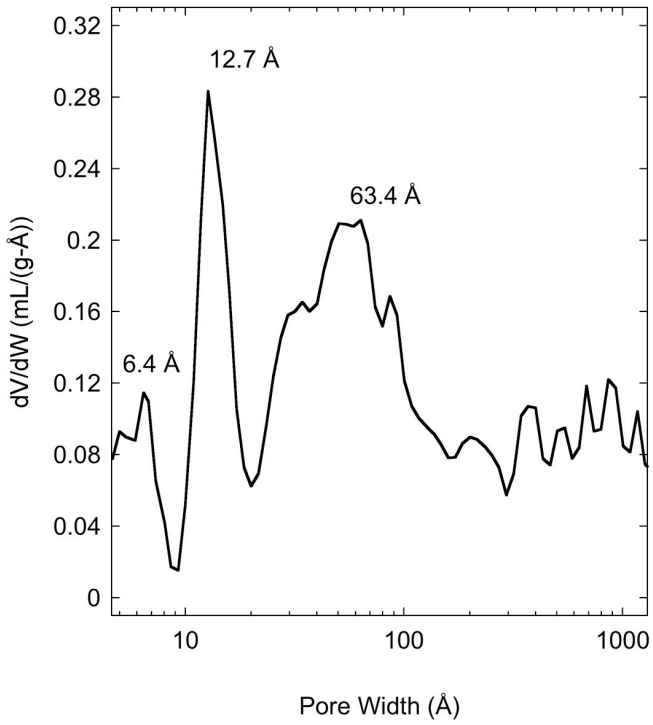

Figure 2.14 Graphite Nanofibers (GNFs), Pore Size Distribution

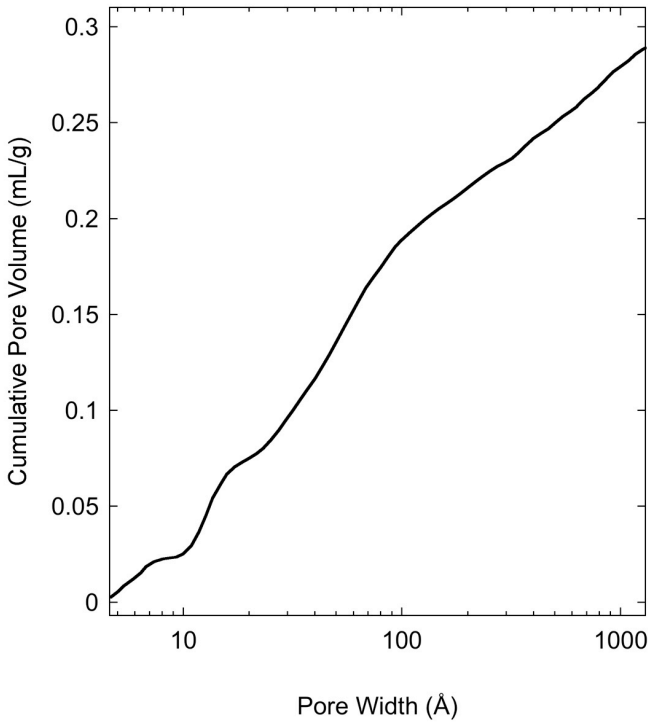

Figure 2.15 Graphite Nanofibers (GNFs), Cumulative Pore Volume

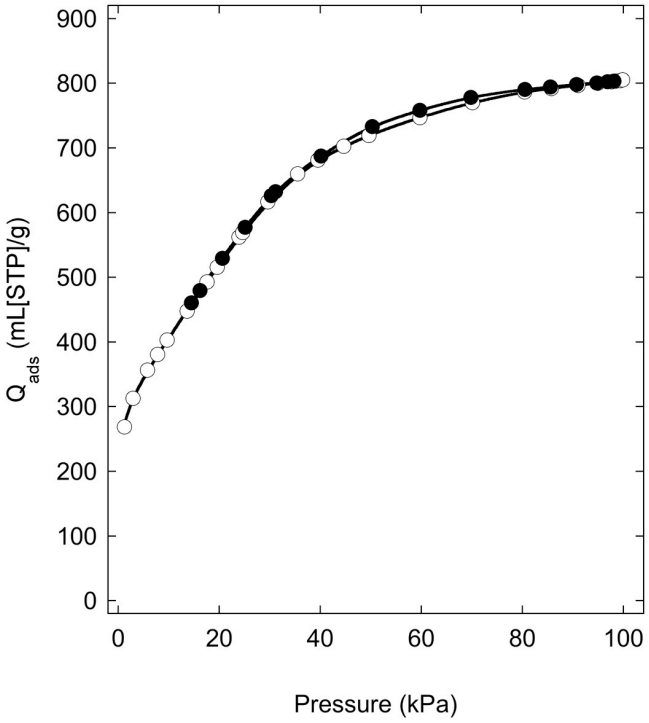

Figure 2.16 Sol-Gel Carbon (SGC), N_2 Isotherm, 77 K

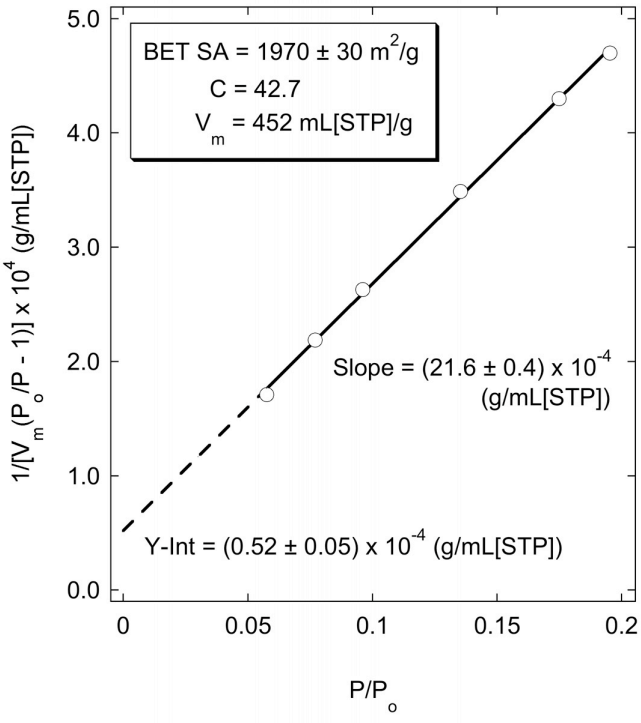

Figure 2.17 Sol-Gel Carbon (SGC), BET Plot With Statistics

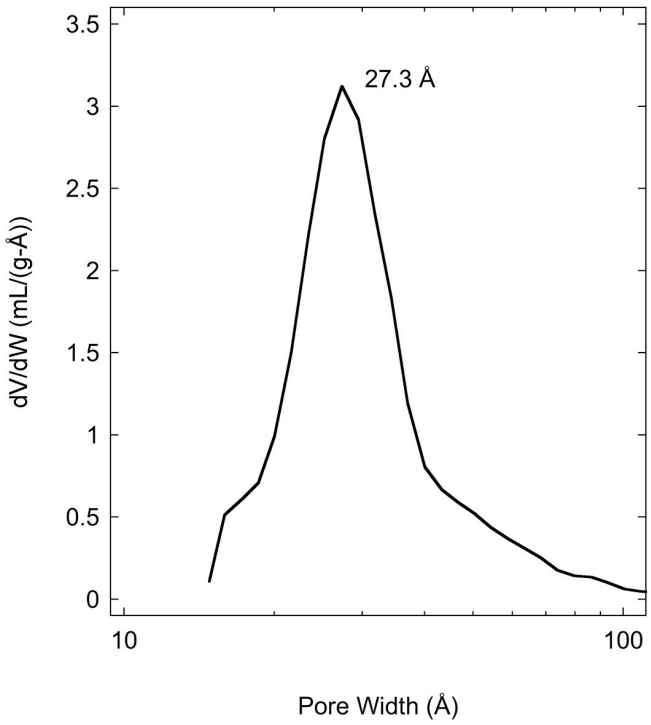

Figure 2.18 Sol-Gel Carbon (SGC), Pore Size Distribution

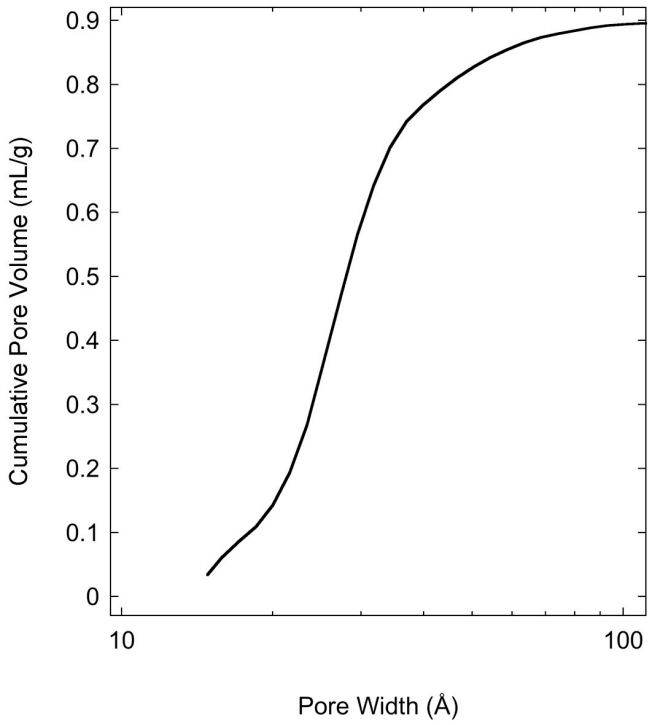

Figure 2.19 Sol-Gel Carbon (SGC), Cumulative Pore Volume

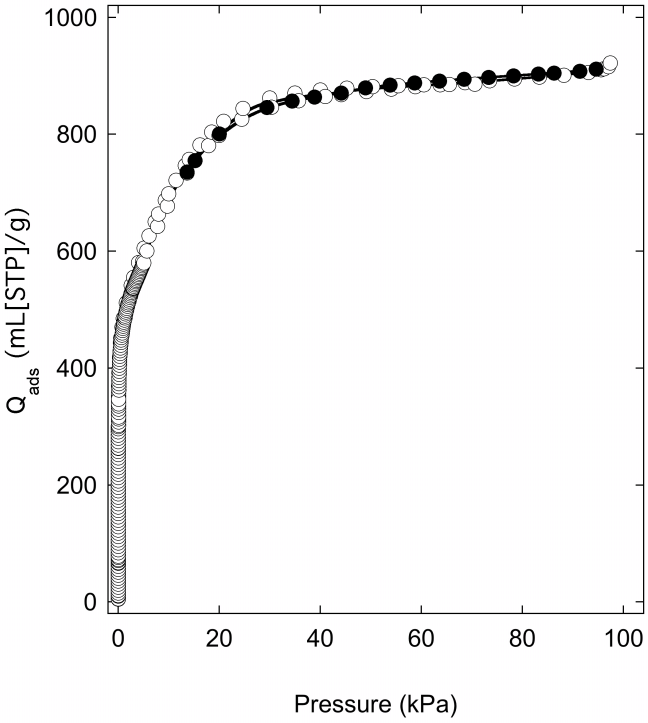

Figure 2.20 AX-21, N_2 Isotherm, 77 K

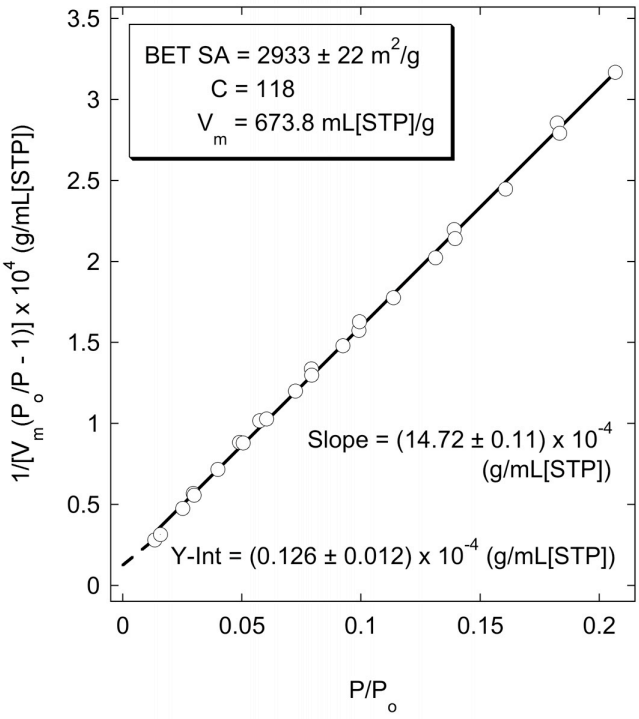

Figure 2.21 AX-21, BET Plot With Statistics

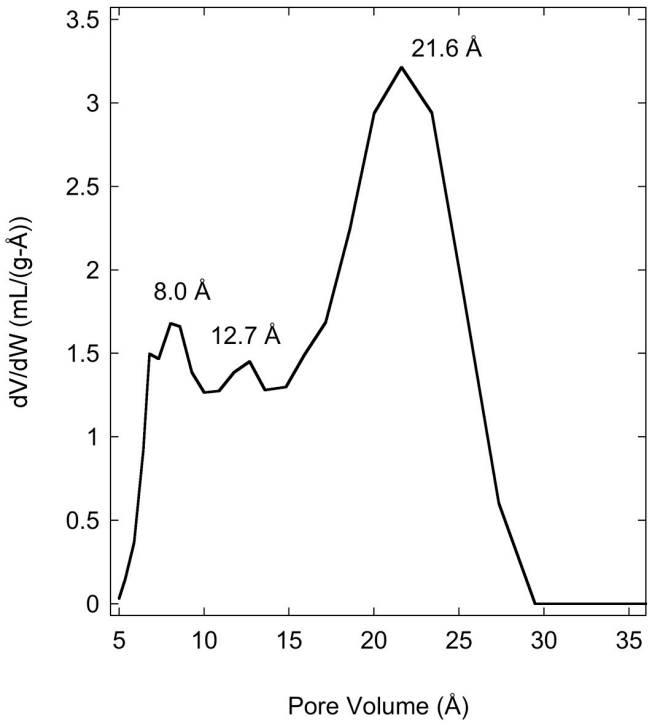

Figure 2.22 AX-21, Pore Size Distribution

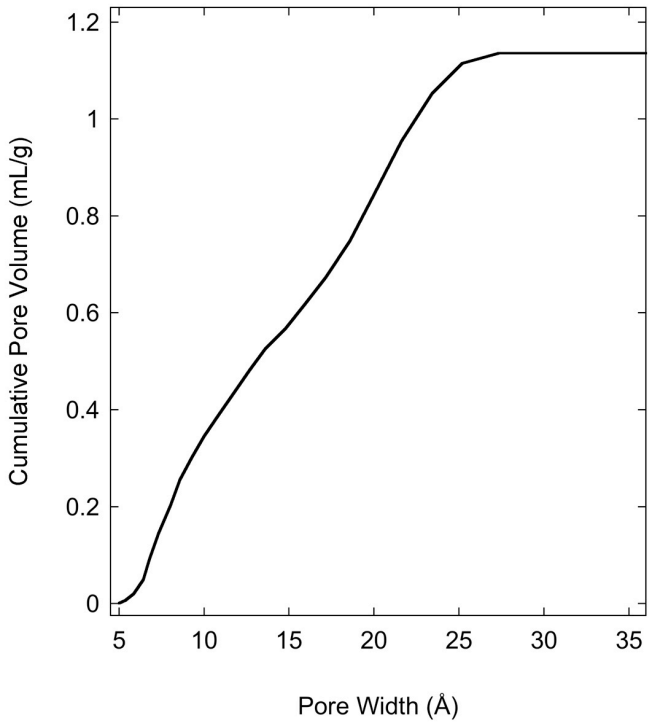

Figure 2.23 AX-21, Cumulative Pore Volume

Table 2.7 Summary of Receptor BET SA and PSD Results

Receptor	BET SA m^2/g	Total PV mL/g	Micro PV mL/g	Major PSD Peaks Pore Width, Å
TC	3379 ± 7	1.4	1.1	7.3, 11.8[m], 14.8, 20.0
SWNT	803.7 ± 1.2	0.35	0.15	12.0[m], 18.4, 20.6
GNF	305.6 ± 1.6	0.32	0.075	12.7
SGC	1970 ± 30	1.2	0.1	27.3
AX-21	2933 ± 22	1.1	0.8	8.0, 12.7, 21.6[m]

[m] = maximum dV/dW

Templated carbon has the highest surface area and percentage of micropores, followed by AX-21. As expected, carbon derived from the sol-gel process is mostly mesoporous.

2.5.1.2 Composites BET SA and PSD

Nitrogen adsorption isotherms, BET SA reduction plots, PSDs, and cumulative pore volume plots are presented for four composite materials: 6 wt% Pt/TC, AX-21/PdC/Bridge (8:1:1), 5 wt% Pd/SGC, and 5 wt% Ni/SGC. These results are shown sequentially in Figures 2.24 through 2.39. Again, BET SA statistics are provided on the respective plots. Characterization reports of the doped TC and bridged AX-21 composites were selectively chosen because they yielded the best hydrogen capacity results as will be shown later. Results for impregnated SGC are shown for reference to a mesoporous carbon material with different sources. Table 2.8 summarizes the results and includes data for the 5 wt% PdC commercial catalyst from Strem Chemicals, Inc.

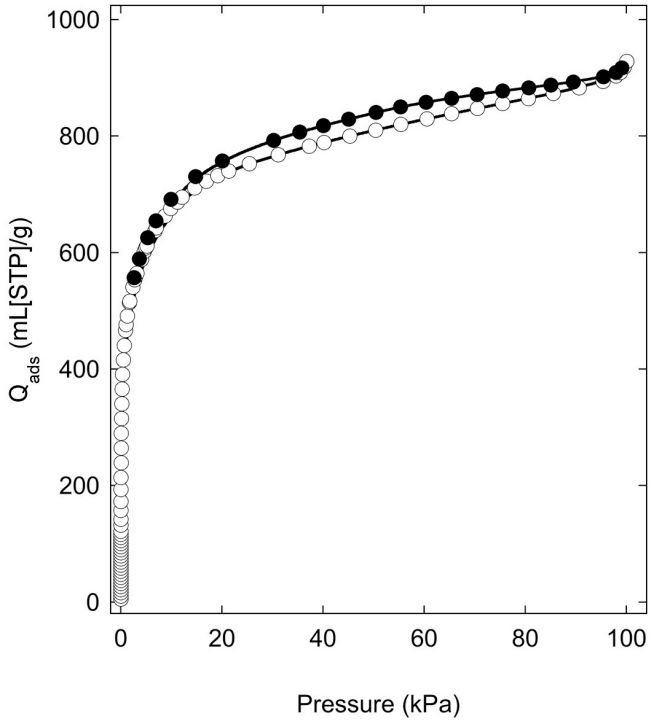

Figure 2.24 6 wt% Pt/TC, N_2 Isotherm, 77 K

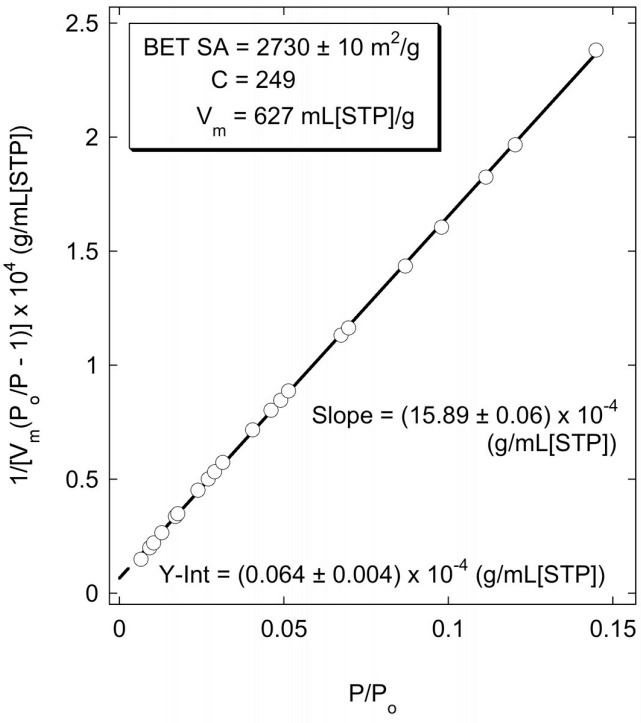

Figure 2.25 6 wt% Pt/TC, BET Plot With Statistics

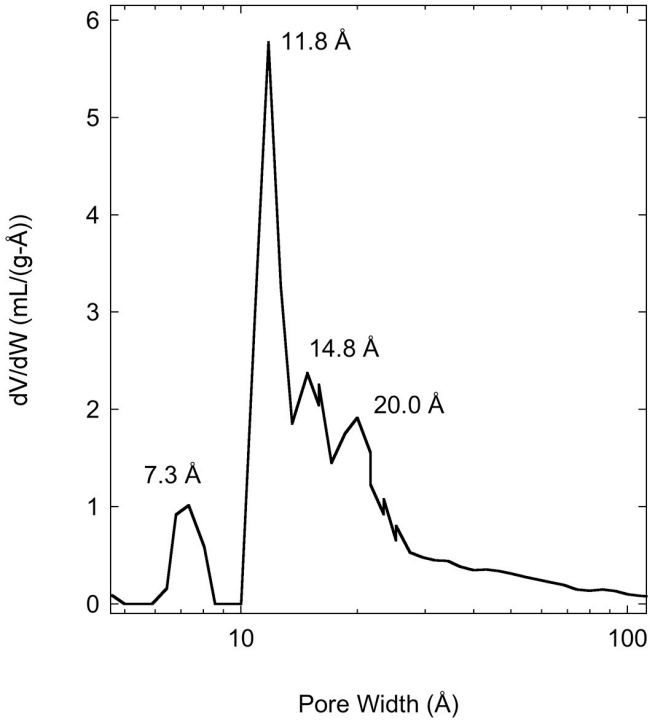

Figure 2.26 6 wt% Pt/TC, Pore Size Distribution

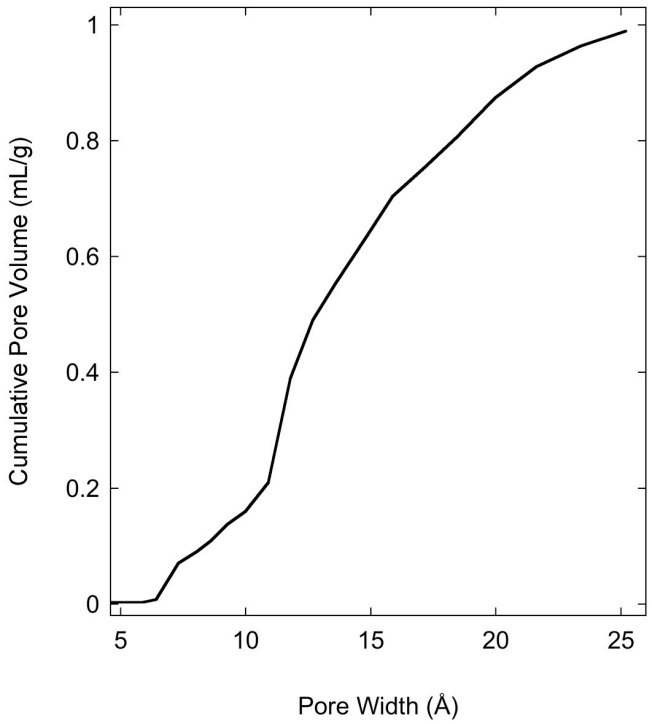

Figure 2.27 6 wt% Pt/TC, Cumulative Pore Volume

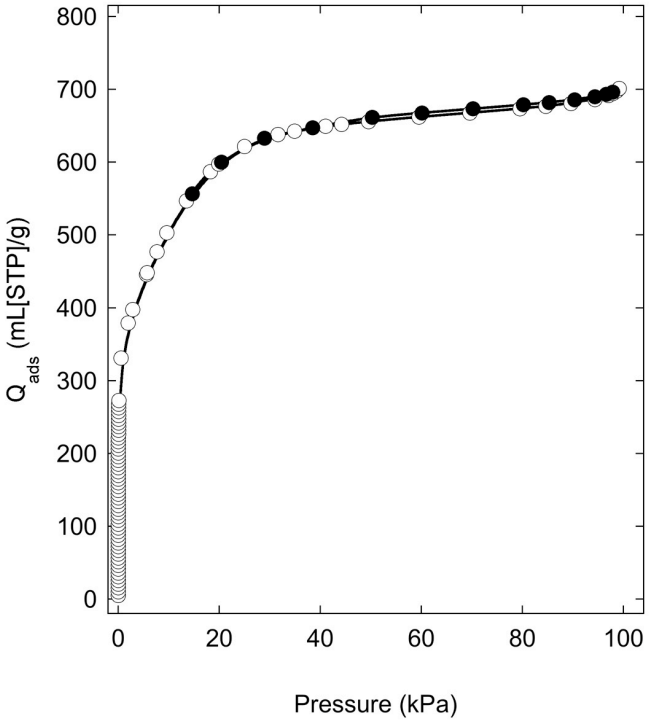

Figure 2.28 AX-21/PdC/Bridge (8:1:1), N_2 Isotherm, 77 K

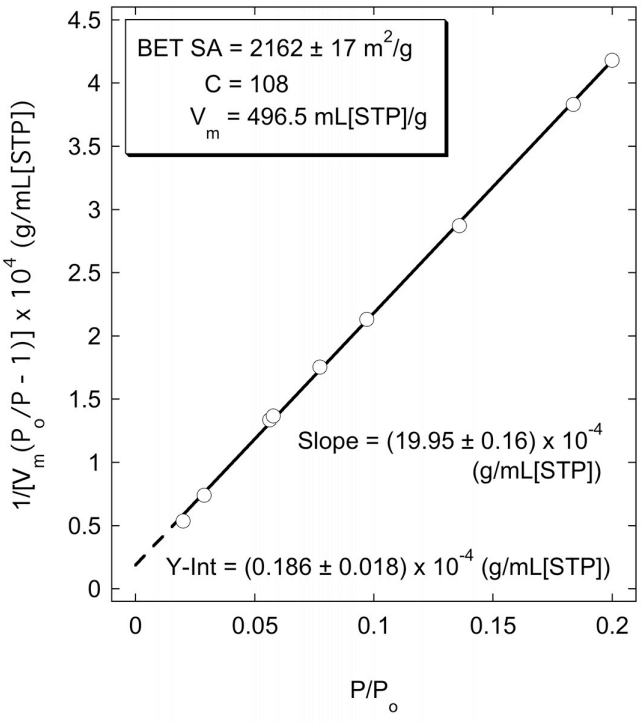

Figure 2.29 AX-21/PdC/Bridge (8:1:1), BET Plot With Statistics

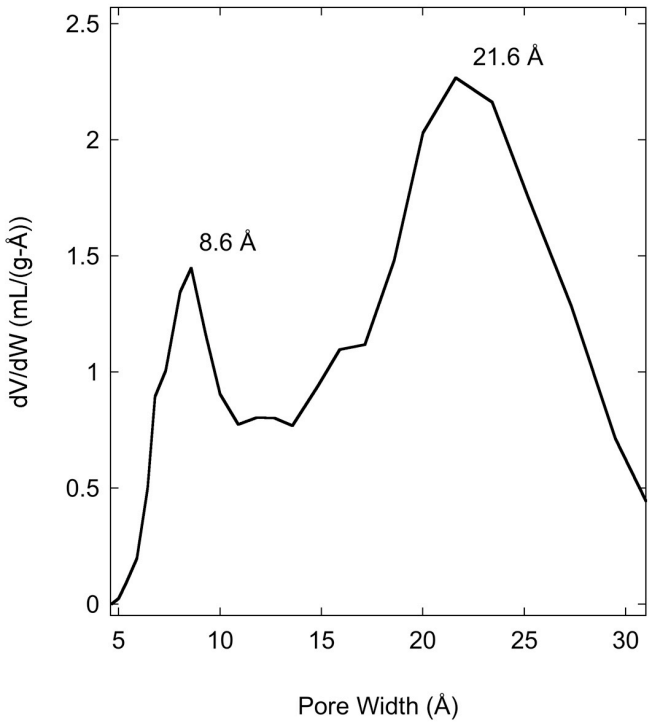

Figure 2.30 AX-21/PdC/Bridge (8:1:1), Pore Size Distribution

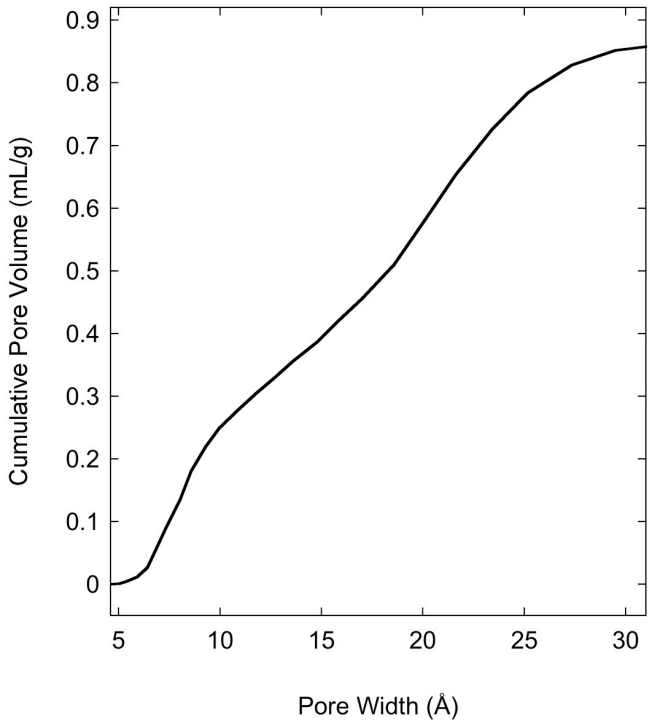

Figure 2.31 AX-21/PdC/Bridge (8:1:1), Cumulative Pore Volume

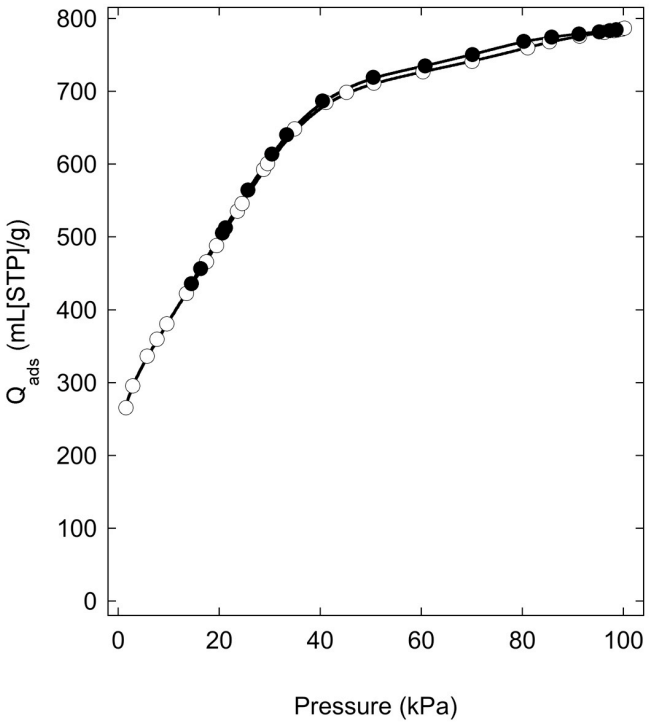

Figure 2.32 5 wt% Pd/SGC, N_2 Isotherm, 77 K

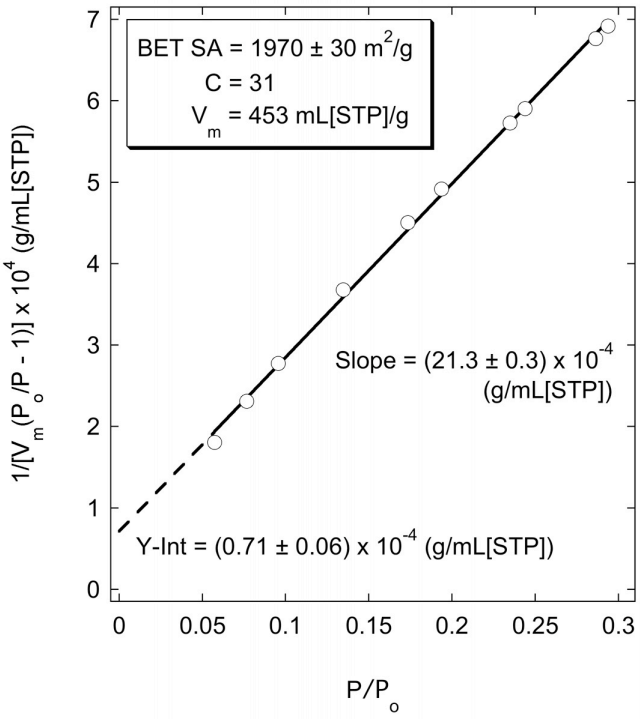

Figure 2.33 5 wt% Pd/SGC, BET Plot With Statistics

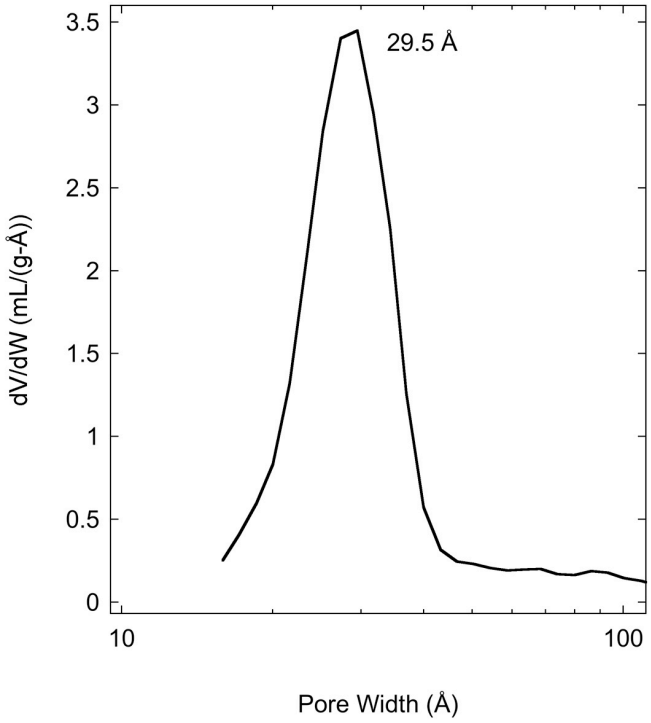

Figure 2.34 5 wt% Pd/SGC, Pore Size Distribution

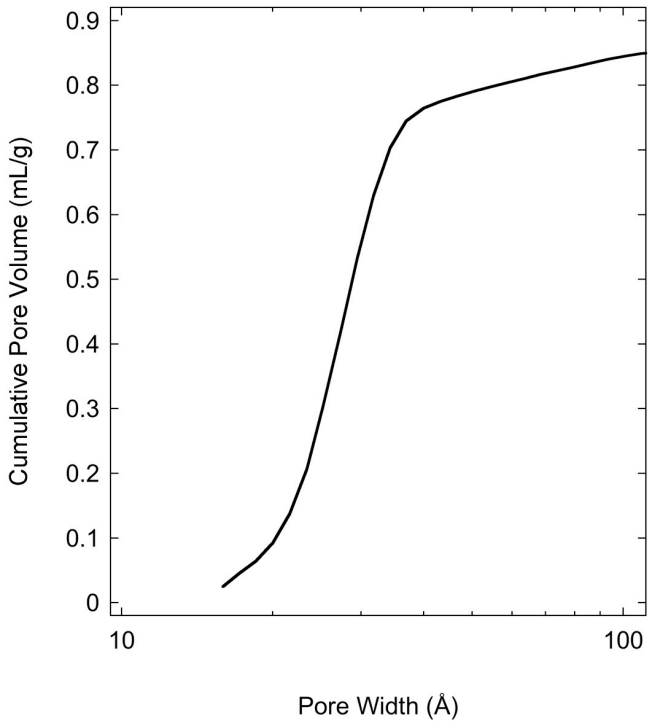

Figure 2.35 5 wt% Pd/SGC, Cumulative Pore Volume

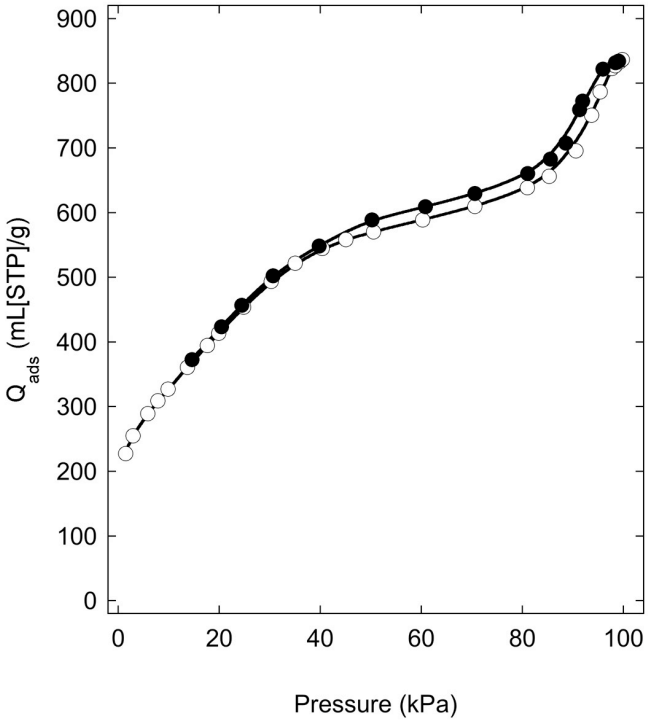

Figure 2.36 5 wt% Ni/SGC, N_2 Isotherm, 77 K

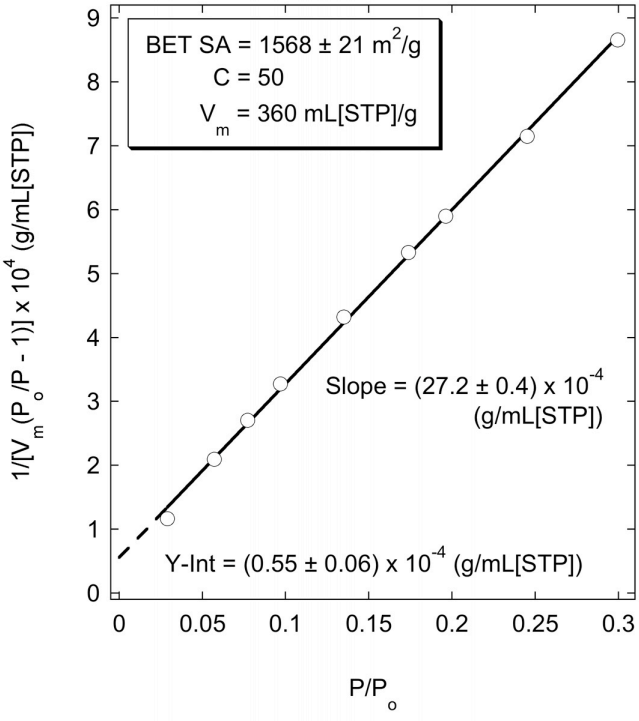

Figure 2.37 5 wt% Ni/SGC, BET Plot With Statistics

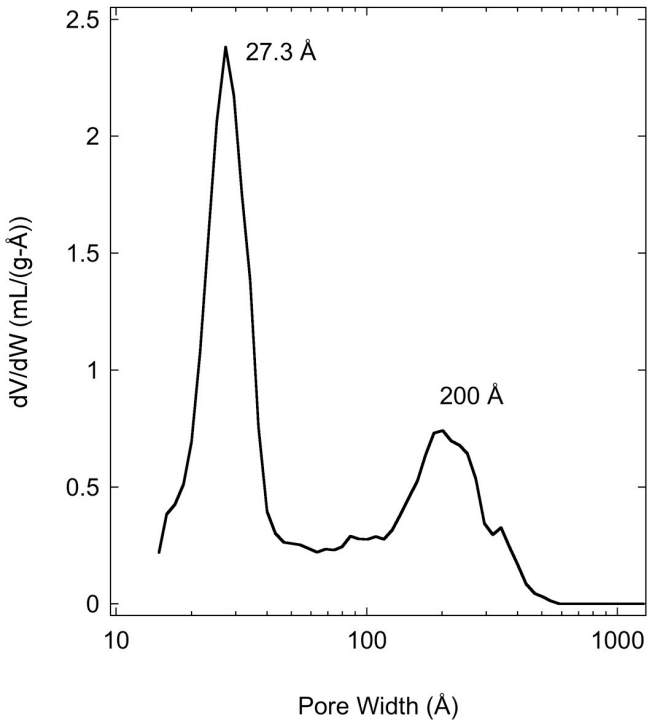

Figure 2.38 5 wt% Ni/SGC, Pore Size Distribution

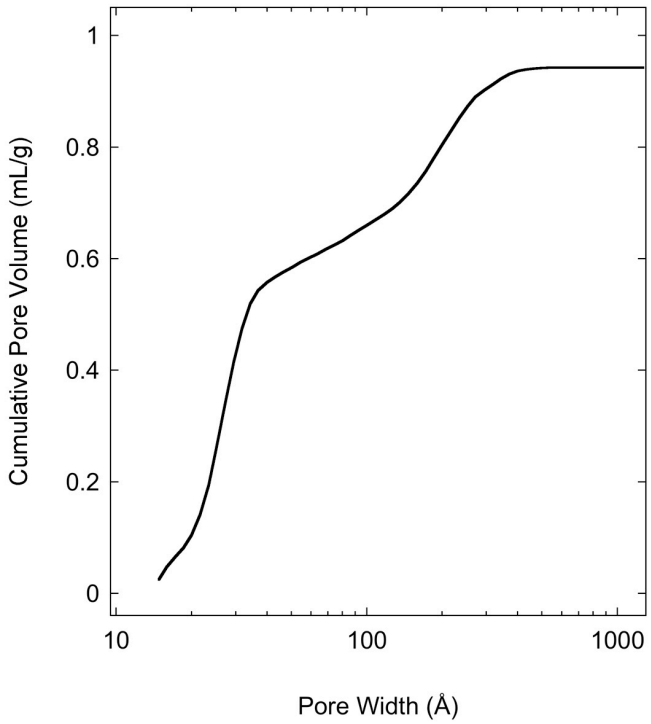

Figure 2.39 5 wt% Ni/SGC, Cumulative Pore Volume

Table 2.8 Summary of Composites BET SA and PSD Results

Composite	**BET SA** m^2/g	**Total PV** mL/g	**Micro PV** mL/g	**Major PSD Peaks** at Pore Width, Å
6 wt% Pt/TC	2730 ± 10	1.4	0.90	7.3, 11.8[m], 14.8, 20.0
AX-21//PdC/Bridge (8:1:1)	2162 ± 17	1.1	0.55	8.6, 21.6[m]
5 wt% Pd/SGC	1970 ± 30	1.2	0.075	29.5
5 wt% Ni/SGC	1568 ± 21	1.0	0.075	27.3[m], 200
5 wt% PdC (Strem)	976 ± 7	0.7	0.275	8.0[m], 14.8

[m] = maximum dV/dW

The results for composite materials indicated that there is a loss of surface area and microporosity due to the synthesis processes. BET SA decreases accordingly. For the doped material 6 wt% Pt/TC, this is likely due to blocking of micropores by metal nanoparticles. A global reduction in the relative amounts of all pore sizes is reflected in the PSD. The bridged source-receptor composite likely shows the effect of glucose penetration and carbonization in some micropores. Based on the PSD, this phenomenon seems to have affected the smallest pore sizes the most, as one might expect. Doping sol-gel derived carbon with transition metals seems to have little effect on the surface characteristics of the palladium material. The nickel material shows a reduction in surface area and a shift in the PSD to higher values. A concern here is that the metal particles are embedded in the carbon since salt solutions are added during the carbon synthesis step. These would not contribute to a change in surface properties if they were not exposed to the gas phase during analysis. Hydrogen adsorption measurements should confirm or refute this hypothesis. Data for 5 wt% PdC (Strem) shows that the active carbon support is microporous with a surface area typical of carbons derived from coconut shells.[2.60]

2.5.2 Metal Dispersion and Particle Size

Metal dispersion is a measure of the amount of metal surface exposed to the gas phase relative to the total metal content in a system. It can be calculated using the hydrogen chemisorption method established by Spenadel and Boudart.[2.61] The method was used for calculation of the dispersion for the 5 wt% PdC source for secondary spillover study. A sample of the material was treated in situ on the Micromeritics® ASAP 2010 instrument with hydrogen at 573 K for 2 h to reduce the Pd surface. It was then evacuated to 1 x 10^{-7} mbar at 623 K for 6 h. The hydrogen isotherm was measured at 298 K for pressures up to 100 kPa and is shown in Figure 2.40, along with data for PCB Carbon (Calgon Carbon Corporation) at the same conditions. PCB Carbon has similar characteristics as the support material (BET SA = 1100 m^2/g, TPV = 0.55 mL/g) and demonstrates that there is no substantial physisorption capacity on the support in the limit of zero pressure. Palladium forms a stable hydride at room temperature by absorbing hydrogen.[2.62] The composition of this hydride at 2.4 kPa is $PdH_{0.6}$ and the point is shown in Figure 2.40. Hydrogen that is not absorbed by the metal lattice or physisorbed to the support is present on the surface of the metal, which is represented by the additional amount adsorbed at 2.4 kPa (0.54 mL[STP]/g). Assuming Pd-H (1:1) on the surface, the dispersion is calculated from

$$M_{surface}(g/g_{ads}) = \frac{Q_{ads}(mL[STP]/g_{ads}) \cdot 2\ atoms H/mol H_2}{22414\ mL[STP]/mol} \cdot MW_{Pd} \tag{2.7}$$

$$Dispersion = \frac{M_{surface}(g/g_{ads})}{M_{total}(g/g_{ads})} \times 100\% \tag{2.8}$$

Applying the calculations to the data for 5 wt% PdC, the dispersion is 10%.

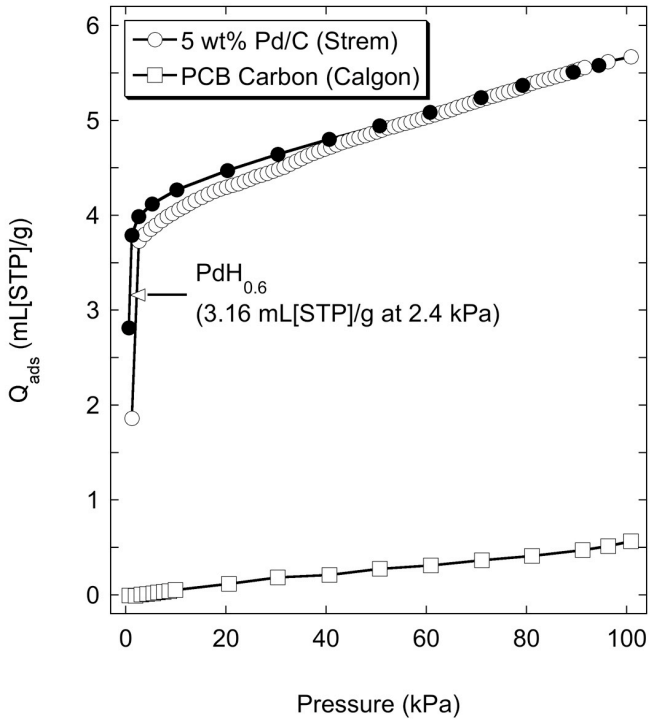

Figure 2.40 Metal Dispersion of 5 wt% PdC (Strem) Using H_2 Chemisorption

The hydrogen chemisorption method is difficult to use when the support material acts as an effective receptor for hydrogen atoms. An alternative to this method is titration with carbon monoxide.[2.63] Two experiments are required for this technique. The first experiment is performed on a reduced and degassed composite material. This establishes the overall adsorption amount. The second experiment is performed after evacuating the sample from the first experiment at room temperature to remove physisorbed carbon monoxide only. The metal retains any chemisorbed CO in this step. The second experiment measures the physisorption capacity of the support material, which should be near zero in the limit of zero pressure.

The carbon monoxide titration method was used to determine the dispersion for 6 wt% Pt/TC. Again, the Micromeritics® ASAP 2010 instrument was used. The sample was

reduced in situ in hydrogen at 573 K for 2 h. It was then evacuated to 1 x 10^{-7} mbar at 623 K for 6 h. In the first experiment, the carbon monoxide isotherm was measured at 298 K up to 60 kPa. The sample was evacuated at room temperature for 2 h and the second experiment was conducted at 298 K up to 60 kPa. The results of these two experiments are shown in Figure 2.41, along with subtraction of the two isotherms. The data for CO physisorption agrees well with literature reports for active carbon at room temperature.[2.64] Platinum dispersion is calculated from the difference (average ~ 2.9 mL[STP]/g) using the following formula for surface metal amount

$$M_{surface}(g/g_{ads}) = \frac{Q_{ads}(mL[STP]/g_{ads}) \cdot 1 molec\,Pt/1.3 molec\,CO}{22414\,mL[STP]/mol} \cdot MW_{Pt} \qquad (2.9)$$

where the relationship between Pt and surface adsorbed CO has been reported for bridged and linear configurations by Gruber.[2.65]

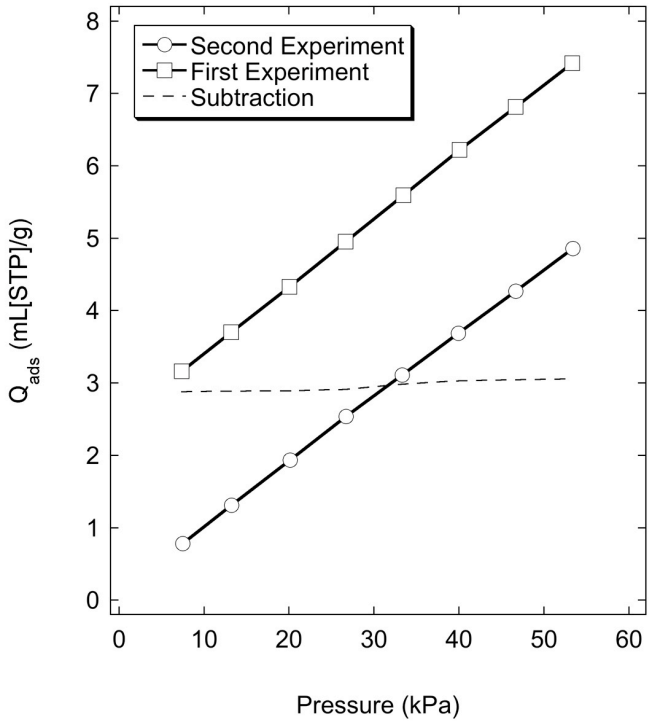

Figure 2.41 Metal Dispersion of 6 wt% Pt/TC Using CO Titration

The dispersion for 6 wt% Pt/TC, computed from Equation 2.8, is 33%. Compared to commercial catalysts, the ultrasound doping technique has improved metal dispersion, as expected.

X-ray diffraction (XRD) analysis was performed using a Rigaku Miniflex X-ray diffractometer (30 kV, 15mA, Cu Kα radiation) scanning with a resolution of 0.02° in 2θ. Figure 2.42 compares the XRD patterns for Na-Y zeolite, TC, and 6 wt % Pt/TC. A peak at 2θ = 6.6° in (b) indicates that the carbon has copied the template structure.[2.20,2.66] Peaks above 2θ = 35° in Figure (c) represent (111), (200), (220), and (311) Pt crystal faces. The average crystallite size, as calculated by the Scherer equation, is 44 Å. These results support the earlier theory that some micropores are blocked by platinum particles given the decrease in micropore volume.

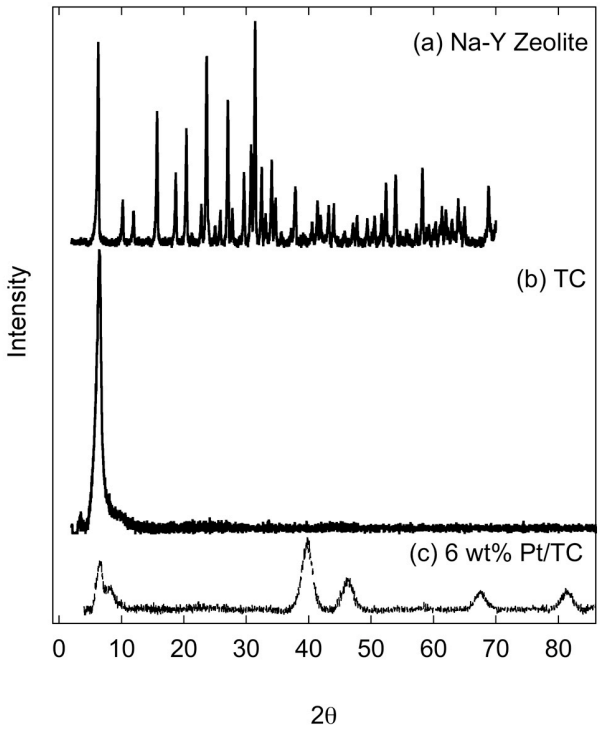

Figure 2.42 XRD Results for 6 wt% Pt/TC

2.5.3 Imaging and Surface Analysis

Transmission electron microscopy (JEOL Ltd. 3011 TEM, 300 kV accelerating voltage) was used to capture images of the 6 wt% Pt/TC material. In situ energy-dispersive X-ray spectroscopy (Edax Ultrathin Window Si-Li X-ray detector) confirmed the composition of the particles observed in the images. Figure 2.43 shows two images captured at different locations on the material surface. The inset in the left image reflects the average particle size of the material, approximately 0.5 μm. The dark dots on the carbon surface are platinum particles. Estimating the size of these particles from the images, good agreement is obtained with the earlier calculation from the Scherer equation (44 Å)

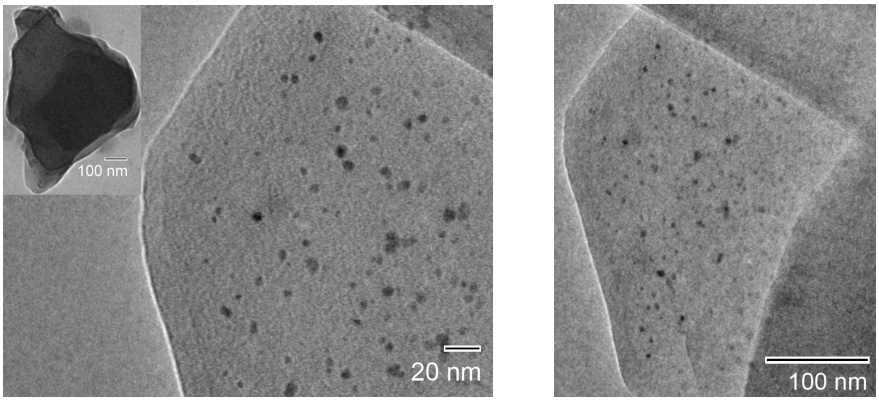

Figure 2.43 TEM Images of 6 wt% Pt/TC

The secondary spillover material, AX-21/PdC/ Bridge (8:1:1) was examined using scanning electron microscopy (SEM) to observe palladium particle size and bridge contacts. A sample of the physical mixture of AX-21 and 5 wt% PdC (9:1) was also evaluated for comparison. A Philips XL30 FEG SEM instrument (accelerating voltage 30 kV) was used to examine the specimens. An X-ray energy-dispersive spectrometry

(XEDS) detector (EDAX, Inc.) enabled identification of palladium particles on the carbon support by elemental analysis. Figure 2.44 shows images of the 5 wt% PdC catalyst (left) and AX-21 receptor (right). The palladium particle is relatively large, on the order of 0.6 μm, which agrees with a lower dispersion calculated for this material relative to 6 wt% Pt/TC. Images of the physical mixture of this catalyst with AX-21 (left) and the bridged material (right) are shown in Figure 2.46. It is difficult to discern substantially different carbon phases, however, in the right image, the PdC catalyst particle appears have improved contact with the receptor through the presumed bridges.

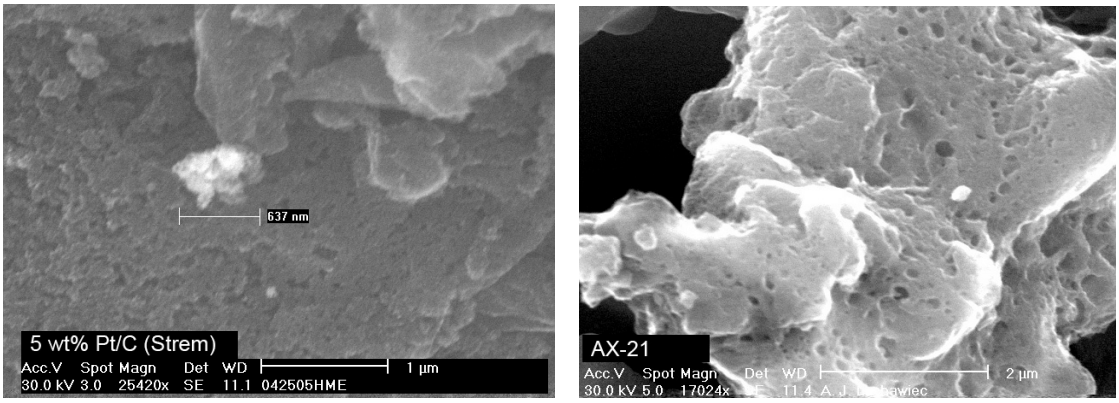

Figure 2.44 SEM Images of 5 wt% PdC and AX-21

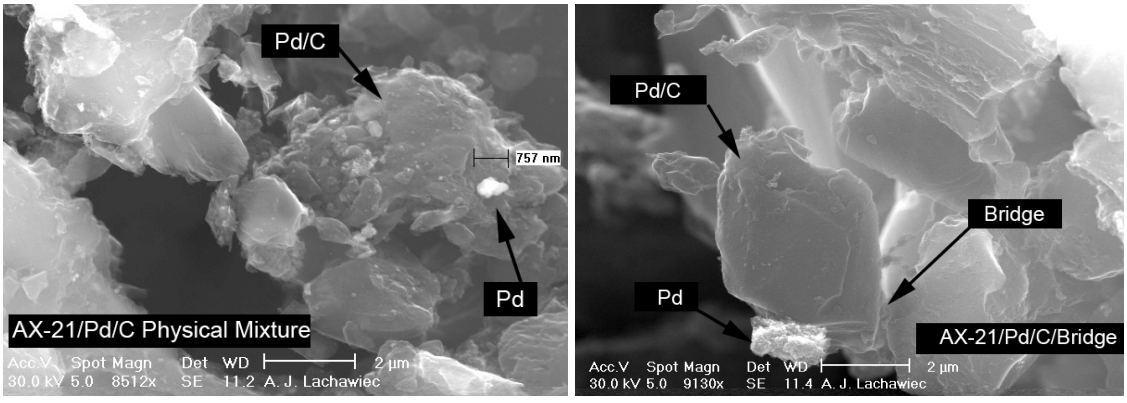

Figure 2.45 SEM Images of AX-21/PdC/Bridge (8:1:1) and AX-21/PdC (9:1)

2.6 Conclusions

Carbon-based adsorbents for hydrogen spillover and adsorption have been synthesized and characterized with traditional analytical techniques. Nanostructured receptors with a high degree of microporosity were synthesized via chemical vapor deposition. Templated carbon had the highest BET surface area and total pore volume. SWNT had the sharpest pore size distribution, with a narrow peak at 12 Å. For comparison with these materials, mesoporous carbon was synthesized using the sol-gel process. This carbon was also doped with transition metals during the synthesis step in order to investigate spillover behavior from embedded sources.

Composite materials for the study of primary or secondary spillover were prepared using ultrasound-assisted solution impregnation or a novel bridge-building technique. The impregnation method allows for a high dispersion of metal particles on the surface of a receptor, while retaining most of its structure and porosity. The bridge building technique sacrifices additional surface area and pore volume, however, it is predicted that these bridges form a diffusion pathway to enhance adsorption capacity and kinetics via spillover.

2.7 Literature Cited

[2.1] Yang, R. T. Nanostructured Adsorbents. In *Nanostructured Materials*; Ying, J., Ed.; Advances in Chemical Engineering; Academic Press: New York, 2001; Vol. 27, p 79-124.

[2.2] Marsh, H.; Rodríguez-Reinoso, F. *Activated Carbon*; Elsevier Ltd.: Oxford, 2006.

[2.3] Bansal, R. C.; Goyal, M. *Activated Carbon Adsorption*; CRC Press: Boca Raton, FL, 2005.

[2.4] Yang, R. T. *Adsorbents: Fundamentals and Applications*; Wiley & Sons: New

York, 2005; p 307.

[2.5] Choi, M.; Ryoo, R. *J. Mater. Chem.* **2007,** *17*, 4204.

[2.6] Lozano-Castello, D.; Lillo-Rodenas, M. A.; Cazorla-Amoros, D.; Linares-Solano, A. *Carbon* **2001,** *39*, 741.

[2.7] Marsh, H.; Crawford, D.; O'Grady, T. M.; Wennerberg, A. *Carbon* **1982,** *20*, 419.

[2.8] Wennerberg, A. N.; O'Grady, T. M. U.S. Patent 4,082,694, April 4, 1978.

[2.9] Otowa, T.; Nojima, Y.; Miyazaki, T. *Carbon* **1997,** *35*, 1315.

[2.10] Otowa, T.; Tanibata, R.; Itoh, M. *Gas Sep. Purif.* **1993,** *7*, 241.

[2.11] Jankowska, H.; Świątkowski, A.; Choma, J. *Active Carbon*; Ellis Horwood: New York, 1991; pp 75-106.

[2.12] Bansal, R. C.; Vastola, F. J.; Walker, Jr., P L. *Carbon* **1971,** *9*, 185.

[2.13] Chahine, R.; Bose, T. K. *Int. J. Hydrogen Energy* **1994,** *19*, 161.

[2.14] Okazaki, M.; Tamon, H.; Toei, R. *AIChE J.* **1981,** *27*, 262.

[2.15] Boudart, M.; Aldag, A. W.; Vannice, M. A. *J. Catal.* **1970,** *18*, 46.

[2.16] Fujimoto, K.; Toyoshi, S. *Stud. Surf. Sci. Catal.* **1981,** *7A*, 235.

[2.17] Su, F.; Zhao, X. S.; Lv, L.; Zhou, Z. *Carbon* **2004,** *42*, 2821.

[2.18] Meyers, C. J.; Shah, S. D.; Patel, S. C.; Sneeringer, R. M.; Bessel, C. A.; Dollahon, N. R.; Leising, R. A.; Takeuchi, E. S. *J. Phys. Chem. B* **2001,** *105*, 2143.

[2.19] Kyotani, T.; Nagai, T.; Inoue, S.; Tomita, A. *Chem. Mater.* **1997,** *9*, 609.

[2.20] Ma, Z.; Kyotani, T.; Tomita, A. *Carbon* **2002,** *40*, 2367.

[2.21] Kyotani, T.; Ma, Z.; Tomita, A. *Carbon* **2003,** *41*, 1451.

[2.22] Ma, Z.; Kyotani, T.; Liu, Z.; Terasaki, O.; Tomita, A. *Chem. Mater.* **2001,** *13*, 4413.

[2.23] Prilipko, A. I.; Il'in, V. G.; Turutina, N. V.; Nazarenko, V. A.; Mel'nichenko, G. N. *Theor. Exp. Chem.* **1990,** *25*, 467.

[2.24] Cassell, A. M.; Raymakers, J. A.; Kong, J.; Dai, H. *J. Phys. Chem. B* **1999,** *103*, 6484.

[2.25] Kim, M. S.; Rodriguez, N. M.; Baker, R. T. K. *J. Catal.* **1991,** *131*, 60.

[2.26] Park, C.; Engel, E. S.; Crowe, A.; Gilbert, T. R.; Rodriguez, N. M. *Langmuir* **2000,** *16*, 8050.

[2.27] Sipos, É.; Fogassy, G.; Tungler, A.; Samant, P. V.; Figueiredo, J. L. *J. Mol. Catal. A* **2004,** *212*, 245.

[2.28] Hu, Q.; Pang, J.; Jiang, N.; Hampsey, J. E.; Lu, Y. *Microporous Mesoporous Mater.* **2005,** *81*, 149.

[2.29] Adamson, A. W.; Gast, A. P. *Physical Chemistry of Surfaces*, 6th ed.; Wiley & Sons: New York, 1997.

[2.30] Surface Tension of Common Liquids, In *CRC Handbook of Chemistry and Physics*, 88th ed.; D. L. Lide, D. L., Ed.; CRC Press/Taylor & Francis: Boca Raton, FL, 2008; Internet Version.

[2.31] Zhou, J.; Sui, Z.; Li, P.; Dai, Y.; Yuan, W. *New Carbon Mater.* **2006,** *21*, 331.

[2.32] Yum, K.; Yu, M.-F. *Nano Lett.* **2006,** *6*, 329.

[2.33] Park, J.-M.; Kim, P. G.; Jang, J.-H.; Wanga, Z.; Kim, J.-W.; Lee, W.-I.; Park, J.-G.; DeVries, K. L. *Composites Part B* **2008,** *39*, 1170.

[2.34] Park, J.-I.; Kim, J.-W.; Lee, J.-S. *J. Korean Ind. Eng. Chem.* **1990,** *1*, 224.

[2.35] Joo, S. H.; Choi, S. J.; Oh, I.; Kwak, J.; Liu, Z.; Terasaki, O.; Ryoo, R. *Nature* **2001,** *412*, 169.

[2.36] Cheng, Z. X.; Yuan, S. B.; Fan, J. W.; Zhu, Q. M.; Zhen, M. S. *Stud. Surf. Sci. Catal.* **1997,** *112*, 261.

[2.37] Li, Y.; Yang, R. T. *J. Phys. Chem. C* **2007,** *111*, 11086.

[2.38] Bedrane, S.; Descorme, C.; Duprez, D. *J. Mater. Chem.* **2002,** *12*, 1563.

[2.39] Schueller, B. S.; Yang, R. T. *Ind. Eng. Chem. Res.* **2001,** *40*, 4912.

[2.40] Yu, J.-S.; Yoon, S. B.; Chai, G. S. *Carbon* **2001,** *39*, 1421.

[2.41] Leboda, R.; Łodyga, A. *Mater. Chem. Phys.* **1994,** *36*, 256.

[2.42] Yang, R. T.; Li, Y.; Qi, G.; Lachawiec, Jr., A. J. Chemical Bridges for Enhancing Hydrogen Storage by Spillover and Methods for Forming the Same. U.S. Patent Appl. 20070082816, April 12, 2007.

[2.43] Hurtta, M; Pitkänen, I.; Knuutinen, J. *Carbohydr. Res.* **2004,** *339*, 2267.

[2.44] Prey, V.; Eichberger, W.; Gruber, H. *Stärke* **1977,** *29*, 60.

[2.45] Mo, X.; López, D. E.; Suwannakarn, K.; Liu, Y.; Lotero, E.; Goodwin Jr., J. G.; Lu, C. *J. Catal.* **2008,** *254*, 332.

[2.46] Okamura, M.; Takagaki, A.; Toda, M.; Kondo, J. N.; Domen, K.; Tatsumi, T.; Hara, M.; Hayashi, S. *Chem. Mater.* **2006,** *18*, 3039.

[2.47] Muller-Fischer, N.; Tobler, P.; Dressler, M.; Fischer, P.; Windhab, E. J. *Exp. Fluids* **2008,** *45*, 917.

[2.48] Pillai, K.; Advani, S. G. *J. Colloid Interface Sci.* **1996,** *183*, 100.

[2.49] Yildirim Erbil, H. *Surface Chemistry of Solid and Liquid Interfaces*; Blackwell Publishing Ltd.: Oxford, 2006; p 141.

[2.50] Lachawiec, Jr., A. J.; Qi, G.; Yang, R. T. *Langmuir* **2005,** *21*, 11418.

[2.51] Srinivas, S. T.; Rao, P. K. *J. Catal.* **1994,** *148*, 470.

[2.52] Gregg, S. J.; Sing, K. S. W. *Adsorption, Surface Area and Porosity*, 2nd ed.; Academic Press: London, 1982; Chapter 2.

[2.53] Kaneko, K.; Ishii, C. *Colloids Surf.* **1992,** *67*, 203.

[2.54] Kruk, M.; Jaroniec, M.; Gadkaree, K. *Langmuir* **1999,** *15*, 1442.

[2.55] Kruk, M.; Jaroniec, M.; Ryoo, R.; Joo, S. H. *J. Phys. Chem. B* **2000,** *104*, 7960.

[2.56] Walton, K. S.; Snurr, R. Q. *J. Am. Chem. Soc.* **2007,** *129*, 8552.

[2.57] Webb, P. A.; Orr, C. *Analytical Methods in Fine Particle Technology*; Micromeritics Instrument Corporation, Norcross, GA, 1997.

[2.58] Horvath, G.; Kawazoe, K. *J. Chem. Eng. Jpn.* **1983,** *16*, 470.

[2.59] Barrett, E. P.; Joyner, L. S.; Halenda, P. P. *J. Am. Chem. Soc.* **1951,** *73*, 373.

[2.60] Bashkova, S.; Bagreev, A.; Bandosz, T J. *Catal. Today* **2005,** *99*, 323.

[2.61] Spenadel, L.; Boudart, M. *J. Phys. Chem.* **1960,** *64*, 204.

[2.62] Lewis, F. A. *The Palladium Hydrogen System*; Academic Press: London, 1967; p 4.

[2.63] Benson, J. E.; Boudart, M. *J. Catal.* **1965,** *4*, 704.

[2.64] Park, J.-H.; Kim, J.-N.; Cho, S. H.; Kim, J.-D.; Yang, R. T. *Chem. Eng. Sci.* **1998,** *53*, 3951.

[2.65] Gruber, H. L. *J. Phys. Chem.* **1962,** *66*, 48.

[2.66] Matsuoka, K.; Yamagishi, Y.; Yamazaki, T.; Setoyama, N.; Tomita, A.; Kyotani, T. *Carbon* **2005,** *43*, 876.

Chapter 3

Hydrogen Adsorption Measurement: Apparatus and Techniques

3.1 Overview of Measurement Methods

The study of adsorbent materials for mobile hydrogen storage applications has prompted the need for accurate measurement of capacity and kinetics near ambient conditions. Most researchers have focused studies on the capacity of practical materials at room temperature and pressure ranging from sub-atmospheric to 10 MPa. The relatively low capacities (< 5 wt%) of these materials compared to those of hydrogen at cryogenic temperatures,[3.1] other adsorbates at room temperature,[3.2] or in metal hydrides[3.3] have presented new challenges for traditional adsorption measurement techniques.[3.4] Variables such as manifold temperature, sample weight, and valve leak rate must now be carefully considered as they can contribute significantly to the overall adsorption measurement.[3.5] In addition, many of the materials studied are microporous and show affinity for helium, which has typically been considered a non-adsorbing species for free space determination. Helium adsorption has been shown to impact skeletal density measurement of active carbons and hence, the dead volume surrounding the sample.[3.6-3.8]

The most common methods for measurement of adsorption capacity in general are gravimetric and volumetric techniques. Additionally, an electrochemical procedure has been employed for measurement of hydrogen capacity; however, the results tend, on

average, to yield larger capacity due to a different storage mechanism.[3.9] Mass spectrometry has been used with temperature programmed desorption experiments to estimate capacity, relying on appropriate calibrations with known hydride compounds.[3.10] This technique is limited to sub-atmospheric pressure and is clearly non-isothermal.

3.1.1 Gravimetric Techniques

Gravimetric methods are the most direct measurement of adsorption capacity and require little dependence on computational methods. These techniques, performed with mechanical balances,[3.11] avoid the problem of free space determination using helium, as weight gain or loss is the measured variable. Some early hydrogen adsorption work on carbon-based adsorbents was performed with a static gravimetric method at cryogenic conditions; however, there was no report of capacity near ambient temperature.[3.12]

Several aspects of gravimetric methods present challenges. Some instrumental designs employ a flowing gas phase. This has an advantage in that it reduces equilibration time for each data point, however, the measurements must be corrected for buoyancy of the gas surrounding the sample. The correction must be carefully performed at each pressure with a 'dummy' sample that adequately simulates the adsorbent.[3.13] A non-static gas phase increases the possibility of material loss from the pan or bucket, which can be interpreted as decreased capacity.

Commercial instruments are available to measure isotherms gravimetrically with a static gas phase to 50 MPa.[3.14-3.16] These devices are highly automated and include sophisticated control schemes to control temperature, pressure and gas phase composition. While limited hydrogen capacity and kinetic data has been published from

studies with these instruments, some authors have demonstrated reproducibility of high-pressure balances comparable to volumetric techniques.[3.17-3.19]

3.1.2 Volumetric Techniques

Measurement of adsorption using volumetric techniques is well established and dates back to the early twentieth century work of Sieverts, who used a low pressure glass apparatus to study absorption and diffusion of gases, notably hydrogen, in metals.[3.20] This research continued into the middle of the century and covered many transition metal and gas combinations. In fact, as a testament to his body of work, many in the metal hydride community refer to volumetric based systems as Sieverts apparati. Langmuir began his pioneering work on adsorption theory with a similar apparatus, measuring adsorption and dissociative adsorption of gases on such substrates as molybdenum, tungsten, and platinum filaments.[3.21] These early volumetric systems continued their evolution and were enhanced by developments in vacuum technique, temperature control, and pressure measurement. With the development of the theory of multimolecular layer adsorption by Brunauer, Emmett, and Teller, characterization of catalytic materials and adsorbents by volumetric adsorption for surface area determination became standard.[3.22] Later it was found that the distribution of pore sizes in the material could also be extracted from adsorption isotherms using various techniques.[3.23-3.29]

Numerous commercial instruments are available with well-established techniques to measure sub-atmospheric adsorption of cryogenic nitrogen or argon, motivated by the

wealth of information provided at these conditions.[a] While these are primarily designed for surface area and pore size determination, they can be adapted to measure hydrogen isotherms if analysis is performed with attention to background response, free space measurement, and temperature control.[3.30-3.33] Many investigators have reported hydrogen adsorption results at cryogenic conditions with such instruments.[3.34] One of the first reports of a hydrogen adsorption isotherm on microporous carbon at ambient temperature was provided by Chahine and Bose.[3.35] Since then, a commercial product offering has not emerged as the standard for volumetric measurements above atmospheric pressure,[b] therefore, hydrogen storage measurement at these conditions has relied upon instruments custom built by each laboratory performing the measurement.[3.36-3.42] These devices are typically static volumetric units, however, Poirier et al. developed a flow-based system to eliminate the build-up of contaminants in the system from successive static expansions that would reduce capacity.[3.13] This method has not seen widespread acceptance in the adsorption community, presumably because it still requires correction for helium adsorption and contamination can be addressed in static experiments with well-maintained purifiers. As one would expect, data for a given material becomes highly dependent upon the design and analytical technique specific to the piece of equipment. Concerns with these analyses are not trivial as nonideality at elevated pressure, correction for helium adsorption, background signal, manifold temperature variation, and potential leaks all play a role in the accuracy of the data.

---

[a] Micromeritics® Instrument Corporation ASAP Series Accelerated Surface Area and Porosimetry Analyzers, Quantachrome Instruments Autosorb® Series Surface Area and Pore Size Analyzers.

[b] Micromeritics® Instrument Corporation recently released preliminary specifications for the ASAP 2050 Xtended Pressure Sorption Analyzer for measurement to 1 MPa; however, it is not in widespread use.

Volumetric systems have frequently required gram-scale quantities of sample, which substantially reduces the effect of weighing error on adsorption measurements. It is often difficult to produce large quantities of stable candidate materials on the laboratory scale. This is particularly the case with metal organic frameworks (MOFs) and covalent organic frameworks (COFs), where several hundred milligrams of material may take one week or more to produce. Additionally, storage of the material before measurement can sometimes degrade the structure and adsorption capacity.[3.43] For this reason, modern volumetric based methods should be designed to minimize sample quantity requirements for adsorption measurement. This criterion implies minimizing the system dead volume, which has an added safety benefit of reducing the amount of gaseous hydrogen required for a complete analysis.

3.2 Design of a High-Pressure Volumetric Apparatus

The design basis and details are presented for a volumetric system capable of reproducibly measuring hydrogen adsorption and desorption from 0.1 MPa to 10 MPa at room temperature. Focus is on capacity measurements near ambient temperature since this is where the most practical application based material is sought. Data is provided from the analysis of several materials that have widely known, reproducible storage capacities to validate the instrument. The issues of nonideality correction, helium adsorption during free space measurement, pressure step size, and manifold temperature fluctuations are also discussed as they greatly influence instrument accuracy.

3.2.1 Equipment Specification and Details

A schematic of the high-pressure volumetric apparatus is shown in Figure 3.1 with nomenclature defined in Table 3.1. This instrument is capable of measuring hydrogen adsorption and desorption at room temperature and up to 10 MPa. All components in contact with hydrogen were constructed from stainless steel (316 or 316L). The gases hydrogen (99.999% purity) and helium (99.999% purity) were purified using beds of Molecular Sieve 3A (Grace Davison, 8-12 mesh beads) dedicated to each gas to prevent cross contamination. A filter (5 μm) was installed after the purifiers to prevent particulates from contaminating the apparatus and causing valve leaks.

All fittings joining components of the reference and sample volumes were VCR® metal gasket face-seal type (Swaglok®). When joined according to the proper procedure, these fittings have a guaranteed leak rate of no more than 4×10^{-9} mL(STP)/s helium (for a single leak this equates to a deviation of less than 1 kPa over a 24 h period). The reference and sample cell volumes were carefully characterized and are depicted in Figure 3.1 by V_{ref} and V_{sam}. All component volumes, except for the downstream side of the bellows valves, were measured with deionized water in triplicate. Liquid was carefully injected with a needle syringe to prevent air bubbles from affecting the measurement. Blank VCR® gaskets were used, as needed, to facilitate measurements of pieces with multiple open ends. Due to their complex geometry, the downstream bellows and valve outlet volume was measured by helium expansion. The bellows valves were positioned such that this method was required for only one downstream bellows.

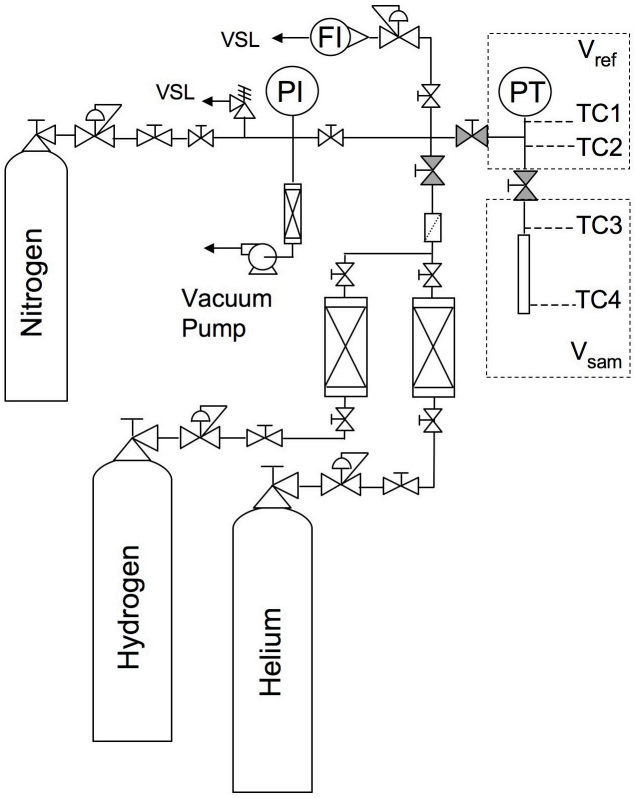

Figure 3.1 Schematic of High-Pressure Volumetric Adsorption Apparatus

Table 3.1 Nomenclature for High-Pressure Volumetric Apparatus Schematic

Tag	Description
FI	Flow Indicator
PI	Pressure Indicator
PT	Pressure Transducer
TC	Thermocouple
V_{ref}	Reference Volume
V_{sam}	Sample Volume
VSL	Vent to Safe Location

These techniques yielded volumes of 3.6 mL and 11.3 mL for V_{ref} and V_{sam}, respectively. The volume measurements were reproducible to within 0.1 mL. In order to further reduce the dead volume, a stainless steel spacer rod (2.9 mL) was inserted into the sample cell after loading the sample. The rod fit loosely in the tube such that the reduction of vacuum conductance was kept to a minimum. A 0.5 μm VCR® filter gasket was used when making up the connection to the reference volume to eliminate the possibility of sample intrusion into the reference volume and valves.

The three valves cycled most frequently during experiments are highlighted in grey in Figure 3.1. The valves used for this application were bellows sealed type (Swagelok®, U Series). These valves offered a combination of low leak rate (4×10^{-9} mL(STP)/s helium) and dead volume comparable to diaphragm valves, which are also often used in high pressure adsorption systems. Given their low leak rate, the affect of seat seal leakage is minimal for data collection over 24 h, which is the duration of most runs when including adsorption and desorption branches. This type of valve offered an extra safety feature of secondary containment above the bellows in the event of a failure and their maximum working pressure exceeded the maximum operating pressure by a factor of 1.7.

The pressure and temperature histories of the apparatus were recorded in order to calculate volume adsorbed and generate isotherm data. The pressure of the reference volume or the combined reference and sample volumes was measured using a pressure transmitter (Dylix Corporation, GX Series) with a range of 0-13.8 MPa (0-2000 psia) and enhanced static accuracy to ± 0.1% full-scale output. This transmitter proved to be accurate even in the low end of its range. Figure 3.2 shows the result of low-range

calibration with helium against a Bourdon tube analog gauge (Ashcroft® Type 1082). The external temperature of the apparatus was measured at four locations with bead-type thermocouples (TC1-TC4) mounted directly to the metal surface with polyimide adhesive tape (Omega Engineering, Inc., 5TC-GG-K-24). The raw signal output of the pressure transmitter and four thermocouples was processed and logged on a computer with a custom LabVIEW program that enabled data collection in user selectable intervals beginning with 5 s.

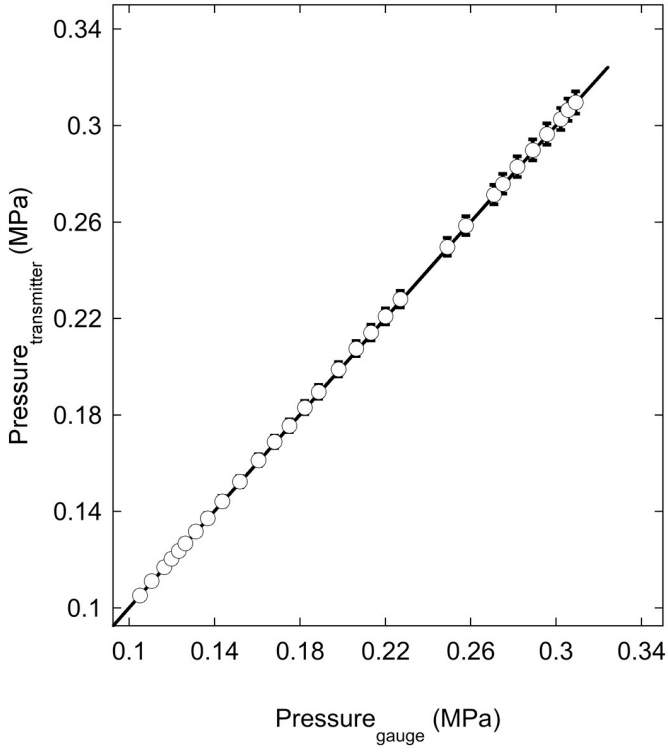

Figure 3.2 Calibration of Pressure Transducer Low Range

A mechanical, two-stage rotary vacuum pump (Edwards Vacuum, Ltd., E2M0.7) was used for evacuation of the apparatus and pretreatment of the sample. This pump consistently achieved a pressure of 2.7 x 10^{-3} mbar at the sample cell. A trap filled with

alumina beads was used to prevent oil vapor backstreaming into the foreline and apparatus piping. Sub-atmospheric pressure was measured with a Convectron® equivalent gauge with integrated controller (Kurt J. Lesker Company, KJL275800) that enabled measurement to 1.3×10^{-4} mbar. The vacuum pump was protected from accidental overpressure using a relief device set to 0.2 MPa. The outlet of this device was plumbed independently to a fume hood with a minimum face velocity of 0.5 m/s.

Aluminum foil, considered a non-adsorbing material, was used to establish a background adsorption signal. The mass of aluminum foil used for this procedure was calculated by matching its occupied volume to that of the carbon samples (ρ_{Al} = 2.7 g/ mL). Any deviation from zero was added or subtracted from the raw data as a blank correction.

3.2.2 Experimental Procedure

The general procedure for any material began with weighing approximately 150-200 mg of the material and transferring it into the tared sample cell. The tared sample cell included the weight of the spacer rod and VCR® filter disk. This facilitated measurement of the post-degas sample weight at the end of the run. The filled sample cell was connected to the apparatus and helium was charged to the entire volume to perform a coarse pressure decay leak test. After ensuring that there was no downward trend in the pressure response over several hours, the fitting was assumed to be leak-free. Helium was vented and the sample cell was evacuated to at least 7×10^{-3} mbar before beginning the temperature program.

The temperature program was sample dependent. For AX-21, a ramp of 2 K/min to 473 K was followed by a 12 h soak. For carbon-based materials exhibiting spillover or materials pre-reduced in flowing hydrogen, the ramp was typically 1 K/min to 623 K followed by a 12 h soak to completely degas residual hydrogen. After heating under vacuum, the sample was not contacted with helium again until after the hydrogen adsorption measurements to prevent interference of residual helium. The post-degas sample weight was estimated from ex-situ experiments and the preliminary free space for the run was calculated by subtracting the sample volume from the empty system volume. These estimates were later verified or updated with a direct free space measurement and final sample weight at the conclusion of the run.

Collection of hydrogen adsorption data commenced after the sample was fully equilibrated with room temperature. The vacuum transmitter response was set to zero and the initial temperature of the apparatus was recorded for several minutes. The sample cell was isolated in vacuum from the reference volume. The reference volume was charged with hydrogen to the pressure desired for the first adsorption step. The pressure and temperature responses (TC1 and TC2) typically took about 15 to 30 min to stabilize, depending on the step size. To ensure complete equilibrium, a full 60 min was allowed to elapse before proceeding to the adsorption step. At that time, the isolation valve between the reference volume and sample cell was opened and the adsorption event proceeded. Adsorption was deemed complete when the pressure response demonstrated stability to within 2 kPa. This typically occurred within 20 min for physisorption and on the order of 60 min for adsorbents demonstrating spillover. Upon reaching adsorption equilibrium, the isolation valve was closed and a pressure rise was observed in the

reference volume. This is due to squeezing of the bellows upon closing the valve. The new pressure was recorded and used to close the material balance. This sequence was repeated for all adsorption steps. The procedure for desorption was similar, however, the reference volume was vented and evacuated prior to each desorption step. If an external leak was suspected at any time when the apparatus was charged with hydrogen, a hydrogen/hydrocarbon leak detector (SRI Instruments, Model 8690) was available to 'sniff' the fittings or bellows. In practice, this type of leak has not been observed after following manufacturer guidelines for fitting assembly.

The final step of the analysis procedure was to confirm the estimated free space and final sample weight. Upon completion of the desorption branch of the isotherm, the sample was evacuated at room temperature for at least 2 h until the pressure was stable at 2.7×10^{-3} mbar. The reference volume was isolated from the sample cell in vacuum and it charged to approximately 0.3 MPa with helium. After the pressure stabilized, the sample was exposed to helium to measure free space. The final pressure was typically 0.1 MPa. Using a pressure near atmospheric was important so that the data could be corrected for helium adsorption by simply using Henry's law (vide infra). Lastly, the sample cell was disconnected, under positive helium pressure (0.12 MPa) to prevent air and moisture intrusion, and weighed immediately to determine the actual post-degas mass. This slight pressure ensured that any flow of gas would initially be helium exiting the tube rather than air intruding into the evacuated space. Transport of air to the sample was then by diffusion, which is sufficiently slow relative to the short time required to transfer and weigh the sample and tube together on a nearby balance (less than 1 min).

By following this procedure, adsorption of air at room temperature accounted for less than 0.5 mg uncertainty in the sample mass.

3.2.3 Data Analysis Method

Raw data generated during an adsorption and desorption isotherm measurement consisted of pressure and temperature histories of the apparatus for each step. The equilibrium pressure and temperatures were used to calculate the moles of hydrogen present in each step of the process. In general, there were three calculations to compute the mole balance – and hence adsorbed amount – for a particular pressure step. These calculations were repeated to measure the entire adsorption and desorption isotherm. The moles of hydrogen charged to the reference volume were computed from

$$n_1 = \frac{P_1 V_{ref}}{Z_1 R T_1} \tag{3.1}$$

where T_1 is an average of the readings for TC1 and TC2 and Z_1 is computed from P_1 and T_1. The moles of hydrogen in the gas phase after exposure to the adsorbent and equilibrium was reached were computed from

$$n_2 = \frac{P_2 (V_{ref} + V_{sam})}{Z_2 R T_2} \tag{3.2}$$

where T_2 is an average of the readings for TC1 through TC4 and Z_2 is computed from P_2 and T_2. The moles of hydrogen present in the reference volume after isolation from the sample and before charging additional hydrogen for the next pressure step were computed from

$$n_3 = \frac{P_3 V_{ref}}{Z_3 R T_3} \tag{3.3}$$

The number of moles of hydrogen present in the gas phase after sample cell isolation could thus be determined from subtraction ($n_2 - n_3$). The amount of adsorbed hydrogen was computed from the direct difference of the moles charged to the reference volume and those measured in the gas phase after equilibrium

$$n_{ads} = \frac{P_1 V_{ref}}{Z_1 R T_1} - \frac{P_2 (V_{ref} + V_{sam})}{Z_2 R T_2} \tag{3.4}$$

The adsorption amount could be computed on a volumetric or weight basis (Q_{ads}) with the appropriate manipulation and conversion(s).

The volumetric data was corrected for non-ideality of the gas phase by using the second (B') and third (C') virial coefficients to calculate a compressibility factor at the measured pressure and temperature.

$$Z(P,T) = 1 + B'(T)\frac{P}{RT} + C'(T)\frac{P^2}{RT} \tag{3.5}$$

$$B'(T) = B(T) \tag{3.6}$$

$$C'(T) = \frac{C(T) - B(T)^2}{RT} \tag{3.7}$$

For temperatures above 100 K, the second and third virial coefficients have been correlated by the following functions, respectively[3.44]

$$B(T) = \sum_{i=1}^{4} b_i x_1^{(2i-1)/4} \tag{3.8}$$

$$C(T) = 1310.5\, x_2^{1/2}\left[1 + 2.1486\, x_2^3\right]\left[1 - \exp\left(1 - x_2^{-3}\right)\right] \tag{3.9}$$

where the b_i constants are $b_1 = 42.464$, $b_2 = -37.1172$, $b_3 = -2.2982$, $b_4 = -3.0484$, and the x_i functions are $x_1 = 109.781$ K / T and $x_2 = 20.615$ K / T.

For kinetic response, the fraction complete was calculated as a function of time by the following relationship

$$F(t) = \frac{M(t)}{M_{\infty}} = \frac{n_{g,initial} - n_g(t)}{n_{g,initial} - n_{g,eq}} \tag{3.10}$$

where the moles of hydrogen are all in the gas phase, n_g, initial represents the initial gas phase moles, and $n_{g,\,eq}$ represents the gas phase moles at equilibrium.

3.2.4 Heuristic to Correct for Helium Adsorption

The traditional practice to determine dead or free space in volumetric adsorption measurement has been to use a non-adsorbing species that sufficiently penetrates the pores of the solid under study. Helium is most often the ideal candidate gas for this purpose as it has the smallest molecular diameter (second only to hydrogen) such that it penetrates into nearly all pores of the solid and it does not have a high affinity for solid surfaces. At room temperature, this is not universally true for certain materials, most notably coals,[3.45] activated carbons[3.6,3.46] and microporous adsorbents.[3.7,3.8,3.47,3.48] This does not preclude helium from being used as a dead space probe for these materials, rather, care must be taken to account for this adsorption, particularly when sample amounts and system volumes are small. Sircar has published a model to describe helium adsorption at various temperatures and atmospheric pressure in terms of a simple Henry's law constant.[3.49] Since the measurement of free space occurs at 298 K, the values for the Henry's law constant at this temperature ($K_{He,298}$) were computed using the formula

$$K(T) = K\left(\frac{T^*}{T} = 1\right)\exp\left[-\lambda(1 - T^*/T)\right] \tag{3.11}$$

with T = 298 K. In this formula, T* is the temperature at which helium adsorption is assumed negligible for the first iteration of the calculation, later being corrected for actual adsorption at T* and λ is defined as

$$\lambda = \Delta H_{ads,He} / RT \tag{3.12}$$

Data was drawn from Sircar's work or references cited therein. These values were compared to the BET surface area of each material. A plot of the data is shown in Figure 3.3, along with the heat of adsorption of helium at 298 K ($\Delta H_{ads,\,He}$) for each material. As one can see, there is a linear relationship between the amount of helium adsorbed and the BET surface area for microporous materials. Helium possesses no permanent dipole moment or quadrupole moment.[3.50] Therefore, the adsorbate-adsorbent interaction is dominated by the nonspecific contributions of dispersion and close-range repulsion energy.[3.51] As a result, despite the charged surface of the zeolites, the heat of adsorption remaining relatively independent of sorbent type (here zeolites and active carbons) is not unexpected for merely loading a proportionally larger surface. Based on the observed relationship, it is reasonable to interpolate $K_{He,298}$ for materials with BET surface area between 500 and 2000 m^2/g. In the absence of data specific to an adsorbent, it also seems valid to extrapolate the existing trend to larger surface area materials, such as AX-21 and molecular sieve Templated Carbon. In this way Henry's law constants have been computed to correct for helium adsorption for all microporous and Nanoporous materials used in this work. These are shown in Table 3.2.

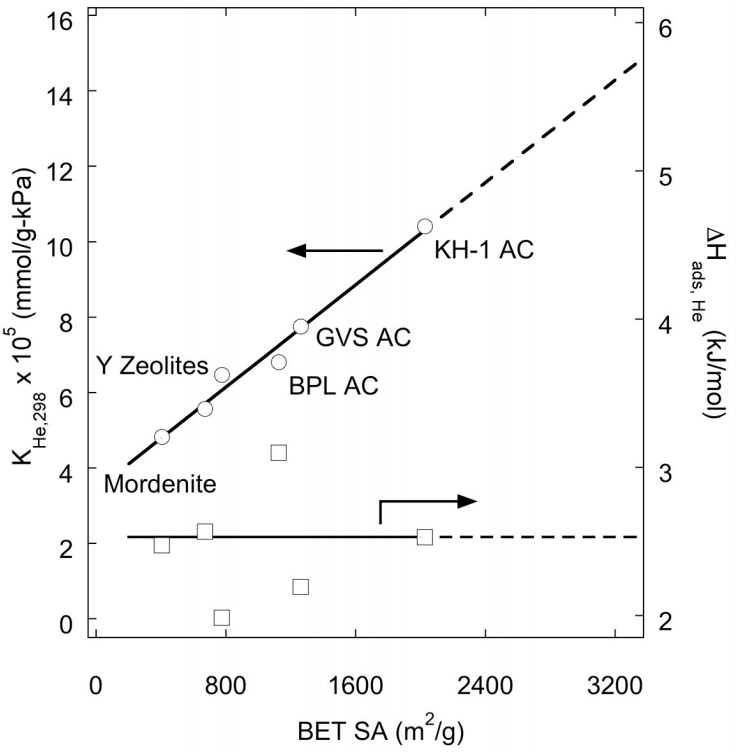

Figure 3.3 Henry's Law Constant and Heat of Adsorption for Helium

Table 3.2 Henry's Law Constants for Nanostructured Adsorbents at 298 K

Material	$\mathbf{K_{He,298}\ x\ 10^5}$, mmol/(g-kPa)
GNF	4.7
Molecular Sieve 5A	5.3
SWNT	6.5
AX-21	12.8
Templated Carbon	14.8

The data of Haas et al.[3.19] for helium adsorption on SWNTs forms the basis of a useful comparison to the prediction of the Henry's law constant with the newly developed heuristic for such nanostructures. The isotherm at room temperature presented by these authors remains linear over the entire pressure range studied (up to 9 MPa).

Although the exact BET SA is not stated for their helium study, their SWNTs range was 670 to 1090 m^2/g. The extended Sircar model predicts $K_{He,298}$ from 5.5 x 10^{-5} to 7.1 x 10^{-5} mmol/(g-kPa) over this range. Estimating a Henry's law constant from the data, one obtains 7.3 x 10^{-5} mmol/(g-kPa).

3.2.5 Error Propagation for Adsorbed Amount

There are several sources of uncertainty that enter into the calculation of adsorbed amount of hydrogen. The uncertainties in pressure, temperature, system volume, and sample mass are quantified directly. Values are provided in Table 3.3.

Table 3.3 Uncertainty in Measured Variables for Adsorption Apparatus

Parameter	Uncertainty
Pressure	14 kPa (2 psi)
Temperature	0.25 K
Volume	0.1 mL
Sample Weight	5 mg

Uncertainty in the compressibility factor is propagated based on the stated 5% uncertainty in second and third virial coefficients.[3.44] The formula is given by

$$\delta_Z = \frac{1}{RT}\left[P^2\Delta_{B'}^2 + P^4\Delta_{C'}^2 + \left(B' + 2C'P\right)^2\Delta_P^2 + \left(\frac{B'P + C'P^2}{T}\right)^2\Delta_T^2\right]^{1/2} \tag{3.13}$$

where δ_Z indicates the propagated uncertainty in the compressibility and Δ reflects the uncertainty in the subscripted variable. The value varied according to the pressure and temperature of the adsorption step; however, it was generally in the range of 1 x 10^{-4} to 2 x 10^{-3}.

Uncertainty in the number of moles adsorbed for a given pressure step was propagated via the following relationship

$$\delta_n = \frac{1}{ZRT}\left[V^2\Delta_P^2 + P^2\Delta_V^2 + \left(\frac{PV}{Z}\right)^2\Delta_Z^2 + \left(\frac{PV}{T}\right)^2\Delta_T^2\right]^{1/2} \quad (3.14)$$

Finally, the uncertainty in the adsorbed amount was calculated from that propagated through the mole balance for each step, n_H, and the uncertainty in the sample weight, w_s,

$$\delta_{Q_{ads}} = \left[\left(\frac{1}{w_s}\right)^2\Delta_{n_H}^2 + \left(\frac{n_H}{w_s^2}\right)^2\Delta_{w_s}^2\right]^{1/2} \quad (3.15)$$

This treatment resulted in an average uncertainty of 25% in the adsorbed amount over the entire adsorption isotherm.

3.3 Validation of Apparatus and Method

3.3.1 Standard Materials

In order to test the accuracy of the measurement and analytical techniques, AX-21 was selected as a standard compound since its hydrogen capacity at room temperature is readily available in the literature and quite reproducible.[3.35,3.52-3.55] An adsorption and desorption isotherm is presented for the alloy $LaNi_5$, (Cerac, Inc., 99.5%, -100 mesh) a metal hydride with a reproducible and well documented storage capacity. However, as Blach and Gray discuss, it is not suitable to rely solely on metal hydride reproducibility to justify the accuracy of the instrument of 'light atom' or low density materials.[3.41] Realizing this, high pressure hydrogen adsorption and desorption has been measured at ambient temperature for graphite powder (Asbury Carbons) and 5A zeolite (Grace Davison, 8-12 mesh) to test the range of the instrument. Results are presented for several

nanostructured carbons, namely single-walled nanotubes (SWNT) and graphite nanofibers (GNF), to further illustrate the applicability of the technique.

Interest in titanium and its alloys has grown as Ti-6Al-4V has been implicated in the increased capacity of carbon-based adsorbents via the spillover mechanism, notably SWNTs that have undergone sonication to cut the tubes,[3.56] and titanium has improved the kinetic cycling of metal hydrides when co-doped with various carbon forms.[3.57] Although detailed measurements were not performed on Ti-6Al-4V alloy powder, a material whose capacity is somewhat debated, hydrogen uptake by this material without rigorous pretreatment has been measured and the result at room temperature and atmospheric pressure (3.0 wt%) is bounded by several recent results in the literature.[3.59,3.60]

3.3.2 Results of Validation Study

The hydrogen adsorption isotherm at 298 K for AX-21 was measured for three different ascending pressure intervals when charging the reference volume: 2 MPa, 4 MPa, and 6 MPa. The intervals were selected based on the maximum allowable working pressure of the apparatus, 12.5 MPa, and accounted for the fact that equal pressure intervals were desired for collection of data up to 10 MPa. This generated reproducibility data and proved that transient effects, such as diurnal temperature changes and the Joule-Thomson effect coupled with gas mixing during depressurization of the reference volume, did not alter the final equilibrium adsorption amount. Desorption was conducted with variable steps, however, the intervals were further limited because of the ratio between the sample cell and reference volumes. The results of this series of experiments

are shown in Figure 3.4. As is common practice, open and closed markers represent adsorption and desorption, respectively. As the figure indicates, regardless of the pressure step size, the equilibrium amount is in agreement with the literature value for AX-21. Data for a similar microporous carbon, GX-31 (BET SA ~ 2500 m^2/g, PV = 1.2 mL (STP)/g), measured using a differential pressure method[3.19] are included for comparison of the two measurement techniques. The data demonstrate that the equilibrium amount is independent of the charging pressure. The adsorption kinetics may show pressure (concentration) dependence, particularly for the spillover mechanism as will be discussed in subsequent chapters.

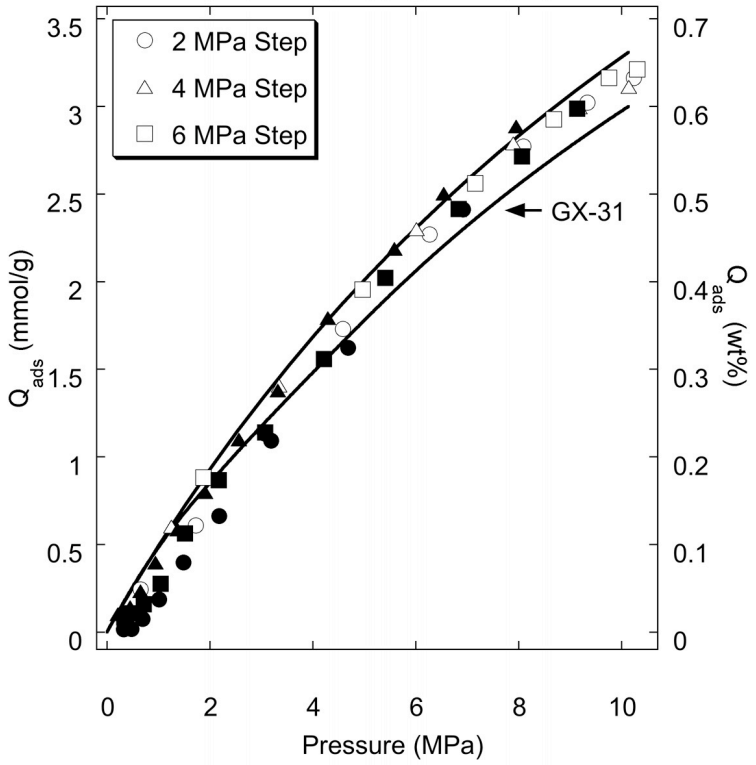

Figure 3.4 AX-21 Repeatability for Variable Pressure Steps

The isotherm result for AX-21 measured using the high pressure system was compared to measurements taken below 0.1 MPa using a Micromeritics® ASAP 2010 instrument. Figure 3.5 shows a comparison of this data and the first generated with the high-pressure apparatus. Extrapolating the linear behavior of the isotherm collected below 0.1 MPa pressure to the lower range of the high-pressure system, good agreement is observed between the data at 298 K for AX-21 given the error limits of both instruments. The isotherms agree to within 0.0017 wt%, which is well within the error limits of the Micromeritics® ASAP 2010. The solid line represents a fit to literature data.[3.52,3.53] Low pressure results deviate slightly from this fit while the first and subsequent data points of the high pressure system agree quite well.

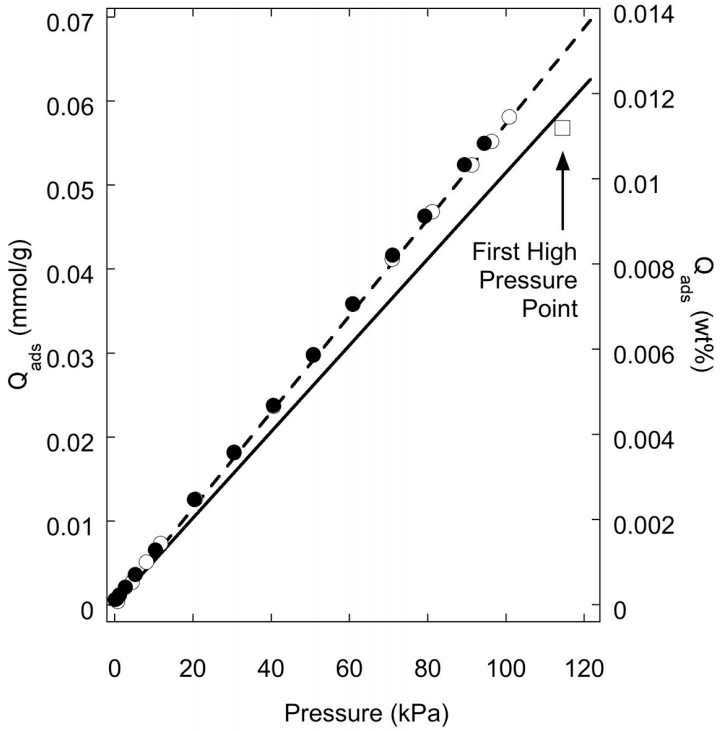

Figure 3.5 Agreement Between High Pressure and Low Pressure Measurements

The accuracy of the high-pressure apparatus is demonstrated by measurement of hydrogen isotherms for materials that have well documented capacity in the literature. Some properties and ambient temperature capacities of these materials are presented in Table 3.4, along with the measured capacities of this study at the specified pressure. The adsorption and desorption isotherms are presented for measurements of selected materials to demonstrate accuracy and reproducibility with respect to those reported in the literature.

Table 3.4 Materials Studied to Demonstrate Instrument Accuracy

Material	**BET SA** m^2/g	**Pore Volume** mL(STP)/g	**Capacity,** wt%	
			Measured	**Literature**
Graphite Powder	3	0	0.037 (a)	0.04 (a)[3.64]
			0.042	
GNF	330	0.26	0.24	0.25[3.69]
SWNT	820	0.44	0.40	0.42[3.19]
AX-21 Carbon	2800	1.2	0.64	0.66[3.53,3.54]
Templated Carbon	3400	1.5	0.79	
5A Zeolite	450	0.21	0.128 (b)	0.142 (b)[3.65,3.66]
			0.21	
$LaNi_5$	-	-	1.44 (c)	1.4 (c)[3.60,3.61]

All data reported at 298 K and 10 MPa, except: (a) 6 MPa, (b) 5 MPa, (c) 0.6 MPa

Lanthanum nickel ($LaNi_5$) alloy has become a standard material to demonstrate measurement accuracy for hydrogen storage. It is relatively easy to activate and has a well-defined capacity at room temperature and near ambient pressure. The hysteresis loop provides opportunity to demonstrate the reproducibility of absorption and desorption. Hydrogen absorption and desorption was measured for $LaNi_5$ at room

temperature and results are presented in Figure 3.6. The results compare favorably with literature capacity and hysteresis, which are indicated by solid and dashed lines.[3.60,3.61]

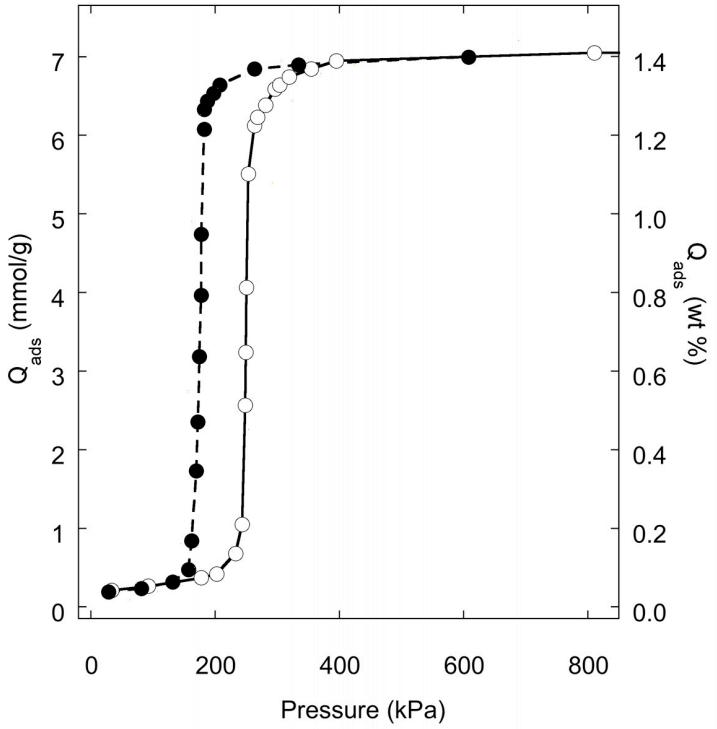

Figure 3.6 Hydrogen Absorption by $LaNi_5$ Using the High Pressure System

In order to evaluate the low range accuracy of the high-pressure apparatus for a light density material, the hydrogen isotherms on graphite powder and 5A zeolite were measured at room temperature. The high-pressure isotherm of hydrogen on graphite is shown in Figure 3.7. As expected, the adsorption capacity is rather low, reaching a maximum of 0.04 wt% over the pressure range studied. Several authors have reported on chemisorbed hydrogen on graphite, however, these studies do not report reversible capacity.[3.62,3.63] Data from this work does agree well with Kajiura et al. who report a single data point of just under 0.05 wt% at 6 MPa for powdered graphite at room temperature.[3.64] Figure 3.8 shows the room temperature hydrogen isotherm on 5A

zeolite. The isotherm is compared with the data of Chen et al. to 5 MPa.[3.65] The inset shows low range data to 2 MPa compared with that of Nam et al.[3.66] In both cases, excellent agreement is observed in comparison with published results for this zeolite.

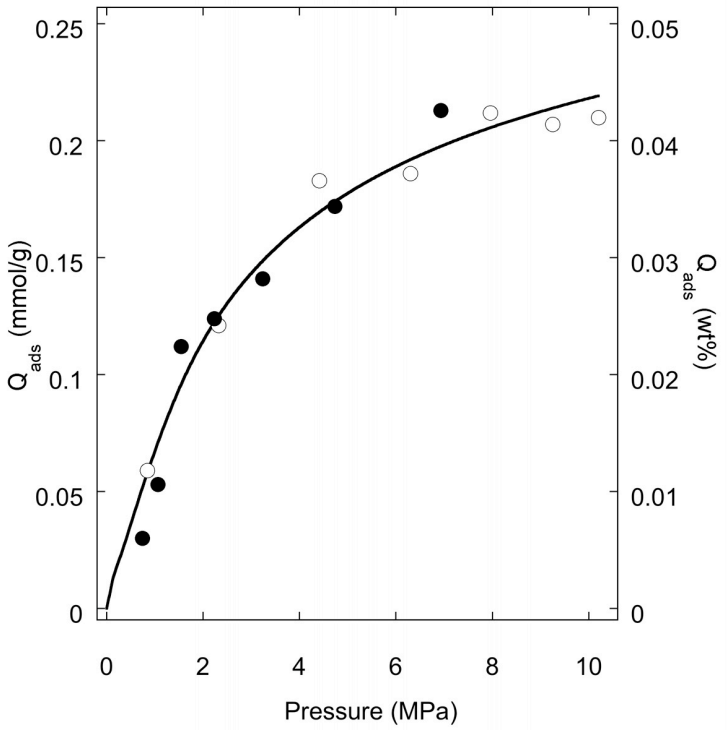

Figure 3.7 Hydrogen Adsorption on Graphite Powder

The hydrogen capacity for several nanostructured carbons has also been measured reliably with the high-pressure volumetric system. One such material was SWNTs synthesized as in Chapter 2.[3.67] The material contained < 1% ash by ASTM D 2866.[3.68] The high-pressure isotherm at 298 K is shown in Figure 3.9. The hydrogen capacity at 10 MPa is approximately 0.4 wt%, which is in good agreement with SWNT materials of comparable BET SA measured by Haas et al.[3.19] The capacity of graphite nanofibers (GNF) synthesized as outlined in Chapter 2 is shown in Table 3.4 and shows good agreement with comparable materials reported in the literature.[3.69]

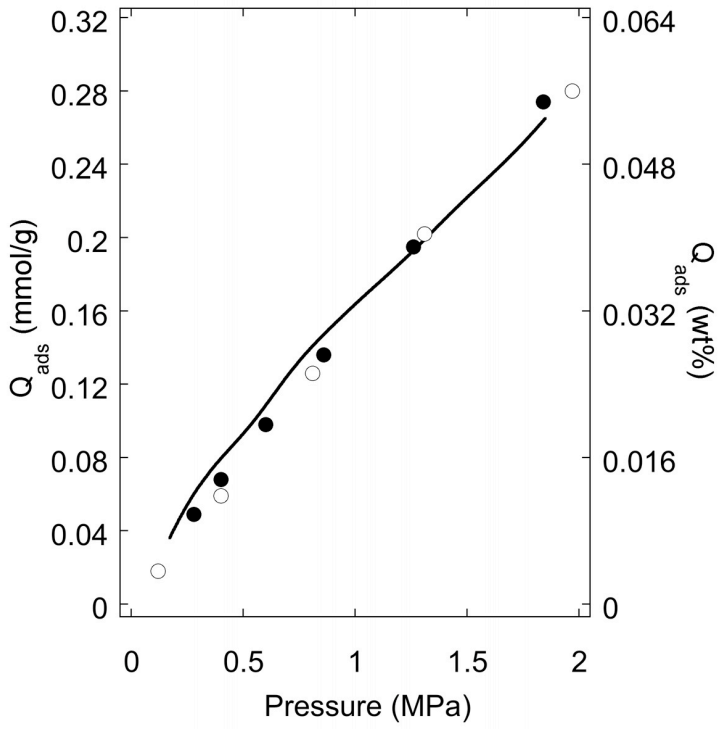

Figure 3.8 Hydrogen Adsorption on 5A Zeolite

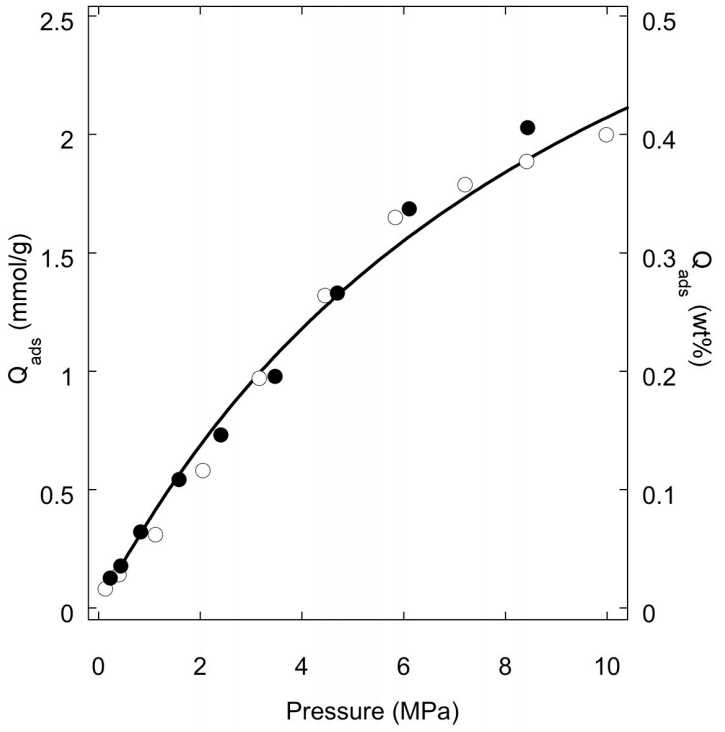

Figure 3.9 Hydrogen Adsorption on SWNTs

3.3.3 Helium Adsorption Correction to Free Space Measurement

The AX-21 data presented for reproducibility of isotherm measurements was corrected for helium adsorption during free space determination. The method outlined in the experimental section was used to calculate the Henry's law constant at 298 K and atmospheric pressure. The free space was measured at atmospheric pressure so that this constant could be applied directly without requiring pressure extrapolation and potential error due to any curvature of the helium isotherm. The helium adsorption data of Malbrunot et al. demonstrate marked curvature for zeolites measured above 10 MPa.[3.47] The skeletal density of AX-21 measured with helium adsorption subtracted is 1.7 g/mL. This agrees well with literature data for various activated carbons.[3.6,3.45] If helium adsorption is not subtracted from the free space measurement, the skeletal density is overestimated as 2.8 g/mL. Hydrogen isotherms on AX-21 were simulated for the case where this helium adsorption is not taken into account to demonstrate the affect on the data. The result is presented in Figure 3.10. As the figure shows, when helium adsorption is not accounted for in the free space measurement at room temperature, the adsorption amount is underpredicted by 25-30%. A similar result was noted by Haas et al.[3.19] when measuring hydrogen adsorption on SWNTs.

3.3.4 Effect of Manifold Temperature Variation

The mole balance used to calculate the adsorbed amount requires a measurement of the gas temperature. Ideally, this temperature would be measured internally in the gas space; however, this is challenging to accomplish in practice. Some instruments have used a temperature-controlled box for maintaining the manifold temperature uniform over

the course of an experiment.[3.70] In the present case, the temperature of the instrument is measured at four external locations and averaged appropriately according to the volume under consideration. The temperature of the instrument is allowed to 'float' with the diurnal temperature change in the room. This variance is often only a few degrees Kelvin during the experiment duration. Although small, it has an effect on the measured pressure because of the small volumes employed and is particularly noticeable as pressure increases.

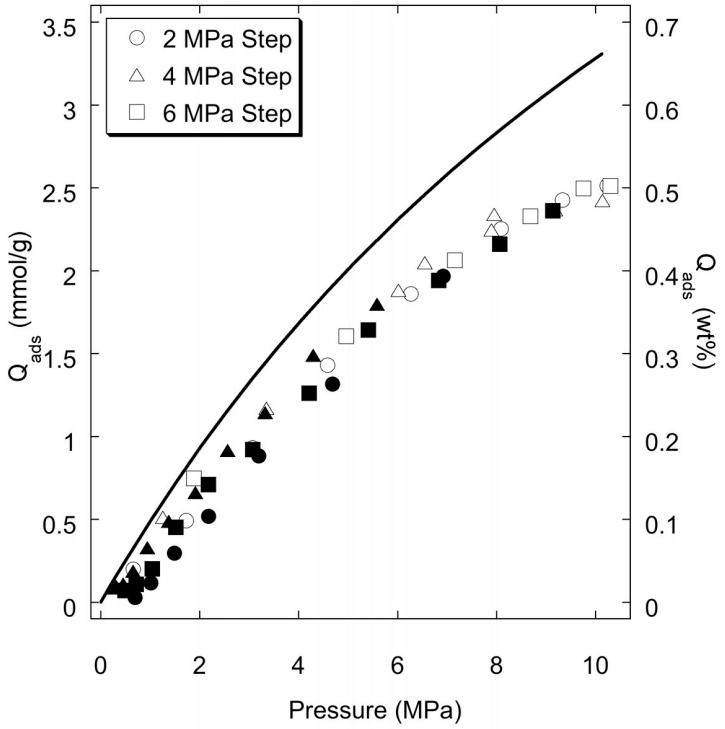

Figure 3.10 Helium Adsorption Influence on Isotherm Accuracy

An example of the temperature effect on the pressure measurement is shown in Figure 3.11. This figure tracks the pressure and temperature response of the apparatus and the sample cell over a 10 h period with the sample statically exposed to hydrogen. The valve was opened at the approximately 1.5 h mark, exposing the sample. The two

temperature traces indicate that the temperature fluctuations of the overall apparatus are dominated by the sample cell variance and the pressure tracks closely to the temperature. The fluctuations normally would cause difficulty in equilibrium determination; however, this is not the case if the moles of hydrogen present in the gas phase are computed point-wise from the data in Figure 3.11. As the results presented in Table 3.5 indicate, the fluctuations induce less than 1% deviation from the average adsorbed amount when moles are computed from each discrete data point. Thus, this criterion is acceptable for verifying equilibrium without installing for a temperature-controlled manifold.

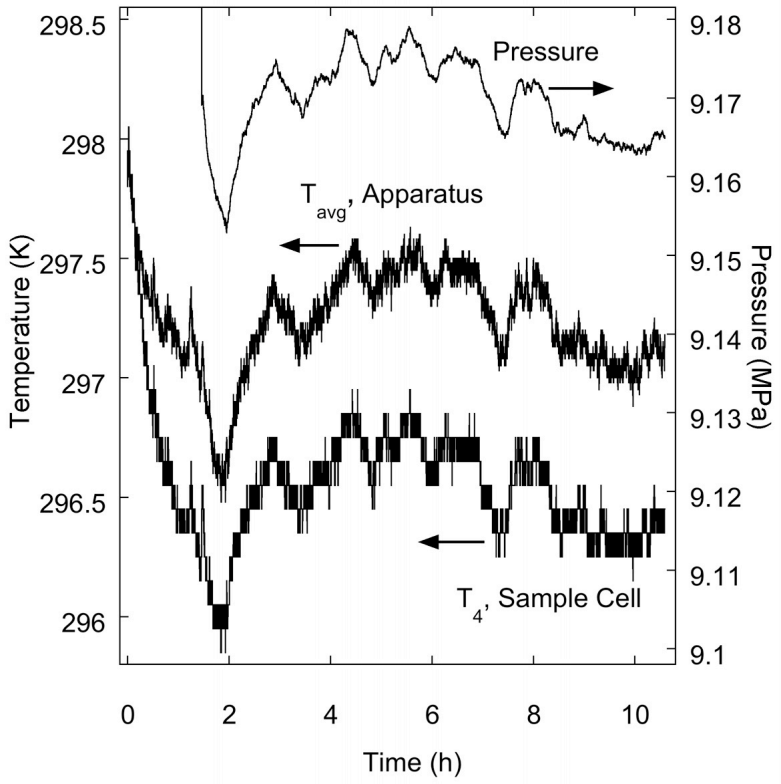

Figure 3.11 Temperature and Pressure Accuracy at Equilibrium

Table 3.5 Variation of Amount Adsorbed for Manifold Temperature Fluctuation

Time h	**Pressure** MPa	T_{avg} K	Q_{ads} mmol/g	Q_{ads} wt%	**Deviation from Avg** %
1.95	9.153	296.73	3.458	0.692	+0.49
2.93	9.175	297.38	3.417	0.683	- 0.69
3.46	9.168	297.18	3.443	0.689	+0.07
5.18	9.176	297.48	3.466	0.693	+0.74
5.55	9.179	297.50	3.410	0.682	- 0.89
7.18	9.170	297.25	3.454	0.691	+0.38
10.0	9.164	297.03	3.433	0.687	- 0.22
Average	9.169	297.22	3.441	0.688	

Note: Valve opened at 1.46 h (i.e. first data point is 1.95 – 1.46 = 0.49 h into adsorption event)

3.3.5 Calculation of Diffusion Time Constant from Kinetic Data

The rate of adsorption for hydrogen on AX-21 was determined by calculating the diffusion time constant ($D_{p,e}/R_p^2$) for arbitrary particle diameter. Here, the subscripts identify the parameters as the effective pore diffusivity and the particle radius, respectively. The particle shape was taken as spherical and although it is recognized that this is an approximation, it permits the use of simplified diffusion equations.

The solution starts by assuming that diffusion follows Fick's law. Fick's second law characterizes the diffusion process and assuming a constant diffusion coefficient can be represented in spherical geometry by

$$\frac{\partial C}{\partial t} = D\left(\frac{\partial^2 C}{\partial r^2} + \frac{2}{r}\frac{\partial C}{\partial r}\right) \tag{3.16}$$

If variables are converted using the relationship u = Cr, the following result is obtained

$$\frac{\partial u}{\partial t} = D\frac{\partial^2 u}{\partial r^2} \tag{3.17}$$

The conversion simplifies the boundary and initial conditions greatly as now

$$u(0,t) = 0 \tag{3.18}$$

$$u(R_p,t) = R_p C_o \tag{3.19}$$

$$u(r,0) = r\,f(r) \tag{3.20}$$

If the adsorbent is initially free of adsorbate, f(r) = 0. For a loaded adsorbent at equilibrium, f(r) = C_{eq}. An analytical solution exists for this problem. The fraction complete, or total amount of hydrogen adsorbed at any time relative to the equilibrium amount for a given step, is given for a spherical particle by[3.71]

$$F(t) = \frac{M(t)}{M_\infty} = 1 - \frac{6}{\pi^2}\sum_{n=1}^{\infty}\frac{1}{n^2}\exp\left(-\frac{D_{p,e}}{R_p^2}(n\pi)^2 t\right) \tag{3.21}$$

where t is measured starting from the beginning of the adsorption step. Although this equation contains a summation, it was observed that only 20 terms were required to converge a solution for the analyses. This form allows the model to be fit over the entire duration of the adsorption step, compared to the truncated form valid for only short times or limited adsorption amounts.[3.72] This is important because the system establishes gas phase equilibrium in the initial stages of the exposure step due to mixing and the Joule-Thomson effect, which can induce a 1-2 K temperature fluctuation depending on the size of the pressure step taken.

A comparison of the model and the data are provided in Figure 3.12. The data reflect adsorption at different pressures for equal steps in adsorbed amount (0.6 mmol/g) along the isotherm. Maintenance of this step size allows direct comparison of the diffusion time constants for pressure (or concentration) dependence. The diffusion time

constant was adjusted to fit the data near equilibrium. As the figure shows, adsorption is complete in less than 10 min for all conditions and the rate shows little concentration dependence. The figure inset shows the trend in values of the diffusion time constant computed from the fitted model for AX-21. Table 3.6 reports the raw values.

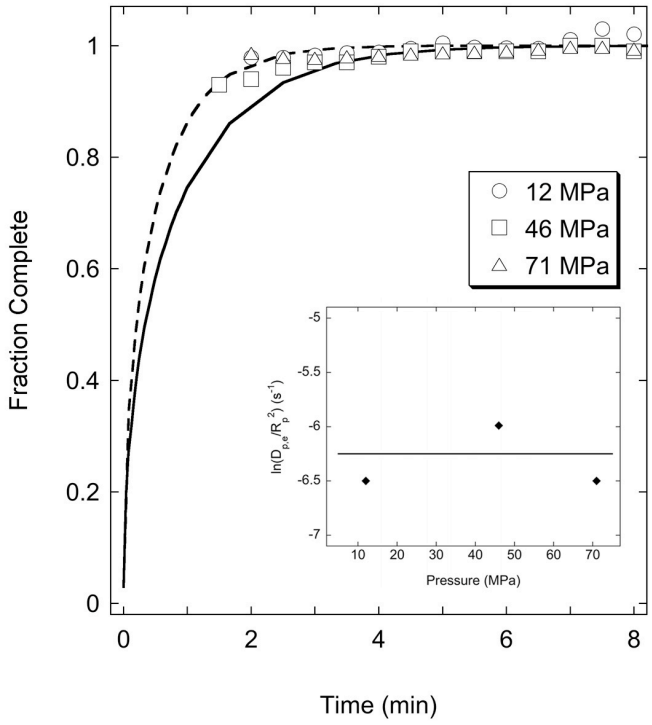

Figure 3.12 Kinetics of Hydrogen Adsorption on AX-21

Table 3.6 Values of the Diffusion Time Constant for AX-21

Pressure MPa	$\mathbf{D_{p,e}/R_p^2}$ s^{-1}
1.2	0.0015
4.6	0.0025
7.2	0.0015

Literature data are limited for hydrogen kinetics on carbon-based adsorbents, especially at room temperature. Kojima and Suzuki[3.73] report kinetic data for hydrogen adsorption at 296 K on material similar to AX-21. The adsorption step is complete in less than 10 min, however, the data are only reported for one step at 5.3 MPa. Zhao et al. observe hydrogen adsorption occurring over 1.5 h on carbon molecular sieve (CMS) at 77 K and 1 kPa.[3.74] Bansal and Goyal reported room temperature adsorption kinetics similar to the hydrogen data collected in this study for O_2, N_2, and several hydrocarbons on CMS.[3.75] Kinetic data, and in particular, diffusion time constants, for other gases on carbon-based adsorbents are more readily available. Walker reports D/R^2 values in the range of 1×10^{-5} to 2.5×10^{-4} s^{-1} for gases such as Ar, CO, CO_2, N_2, and O_2 on CMS.[3.76] Bae and Lee measured the pressure dependence of D/R^2, reporting values for methane ranging from 10^{-6} to 10^{-5} s^{-1} over the pressure range from 0.1 to 1.6 MPa.[3.77] In general, data for hydrogen adsorption on AX-21 generated with the high pressure apparatus are consistent with literature reports and demonstrate more rapid kinetics relative to most gases on carbon-based adsorbents.

3.4 Conclusions

This work has demonstrated the accuracy, reproducibility, and stability of a high-pressure volumetric apparatus and the data reduction technique for measuring hydrogen capacity of adsorbents. The apparatus was designed to measure adsorption and desorption for microporous and nanoporous adsorbents at room temperature and up to 10 MPa pressure.

The techniques used for measurement and calculation can be applied to determine the equilibrium capacity of adsorbents demonstrating purely physisorption and those exhibiting the hydrogen spillover phenomenon. Reduction of pressure and temperature histories for the instrument can provide kinetic data. In a subsequent chapter, this data is used to calculate the diffusion time constant for spillover of hydrogen.

Results with several materials that demonstrate well documented literature capacities compare favorably with recently developed differential pressure techniques.[3.78] Thus, the apparatus and method provides a simple alternative to such systems when considering fabrication and material costs.

3.5 Literature Cited

[3.1] Pradhan, B. K.; Harutyunyan, A. R.; Stojkovic, D.; Grossman, J. C.; Zhang, P.; Cole, M. W.; Crespi, V.; Goto, H.; Fujiwara, J.; Eklund, P. C. *J. Mater. Res.* **2002,** *17*, 2209.

[3.2] Barton, S. S.; Evans, M. J. B.; Holland, J.; Koresh, J. E. *Carbon* **1984,** *22*, 265.

[3.3] Zaluska, A.; Zaluski, L.; Ström-Olsen, J. O. *Appl. Phys. A* **2001,** *72*, 157.

[3.4] Broom, D. P. *J. Alloys Compd.* **2007,** *446-447*, 687.

[3.5] Tibbetts, G. G.; Meisner, G. P.; Olk, C. H. *Carbon* **2001,** *39*, 2291.

[3.6] Maggs, F. A. P.; Schwabe, P. H.; Williams, J. H. *Nature* **1960,** *186*, 956.

[3.7] Springer, C.; Major, C. J.; Kammermeyer, K. *J. Chem. Eng. Data* **1969,** *14*, 78.

[3.8] Sircar, S. *AIChE J.* **2001,** *47*, 1169.

[3.9] Zhao, X. B.; Xiao, B.; Fletcher, A. J.; Thomas, K. M. *J. Phys. Chem. B* **2005,** *109*, 8880.

[3.10] Dillon, A. C.; Jones, K. M.; Bekkedahl, T. A.; Kiang, C. H.; Bethune, D. S.; Heben, M. J. *Nature* **1997,** *386*, 377.

[3.11] Freiman, S.; Hooker, S.; Migler, K.; Arepalli, S. *Measurement Issues in Single Wall Carbon Nanotubes*; NIST Recommended Practice Guide, Special Publication 960-19; National Institute of Standards and Technology: Washington, DC, 2008.

[3.12] Agarwal, R. K.; Noh, J. S.; Schwarz, J. A.; Davini, P. *Carbon* **1987,** *25*, 219.

[3.13] Poirier, E.; Chahine, R.; Tessier, A.; Bose, T. K. *Rev. Sci. Instrum.* **2005,** *76*, 055101.

[3.14] Hiden Isochema. IGA-001 Gas Sorption Analyser. http://www.hidenisochema.com (accessed Dec 2008).

[3.15] *Sorption: ISOSORP – The New Sorption Suspension Balance*; Rubotherm, Prazisionsmesstechnik GmbH, Bochum, Germany, 2007.

[3.16] *GHP Sorption Analyzers*; VTI Scientific Instruments, VTI Corporation, Hialeah, FL, 2007.

[3.17] Vestbø, A. P.; Jensen, J. O.; Bjerrum, N. J. *J. Alloys Compd.* **2007,** *446-447*, 703.

[3.18] Langmi, H. W.; Walton, A.; Al-Mamouri, M. M.; Johnson, S. R.; Book, D.; Speight, J. D.; Edwards, P. P.; Gameson, I.; Anderson, P. A.; Harris, I. R. *J. Alloys Compd.* **2003,** *356-357*, 710.

[3.19] Haas, M. K.; Zielinski, J. M.; Dantsin, G.; Coe, C. G.; Pez, G. P.; Cooper, A. C. *J. Mater. Res.* **2005,** *20*, 3214.

[3.20] Sieverts, A. *Z. Physik. Chem.* (Leipzig) **1908,** *60*, 129.

[3.21] Langmuir, I. *J. Am. Chem. Soc.* **1915,** *37*, 1139.

[3.22] Brunauer, S.; Emmett, P. H.; Teller, E. *J. Am. Chem. Soc.* **1938,** *60*, 309.

[3.23] Barrett, E. P.; Joyner, L. S.; Halenda, P. P. *J. Am. Chem. Soc.* **1951,** *73*, 373.

[3.24] Horvath, G.; Kawazoe, K. *J. Chem. Eng. Jpn.* **1983,** *16*, 470.

[3.25] Saito, A.; Foley, H. C. *AIChE J.* **1991,** *37*, 429.

[3.26] Cheng, L. S.; Yang, R. T. *Chem. Eng. Sci.* **1994,** *49*, 2599.

[3.27] Ross, S.; Olivier, J. P. *On Physical Adsorption*; Wiley & Sons: New York, 1964.

[3.28] Dubinin, M. *Carbon* **1983,** *21*, 359.

[3.29] Dubinin, M.; Astakhov, V. *Adv. Chem. Ser.* **1970,** *102*, 69.

[3.30] Webb, P. A.; Orr, C. *Analytical Methods in Fine Particle Technology*; Micromeritics Instrument Corporation: Norcross, GA, 1997.

[3.31] *Helium Effects on ASAP Series Micropore Analyses*; Application Note 105; Micromeritics Instrument Corporation: Norcross, GA.

[3.32] *Determining Free-Space Values for ASAP Series Micropore Analyses*; Application Note 104; Micromeritics Instrument Corporation: Norcross, GA.

[3.33] *Using the ASAP 2020 for Determining the Hydrogen Adsorption Capacity of Powders and Porous Materials*; Application Note 136; Micromeritics Instrument Corporation: Norcross, GA.

[3.34] Ansón, A.; M. Benham, M.; Jagiello, J.; Callejas, M. A.; Benito, A. M.; Maser, W. K.; Züttel, A.; Sudan, P.; Martínez, M. T. *Nano Technology* **2004,** *15*, 1503.

[3.35] Chahine R.; Bose, T. K. *Int. J. Hydrogen Energy* **1994,** *19*, 161.

[3.36] Ahn, C. C.; Ye, Y.; Ratnakumar, B. V.; Witham, C.; Bowman, Jr., R. C.; Fultz, B. *Appl. Phys. Lett.* **1998,** *73*, 3378.

[3.37] Browning, D. J.; Gerrard, M. L.; Lakeman, J. B.; Mellor, I. M.; Mortimer, R. J.; Turpin, M. C. *Nano Lett.* **2002,** *2*, 201.

[3.38] Checchetto, R.; Trettel, G.; Miotello, A. *Meas. Sci. Technol.* **2004,** *15*, 127.

[3.39] Panella, B.; Hirscher, M.; Roth, S. *Carbon* **2005,** *43*, 2209.

[3.40] Poirier, E.; Chahine, R.; Bénard, P.; Lafi, L.; Dorval-Douville, G.; Chandonia, P. A. *Langmuir* **2006,** *22*, 8784.

[3.41] Blach, T. P.; Gray, E. MacA. *J. Alloys Compd.* **2007,** *446-447*, 692.

[3.42] Zhou, W.; Wu, H.; Hartman, M. R.; Yildirim, T. *J. Phys. Chem. C* **2007,** *111*, 16131.

[3.43] Li, Y.; Yang, R. T. *AIChE J.* **2008,** *54*, 273.

[3.44] McCarty, R. D. In *Hydrogen: Its Technology and Implications, Hydrogen Properties*; Cox, K. E., Williamson, K. D., Eds.; CRC Press: Cleveland, OH, 1975; Vol. III, pp.18-19.

[3.45] Franklin, R. E. *Trans. Faraday Soc.* **1949,** *45*, 274.

[3.46] Fernbacher, J. M.; Wenzel, L. A. *Ind. Eng. Chem. Fundam.* **1972,** *11*, 457.

[3.47] Malbrunot, P.; Vidal, D.; Vermesse, J.; Chahine, R.; Bose, T. K. *Langmuir* **1997,** *13*, 539.

[3.48] Koresh, J. E.; Kim, T. H.; Koros, W. J. *J. Chem. Soc., Faraday Trans. 1* **1989,** *85*, 1537.

[3.49] Sircar, S. In *Fundamentals of Adsorption*; Kaneko, K., Kanoh, H., Hanzawa, Y., Eds.; IK International: Chiba, 2002; Vol. 7, pp.656-663.

[3.50] Table of the Isotopes, In *CRC Handbook of Chemistry and Physics*, 88th ed.; D. L. Lide, D. L., Ed.; CRC Press/Taylor & Francis: Boca Raton, FL, 2008; Internet Version.

[3.51] Yang, R. T. Nanostructured Adsorbents. In *Nanostructured Materials*; Ying, J., Ed.; Advances in Chemical Engineering; Academic Press: New York, 2001; Vol. 27, p 79-124.

[3.52] Zhou, L.; Zhou, Y. *Ind. Eng. Chem. Res.* **1996,** *35*, 4166.

[3.53] Zhou, L.; Zhou, Y. *Chem. Eng. Sci.* **1998,** *53*, 2531.

[3.54] Benard, P.; Chahine, R. *Langmuir* **2001,** *17*, 1950.

[3.55] Zhou, L.; Zhou, Y.; Sun, Y. *Int. J. Hydrogen Energy* **2006,** *31*, 259.

[3.56] Hirscher, M.; Becher, M.; Haluska, M.; Dettlaff-Weglikowska, U.; Quintel, A.; Duesberg, G. S.; Choi, Y. M.; Downes, P.; Hulman, M.; Roth, S.; Stepanek, I.; Bernier, P. *Appl. Phys. A* **2001,** *72*, 129.

[3.57] Wang, J.; Ebner, A. D.; Ritter, J. A. *J. Phys. Chem. B* **2006,** *110*, 17353.

[3.58] Poirier, E.; Chahine, R.; Bénard, P.; Cossement, D.; Lafi, L.; Mélançon, E.; Bose, T. K.; Désilets, S. *App. Phys. A* **2004,** *78*, 961.

[3.59] Blackburn, J. L.; Parilla, P. A.; Gennett, T.; Hurst, K. E.; Dillon, A. C.; Heben, M. J. *J. Alloys Compd.* **2008,** *454*, 483.

[3.60] Goodell, P. D. *J. Less-Common Met.* **1984,** *99*, 1.

[3.61] Lundin, C. E.; Lynch, F. E. *IECEC Record* **1975,** *10*, 1380.

[3.62] Bansal, R. C.; Vastola, F. J.; Walker, Jr., P L. *Carbon* **1971,** *9*, 185.

[3.63] Chen, D. M.; Ichikawa, T.; Fujii, H.; Ogita, N.; Udagawa, M.; Kitano, Y.; Tanabe,

E. *J. Alloys Compd.* **2003,** *354*, L5.

[3.64] Kajiura, H.; Tsutsui, S.; Kadono, K.; Kakuta, M.; Ata, M.; Murakami, Y. *App. Phys. Lett.* **2003,** *82*, 1105.

[3.65] Chen, Y. D.; Ritter, J. A.; Yang, R. T. *Chem. Eng. Sci.* **1990,** *45*, 2877.

[3.66] Nam, G. M.; Jeong, B. M.; Kang, S. H.; Lee, B. K.; Choi, D. K. *J. Chem. Eng. Data* **2005,** *50*, 72.

[3.67] Cassell, A. M.; Raymakers, J. A.; Kong, J.; Dai, H. *J. Phys. Chem. B* **1999,** *103*, 6484.

[3.68] ASTM D 2866. 2003 (2004), "Standard Test Method for Total Ash Content of Activated Carbon," ASTM International, West Conshohocken, PA, 2009.

[3.69] Blackman, J. M.; Patrick, J. W.; Arenillas, A.; Shi, W.; Snape, C. E. *Carbon* **2006,** *44*, 1376.

[3.70] Ramaprabhu, S.; Rajalakshmi, N.; Weiss, A. *Int. J. Hydrogen Energy* **1998,** *23*, 797.

[3.71] Crank, J. *The Mathematics of Diffusion*; Oxford University Press: London, 1956.

[3.72] Rong, Z.; Vadgama, P. J. *Colloid Interface Sci.* **2006,** *303*, 75.

[3.73] Kojima, Y.; Suzuki, N. *Appl. Phys. Lett.* **2004,** *84*, 4113.

[3.74] Zhao, X.; Villar-Rodil, S.; Fletcher, A.; Thomas, K. M. *J. Phys. Chem. B* **2006,** 110, 9947.

[3.75] Bansal, R. C.; Goyal, M. *Activated Carbon Adsorption*; CRC: Boca Raton, FL, 2005, pp. 229–230.

[3.76] Walker, Jr., P. L. *Carbon* **1990,** *28*, 261.

[3.77] Bae, Y.-S.; Lee, C.-H. *Carbon* **2005,** *43*, 95.

[3.78] Zielinski, J. M.; Coe, C. G.; Nickel, R. J.; Romeo, A. M.; Cooper, A. C.; Pez, G. P. *Adsorption* **2007,** *13*, 1.

Chapter 4

Hydrogen Adsorption Properties of Carbon-Based Materials

4.1 Parameters Obtained from Volumetric Adsorption Measurement

4.1.1 Adsorbed Amount

The amount adsorbed as a function of pressure for a constant temperature is an adsorption isotherm. This is the most practical way to represent the data for hydrogen storage applications, since on-board storage will be operated at relatively constant ambient conditions.[4.1] Overall, ambient conditions are expected to vary in a relatively narrow window (from an adsorption standpoint) of 50 K (from 273 to 323 K). These conditions are easy to simulate in laboratory experiments with ice water, room temperature, or heated recirculation baths. Waste heat from the vehicle power plant may be available to desorb hydrogen, however, the adsorbent must perform adequately under conditions such as startup or high flow demands where additional energy may not be available or sufficient for desorption. Therefore, full reversibility at constant temperature is desirable.

The most common isotherm for adsorbents is represented by the well-known Langmuir equation[4.2]

$$Q_{ads} = Q_{ads,m}\left(\frac{bP}{1+bP}\right) \tag{4.1}$$

where $Q_{ads,m}$ is the adsorption monolayer amount and b is a constant that is dependent on temperature. The assumptions of this isotherm are well documented, including one molecule per adsorption site, energetically uniform sites, and no interaction between neighboring adsorbed species.[4.3] At low pressure and coverage, the isotherm reduces to a Henry's Law linear form ($Q_{ads} = Q_{ads,m} bP$). For adsorbents that rely solely on physisorption, hydrogen coverage on the surface is quite low at ambient conditions (generally 1 to 2% of the saturation coverage) because the conditions are very far from liquid pore filling estimated from the Gurvitsch rule.[4.4] Many of the hydrogen isotherms on such materials are linear or display gentle curvature that is captured by the Langmuir isotherm.[4.5-4.12]

Langmuir extended the isotherm to systems where a species dissociates upon adsorption. In this case, two sites are occupied for each molecule that is adsorbed and the isotherm equation takes the form

$$Q_{ads} = Q_{ads,m}\left(\frac{b'\sqrt{P}}{1+b'\sqrt{P}}\right) \tag{4.2}$$

where b′ is the Langmuir constant for dissociative adsorption. An isotherm of this functionality is expected – in part – to capture the spillover mechanism, which relies on the dissociation of hydrogen molecules. This led Yang et al. to recently develop a theoretical spillover isotherm based upon radial diffusion away from sources to receptors for composite adsorbents.[4.13,4.14]

$$Q_{ads} = \frac{K_1 k_1 \sqrt{P}}{1 + k_2\sqrt{P} - K' k_1 \sqrt{P}} \tag{4.3}$$

where the K parameters represent equilibrium constants for hydrogen concentration distribution on the source and receptor and k_n are constants in the dissociative Langmuir

equation for adsorption on platinum. At low pressure, the isotherm again reduces to Henry's law behavior. At high pressure, the equation predicts a constant saturation limit. Isotherm predictions capture the linearity of data over a wider pressure range that was observed for bridged composite materials, including those with metal organic framework (MOF) and nanostructured carbon receptors.

4.1.2 Isosteric Heat of Adsorption

The isosteric heat of adsorption ($-\Delta H_{ads}$) is a measure of the strength of interaction of a species with a surface. The phenomenon of adsorption is exothermic and therefore the enthalpy of adsorption is a negative number. The Clausius-Clapeyron equation relates the enthalpy of adsorption to physically measurable properties, namely pressure and temperature.[4.4] The relationship at low pressure, where the gas phase can be considered ideal, is

$$\left(\frac{d\ln P}{dT}\right)_{Q_{ads}} = \frac{(-\Delta H_{ads})}{RT^2} \tag{4.4}$$

where P is the equilibrium pressure attained for a fixed adsorption amount (Q_{ads}) at a given temperature. The isosteric heat of adsorption can be easily calculated from a minimum of two isotherm data points via

$$-\Delta H_{ads} = \frac{RT_2T_1}{(T_2 - T_1)}(\ln P_2 - \ln P_1)_{Q_{ads}} \tag{4.5}$$

If isotherms at three or more temperatures are available, the relationship takes a different form of an adsorption isostere, where Equation 4.4 has been integrated to yield

$$(\ln P)_{Q_{ads}} = \frac{(-\Delta H_{ads})}{RT} + \text{constant} \tag{4.6}$$

The calculation proceeds by obtaining equilibrium pressures at variable temperature for a common adsorption amount. A plot of the pressure variable (ln P) versus reciprocal temperature (1/T) should be nearly linear with a slope ($-\Delta H_{ads}/R$).

In this manner, the isosteric heat of adsorption can be obtained for a range of equilibrium points on the isotherm. The behavior as a function of adsorbed amount, which is taken as a measure of surface coverage, generally shows a decreasing trend due to increased adsorbate-adsorbate interactions with the adsorption of more species.

The isosteric heat of adsorption for physisorption of hydrogen molecules on most common adsorbents with capacity less than 0.6 wt% at 10 MPa is near - 8 kJ/mol. This is the lower boundary for the parameter when searching for novel hydrogen adsorbents. The upper limit is set by the conditions for reversibility of the material. High interaction energy comes with a price, substantial energy input to recover adsorbed hydrogen, as was documented in Chapter 1. Hydride formation and chemisorption of hydrogen to transition metals yields interaction enthalpies from - 40 kJ/mol to - 120 kJ/mol.[4.15-4.19] It is desirable for a combination of improved capacity and reversibility at moderate conditions, therefore, to create adsorbents with isosteric heats of adsorption that meet the following rough criterion

$$8\ \text{kJ/mol} < \left(-\Delta H_{ads}\right) < 40\ \text{kJ/mol} \tag{4.7}$$

4.1.3 Diffusion Time Constant

Kinetic response of adsorbents is important for applications. A high capacity material is unusable if the adsorbate species cannot be released at the rate suitable for application. An example of this is many metal hydrides, which often approach the 6 wt%

target capacity but do not release hydrogen at a rate suitable for use by a fuel cell at normal operating conditions.

Adsorption kinetics can be measured using volumetric techniques to capture the time response of an adsorbent to a step increase or decrease in pressure. The method was outlined in Chapter 3. The closed form solution of the diffusion equation is valid if the relative film resistance at the surface is small compared to diffusion resistance in the particle, as it is for most gas phase applications (Biot Number, Bi ~ 10 to 100).[4.20] The fractional uptake as a function of time, F(t), is once again shown for clarity,

$$F(t) = 1 - \frac{6}{\pi^2} \sum_{n=1}^{\infty} \frac{1}{n^2} \exp\left(-\frac{D_{p,e}}{R_p^2} n^2 \pi^2 t \right) \tag{4.8}$$

where $D_{p,e}$ is the effective diffusion coefficient and R_p is the particle radius. The model is frequently used to compare relative kinetics of adsorption and desorption processes.[4.21,4.22]

The spillover phenomenon occurs as atoms hop along the surface due to a concentration gradient.[4.13,4.23,4.24] This type of surface diffusion process is best represented by a two-dimensional, radial coordinate system. Figure 4.1 depicts the situation for a secondary spillover source and receptor system. With the techniques outlined in Chapter 2, bridges are formed between the support material of the source (PR = primary receptor) and the secondary receptor.

There is no simple analytical solution for the boundary condition of a step increase in concentration at the center of the geometry; however, one exists for a step increase at the outer boundary. Yang et al. describe the inaccuracies in the diffusion time constant caused by implementing this solution.[4.13] The values calculated from experimental data are predicted lower than the actual values for adsorption as the surface

is assumed to load in the opposite direction. Concentration and temperature behavior is correct and is useful for comparing relative rates as these conditions vary.

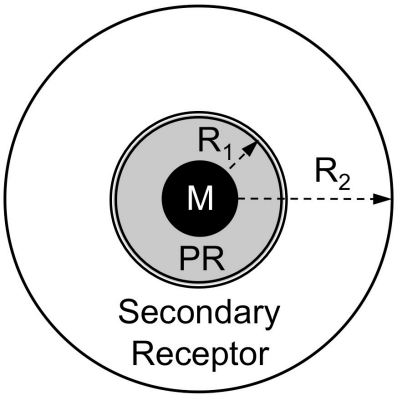

Figure 4.1 Schematic of Spillover Geometry

Fick's second law for a two dimensional, radial geometry becomes

$$\frac{\partial C}{\partial t} = \frac{1}{r}\frac{\partial}{\partial r}\left(r D_{s,e} \frac{\partial C}{\partial r} \right) \tag{4.9}$$

This equation may be solved by the method of separation of variables. Defining as a solution

$$C = u(r)\exp\left(-\alpha^2 \tau\right) \tag{4.10}$$

assuming a constant surface diffusion coefficient ($D_{s,e}$) with dimensionless time, $\tau = (D_{s,e}t)/R_s^2$, and satisfying Bessel's equation of order zero.

$$\frac{d^2u}{dr^2} + \frac{1}{r}\frac{du}{dr} + \alpha^2 u = 0 \tag{4.11}$$

For constant concentration at the outer boundary of spillover, $r = R_s$ and with a constant initial concentration on the surface, $C(r,0) = C_i$, the solution is

$$F(t) = 1 - 4\sum_{n=1}^{\infty} \frac{1}{\alpha_n^2} \exp\left(-\frac{D_{s,e}}{R_s^2}\alpha_n^2 t\right) \tag{4.12}$$

with α_n values equal to the positive roots of the Bessel function of the first kind, order zero ($J_o(\alpha_n) = 0$). Note that the diffusion time constant appears in this relationship as a result of substituting the relationship for dimensionless time. The advantage of this solution is that it is valid over the entire adsorption event, compared to the short time solution employed previously.[4.13] This enables asymptotic behavior of the data at equilibrium to be adequately captured when calculating the diffusion time constant.

4.2 Results for Receptors

Hydrogen adsorption isotherms for carbon-based materials used as receptors are presented in this section. Adsorption isotherms are measured for a minimum of two temperatures and in some cases three (77K, 273 K, 298 K, or 323 K) up to 100 kPa to determine isosteric heat of adsorption. Low pressure results (up to 100 kPa) were measured using a Micromeritics® ASAP 2010 instrument and high pressure results were generated using the custom high pressure volumetric apparatus as outlined in Chapter 3. In addition to the reduction treatments outlined in Chapter 2, all materials were degassed in situ to 1 x 10^{-3} mbar at 623 K for 8 h prior to isotherm measurements. High-pressure isotherms up to 10 MPa and at 298 K are reported for AX-21 and SWNT in Chapter 3.[4.25] High-pressure isotherms for GNF and TC are reported in this section. Isotherms are reported in Figure 4.2 through Figure 4.8 and results are summarized in Table 4.1

Table 4.1 Hydrogen Adsorption Characteristics of Receptors

Receptor	**BET SA** m^2/g	**TPV** mL/g	**- ΔH_{ads}** kJ/mol	**$K_{H2,298}$ x 10^4** mmol/(g-kPa)	**Q_m** mmol/g	**b x 10^5** 1/kPa
GNF	305.6	0.32	8.0 ± 0.5	0.6 ± 0.5	2.1 ± 0.3	15 ± 3
SWNT	803.7	0.35	7.5 ± 0.5	2.7 ± 0.3	3.9 ± 0.4	11 ± 2
SGC	1970	1.2	8.3 ± 0.1	4.2 ± 0.3	-	-
AX-21	2933	1.1	7.1 ± 0.2	5.2 ± 0.2	9.1 ± 0.4	5.4 ± 0.3
TC	3379	1.4	7.9 ± 0.8	5.3 ± 0.2	13 ± 3	4.1 ± 0.1

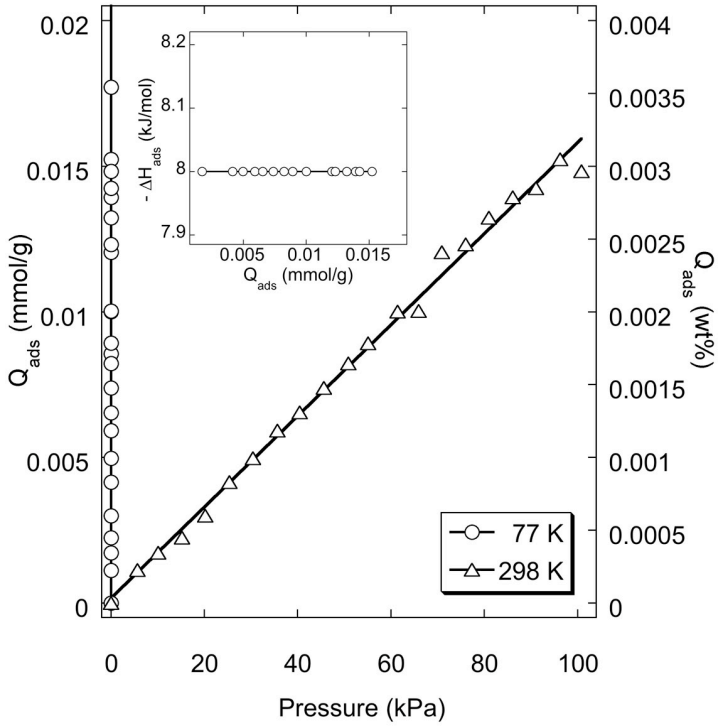

Figure 4.2 H_2 Adsorption Capacity and Enthalpy for GNF Below 100 kPa

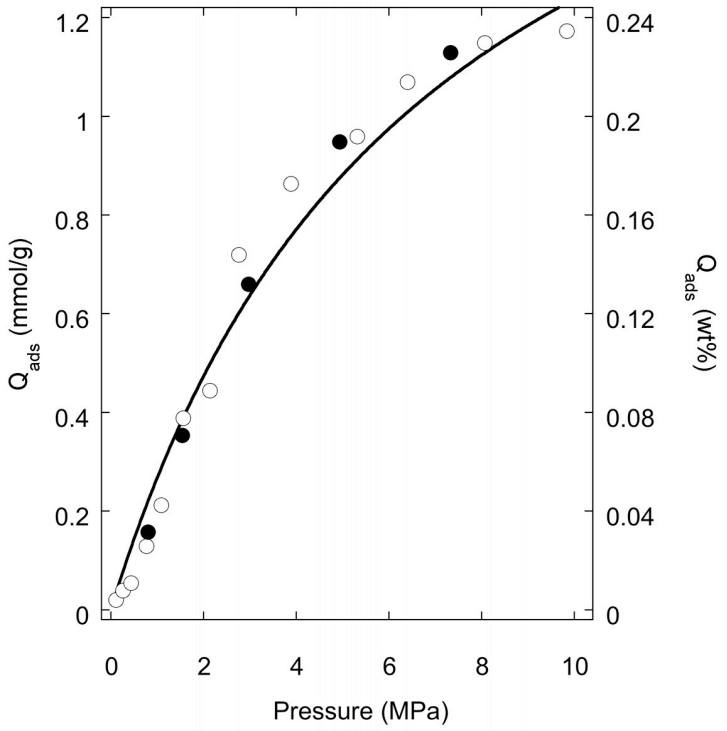

Figure 4.3 H_2 Adsorption Capacity for GNF at 298 K to 10 MPa

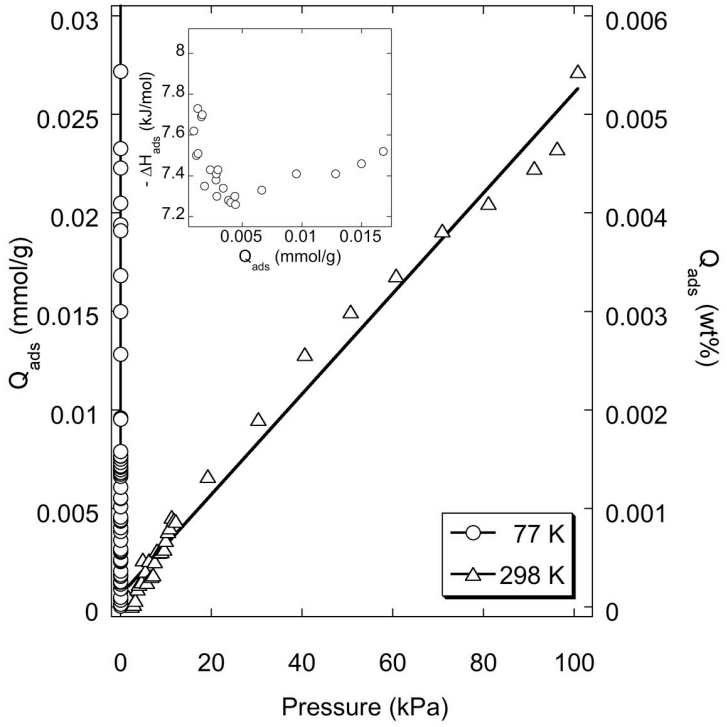

Figure 4.4 H_2 Adsorption Capacity and Enthalpy for SWNT Below 100 kPa

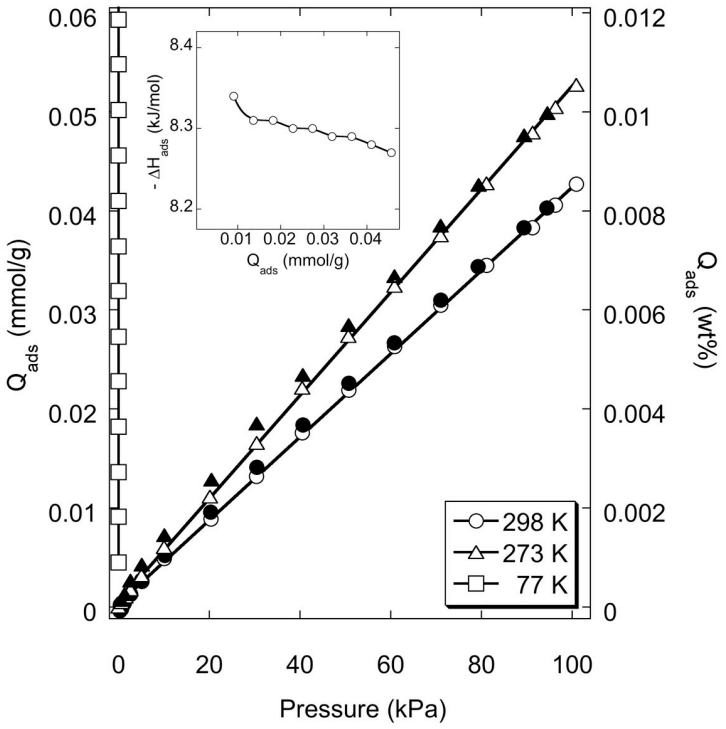

Figure 4.5 H_2 Adsorption Capacity and Enthalpy for SGC Below 100 kPa

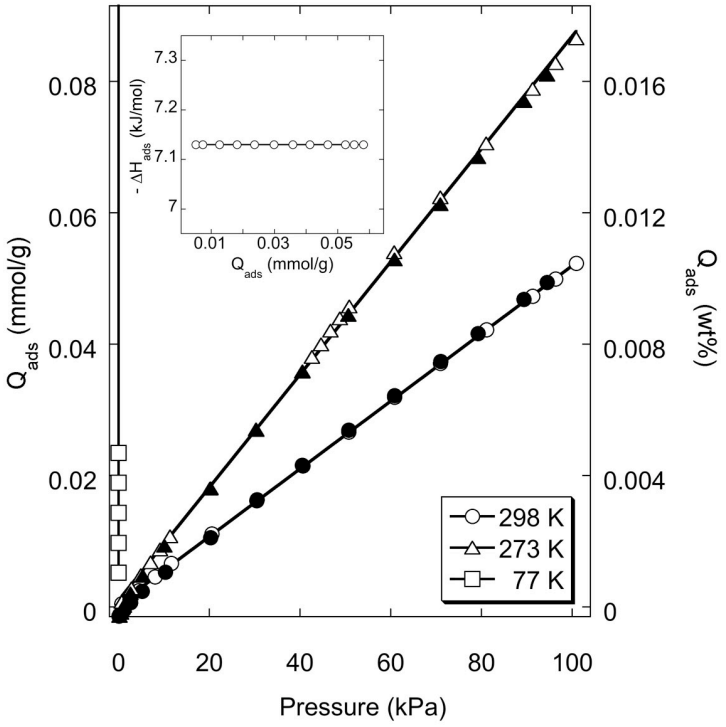

Figure 4.6 H_2 Adsorption Capacity and Enthalpy for AX-21 Below 100 kPa

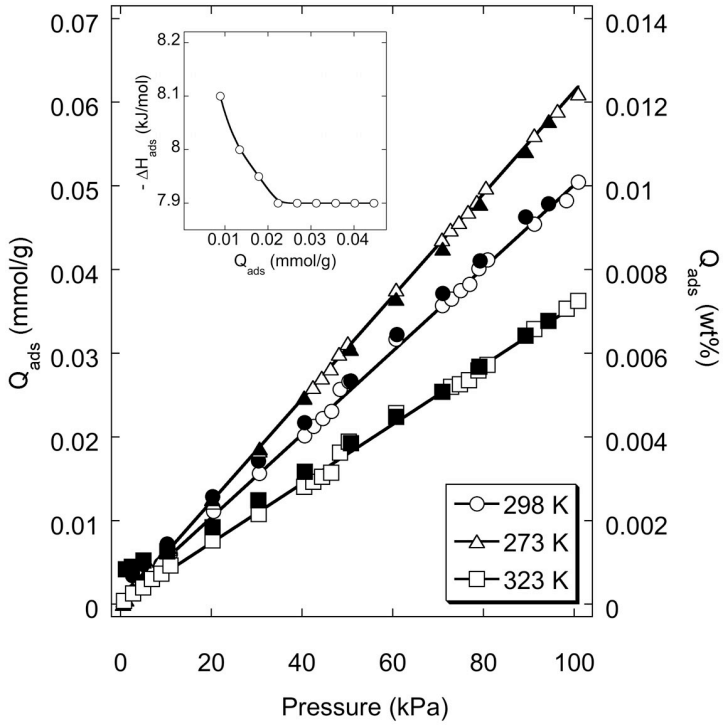

Figure 4.7 H_2 Adsorption Capacity and Enthalpy for TC Below 100 kPa

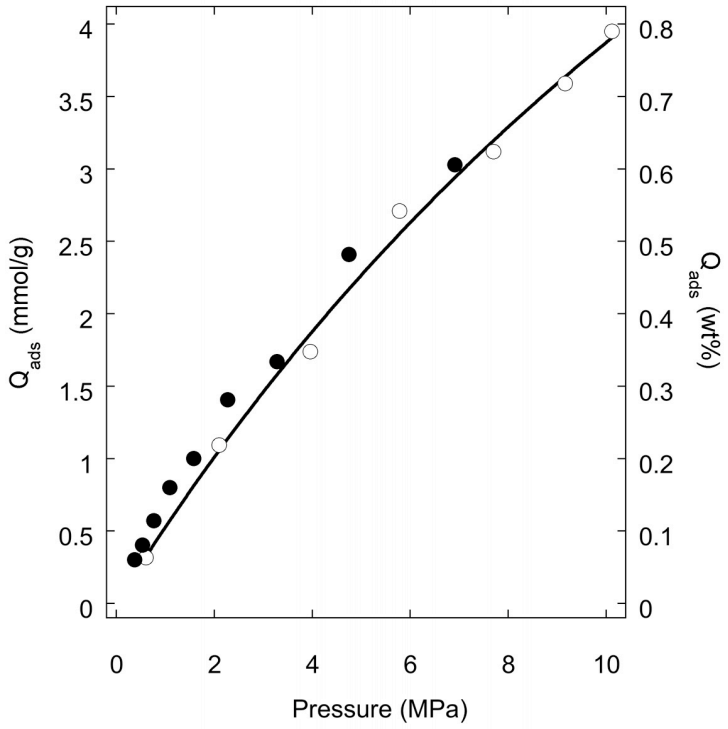

Figure 4.8 H_2 Adsorption Capacity for TC at 298 K to 10 MPa

As the data shows, the hydrogen adsorption capacity of a nanostructured receptor increases with BET SA and TPV. The enthalpy of adsorption is in the narrow range between – 6.9 to – 8.4 kJ/mol. All receptors exhibit full reversibility at the conditions studied here, as one would expect for physisorption of hydrogen molecules. The results compare favorably with many reported results of hydrogen adsorption on active carbon materials.[4.26-4.29] All nanostructured materials agree with Langmuir isotherm theory and the parameters Q_m and b are shown in Table 4.1. The general trend of the Langmuir constant (b) follows from its relationship with the isosteric heat of adsorption

$$b \propto \exp\left(\frac{-\Delta H_{ads}}{RT}\right) \tag{4.13}$$

4.3 Results for Primary Spillover Adsorbents

The adsorbents prepared to study primary spillover were evaluated for hydrogen storage capacity using high pressure and low pressure volumetric techniques. Instrumentation and in situ preparation conditions were identical to those outlined for receptors in the previous section.

Exceptional hydrogen adsorption capacity has been reported and debated for GNFs.[4.30,4.31] This material was studied first to screen its suitability as a spillover receptor. Results for 5 wt% Pt/GNF are shown in Figure 4.9. The dotted line reflects the Langmuir fit of the results for the GNF receptor, as presented earlier. As the data shows, there is an increase in the adsorption capacity for the composite material. The increase in capacity cannot be explained by uptake on platinum alone, as the metal has a low surface area (37 m^2/g) and if ideally was atomically dispersed on the surface would adsorb 0.25 mmol/g (0.05 wt%). The actual dispersion is lower, so the additional capacity must be

due to spillover of hydrogen atoms from platinum to GNF. Although enhancement has been demonstrated and the capacity has nearly been doubled at 10 MPa and 298 K, the adsorbent would not be suitable for on-board applications due to its low capacity even with substantial metal loading.

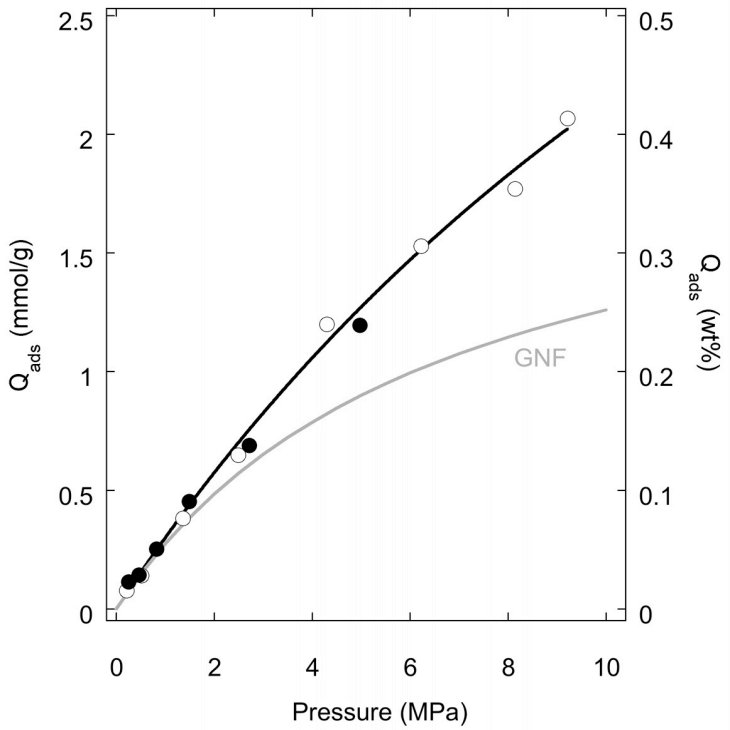

Figure 4.9 H_2 Adsorption Capacity for 6 wt% Pt/GNF at 298 K to 10 MPa

Sol-gel derived mesoporous carbons doped with transition metals have shown increased catalytic activity; however, no report has been provided on hydrogen capacity.[4.32] The synthesis procedure for these types of materials allows a metal salt to be added during carbonization, as outlined in Chapter 2. One-step synthesis simplifies manufacturing processes and may enhance the source-receptor contact that is critical to the spillover phenomenon. The applicability of the materials as hydrogen spillover

adsorbents was evaluated for two sources: palladium and nickel. Nickel was investigated to determine if a more cost-effective metal could be used as a source for atomic hydrogen in spillover adsorbents.

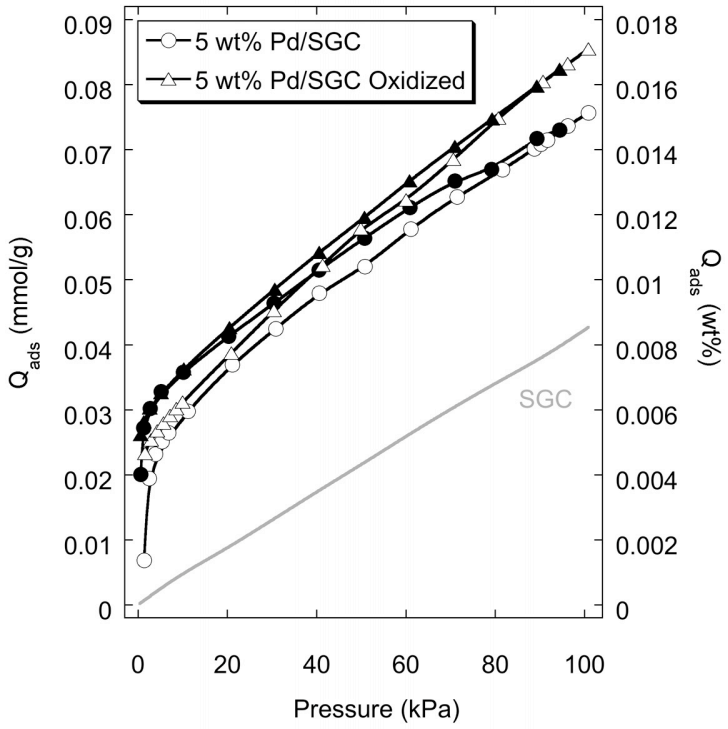

Figure 4.10 H_2 Adsorption Capacity for 5 wt% Pd/SGC at 298 K Below 100 kPa

The results for 5 wt% Pd/SGC are presented in Figure 4.10. There is a clear capacity enhancement over plain SGC. Since palladium forms a stable hydride, this amount must be considered when evaluating the effectiveness of spillover. The hydride amount for 5 wt% Pd/SGC for a stoichiometry of $PdH_{0.6}$ is 0.14 mmol/g (3.16 mL(STP)/g) at 2.4 kPa. The uptake for the material is much less than the hydride at 2.4 kPa (~ 0.03 mmol/g), indicating that not all of the palladium is accessible to hydrogen. Over 70% of the metal particles are encapsulated in carbon. The capacity increase is

mostly due to hydride formation, not spillover. The material was oxidized in flowing air (100 mL(STP)/min) at 573 K for 4 h in an attempt to expose additional palladium by gasifying carbon. The conditions are relatively mild in order to maintain the porous structure of the carbon.[4.33] As Figure 4.10 indicates, oxidation treatment appears to liberate a small fraction of palladium particles from carbon as the hydrogen capacity increases slightly. Oxygen functional groups deposited on the surface could also contribute to the capacity increase, albeit small.[4.34] However, comparing the result with the 5 wt% PdC commercial catalyst dispersion analysis in Chapter 2, the adsorbed amount is much less relative to a material derived from solution impregnation methods.

The 5 wt% Ni/SGC material was oxidized with a similar treatment prior to hydrogen capacity measurement. The results are presented in Figure 4.11. Nickel does not form a hydride in the absence of magnesium; therefore, any capacity enhancement observed for 5 wt% Ni/SGC is attributable to spillover. The material does not exhibit net enhanced capacity due to spillover. It is interesting to note that the hydrogen adsorption amount remains identical to a plain SGC sample despite a 20% reduction in surface area and porosity, a behavior that could be due to a small fraction of spillover.

The hydrogen spillover and adsorption capacity for a well-dispersed source on a high surface area, nanoporous receptor was evaluated with 6 wt% Pt/AX-21 material. The results are shown in Figure 4.12. As the results indicate, there is significant enhancement to the capacity of AX-21 when it is a receptor for spillover hydrogen atoms. The adsorption amount at 10 MPa is increased by nearly 70 % compared to plain AX-21.

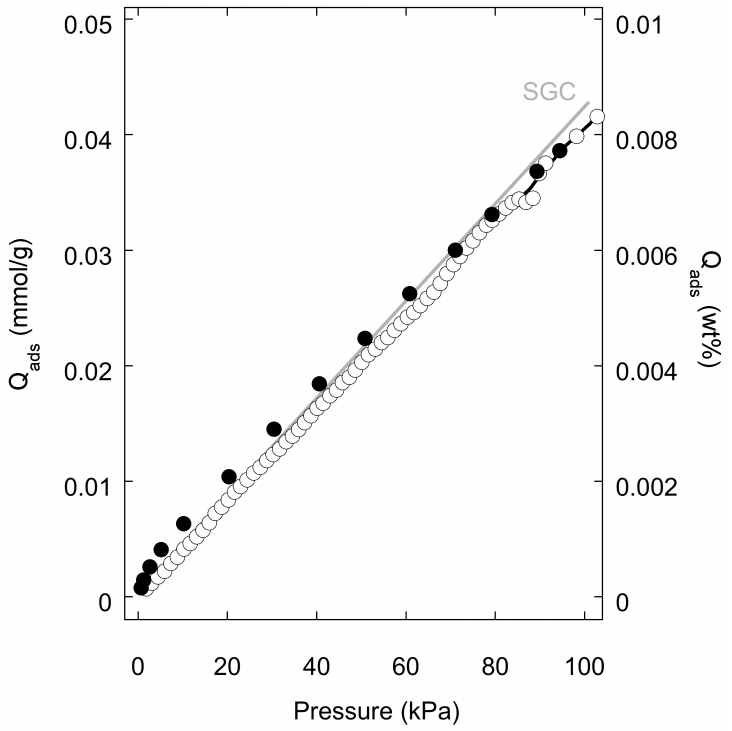

Figure 4.11 H_2 Adsorption Capacity for 5 wt% Ni/SGC at 298 K Below 100 kPa

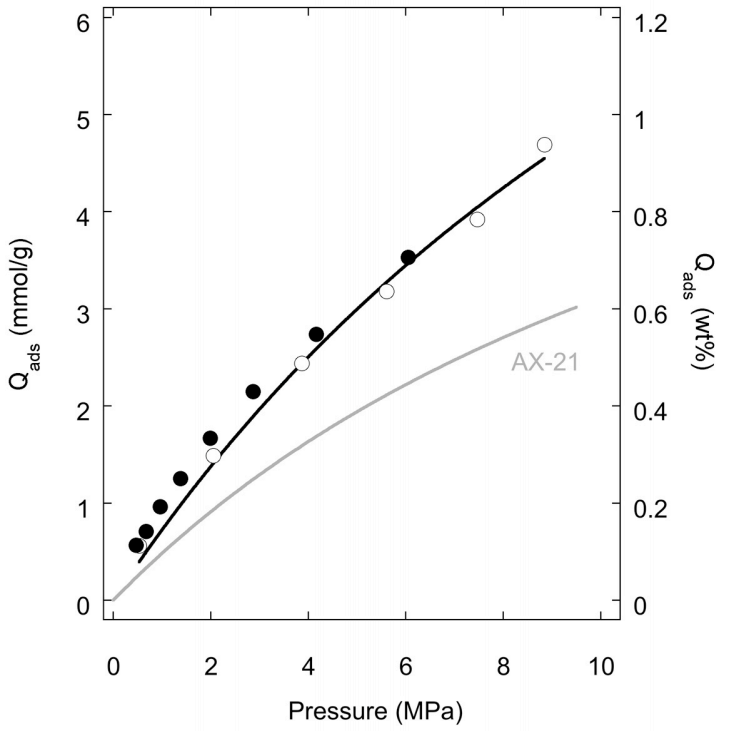

Figure 4.12 H_2 Adsorption Capacity for 6 wt% Pt/AX-21 at 298 K to 10 MPa

In order to assess the hydrogen storage capacity as the receptor surface area and pore volume increases, 6 wt% Pt/TC was evaluated at room temperature up to 10 MPa. The result is shown in Figure 4.13. There has been evidence that residual chlorine from synthesis techniques can influence the catalytic activity of the final material. In some cases, it has acted as a poison[4.35-4.38] and in others it has served to enhance catalysis.[4.39] The material was synthesized via ultrasound assisted solution impregnation via two different metal precursors: $H_2PtCl_6 \cdot 6H_2O$ and $H_2Pt(OH)_6$ (see Chapter 2 for details) to assess the behavior with respect to hydrogen spillover and adsorption.

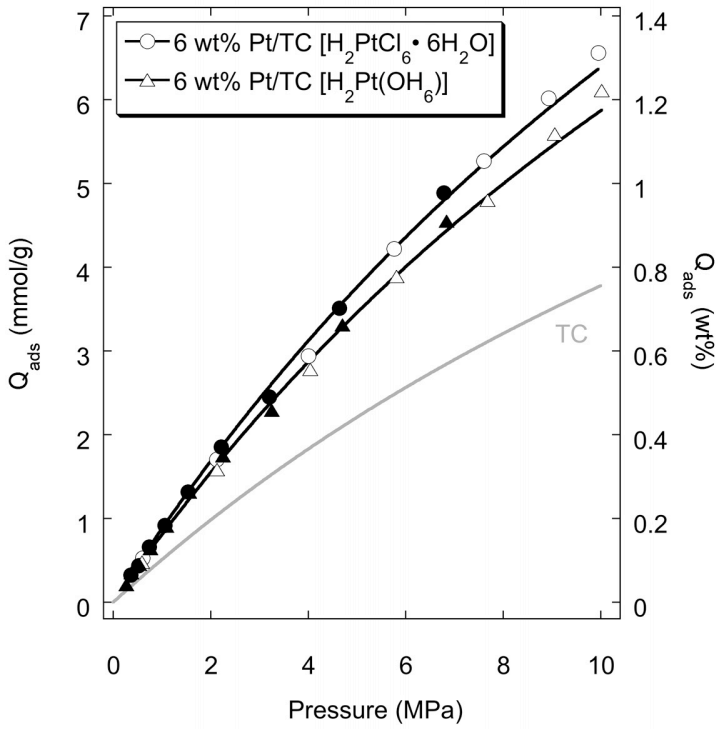

Figure 4.13 H_2 Adsorption Capacity for 6 wt% Pt/TC at 298 K to 10MPa

The data in Figure 4.13 shows the increase in capacity due to spillover for the 6 wt% Pt/TC material synthesized by both metal salt precursors is significant. The

enhancement is 60% above the plain TC. The difference between the two metal salt synthesis routes is less than 15%, which is within the instrument accuracy for the high pressure system.[4.25] Chlorine appears to have no detrimental effect on the equilibrium hydrogen storage capacity; however, there may be some influence on kinetics, which will be addressed later. It is interesting to note that the composite material has a surface area and micropore volume close to AX-21, as shown by characterization studies in Chapter 2. If there was no spillover active on the composite material, the hydrogen adsorption isotherm should be close to the equilibrium isotherm for plain AX-21 at 298 K since adsorption on platinum is negligible (~ 0.13 mmol/g).

The metal loading effect on hydrogen spillover was evaluated by synthesizing a material with the composition 1.5 wt% Pt/TC. The hydrogen adsorption results are presented in Figure 4.14.

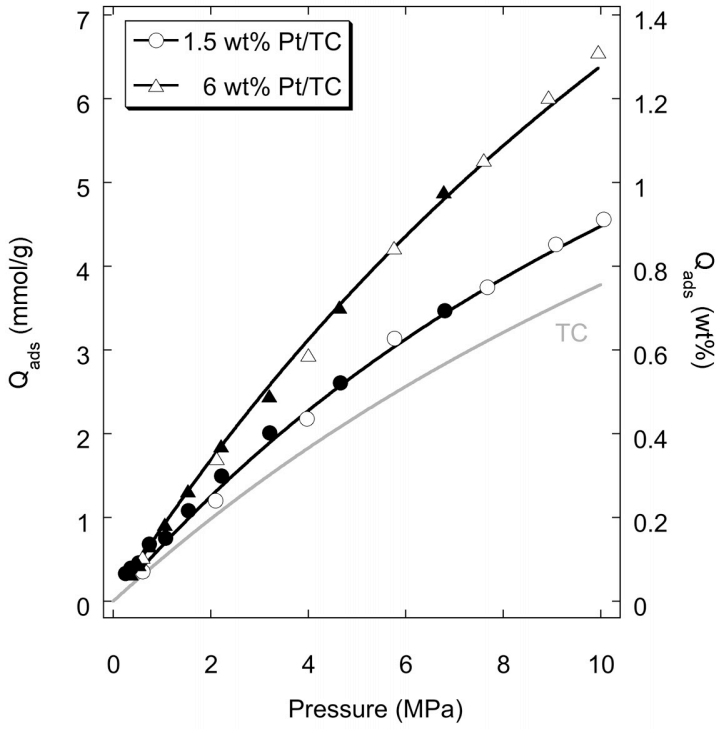

Figure 4.14 H_2 Adsorption Capacity for 1.5 wt% Pt/TC at 298 K to 10MPa

The data in Figure 4.14 indicate that the hydrogen spillover capacity is dependent upon metal loading. Loading the TC receptor to 1.2 wt% Pt, the capacity is enhanced by 20%. The enhancement is not expected to continue indefinitely with metal loading; however, as increasing the density of platinum particles removes receptor pore volume and surface area for adsorption, as Chapter 2 has shown. This work was intended to identify adsorbent composites and study the mechanism of hydrogen spillover; therefore, the critical platinum loading where hydrogen spillover loses effectiveness has not been explicitly identified for TC and remains a problem for optimization. It is recognized that lower loadings are preferred due to the cost of precious metals.

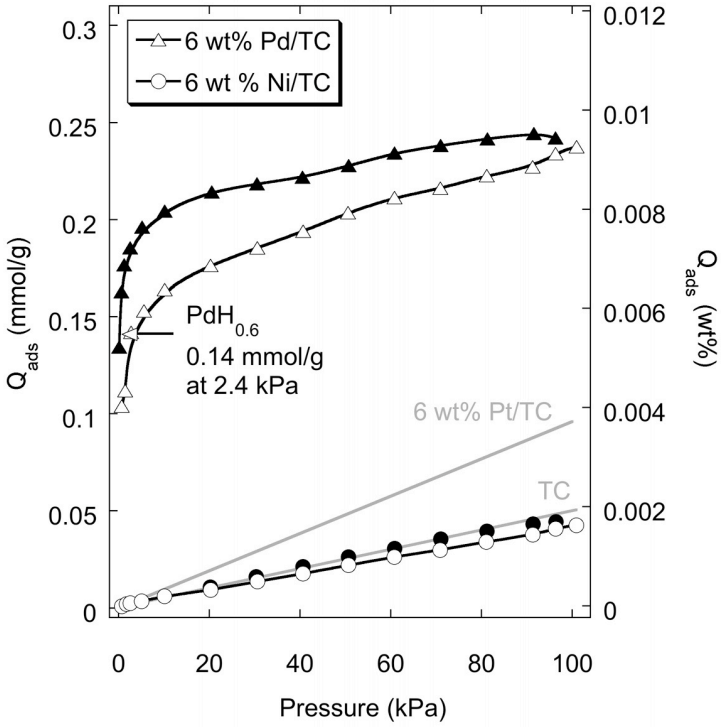

Figure 4.15 H_2 Adsorption Capacity for Ni/TC and Pd/TC at 298 K Below 100 kPa

Composites containing 6 wt% Ni and 6 wt% Pd were synthesized to evaluate alternative metal source performance. The results are presented in Figure 4.15 along with

reference data for TC and 6 wt% Pt/TC. The palladium hydride amount is indicated in the plot. The enhancement due to spillover must be considered after discounting this effect. The overall capacity is enhanced substantially over TC and even 6 wt% Pt/TC; however, the net spillover amount is nearly the same as that for the platinum source (0.24 mmol/g – 0.14 mmol/g = 0.10 mmol/g at 100 kPa). These two metals are effective spillover sources and perform similarly after considering the hydride forming capability of palladium. Nickel, on the other hand, does not yield spillover enhancement at room temperature and the result is similar to the Ni/SGC composite discussed earlier. It is noteworthy that Wang and Yang have observed moderate spillover enhancement when the nitrate salt was used as a dopant, implying some dependence on the precursor for this system.[4.40] In general, nickel, although a relatively cheap catalyst that adsorbs, dissociates, and exhibits spillover at elevated temperatures (> 573 K),[4.41-4.43] does not perform sufficiently to be considered as a spillover source at the desired application conditions.

Table 4.2 Primary Spillover of Hydrogen on Composite Adsorbents at 298 K

Adsorbent	**Q_{ads} (100 kPa)** mmol/g	**Q_{ads} (10 MPa)** mmol/g
6 wt% Pt/TC[a]	0.097	6.8
6 wt% Pt/TC[b]	-	6.0
6 wt% Pt/AX-21	0.075	4.8
1.5 wt% Pt/TC	-	4.5
6 wt% Pt/GNF	-	2.0
6 wt% Pd/TC	0.24[c]	-
5 wt% Pd/SGC	0.08	-
6 wt% Ni/TC	0.04	-
5 wt% Ni/SGC	0.04	-

Notes: (a) from chloroplatinate salt, (b) from platinate salt, (c) 0.14 mmol/g due to $PdH_{0.6}$

The results of primary spillover adsorbent evaluation are shown in Table 4.2. The material selected for further study of the spillover mechanism is 6 wt% Pt/TC due to its full reversibility at room temperature, lack of hydride formation to convolute results, and significant capacity enhancement.

4.4 Results for Secondary Spillover Adsorbents

As the results for primary spillover have shown, the receptor plays a key role in the equilibrium capacity of a hydrogen spillover adsorbent. The receptor must have suitable pore volume and the size distribution of those pores must allow for adequate interaction potential to retain hydrogen. Novel adsorbents are continually synthesized that may prove effective spillover hydrogen receptors; however, they frequently lack the appropriate source. Metal Organic Frameworks (MOFs),[4.44] Covalent Organic Frameworks (COFs),[4.45,4.46] nanotubes (SWNTs, MWNTs)[4.47,4.48] and other nanostructured carbons are examples of such adsorbents. Primary spillover adsorbents demonstrate that an impregnation technique can effectively place a source on the surface of a receptor. For adsorbents that may be damaged by such techniques, the bridge-building method has been developed as outlined in Chapter 2.

Results for two secondary receptors: SWNTs and AX-21 are presented in this section. The influence of bridges is demonstrated by comparing results of bridged materials to those of physical mixtures of source and receptor. Srinivas and Rao[4.49] demonstrated that the spillover hydrogen atoms increased approaching a 9:1 proportion of receptor to source in physical mixtures. The functionality is logical: too much receptor decreases hydrogen atoms available for spillover while too much source decreases pore

volume available for adsorption. In these studies, receptor is sacrificed for bridge to maintain the proportion of receptor and bridge/source at 9:1. This ensures that on a mass basis, there is an equal amount of bridges and primary spillover sources.

A composite containing SWNTs, 5 wt% PdC catalyst, and bridges was formed according to the preparation outlined in Chapter 2. The proportion of components in the final material was 8:1:1 SWNT/PdC/Bridges. The adsorbent was given an in situ vacuum degassing to 1 x 10^{-3} mbar at 623 K for 8 h prior to isotherm measurements. Results are presented in Figure 4.16.

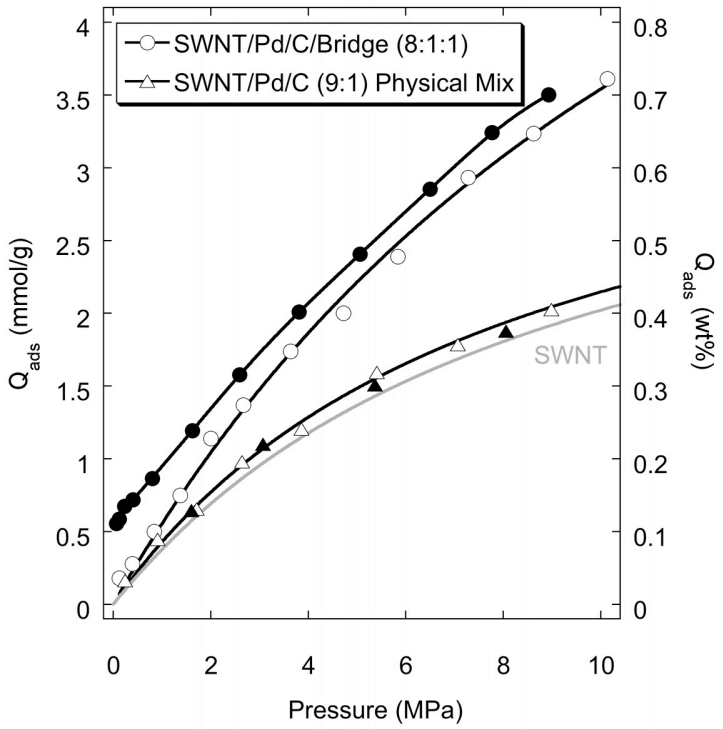

Figure 4.16 H_2 Adsorption Capacity for SWNT Secondary Receptor at 298 K

The data indicate a clear enhancement due to spillover. The bridged material demonstrates a 75% increase in capacity at 10 MPa compared to SWNT alone. The influence of bridges is shown when considering the isotherm of the physical mixture

(9:1) of the two components. The unbridged result agrees approximately with the prediction of a simple addition of the fractional amounts registered for the source and receptor isotherms. There is a small gain due to limited spillover on the unbridged material; however, it is not substantial, as Figure 4.16 indicates.

An interesting feature of Figure 4.16 is the hysteresis loop observed during desorption. A small fraction of this hysteresis is due to the loop present in palladium hydride. The bulk of the hysteresis is likely due to hydrogen atoms that have been more strongly adsorbed in the small pores of nanotubes. The energy distribution of various sites in SWNTs has been documented by Yang and Yang[4.50] and hysteresis for these bridged materials has been discussed in light of experimental observations.[4.51] Full capacity was restored after an extended degassing period (12 h) at room temperature or heating to 423 K for 2 h in vacuum to 1 x 10^{-3} mbar.

The capacity of AX-21 as a receptor has been shown to be greater than SWNTs owing to its large micropore volume and corresponding surface area. AX-21 was studied as a secondary spillover receptor from two sources: 5 wt% PdC and 5 wt% PtC catalysts. The proportion of both composites was 8:1:1 receptor/source/bridge and they were subjected to the identical in situ degassing prior to measurements. The AX-21/PdC/Bridge material was cycled twice to demonstrate repeatability. While this is not a guarantee that the material will not degrade over the hundreds of cycles required by DOE, it does demonstrate that enhancement due to spillover is not limited to initial hydrogen exposure. Results are presented in Figure 4.17.

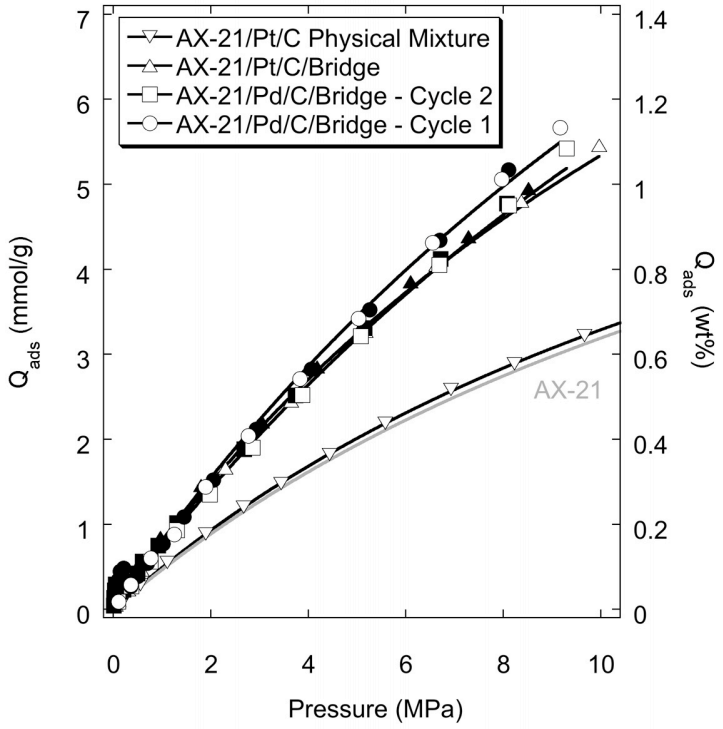

Figure 4.17 H_2 Adsorption Capacity for AX-21 Secondary Receptor at 298 K

The composite, bridged material with AX-21 receptor again demonstrates spillover capacity enhancement. The adsorption amount has increased by at least 70% for both platinum and palladium sources, with both sources exhibiting similar performance with respect to equilibrium amount. AX-21/PdC/Bridge does not exhibit the same hysteresis loop as observed for the SWNT receptor. This supports the explanation postulated earlier – that the hysteresis is largely due to spillover and adsorption of hydrogen atoms at high energy sites in the nanotube structure. The cyclic performance of the secondary spillover adsorbent with PdC as a source demonstrates that adsorption enhanced by spillover is fully reversible at room temperature. The sample did not require elevated temperature degassing between cycles to regenerate the adsorbent, a useful feature from an application perspective.

The proportion of bridges was reduced such that the composition of the overall mixture was altered from 8:1:1 to 8.6:1:0.4 to examine the impact on spillover. The source was maintained constant to ensure the same amount of hydrogen atoms were generated at the primary source. The results are shown in Figure 4.18 for 298 K.

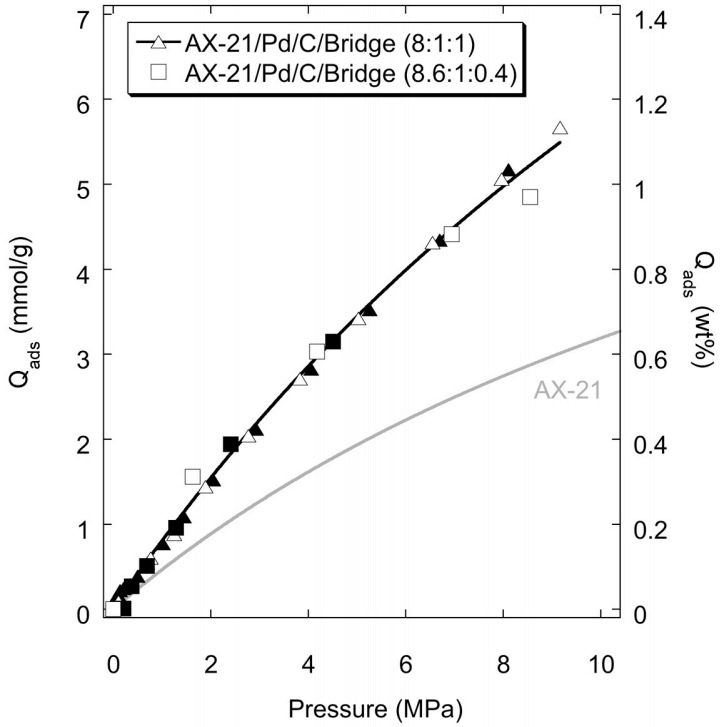

Figure 4.18 H_2 Adsorption Capacity for Variable Bridge Proportion, AX-21 Receptor

The results indicate that the amount of bridges can be reduced by 60% from the original 8:1:1 proportion without decreasing the equilibrium capacity of the adsorbent. Enhancement of adsorption by bridge formation relies upon the physical pathway that is built between the receptor and source, which does not require the source and bridges to be equal to generate adequate contact area. At room temperature, the adsorbent appears to be near an optimum where the balance of hydrogen atoms generated is matched by the available receptor sites.

4.5 Application of Spillover Isotherm Model and - ΔH_{ads}

The spillover isotherm model developed by Yang et al.[4.13,4.14] was used to analyze the results for 6 wt% Pt/TC and AX-21/PtC/Bridge (8:1:1). These were the two highest capacity, fully reversible materials and are of interest for spillover characterization.

The spillover isotherm, outlined earlier, requires the Langmuir parameters for platinum. Limited data exists to calculate these parameters.[4.52] An experiment was performed using platinum black (27-36 m^2/g, Aldrich #520799) to determine the Langmuir constants. Hydrogen adsorption was measured using a Micromertics® 2010 instrument. Platinum black was evaluated before and after hydrogen treatments. The first experiment was completed after in situ degassing of the material at 623 K to 1 x 10^{-6} mbar for 8 h. The measurement behavior was erratic, as there was additional surface oxide reduction. Subsequent measurements, after degassing the hydrogen treated material at 623 K in vacuum to 1 x 10^{-6} mbar for 8 h, were consistent and matched those reported by Benton.[4.52] Figure 4.19 shows the platinum black isotherm at 298 K along with the dissociative Langmuir isotherm parameters as defined in Equation 4.2. These results are most applicable to the spillover adsorbent case, as the pretreatment matches the reduction and degassing prior to gathering adsorbent isotherms.

In Equation 4.3,

$$k_1 = Q_{m,ads} b' \tag{4.14}$$

$$k_2 = b' \tag{4.15}$$

and the two undetermined parameters are the partition coefficients, K and K'. While some inaccuracy is incurred by assuming platinum Langmuir constants do not vary with temperature, it is expected to be small over the 50 K temperature range studied here.

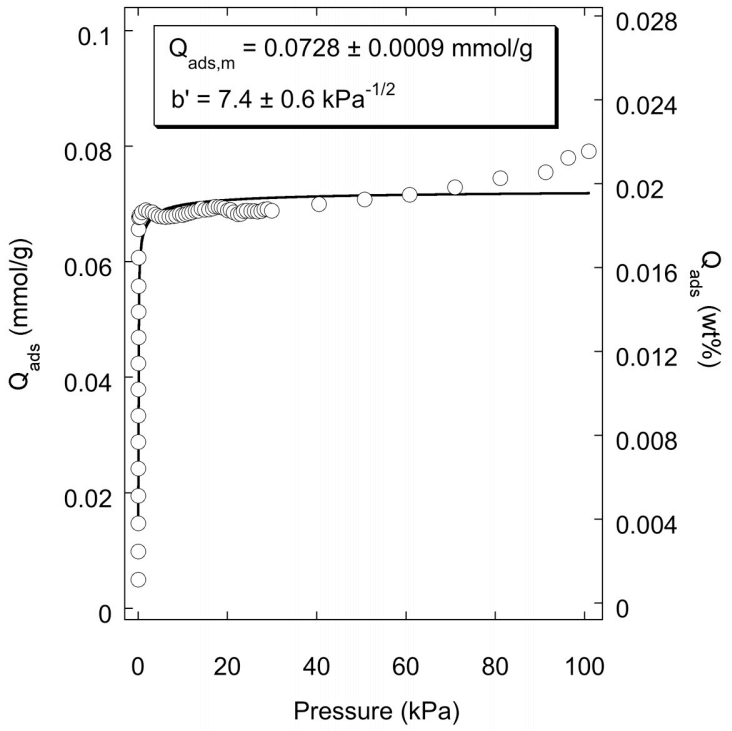

Figure 4.19 H_2 Adsorption on Platinum Black at 298 K

The spillover and adsorption of hydrogen on 6 wt%/TC was measured up to 100 kPa at three temperatures: 273 K, 293 K, and 323 K. The results are presented in Figure 4.20, with curves representing fits of the spillover isotherm for each temperature. The spillover isotherm partition coefficients are summarized in Table 4.3.

Table 4.3 Spillover Isotherm Partition Coefficients for 6 wt% Pt/TC

Temperature K	**K_1 x 10^3**	**K'**	**K'/K_1**
273	9.1 ± 0.6	13.85 ± 0.01	1522
293	7.4 ± 0.4	13.85 ± 0.01	1871
323	3.9 ± 0.2	13.86 ± 0.01	3518

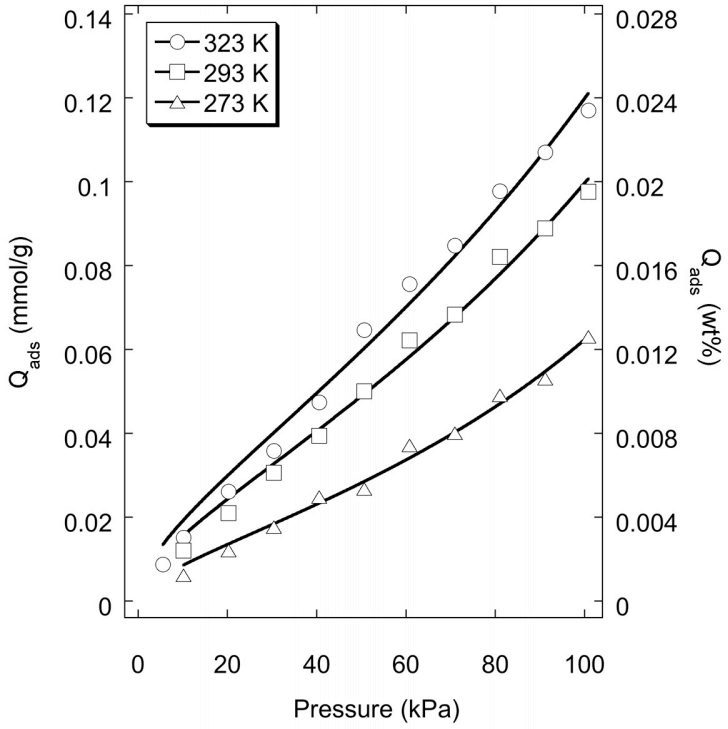

Figure 4.20 H_2 Isotherms and Spillover Model, 6 wt% Pt/TC

The partition coefficients are proportional to the ratio of atomic hydrogen concentrations as follows

$$K_1 = C_{PR}/C_{Pt} \tag{4.16}$$

$$K' = (k'/R_1)^3 (C_{Rec}/C_{Pt}) \tag{4.17}$$

with R_1 as the radius encompassing the primary receptor (PR) or, in this case, the radius of a fixed region near the platinum particle. The variable k' is a proportionality between R_2 (the diffusion distance) and amount adsorbed that is theorized to account for hydrogen atoms at adsorbed edge sites[4.53] acting as bridges to extend spillover

$$k' = R_2/Q_{ads}^{1/3} \tag{4.18}$$

therefore

$$\frac{K'}{K_1} = \left(\frac{C_{Rec}}{C_{PR}}\right)\left(\frac{R_2}{R_1}\right)^3 \frac{1}{Q_{ads}} \tag{4.19}$$

At equilibrium, the concentrations in region bounded by R_1 and on the receptor (Rec) should be equal. As the temperature increases, K'/K_1 increases while the adsorbed amount decreases. Based on Equation 4.19, the diffusion distance (R_2) must increase with increasing temperature. The spillover hydrogen is distributed in a larger region around the platinum source.

Enthalpy of adsorption was computed for 6 wt% Pt/TC based on the data in Figure 4.20. The relationship in Equation 4.6 was used and the result is shown in Figure 4.21. The isosteric adsorption enthalpy increased to 10.6 kJ/mol, 34% over plain TC, and in the range desired for hydrogen spillover adsorbents.

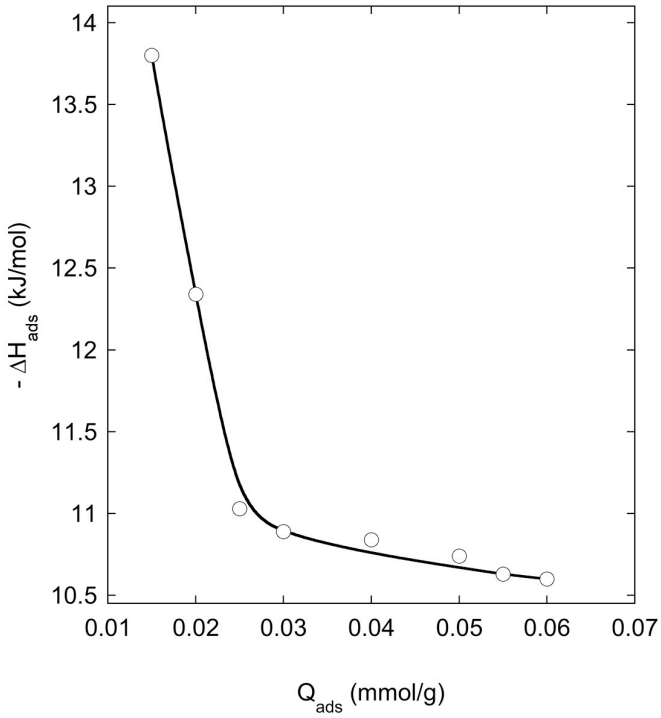

Figure 4.21 H_2 Enthalpy of Adsorption, 6 wt% Pt/TC

A similar analysis was performed with AX-21/PtC/Bridge material. Figure 4.22 presents the isotherms and spillover model for 293 K and 273 K. The parameters for the spillover model are shown in Table 4.4.

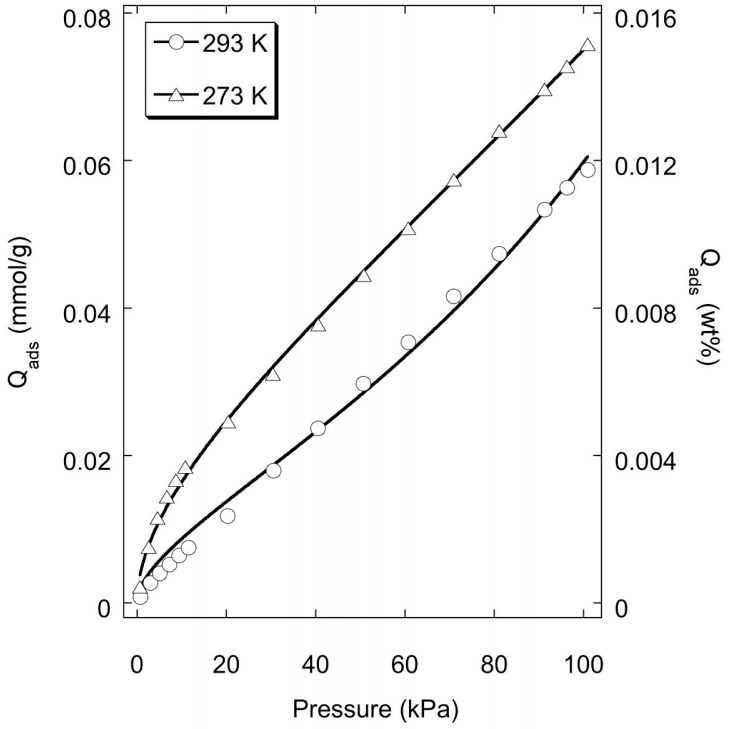

Figure 4.22 H_2 Isotherms and Spillover Model, AX-21/PtC/Bridge (8:1:1)

Table 4.4 Spillover Isotherm Partition Coefficients for AX-21/PtC/Bridge (8:1:1)

Temperature K	**K_1 x 10^3**	**K'**	**K'/K_1**
273	8.4 ± 0.2	13.81 ± 0.01	1642
293	4.1 ± 0.2	13.86 ± 0.01	3380

Secondary spillover is characterized by similar behavior to primary spillover with respect to modeling. The partition coefficient ratio increases with increasing temperature,

indicating that the diffusion distance (or reachable distance) is farther from the platinum source and primary receptor.

The isosteric enthalpy of adsorption was calculated for the bridged composite and the result shown in Figure 4.23. The value decreases steadily to 10 kJ/mol over the range of adsorption amounts studied, with values at low loading tending toward the isosteric enthalpy of adsorption on platinum.[4.54] This secondary spillover adsorbent exhibits increased interaction potential, similar to the primary spillover material 6 wt% Pt/TC.

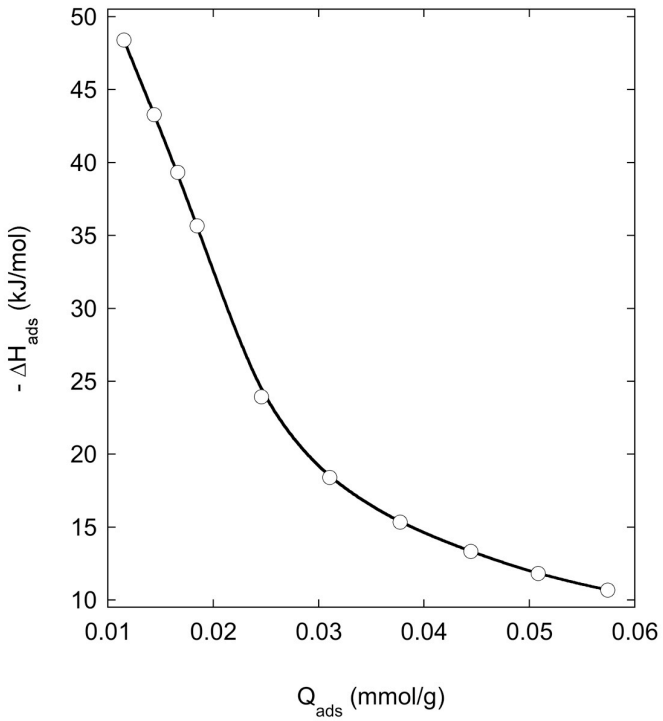

Figure 4.23 H_2 Enthalpy of Adsorption, AX-21/PtC/Bridge (8:1:1)

4.6 Kinetic Results and Diffusion Time Constant ($D_{s,e}/R_s^2$)

Enhanced hydrogen adsorption capacity is one characteristic of an effective adsorbent. The material must also adsorb and release the adsorbate in a timely manner.

The kinetic response of charging and discharging full capacity of hydrogen adsorbents should ideally be on the order of minutes. To date, high capacity metal hydrides demonstrate kinetics on the order of hours, even at elevated temperatures (minimum 360 K).[4.55-4.57]

The high pressure volumetric adsorption apparatus discussed in Chapter 3 has the capability to measure adsorption and desorption rates at room temperature. Many commercial instruments only allow the collection of adsorption rate data at pressures below 100 kPa. Kinetics of both adsorption and desorption are important at high pressure, as most materials have practical capacity extending beyond atmospheric pressure. Adsorption and desorption kinetics of primary and secondary spillover for 6 wt% Pt/TC and AX-21/PtC/Bridge (8:1:1) composites were evaluated at ambient temperature.

Figure 4.24 is a plot of the solution to the two dimensional Fick diffusion relationship (Equation 4.12) for several pressures on the 6 wt% Pt/TC equilibrium adsorption isotherm. As data indicate, the rate of adsorption for primary spillover increases with pressure (and surface loading). Desorption behavior is shown in Figure 4.25. It is interesting to note that the rate of desorption is faster than the rate of adsorption for all points on the isotherm. A theory for this phenomenon involving recombination of hydrogen atoms is proposed in the next chapter. The fitting parameter for Equation 4.12 is the diffusion time constant. Values for this parameter are plotted in Figure 4.26 for adsorption and desorption as a function of adsorbed amount. No literature values of D/R^2 were readily available for hydrogen; however, the values are two orders of magnitude higher than those reported for nitrogen on molecular sieve carbon (7.0×10^{-6} s^{-1}).[4.58] The parameter is lower compared to pore diffusion in physisorption modeling (Chapter 3).

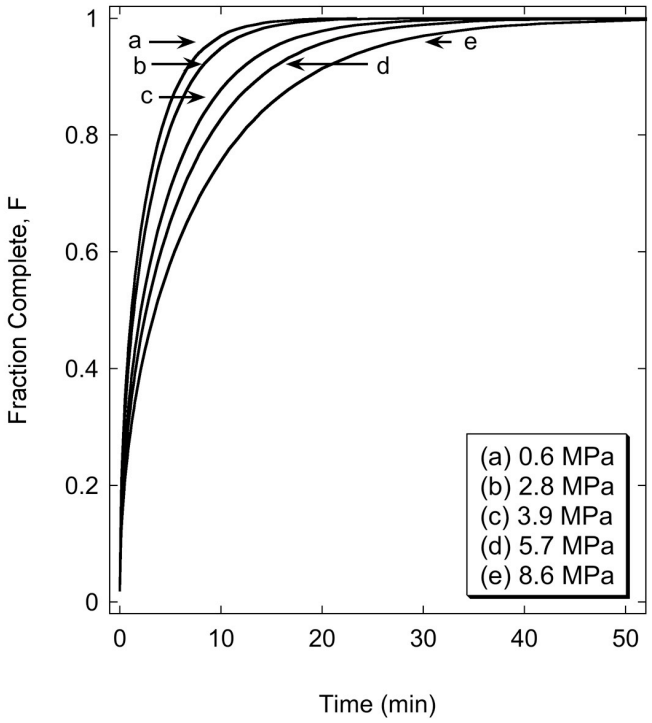

Figure 4.24 Fick's Law Diffusion Model for Adsorption, 6 wt% Pt/TC

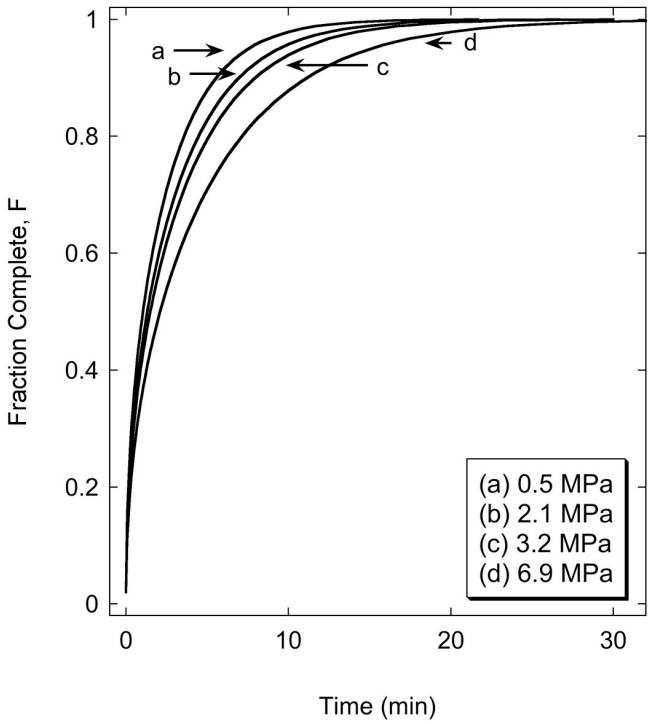

Figure 4.25 Fick's Law Diffusion Model for Desorption, 6 wt% Pt/TC

Since the approximate diffusion distance is known from TEM images (Figure 2.43), the atomic hydrogen diffusion coefficient may be roughly estimated from the time constant. On average, platinum sources are 300 Å apart, so the maximum diffusion distance, R_s, is 150 Å. Using the values of the diffusion time constant in Figure 4.26, the diffusion coefficient for hydrogen atoms on carbon is estimated as 2 x 10^{-15} - 5 x 10^{-16} cm^2/s. These values are one order of magnitude higher compared to a prediction from literature using an Arrhenius relationship to estimate $D_{eff, H}$ (298 K) = 4 x 10^{-17} cm^2/s, [4.59-4.61] indicating that hydrogen atoms may have not reached the distance assumed above.

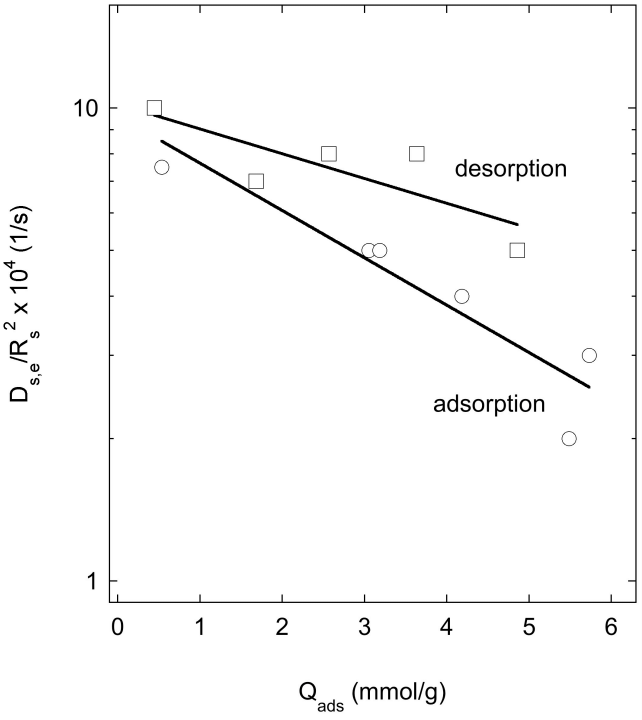

Figure 4.26 Diffusion Time Constants for Spillover of H, 6 wt% Pt/TC

A similar analysis was performed for the selected secondary spillover adsorbent. The results of Fick's diffusion model applied to AX-21/PtC/Bridge (8:1:1) are reported for adsorption and desorption in Figure 4.27 and Figure 4.28, respectively.

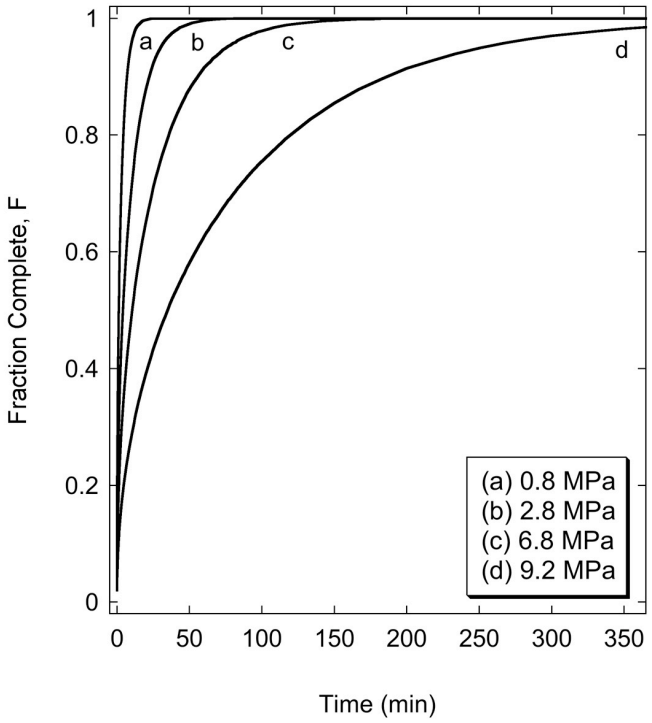

Figure 4.27 Fick's Law Diffusion Model for Adsorption, AX-21/PtC/Bridge

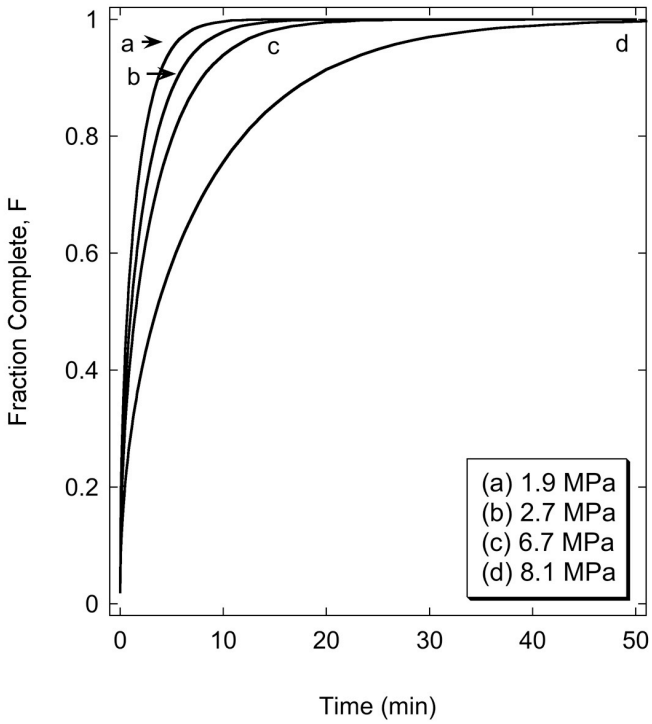

Figure 4.28 Fick's Law Diffusion Model for Desorption, AX-21/PtC/Bridge

Adsorption kinetics are slower for the secondary spillover adsorbent relative to the primary spillover adsorbent. In both cases, desorption is faster relative to adsorption with substantial differences at high pressure. The diffusion time constant is plotted versus adsorbed amount in Figure 4.29.

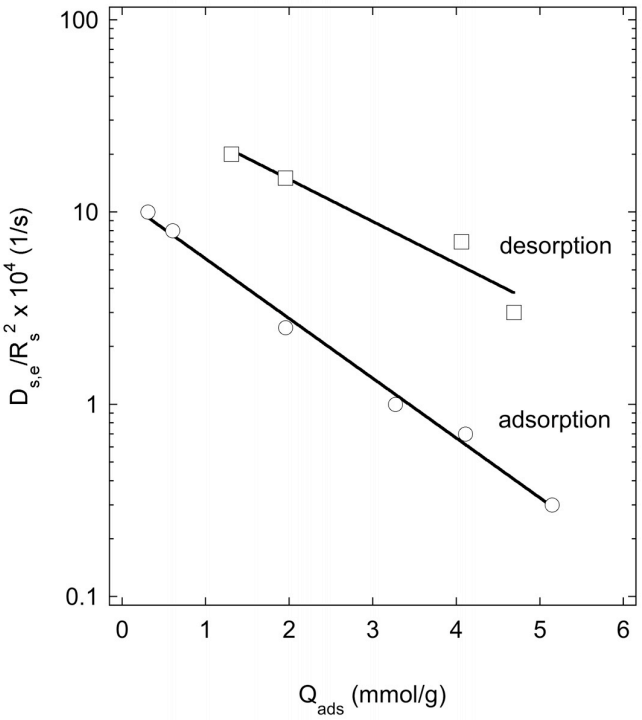

Figure 4.29 Diffusion Time Constants for Spillover of H, AX-21/PtC/Bridge

The reachable distance of hydrogen atoms is not as well characterized in this case. If the range of diffusion coefficients calculated above are assumed to apply to secondary spillover, the spillover distance lies in the range 100 to 800 Å. Considering that most adsorbent particles are several thousand angstroms in diameter, this diffusion distance confirms the assumption that sources should be highly dispersed on receptors to maximize the extent of spillover.

4.7 Conclusions

This chapter outlines the key parameters used to evaluate the performance of hydrogen adsorbents. Adsorption isotherms, isosteric enthalpy of adsorption, and diffusion time constants were reported for primary and secondary spillover adsorbents. Selection of a primary and secondary spillover adsorbent was made based on capacity enhancement and isotherm reversibility. In general, receptors with high pore volume and surface area were the best candidates for spillover adsorbents. For primary spillover, lowering the spillover source content decreased capacity. The fraction of bridges for secondary spillover adsorbents is not required to follow a 1:1 proportion with the source to form effective diffusion pathways.

The best primary spillover adsorbent, 6 wt% Pt/TC, demonstrated a 60% capacity enhancement at 10 MPa and 298 K (1.4 wt%) over plain TC. The isosteric enthalpy of adsorption was 10.6 kJ/mol at 100 kPa, a 34% increase over physisorption of molecular hydrogen on TC. The rate of adsorption was slower than the kinetics of physisorption, as evidenced by a larger value of the diffusion time constant. Diffusion coefficients for hydrogen atoms on TC were estimated between 2×10^{-15} to 5×10^{-16} cm^2/s at 298 K.

The best secondary spillover adsorbent, AX-21/PtC/Bridge (8:1:1), increased in capacity by 70% over the receptor amount. The adsorption capacity was 1.2 wt% at 10 MPa and 298 K. The isosteric enthalpy of adsorption was 10 kJ/mol at 100 kPa. The kinetics of adsorption were slower for the bridged material. This is expected, as hydrogen atoms must diffuse across the physical bridge before finding adsorption sites. Reachable distances of up to 400 Å were calculated based on the diffusion coefficients measured for hydrogen atoms on TC.

For both adsorbents, the kinetics of desorption were faster than those of adsorption, indicating a difference in the mechanism of forward and reverse spillover. This issue is addressed in the next chapter with isotope tracer studies.

Capacity enhancement due to spillover is tenable when carefully considering atomic hydrogen mobility from platinum - or other transition metals that adsorb and dissociate hydrogen - to receptors. Platinum is known to chemisorb and dissociate hydrogen molecules.[4.2] Several experimental results support the existence of weakly bound hydrogen atoms,[4.62,4.63] mobile layers of hydrogen atoms,[4.64] and diffusion from platinum to carbon.[4.65] More recently, inelastic neutron scattering has demonstrated qualitative hydrogen spillover for Pt/C fuel cell catalysts.[4.66-4.68]

Several simulation results support the concept of room temperature hydrogen spillover. The first demonstrated that atomic hydrogen diffusion from a platinum particle to a carbon surface was energetically favorable at ambient conditions and could form weak physisorbed species upon reaching a receptor.[4.69] The second discussed the stability of those hydrogen atoms as weakly bound, physisorbed species on a graphene sheet. The hydrogen atoms for stable six-member ring structures, bonding to a carbon and alternating on either side of the sheet.[4.70] Finally, isosteric enthalpy of adsorption calculations for hydrogen atoms with coronene ($C_{24}H_{12}$) as a graphite model have fallen in the range of 9.65 kJ/mol for basal plane bonding to 21.7 kJ/mol for bridge sites between two carbons in the graphite plane.[4.68] These simulation results agree with and support the observed capacity enhancements due to spillover at room temperature.

4.8 Literature Cited

[4.1] Satyapal, S.; Petrovic, J.; Read, C.; Thomas, G.; Ordaz, G. *Catal. Today* **2007,** *120*, 246.

[4.2] Langmuir, I. *J. Am. Chem. Soc.* **1918,** *40*, 1361.

[4.3] Yang, R. T. *Gas Separation by Adsorption Processes*; Imperial College Press: London, 1997; pp 255-258.

[4.4] Gregg, S. J.; Sing, K. S. W. *Adsorption, Surface Area and Porosity*, 2nd ed.; Academic Press: London, 1982; Chapter 2.

[4.5] Li, Y.; Yang, R. T. *J. Phys. Chem. B* **2006,** *110*, 17175.

[4.6] Nam, G. M.; Jeong, B. M.; Kang, S. H.; Lee, B. K.; Choi, D. K. *J. Chem. Eng. Data* **2005,** *50*, 72.

[4.7] Takagi, H.; Hatori, H.; Yamada, Y.; Matsuo, S.; Shiraishi, M. *J. Alloys Compd.* **2004,** *385*, 257.

[4.8] Takagi, H.; Hatori, H.; Soneda, Y.; Yoshizawa, N.; Yamada, Y. *Mater. Sci. Eng., B* **2004,** *108*, 143.

[4.9] Langmi, H. W.; Walton, A.; Al-Mamouri, M. M.; Johnson, S. R.; Book, D.; Speight, J. D.; Edwards, P. P.; Gameson, I.; Anderson, P. A.; Harris, I. R. *J. Alloys Compd.* **2003,** *356-357*, 710.

[4.10] Weitkamp, J.; Fritz, M.; Ernst, S. *Int. J. Hydrogen Energy* **1995,** *20*, 967.

[4.11] Chahine, R.; Bose, T. K. *Int. J. Hydrogen Energy* **1994,** *19*, 161.

[4.12] Chen, Y. D.; Ritter, J. A.; Yang, R. T. *Chem. Eng. Sci.* **1990,** *45*, 2877.

[4.13] Li, Y.; Yang, F. H.; Yang, R. T. *J. Phys. Chem. C* **2007,** *111*, 3405.

[4.14] Li, Y.; Yang, R. T. *J. Phys. Chem. C* **2007,** *111*, 11086.

[4.15] Madhavan, P.; Whitten, J. L. *J. Chem. Phys.* **1982,** *77*, 2673.

[4.16] Norton, P. R.; Davies, J. A.; Jackman, T. E. *Surf. Sci.* **1982,** *121*, 103.

[4.17] Chornet, E.; Coughlin, R. W. *J. Catal.* **1972,** *27*, 246.

[4.18] Rideal, E.; Sweett, F. *Proc. R. Soc. London, Ser. A* **1960,** *257*, 291.

[4.19] Kavtaradze, N. N. *Zh. Fiz. Khim.* **1958,** *32*, 1055.

[4.20] Do, D. D. *Adsorption Analysis: Equilibria and Kinetics*; Imperial College Press: London, 1998.

[4.21] Rutherford, S. W.; Coons, J. E. *Langmuir* **2004,** *20*, 8681.

[4.22] Rong, Z.; Vadgama, P. *J. Colloid Interface Sci.* **2006,** *303*, 75.

[4.23] Okazaki, M.; Tamon, H.; Toei, R. *AIChE J.* **1981,** *27*, 262.

[4.24] Higashi, K.; Ito, H.; Oishi, J. *J. Atom. Energ. Soc. Jpn.* **1963,** *5*, 846.

[4.25] Lachawiec, Jr.; A. J.; DiRaimondo, T. R.; Yang, R. T. *Rev. Sci. Instrum.* **2008,** *79*, 063906.

[4.26] Bhatia, S. K.; Myers, A. L. *Langmuir* **2006,** *22*,1688.

[4.27] Kojima, Y; Kawai, Y.; Koiwai, A.; Suzuki, N.; Haga, T.; Hioki, T.; Tange, K. *J. Alloys Compd.* **2006,** *421*, 204.

[4.28] Bénard, P.; Chahine, R. *Langmuir* **2001,** *17*, 1950.

[4.29] Chahine, R.; Bénard, P. Assessment of Hydrogen Storage on Different Carbons; Project No. C-3, IEA Task 12: Metal Hydrides and Carbon for Hydrogen Storage; International Energy Agency: Paris, France, 2001; p 104-107.

[4.30] Lueking, A. D.; Yang, R. T.; Rodriguez, N. M.; Baker, R. T. K. *Langmuir* **2004,** *20*, 714.

[4.31] Lueking, A. D.; Yang, R. T. *AIChE J.* **2003,** *49*, 1556.

[4.32] Hu, Q.; Pang, J.; Jiang, N.; Hampsey, J. E.; Lu, Y. *Microporous Mesoporous Mater.* **2005,** *81*, 149.

[4.33] Yang, R. T. *Adsorbents: Fundamentals and Applications*; Wiley & Sons: New York, 2005; p 307.

[4.34] Jankowska, H.; Świątkowski, A.; Choma, J. *Active Carbon*; Ellis Horwood: New York, 1991; pp 75-106.

[4.35] Sermon, P. A.; Bond, G. C. *J. Chem. Soc., Faraday Trans. 1* **1976,** *72*, 730.

[4.36] Pajonk, G. M. *Stud. Surf. Sci. Catal.* **2001,** *138*, 165.

[4.37] Martin, D.; Duprez, D. *J. Phys. Chem.* **1996,** *100*, 9429.

[4.38] Abderrahim, H.; Duprez, D. *Stud. Surf. Sci. Catal.* **1987,** *30*, 359.

[4.39] Lu, K.; Tatarchuk, B. J. *J. Catal.* **1987,** *106*, 166.

[4.40] Wang, L.; Yang, R. T. *J. Phys. Chem. C* **2008,** *112*, 12486.

[4.41] Gardes, G. E. E.; Pajonk, G. M.; Teichner, S. J. *J. Catal.* **1974,** *33*, 145.

[4.42] Spenadel, L.; Boudart, M. *J. Phys. Chem.* **1960,** *64*, 204.

[4.43] Vaska, L.; Selwood, P. W. *J. Am. Chem. Soc.* **1958,** *80*, 1331.

[4.44] Rowsell, J. L. C.; Yaghi, O. M. *Microporous Mesoporous Mater.* **2004,** *73*, 3.

[4.45] Campbell, N. L.; Clowes, R.; Ritchie, L. K.; Cooper, A. I. *Chem. Mater.* **2009,** *21*, 204.

[4.46] Tilford, R. W.; Mugavero, S. J.; Pellechia, P. J. *Adv. Mater.* **2008,** *20*, 2741.

[4.47] Bacsa, R. R.; Laurent, C.; Peigney, A.; Vaugien, T.; Flahaut, E.; Bacsa, W. S.; Rousset, A. *J. Am. Chem. Soc.* **2002,** *85*, 2666.

[4.48] Chen, X. H.; Chen, C. S.; Chen, Q.; Cheng, F. Q.; Zhang, G.; Chen, Z. Z. *Mater. Lett.* **2002,** *57*, 734.

[4.49] Srinivas, S. T.; Rao, P. K. *J. Catal.* **1994,** *148*, 470.

[4.50] Yang, F. H.; Yang, R. T. *Carbon* **2002,** *40*, 437.

[4.51] Yang, F. H.; Lachawiec, Jr.; A. J.; Yang, R. T. *J. Phys. Chem B* **2006,** *110*, 6236.

[4.52] Benton, A. F. *J. Am. Chem. Soc.* **1926,** *48*, 1850.

[4.53] Bansal, R. C.; Vastola, F. J.; Walker, Jr., P. L. *Carbon* **1971,** *9*, 185.

[4.54] Norton, P. R.; Richards, P. J. *Surf. Sci.* **1974,** *44*, 129.

[4.55] Wang, J.; Ebner, A. D.; Ritter J. A. *J. Phys. Chem. B* **2006,** *110*, 17353.

[4.56] Gross, K. J.; G.J. Thomas, G. J.; Jensen, C. M. *J. Alloys Compd.* **2002,** *330-332*, 683.

[4.57] Zaluska, L.; Zaluski, A.; Ström-Olsen, J. O. *J. Alloys Compd.* **1997,** *253-254*, 70.

[4.58] Knoblauch, K. *Chem. Eng.* **1978,** *85*, 87.

[4.59] Conner, Jr.; W. C. Spillover of Hydrogen. In *Hydrogen Effects in Catalysis: Fundamentals and Practical Applications*; Paál, Z., Menon, P. G., Eds.; Marcel Dekker, Inc.: New York, 1988; Vol. 31, p 311-346.

[4.60] Schwabe, U.; Bechtold, E. *J. Catal.* **1972,** *26*, 427.

[4.61] Fleisch, T.; Abermann, R. *J. Catal.* **1977,** *50*, 268.

[4.62] Menon, P. G.; Froment, G. F. *Stud. Surf. Sci. Catal.* **1982,** *11*, 171.

[4.63] Pliskin, W. A.; Eischens, R. P. *Z. Phys. Chem. (Leipzig)* **1960,** *24*, S11.

[4.64] Norton, P. R.; Davies, J. A.; Jackman, T. E. *Surf. Sci.* **1982,** *121*, 103.

[4.65] Bond, G. C.; Mallát, T. *J. Chem Soc., Faraday Trans. 1* **1981,** *77*, 1743.

[4.66] Ramirez-Cuesta, A. J.; Mitchell, P. C. H.; Parker, S. F.; Tomkinson, J.; Thompsett, D. *Stud. Surf. Sci. Catal.* **2001,** *138*, 55.

[4.67] Mitchell, P. C. H.; Ramirez-Cuesta, A. J.; Parker, S. F.; Tomkinson, J. *J. Mol. Struct.* **2003,** *651-653*, 781.

[4.68] Mitchell, P. C. H.; Ramirez-Cuesta, A. J.; Parker, S. F.; Tomkinson, J.; Thompsett, D. *J. Phys. Chem. B* **2003,** *107*, 6838.

[4.69] Chen, L.; Cooper, A. C.; Pez, G. P.; Cheng, H. *J. Phys. Chem. C* **2007,** *111*, 18995.

[4.70] Lin, Y.; Ding, F.; Yakobson, B. I. *Phys. Rev. B: Condens. Matter* **2008,** *78*, 041402.

Chapter 5

Isotope Tracer Evaluation of Hydrogen Spillover

5.1 Introduction to Hydrogen Isotopic Exchange

5.1.1 Hydrogen/Deuterium Exchange Reaction

Hydrogen and deuterium undergo an exchange reaction catalyzed by surfaces, notably platinum and nickel.[5.1,5.2] The reaction of interest is

$$H_2 + D_2 \leftrightarrow 2HD \tag{5.1}$$

At room temperature and near atmospheric pressure, the equilibration reaction on metal surfaces occurs quickly, on the order of one minute.[5.3,5.4] The equilibrium constant, K_{eq}, for the reaction depends on temperature according to the data in Table 5.1, as reported by Urey and Rittenberg.[5.5] At room temperature, for an initial mixture of equal parts deuterium and hydrogen, the equilibrium deuterium hydride composition is 95%.

Christmann et al.[5.6] observed the exchange reaction for Pt(111) for mixtures of hydrogen and deuterium. They noted that even when the species were dosed sequentially, complete equilibration to deuterium hydride was observed in the TPD spectrum. Equilibration does not occur below 120 K on platinum if hydrogen or deuterium has saturated the surface upon exposure to the alternate gas phase.[5.7]

Table 5.1 Equilibrium Constant for $H_2 + D_2 \leftrightarrow 2HD$

Temperature K	$\mathbf{K_{eq}}$
50	1.13
100	2.23
200	2.90
298	3.27
400	3.49
575	3.71
700	3.80

5.1.2 Mass Spectral Methods in Hydrogen Spillover Research

There have been an abundance of studies published using the hydrogen isotope deuterium to probe spillover. Nearly all of the studies focus on temperature programmed desorption (TPD), which employs a fixed temperature rate to induce desorption of species from an adsorbent.[5.8] The desorbed species are analyzed using a mass spectrometer, a device that ionizes molecules with high-energy electron bombardment. A magnetic field is used to deflect the ions according to their mass, generating a spectrum of ion currents. The path of these ions is scanned and correlated with mass-to-charge ratio (m/z) to identify the species present. When molecules undergo ionization, they fragment and the most abundant ion is termed the base peak. In positive-ion mass spectrometry, a molecule such as water ionizes to H_2O^+ and fragments OH^+, O^+, H_2^+, and H^+ giving signals at m/z values of 18, 17, 16, 2, and 1 respectively.[5.9] Since water is always present at low levels in vacuum systems due to ambient moisture adsorbed to solid surfaces, systems are baked at temperatures up to 573 K and background spectra are gathered to

subtract from raw data. This is particularly important for hydrogen spillover analysis, where H_2^+ and H^+ from water can obscure the spillover signal.

5.1.3 Mechanistic Observations of Spillover

The use of isotopic exchange experiments has provided useful insight into the spillover of hydrogen on supported catalysts. In several studies by Beck et al.,[5.10-5.12] the isotope deuterium was used to trace room temperature spillover on platinum supported on titania (Pt/TiO_2). The flash TPD technique was extended to Pt/Al_2O_3 in the later work of Chen and White.[5.13] Sequential dosing results characterized forward spillover as it was proposed that hydrogen or deuterium dissociated and diffused on the catalyst support and followed a reverse spillover path back to the metal particle in order to desorb. More recently, temperature-programmed reduction of carbon-supported palladium demonstrated hydrogen consumption below 573 K in excess of the palladium hydride amount, a behavior attributed to hydrogen spillover.[5.14] This is attractive especially because, on the basis of receptor site density calculations, carbon has been proven to be a better spillover hydrogen acceptor than alumina or silica.[5.15]

Exchange of deuterium with hydrogen contained in oxygen functional groups on the surface of metal oxides has been used to measure spillover.[5.16-5.19] TPD experiments generally require exposure temperatures above ambient (> 400 K) to observe exchange. Dmitriev et al. observed that platinum was more effective than palladium for promoting exchange on sodium-Y zeolites.[5.20] Nickel did not promote functional group exchange on zeolites. This is in agreement with results for carbon-based primary spillover adsorbents presented in Chapter 4. Later, it was shown that hydrogen/deuterium exchange occurs on

nickel supported metal oxides but the concentration of surface hydroxyl groups plays a key role.[5.21,5.22] The concentration of surface hydroxyl groups for platinum supported on ZSM molecular sieve altered the hydrogen/deuterium exchange at 623 K.[5.23] These reports emphasize the importance of receptor physical properties for hydrogen spillover.

Duprez and co-workers advanced the concept of isothermal isotopic exchange to measure surface diffusion properties of transition metal supported catalysts.[5.24-5.28] Early work was performed using isotopic oxygen on rhodium supported metal oxides. Functional group exchange was not initiated for these materials until temperatures reached at least 523 K. The supports alone were not active for the exchange reaction until a minimum temperature of 673 K. The study was extended to deuterium exchange for these materials and spillover from the source to the receptor was the rate-controlling step at room temperature.[5.29] Surface diffusion control on metal oxides was observed above 348 K.

Noteworthy in all of these studies is the absence of carbon-based adsorbents as receptors. Single walled nanotubes (SWNTs) were studied using hydrogen deuterium exchange at room temperature.[5.30] TPD showed exchange of hydrogen and deuterium for materials treated with ultrasound systems employing titanium alloy (Ti-Al-V) probes or for those ball milled with nickel/iron media. Purified materials did not exchange the isotopes and only exhibited physisorbed molecular hydrogen desorption on TPD, indicating the spillover mechanism was not active. The maximum capacity of the SWNT composite with titanium was reported as 0.46 wt%. Based on this result, temperature programmed desorption (TPD) is a useful technique to exploit for study of primary and secondary spillover mechanisms.

5.2 Experimental Methods for Temperature Programmed Desorption

5.2.1 TPD Apparatus

The apparatus for sequential dosing and analysis of TPD experiments consisted of a dosing manifold and an analysis manifold connected to a mass spectrometer. A schematic of the equipment is shown in Figure 5.1 and nomenclature is defined in Table 5.2

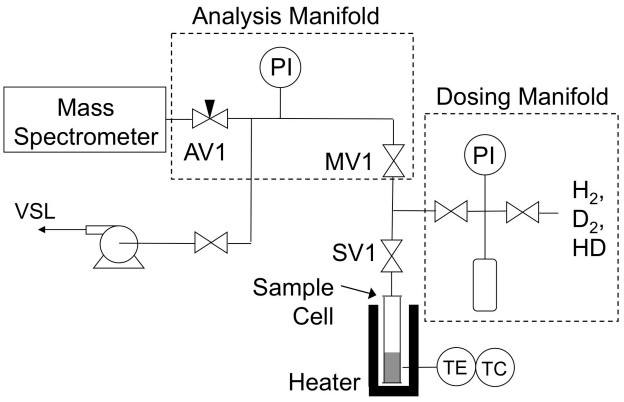

Figure 5.1 TPD Manifold and Sample Cell

Table 5.2 Nomenclature for TPD Apparatus

Tag	Description
AV1	Analysis Valve, Molecular Leak
MV1	Manifold Valve, Diaphragm
PI	Pressure Indicator
SV1	Sample Valve, Bellows Seal
TC	Temperature Controller
TE	Temperature Element (K Thermocouple)
VSL	Vent to Safe Location

Analysis of evolved gases during TPD experiments was performed with an AeroVac 1200 Magnetic Sector mass spectrometer (VTI, Inc.), operated at an accelerating voltage of 70 eV. An electron multiplier, operating at 1000 V, was used to increase the sensitivity to low current signals. A thin 316 SS tube was used to deliver evolved gas directly to the inlet of a molecular leak valve (Varian, Inc.). A sheath around the sampler was dynamically pumped with a mechanical vacuum pump to remove residual gas and ensure that the sample was composed solely of gas issuing from the surface of the adsorbent. The pumping rate was adjusted to maintain constant pressure in the sampling line during the TPD experiment. Heating was accomplished using an external heater constructed from nichrome wire.

The sample holder for TPD was a single ended tubular chamber constructed from 316 stainless steel. All connections were made with VCR® fittings (described in Chapter 3) to ensure high leak integrity. The sample was placed at the end of a 30 cm length of tube to enable suspension in a temperature bath. A filter disk (0.5 μm) was placed at the outlet VCR® fitting to prevent particle intrusion at the manifolds. A bellows valve was installed at one end to allow transfer of the sample under vacuum at cryogenic conditions from the dosing to the analysis manifold.

Dosing was completed on a Micromeritics® ASAP 2000 instrument, which enabled high accuracy pressure measurements. Samples could be dosed directly at the analysis manifold if necessary, but the pressure gauge was less accurate. Freezing spillover to 77 K was required prior to TPD and provided ample time to transfer the sample between dosing and analysis manifolds. The analysis manifold was outfitted with

isolation valves to maintain roughing vacuum in the line (1 x 10^{-3} mbar) and prevent moisture intrusion while idle.

As mentioned in Section 5.1.2, moisture contamination can cause errors in measurement of hydrogen fragments. Attention was given to the purity of all gases used in this study. Ultrahigh-purity helium (99.995%) and hydrogen (99.995%) were passed through molecular sieve 5A beds to ensure the gases were dry and free of contaminants. Deuterium (UHP, 99.97%) was used without further purification.

5.2.2 Samples for Studying the Spillover Mechanism

Two samples were chosen to study the mechanism of hydrogen spillover. Primary spillover was studied using 6 wt% Pt/TC. The details of synthesis and hydrogen storage capacity of this material are provided in Chapter 2 and Chapter 4, respectively. Secondary spillover was studied using a composite material with an isoreticular metal organic framework (IRMOF) receptor. The material was synthesized according to the procedure reported by Li and Yang, who also report full characterization of the material.[5.31] It consisted of IRMOF-8 bridged to PtC commercial catalyst (Strem Chemicals, Inc. 78-1600), thus, the material was similar to the secondary spillover adsorbent studied in Chapter 4, with the only difference in the receptor. This material was used because it exhibited enhanced hydrogen capacity (~ 2 wt% at 10 MPa) beyond AX-21 or TC receptors. The isosteric heat of adsorption was also nearly double that of 6 wt% Pt/TC (~ 21 kJ/mol).

5.2.3 Rate Measurements to Determine the Dose Time Scale

Rates of hydrogen and deuterium adsorption on 6 wt% Pt/TC at 298 K were measured at 0.4 bar (0.04 mmol/g loading) in order to establish the time scale for doses. The experiment was performed using a Micromeritics® ASAP 2010 analyzer. The results are presented in Figure 5.2, which shows two regions of adsorption behavior. At short times, reflected in the inset, there is a rapid initial rate of adsorption. Realizing that spillover first requires adsorption and dissociation by metal particles, this region is attributed to such phenomena, as equilibration on metal surfaces is known to occur rapidly. Spillover of atoms to carbon local to the metal particle also occurs during this step. The second region, which occurs over a time scale of tens of minutes, is attributed to the slow diffusion of hydrogen on the receptor. Of course, during this period, additional hydrogen molecules are arriving at the metal particle and dissociating to replenish source atoms. This behavior is coupled to the diffusion process; however, surface diffusion becomes limiting with regard to spillover rate.

It is noteworthy that the hydrogen and deuterium uptake rates on the platinum particle and on carbon local to it are nearly identical, whereas the surface diffusion of hydrogen atoms is faster relative to that of deuterium atoms. This kinetic isotope effect is as expected given the molecular weight[5.32] and diffusion activation energy differences[5.33] of the species. Rate data provide a means to design a TPD procedure. It appears that an exposure time of 5 min is adequate to establish a substantial amount of spillover atoms on the receptor at 298 K. Assuming that the reverse spillover rate is similar for desorption, a brief 1 min evacuation (at 298 K) should be sufficient to remove the bulk gas phase to perform subsequent doses and retain spillover species for TPD analysis.

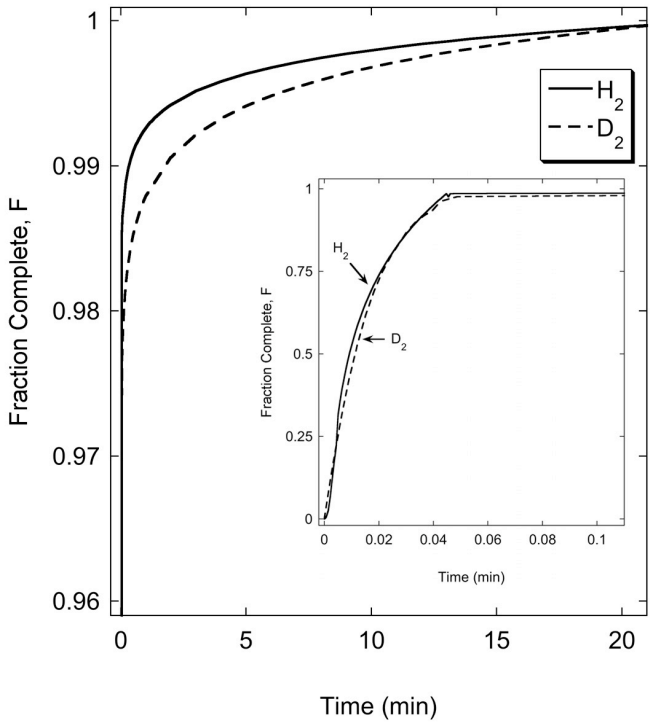

Figure 5.2 Rate of Adsorption of H_2 and D_2 on 6wt%Pt/TC, 0.4 bar and 298 K. Inset: Behavior for Short Time

5.2.4 Sequential Dosing Procedure

The dosing procedure was similar for all experiments, and the only changes were to the sequence of gases.[5.34] After the sample was degassed and equilibrated for at least 2 h at room temperature in vacuum (1.3×10^{-7} mbar), it was isolated from the manifold. The manifold was charged with gas to the desired dosing pressure. The dosing procedure was performed at room temperature with sequential exposures to 0.4 bar of the desired gas for 5 min. The sample was evacuated for 1 min after each dose to remove the gas phase. The chamber typically reached 1.3 kPa during this step. After the second dose and 1 min evacuation, the sample was isolated and immediately cooled in a liquid nitrogen

bath at 77 K. Prior to TPD, the sample was evacuated to 3 x 10^{-3} mbar and held at that pressure for at 77 K for 1 h.

For templated carbon and 6 wt % Pt/TC, the upper limit of TPD was 650 K to prevent Pt sintering[5.35,5.36] and carbon gasification.[5.37] TPD was limited to 523 K for the IRMOF-8 bridged PtC material to prevent its decomposition. The controlled temperature was measured with an external surface thermocouple, and the sample temperature was calculated using a calibrated offset. Rates studied were 10, 15, and 20 K/min. The sample was treated at 650 K (TC receptor) or 523 K (IRMOF-8 receptor) and 1.3 x 10^{-7} mbar for 3 h between each TPD experiment to remove atomic hydrogen and deuterium that might have remained from prior exposure. Repeat experiments confirmed that atoms remaining after this treatment were sufficiently anchored to prevent interaction with subsequent doses.

An empty chamber was sequentially dosed at 298 K and analyzed to establish a background signal for subtraction. The cell was triple-rinsed with water, then acetone, and finally dried in vacuum at 650 K for 12 h before measurement. The results are presented in Figure 5.3. The result shows that the background contributions of all species are insignificant up to approximately 500 K. At this temperature, an increase in the signal for hydrogen is observed. This feature is also observed in the raw results for TPD with sample present but disappears when subtracting the background. Such reductions of the raw data have been performed for all TPD results presented in this study. It is theorized that the background hydrogen signal is a result of desorption of hydrogen from the 316 SS sample chamber walls as the TPD temperature begins to approach the maximum used in preparation steps (650 K). It is reasonable to expect some hydrogen from the

outgassing of parts-per-million levels of water adsorbed to the chamber walls, particularly at such elevated temperatures.

Plain TC and platinum black were also examined to serve as a baseline for comparison of spillover response. The amount of platinum black used in baseline testing was determined such that the total surface area available was equal to the amount of surface platinum atoms estimated from the particle size measured via TEM (Figure 2.43) and XRD and dispersion. The platinum black BET SA was 37 m^2/g (measured using the methods described in Chapter 2) and the amount of platinum required for equivalence with 6 wt% Pt/TC was 0.05 mg Pt black/mg sample. Procedures for preparation, dosing, and analysis were identical to those previously described for samples under consideration. The results of TPD for TC and platinum black are shown in Figure 5.4 and Figure 5.5, respectively. Signals for all species are, on average, near zero (< 0.05 a. u.) and overlap on the plots, with the exception of the hydrogen signal for TC at temperatures less than 300 K. This behavior indicates the presence of physisorbed hydrogen. The TC result serves as a baseline for the conditions of exposure such that the effect of spillover caused by the addition of platinum nanoparticles is easily discerned. The absence of peaks for platinum black indicates that using this dosing procedure, isotope signals are not simply from exchange on platinum alone. Small baselines were observed irrespective of dose sequence.

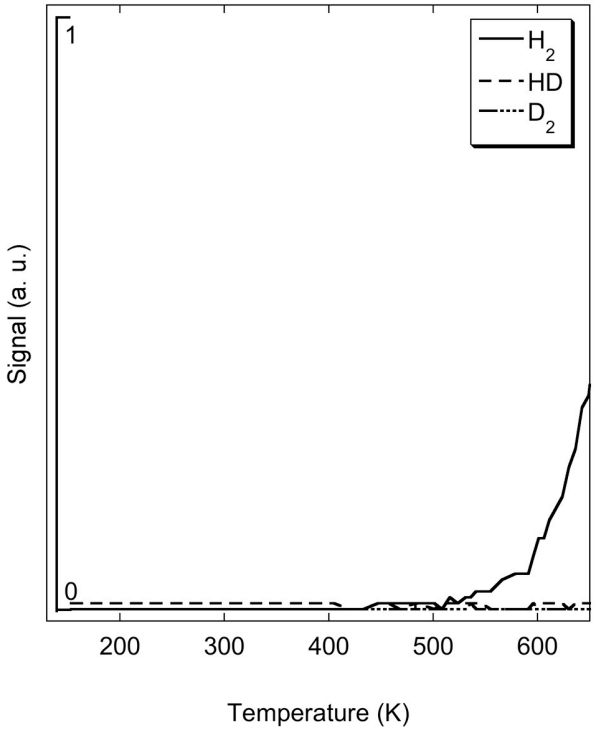

Figure 5.3 TPD Result for Sequential D_2/H_2 Dose, Empty Chamber

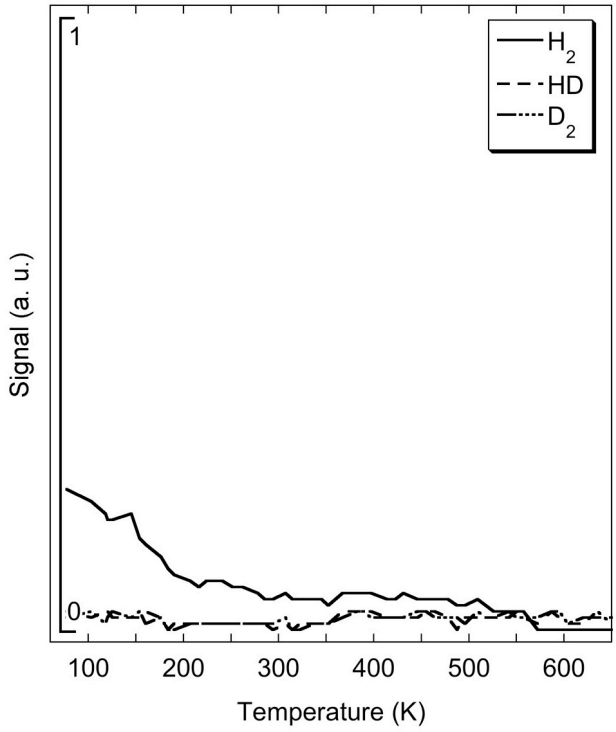

Figure 5.4 TPD Result for Sequential D_2/H_2 Dose, TC

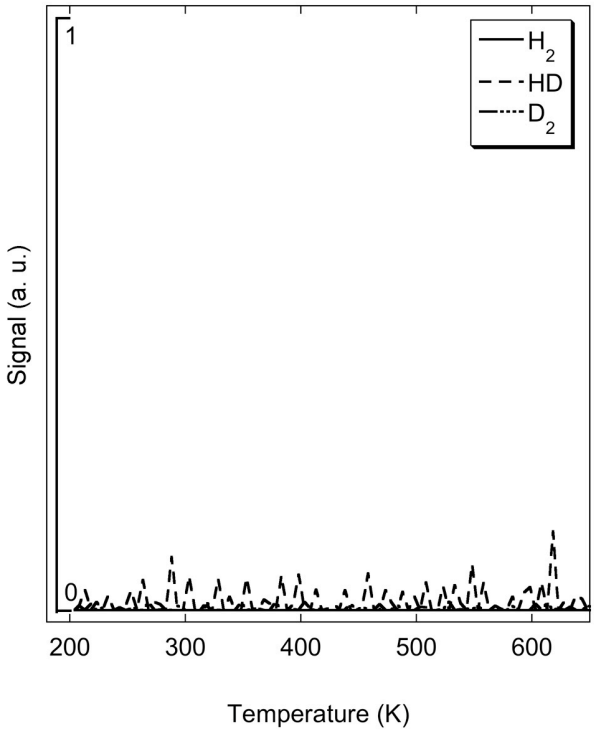

Figure 5.5 TPD Result for Sequential D_2/H_2 Dose, Platinum Black

5.2.5 Deuterium Hydride Equilibration Procedure

An alternative procedure was used to observe the reverse spillover mechanism. Deuterium hydride (96 atom% D, Aldrich 488690) was used as the dosing species. All sample preparation procedures were identical to sequential dosing. The sample was equilibrated at the desired temperature under a dose of 0.4 bar HD for 1 h to ensure an equilibrium distribution of hydrogen and deuterium atoms on the surface of the adsorbent. The time was selected based kinetics of spillover at pressures less than 100 kPa. Additional experiments performed with dose times of 2 h and 8 h confirmed the equilibration period. The sample was cooled to 77 K in order to prevent desorption via reverse spillover. The gas phase was evacuated and after transfer to the analysis manifold, TPD was performed as in sequential dosing experiments.

5.3 Sequential Dosing Results

The results of a series of TPD experiments using 6 wt % Pt/TC as the adsorbent are shown in Figure 5.6. The sample was exposed to sequential doses of 0.4 bar hydrogen followed by deuterium, each for 5 min at room temperature. The full procedure was as described in Section 5.2.4. The sequence of desorption products is the same for all heating rates. The sequence of D_2, HD, and H_2 is consistent with a reverse spillover mechanism for desorption.[5.10-5.12]

The reverse spillover phenomenon is explained in the context of a H_2/D_2 dose sequence. A schematic is provided in Figure 5.7. Hydrogen is dosed first and atoms (H) migrate away from the platinum dissociation center. Some atoms reverse direction during the intermediate evacuation step. A concentration gradient exists in both directions on the carbon surface; thus, some of the atoms continue outward movement. During the deuterium dose, it dissociates to atoms (D) and spills over to the carbon. Diffusion is slower for D due to the kinetic isotope effect,[5.32] and for an equal dose time, it diffuses a shorter distance from the platinum center. As deuterium atoms spread, some reach the region containing hydrogen atoms. During TPD, the process occurs in reverse. Deuterium atoms closest to the platinum particle recombine, generating a D_2 peak. Hydrogen atoms, moving faster relative to deuterium atoms, begin arriving at platinum with increasing frequency, producing a HD peak. The quantity of deuterium atoms is eventually exhausted, and hydrogen atoms that have traveled the farthest from the platinum site finally combine to yield the H_2 peak.

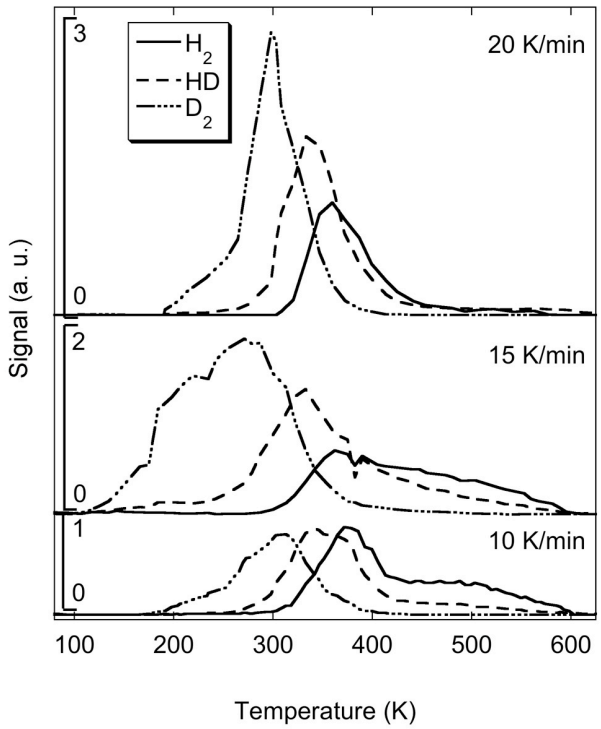

Figure 5.6 TPD Result for Sequential H_2/D_2 Dose, 6 wt% Pt/TC at 298 K

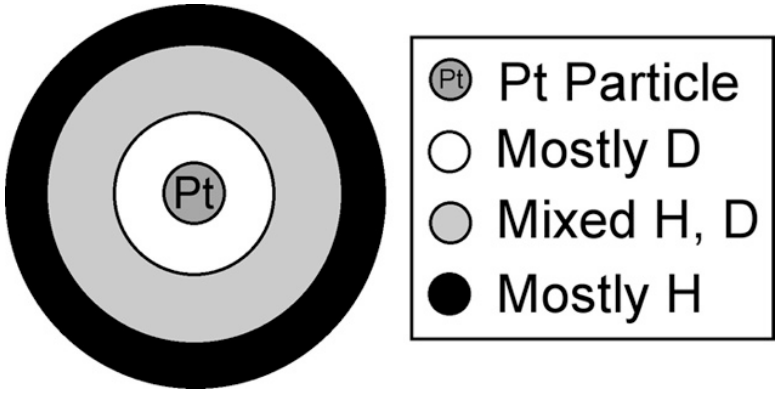

Figure 5.7 Schematic of Hydrogen Spillover Patterns for H_2/D_2 Dose

The experimental result and description of reverse spillover implies that surface diffusion is more important relative to pore diffusion. This is the case for adsorbents of large surface area and mobile adsorbate species where diffusion is due to the gradient of adsorbed concentrations not the amount.[5.38,5.39] The interpretation of the role of surface

diffusion and reverse spillover at these experimental conditions is consistent with aforementioned (Chapter 4) inelastic neutron scattering studies[5.40,5.41] The migration of hydrogen atoms far away from the platinum particle in those studies was on the order of 1 h. The results presented here indicate the short exposure was sufficient to allow diffusion in the vicinity of the source. Direct isotopic exchange on the carbon surface may be discounted, as studies using activated Graphon have identified a longer time scale for this process.[5.42] Below 523 K, Duprez observed that spillover controlled the temperature-programmed isotopic exchange of hydrogen and deuterium mixtures on metal oxide supported catalysts.[5.24]

The behavior for different heating rates is interesting to consider. In all cases, the peaks for various products are distinctly different from those generated by TPD from unsupported crystal planes of platinum.[5.43] The peak temperature shows a weak dependence on heating rate. The peaks do not demonstrate a consistent symmetry that typically would define a purely second order process, such as dissociative adsorption.[5.8] This observation is not unexpected, as reverse spillover is more complex and kinetically influenced by both diffusion and recombination of atoms.

The TPD response of the sample was measured upon reversing the dose sequence of the gases. Figure 5.8 shows the result of TPD for the 6 wt % Pt/TC sample when exposed to deuterium followed by hydrogen with all other conditions being equal. The programmed rate was 10 K/min. The first two peaks exhibit similar order of magnitude to those of the mirror image dose sequence shown in Figure 5.6. The observed sequence is consistent with reverse spillover of the species as proposed earlier. In this case, a high concentration of hydrogen atoms would be closest to the platinum particle, followed by a

mixture of hydrogen and deuterium atoms, and finally a thin region of deuterium atoms due to their slow surface diffusion. This pattern is sketched in Figure 5.9.

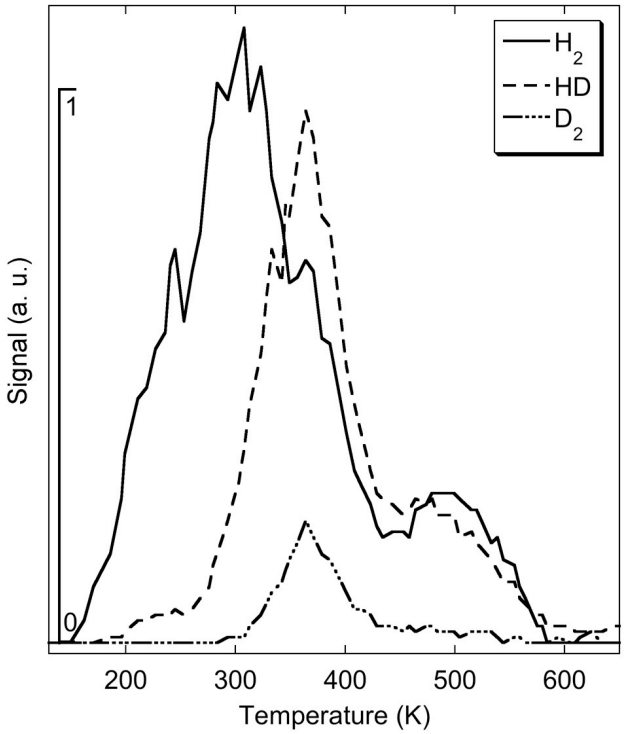

Figure 5.8 TPD Result for Sequential D_2/H_2 Dose, 6 wt% Pt/TC at 298 K

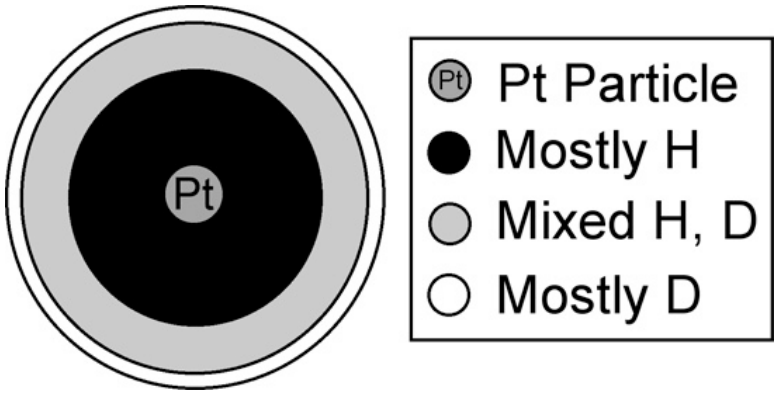

Figure 5.9 Schematic of Hydrogen Spillover Patterns for D_2/H_2 Dose

The hydrogen peak in the D_2/H_2 sequence has broadened relative to the deuterium peak in the H_2/D_2 sequence. The magnitude and shape are similar for the HD peak. The deuterium peak is much smaller than the companion hydrogen peak in Figure 5.6. This is consistent with the schematic in Figure 5.9 considering that, upon reverse spillover during desorption, surface diffusion of hydrogen atoms is fastest, followed by deuterium atoms arriving from the mixed zone. The supply of hydrogen atoms is maintained throughout much of the TPD experiment, even after the high concentration of deuterium atoms is desorbed. This is a simplistic model of a single spillover center and receptor surface. Many of these spillover "spheres of influence" can, and from the observations of peak overlap do, coincide. Such patterns contribute additional hydrogen atoms to the outer ring in Figure 5.9.

A single gas dosing experiment was performed with hydrogen in order to confirm the effectiveness of the intermediate treatment step and put the exchange reaction in perspective for our experimental configuration. The procedure was unchanged, except for replacement of the deuterium condition with a second hydrogen exposure. The result is shown in Figure 5.10. Several points are noteworthy regarding this result. The intermediate treatment procedure at 650 K appears to be adequate to remove spillover atoms from previous runs. Small quantities of HD and deuterium are observed at approximately 340 K; however, they are inconsequential relative to the response for hydrogen. This is confirmed by reproducibility of results for sequential dosing experiments. Comparing the hydrogen response in this experiment to sequential dosing experiments (Figures 5.6 and 5.8), the magnitude of the peak is greater and its temperature location falls between those observed for sequential dosing.

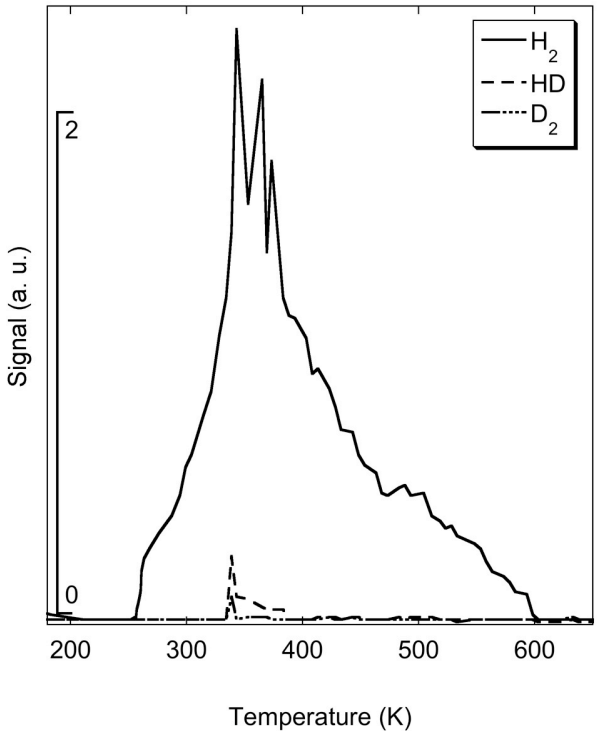

Figure 5.10 TPD Result for Dual H_2 Doses, 6 wt% Pt/TC at 298 K

This study was extended to the composite material IRMOF-8/PtC/Bridge (8:1:1). The dosing procedure was identical to that performed using 6 wt % Pt/TC; however, the TPD maximum temperature was limited to 523 K to prevent destruction of the IRMOF-8 structure. The results for sequential H_2/D_2 doses at 298 K are shown in Figure 5.11.

Once again, the sequence is D_2, HD, and H_2, which is expected since the reverse spillover is expected to be active in desorption from this material. The relative size and shape of the peaks are different when comparing the result to the 6 wt % Pt/TC material. Many of the peaks appear to be more symmetric. The deuterium peak is smallest for each run, which seems to indicate that the capacity local to the platinum particle is lower compared to a TC receptor. This is easily confirmed when one considers that the

commercial carbon used in the catalyst support has less than half of the surface area (976 m^2/g) and pore volume (0.7 cc/g) compared to templated carbon, even after platinum doping. The hydrogen peak, appearing last in all experiments, is the largest of the peaks. Li and Yang reported on the strong bonds between IRMOF-8 and spillover hydrogen,[5.31] stronger relative to the bonding on carbon. This pattern is evidence of those strong bonds, as it appears that more atomic hydrogen collects on the receptor during the first dose. In addition to being bound more strongly, it must cross the carbon bridge to the primary receptor. This seems to delay its arrival at the platinum particle in the reverse spillover process. At the highest TPD rate (20 K/min), a secondary peak begins to form. These results are strong evidence for the reverse secondary spillover process occurring on the IRMOF-8 bridged to PtC.

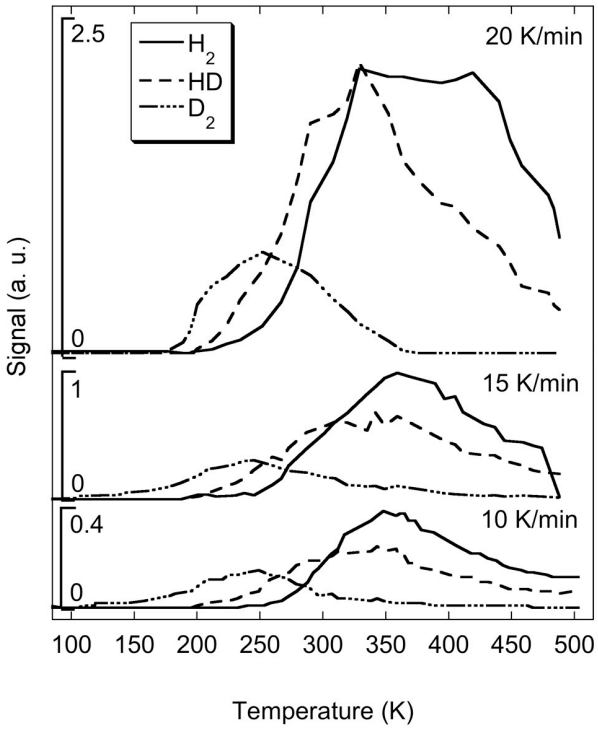

Figure 5.11 TPD Result for Sequential D_2/H_2 Dose, IRMOF-8/PtC/Bridge at 298 K

5.4 Deuterium Hydride Equilibration Results

Deuterium hydride was equilibrated on the surface of 6 wt% Pt/TC for 1 h at 298 K. After cooling the sample to 77 K and pumping off the gas phase, TPD was performed and the result is shown in Figure 5.12.

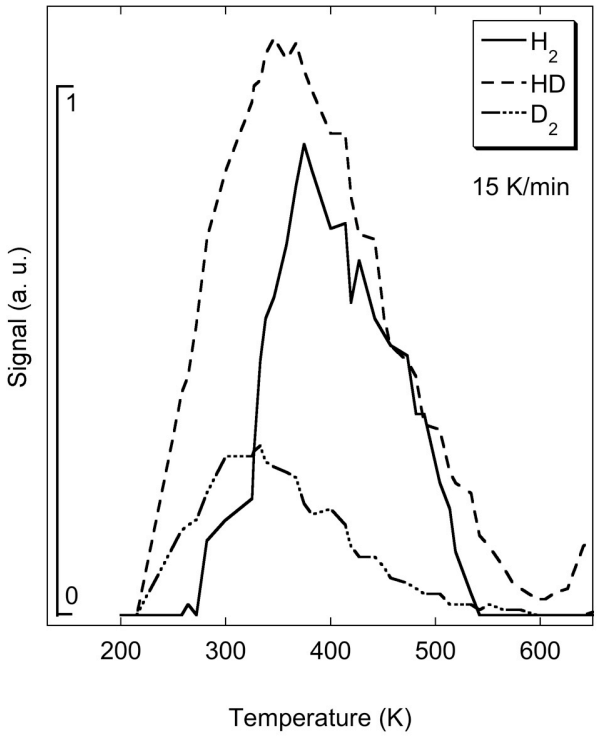

Figure 5.12 TPD Result for HD Equilibration on 6 wt% Pt/TC at 298 K

Physisorbed deuterium hydride below 200 K is subtracted from this spectrum. As the temperature increases, HD and D_2 peaks begin to form. The D_2 peak is substantially smaller relative to the HD peak and its maximum occurs at a lower temperature. For uniformly distributed hydrogen and deuterium atoms at equilibrium, a single peak of deuterium hydride would be expected. The result implies that there is some partitioning of species on the carbon surface after spillover. If the difference in bond energies for species containing deuterium are compared with those containing hydrogen (see Table

5.3), the former are always more energetic.[5.44] While these bond energies are not exact for the physisorbed species that are predicted by simulation,[5.45,5.46] a similar trend is likely to hold. Deuterium has a higher probability to cluster together since the interaction energy is slightly greater relative to hydrogen. On desorption, deuterium atoms would then be more likely to recombine with each other as they diffuse on the surface by hopping. This would cause them to desorb from the surface prematurely, since the strength of the D_2 bond is larger than that of H_2. This behavior is a plausible explanation for the consistently smaller deuterium peaks in the TPD results.

The earlier assumption that all of the spillover atoms desorb through a reverse spillover mechanism may be incorrect. A certain fraction of these atoms seem to undergo recombination on the receptor during the desorption step.

Table 5.3 Bond Energies for Species Containing Hydrogen and Deuterium

Species	**Energy** kJ/mol
C-H	338.4
C-D	341.4
H-H	435.78
H-D	439.22
CH_3-H	439.3
CH_3-D	-
D-D	443.32
C_6H_5-H	472.2

HD equilibration was also measured for IRMOF-8/PtC/Bridge material to observe the response for a secondary spillover adsorbent. The results are shown in Figure 5.13. A

desorption spectrum similar to Figure 5.12 is observed, with a shift of peak temperatures to lower temperatures.

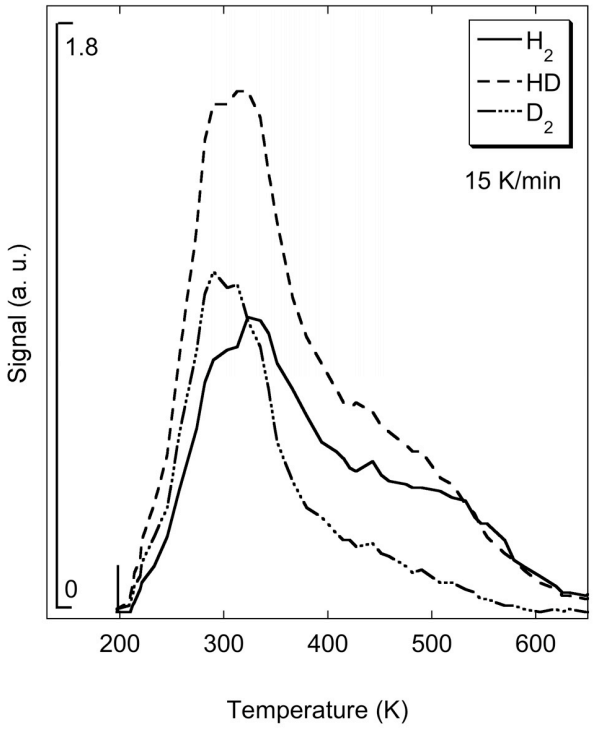

Figure 5.13 TPD Result for HD Equilibration on IRMOF-8/PtC/Bridge at 298 K

Deuterium appears to be tracing recombination on the surface that would explain faster desorption rates. In a system of uniform hydrogen concentration, clusters of hydrogen atoms could form at high-energy defect sites or on surface functional groups. The simulation work of Yakobson and co-workers demonstrated stable clusters of six hydrogen atoms that spilled over onto a model graphene sheet.[5.45] Recombination of these clusters without the need to fully reverse back to the source particle favors the observation of increased desorption kinetics.

5.4 Recombination Phenomenon on Desorption

An effort was made to further describe the proposed recombination process with a series of step or 'flash' desorption experiments. The procedure employed the same deuterium hydride dosing technique. Equilibrium was established for 1 h at the desired temperature and 0.4 bar. The sample was cooled to 200 K to prevent excessive deuterium hydride physisorption that might obscure results. After pumping away the gas phase at 200 K, the sample was rapidly warmed to room temperature by plunging the holder into a circulating bath. Desorbed species were monitored as a function of time with the mass spectrometer. The sample warmed from 200 K to 298 K in approximately 2 min (initial heating rate ~ 48 K/min) and remained constant for the remainder of the experiment.

Results of step desorption for 6 wt% Pt/TC at 298 K and 273 K exposure temperatures is shown in Figure 5.14 and Figure 5.15, respectively. In both cases, there is a large initial peak for all three species, indicating sudden desorption via recombination of hydrogen and deuterium atoms. Peaks containing deuterium are of greater magnitude relative to molecular hydrogen, which implies a higher probability for deuterium atoms recombining relative to hydrogen atoms.

An interesting feature is the tail of the main peak, which begins at approximately 4 min. The tails for D_2 and HD are sustained for a longer period of time relative to H_2. This implies that there are more deuterium atoms issuing from the surface, either through reverse spillover, recombination, or both. Comparing the results for two dosing temperatures, shorter tails are observed for 273 K equilibration relative to 298 K. This is reasonable, since diffusion rates decrease with temperature and thus the extent of the spillover species is smaller, as predicted with the spillover isotherm in Chapter 4.

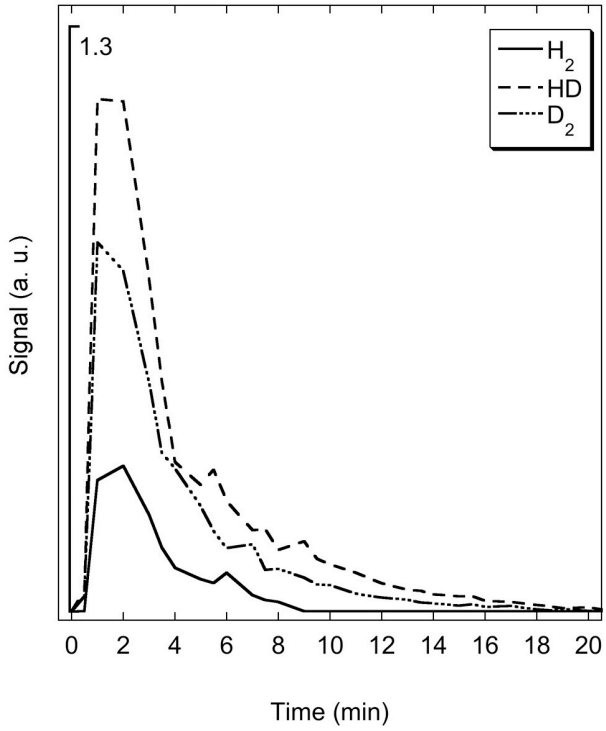

Figure 5.14 Step Desorption for HD Equilibration on 6 wt% Pt/TC at 298 K

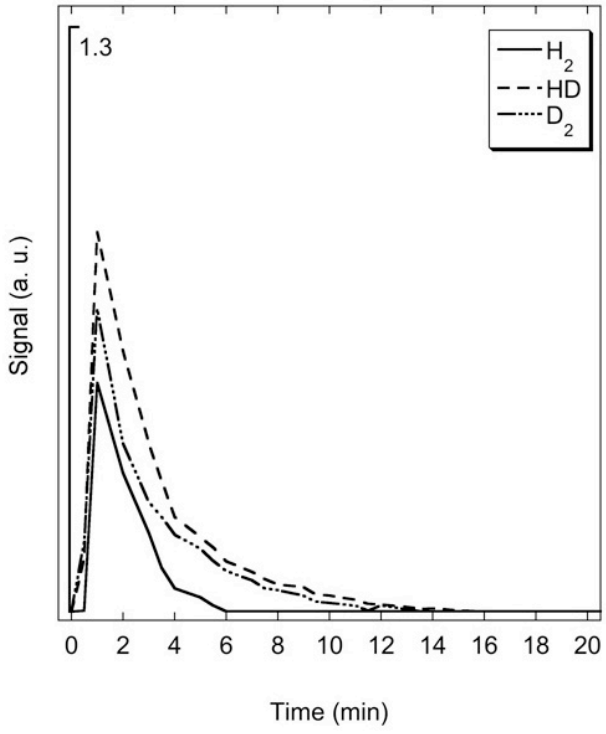

Figure 5.15 Step Desorption for HD Equilibration on 6 wt% Pt/TC at 273 K

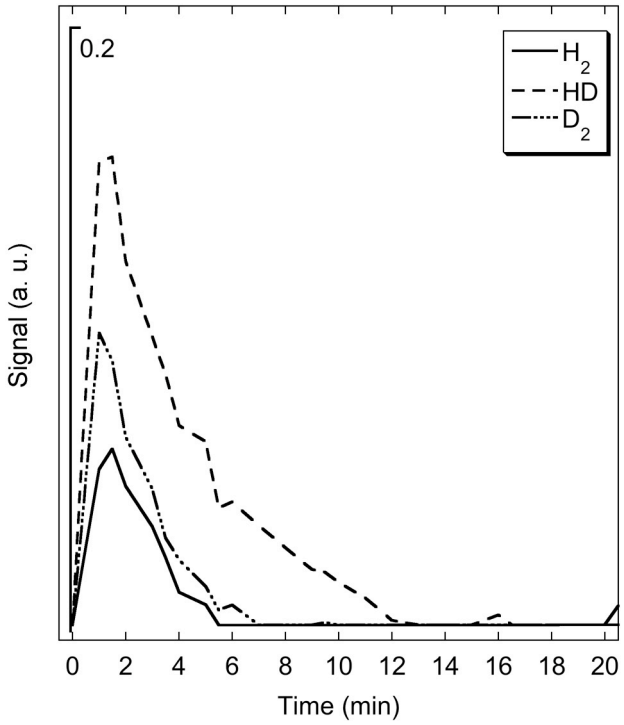

Figure 5.16 Step Desorption for HD Equilibration on IRMOF-8/PtC/Bridge at 298 K

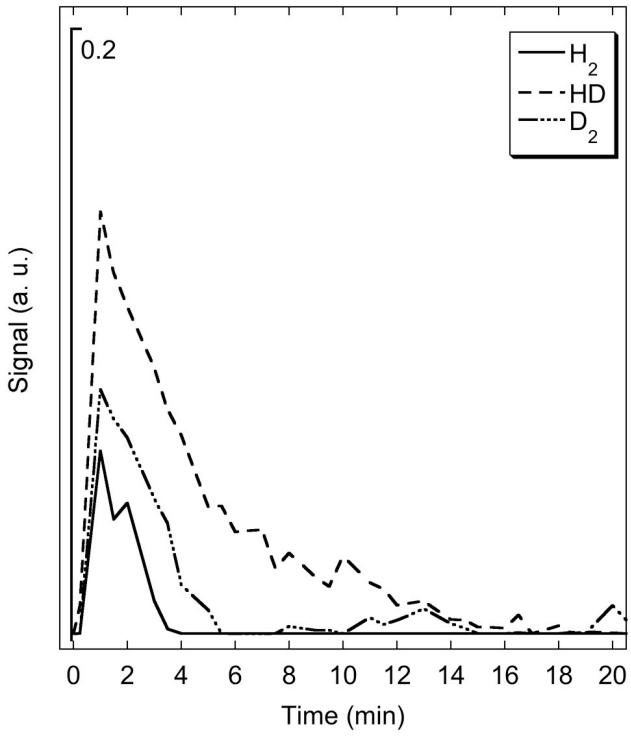

Figure 5.17 Step Desorption for HD Equilibration on IRMOF-8/PtC/Bridge at 273 K

A similar trend of peak tailing was observed for IRMOF-8/PtC/Bridge material. The exception was that the magnitude of the tails was smaller in this case. The overall extent of spillover is shorter due to diffusion across the bridge material. The timing of H_2 and D_2 tails seem to indicate a more uniform distribution of hydrogen and deuterium relative to 6 wt% Pt/TC. Functionalities and defects on carbon surfaces can potentially disrupt such a uniform distribution.

As experimental results continued to point toward recombination affecting spillover rates, an additional study was undertaken to characterize the process using 6 wt% Pt/TC. The adsorption isotherm was measured for deuterium at 298 K and results are presented in Figure 5.18. Deuterium compressibility factors for use in analysis were calculated from literature data.[5.47] The procedure and data reduction techniques were described in Chapter 3. Analysis pressures were limited to less than 6 MPa based on maximum delivery pressure of deuterium. Note that although deuterium is adsorbed in smaller quantities than hydrogen, the deviation is minor at TPD experimental conditions of 0.4 bar. Data for the deuterium isotherm at high pressure enabled calculation of the time constant for surface diffusion during adsorption and desorption using the methods described in Chapter 4.

If the theory of atomic hydrogen cluster stability is accepted, then there is likely to be some recombination during adsorption until equilibrium is reached. This serves to slow down the net adsorption rate. The calculation technique to describe spillover kinetics does not couple the net uptake of hydrogen atoms to recombination. Desorption is a measure of both recombination and reverse spillover. The difference in the observed adsorption and desorption rates should give an estimate of the rate of recombination.

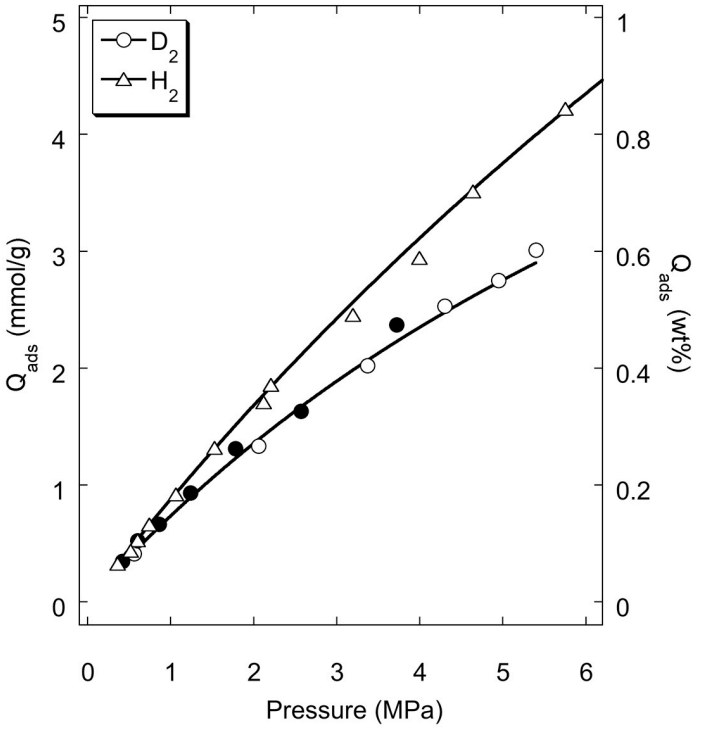

Figure 5.18 Deuterium Adsorption Isotherm for 6 wt% Pt/TC at 298 K

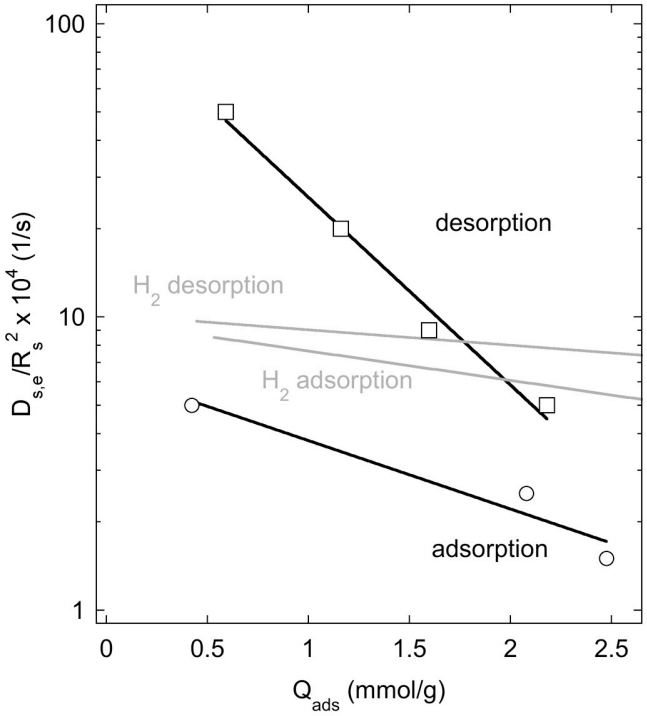

Figure 5.19 Diffusion Time Constant for Deuterium on 6 wt% Pt/TC

Methods outlined in Chapter 4 were used to calculate the diffusion time constant for deuterium adsorption and desorption on 6 wt% Pt/TC at 298 K. The result is shown in Figure 5.19 along with traces of the values for hydrogen to facilitate comparison. As expected, deuterium adsorption rates are slower, represented by lower diffusion time constants, due to kinetic effects.[5.32] An interesting behavior occurs for desorption as loading decreases. The expected trend is not followed and deuterium diffusion time constants are larger relative to hydrogen at nearly all conditions in this study. The rate of recombination influences the magnitude of the difference.

Direct subtraction of adsorption from desorption time constants yields a time constant for recombination. This parameter is used to capture recombination behavior, although it obviously does not have an identical physical meaning as the diffusion time constants from which it is derived.

Figure 5.20 indicates the result for subtraction of the diffusion time constant for adsorption from that of desorption. The recombination time constant is higher for deuterium relative to hydrogen. The trends are much different for the two isotopes. The value for hydrogen is nearly invariant over the loadings studied. The parameter demonstrates a strong inverse loading dependence for deuterium. It is possible that deuterium requires a higher density of atoms to cluster before it is stable on the receptor surface. The rate of recombination would show the corresponding decreasing trend with pressure.

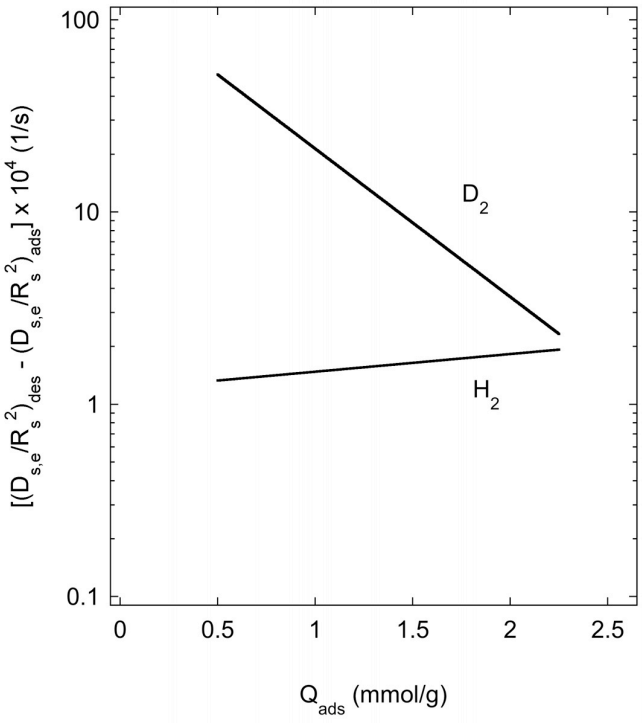

Figure 5.20 Recombination Time Constant for H_2 and D_2 on 6 wt% Pt/TC at 298 K

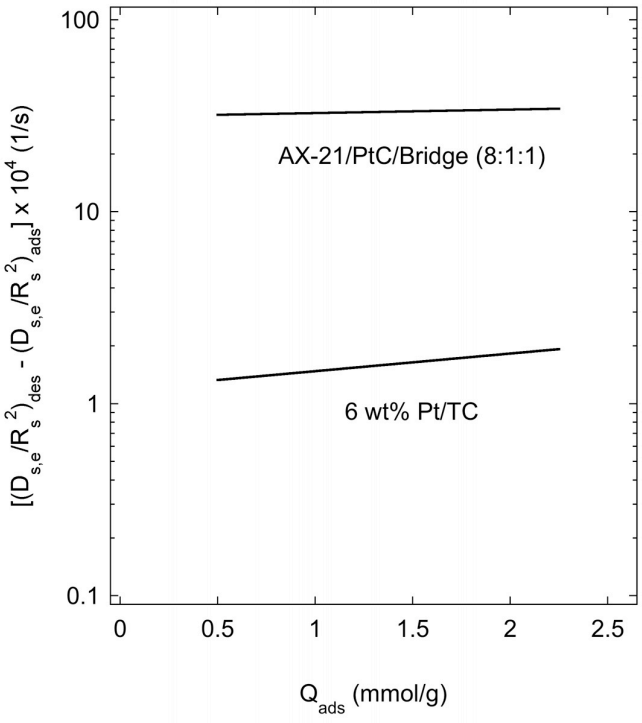

Figure 5.21 Recombination Time Constant for Hydrogen: Adsorbent Comparison

A final calculation was performed to compare the recombination time constant for primary and secondary spillover adsorbents. In Chapter 4, these parameters were calculated as a function of hydrogen adsorption. The difference between adsorption and desorption values are shown in Figure 5.21 for 6 wt% Pt/TC and AX-21/PtC/Bridge (8:1:1). The recombination time constant for secondary spillover is nearly one order of magnitude larger compared to primary spillover. Both are invariant as loading increases. Such behavior indicates stability of adsorbed configurations. Recombination, though not dependent on adsorbed amount, is significantly altered by the receptor.

5.6 Conclusions

Isotope tracer experiments to characterize spillover were discussed in this chapter. Detailed history of isotopic tracer work in the spillover field was provided and analysis techniques were described. Three methods of isotopic tracer analysis were used to evaluate the hydrogen spillover mechanism: sequential dosing, deuterium hydride equilibration, and step desorption.

Sequential dosing experiments employed deuterium and hydrogen alternating doses to determine the diffusion path configuration. Results of deuterium doses followed by hydrogen doses at room temperature gave peaks in the sequence of H_2, HD, and D_2. Reversing the dose yielded the opposite spectrum. Behavior was similar for both primary and secondary spillover materials. This provided evidence of a radial diffusion mechanism for forward and reverse spillover.[5.10-5.12,5.34] Deuterium peaks were consistently smaller than the others, indicating this mechanism did not fully describe the spillover phenomenon.

Deuterium hydride equilibration was used to determine the mechanism of reverse spillover as hydrogen and deuterium atoms were evenly distributed on the surface. TPD of the equilibrated materials consistently showed spectra with deuterium peaks first in a sequence of D_2, HD, H_2. For uniform distribution and solely reverse spillover desorption, uniform, concurrent peaks were expected. This is evidence of deuterium prematurely desorbing from the surface as recombination takes place before it diffuses back to the spillover source.

Step desorption, also called 'flash' desorption, was employed to confirm the theory that deuterium is undergoing recombination during reverse spillover. Tails for the instantaneous desorption spectra are extended for D_2 and HD, indicating a greater proportion of deuterium atoms are issuing from the surface.

After obtaining plausible proof of an alternate desorption route for deuterium, the recombination time constant was calculated to quantify the phenomenon. Uptake measurements do not measure rates of recombination, however, desorption methods capture both reverse spillover and recombination. Subtracting the time constants for both processes gave a time constant for recombination. Values depended on the atomic species and the nature of the adsorbent. A secondary spillover adsorbent demonstrated a recombination time constant one order of magnitude higher relative to a primary spillover adsorbent. In general, the recombination phenomenon has broad implications for the design of materials with improved kinetic performance.

5.7 Literature Cited

[5.1] Breakspere, R. J.; Eley, D. D.; Norton, P. R. *J. Catal.* **1972,** *27*, 215.

[5.2] Eley, D. D.; Norton, P. R. *Proc. R. Soc., London, Ser. A* **1970,** *314*, 319.

[5.3] Norton, P. R.; Richards, P. J. *Surf. Sci.* **1974,** *44*, 129.

[5.4] Norton, P. R.; Richards, P. J. *Surf. Sci.* **1974,** *41*, 293.

[5.5] Urey, H. C.; Rittenberg, D. *J. Chem. Phys.* **1933,** *1*, 137.

[5.6] Christmann, K.; Ertl, G.; Pignet, T. *Surf. Sci.* **1976,** *54*, 365.

[5.7] Greenlief, C. M.; Akhter, S.; White, J. M. *J. Phys. Chem.* **1986,** *90*, 4080.

[5.8] Masel, R. I. *Principles of Adsorption and Reaction on Solid Surfaces*; Wiley & Sons: New York, 1996; pp 507-522.

[5.9] Ameel, T. A.; Kim, K. J.; Wood, B. D. *J. Thermophys. Heat Transfer* **1997,** *11*, 582.

[5.10] Beck, D. D.; White, J. M. *J. Phys. Chem.* **1984,** *88*, 2764.

[5.11] Beck, D. D.; White, J. M. *J. Phys. Chem.* **1984,** *88*, 174.

[5.12] Beck, D. D.; Bawagan, A. O.; White, J. M. *J. Phys. Chem.* **1984,** *88*, 2771.

[5.13] Chen, H.-W.; White, J. M. *J. Mol. Catal.* **1986,** *35*, 355.

[5.14] Ramos, A. L. D.; Aranda, D. A. G.; Schmal, M. *Stud. Surf. Sci. Catal.* **2001,** *138*, 291.

[5.15] Bond, G. C.; Mallat, T. *J. Chem. Soc., Faraday Trans. 1* **1981,** *77*, 1743.

[5.16] Alexeev, O.; Kim, D.-W.; Graham, G. W.; Shelef, M.; Gates, B. C. *J. Catal.* **1999,** *185*, 170.

[5.17] Bianchi, D.; Maret, D.; Pajonk, G. M.; Teichner, S. J. *Stud. Surf. Sci. Catal.* **1983,** *17*, 45.

[5.18] Hall, W. K.; Leftin, H. P.; Cheselske, F. J.; O'Reilly, D. E. *J. Catal.* **1963,** *2*, 506.

[5.19] Hall, W. K.; Lutinski, F. E. *J. Catal.* **1963,** *2*, 518.

[5.20] Dmitriev, R. V.; Detjuk, A. N.; Minachev, C. M.; Steinberg, K. H. *Stud. Surf. Sci. Catal.* **1983,** *17*, 17.

[5.21] Almasan, V.; Lazar, M.; Marginean, P. *Stud. Surf. Sci. Catal.* **1999,** *122*, 435.

[5.22] Hassan, A.; Fujimoto, K.; Tomishige, K.; Kusakari, T.; Akasaka, A. *Stud. Surf. Sci. Catal.* **2001,** *138*, 39.

[5.23] Schuetze, F.-W.; Roessner, F.; Meusinger, J.; Papp, H. *Stud. Surf. Sci. Catal.* **1997,** *112*, 127.

[5.24] Duprez, D. *Stud. Surf. Sci. Catal.* **1997,** *112*, 13.

[5.25] Martin, D.; Duprez, D. *J. Phys. Chem.* **1996,** *100*, 9429.

[5.26] Martin, D.; Duprez, D. *Stud. Surf. Sci. Catal.* **1993,** *77*, 201.

[5.27] Abderrahim, H.; Duprez, D. In *Proceedings of the 9th International Congress on Catalysis*; Phillips, M. J., Ternan, M., Eds.; The Chemical Institute of Canada: Ottawa, ON, 1988; pp 1246-1252.

[5.28] Abderrahim, H.; Duprez, D. *Stud. Surf. Sci. Catal.* **1987,** *30*, 359.

[5.29] Martin, D.; Duprez, D. *J. Phys. Chem. B* **1997,** *101*, 4428.

[5.30] Haluska, M.; Hirscher, M.; Becher, M.; Dettlaff-Weglikowska, U.; Chen, X.; Roth, S. *Mater. Sci. Eng., B* **2004,** *108*, 130.

[5.31] Li, Y.; Yang, R. T. *J. Am. Chem. Soc.* **2006,** *128*, 8136.

[5.32] Bigeleisen, J. *Science* **1949,** *110*, 14.

[5.33] Farkas, A.; Farkas, L. *Proc. R. Soc., London, Ser. A* **1934,** *144*, 467.

[5.34] Lachawiec, Jr., A. J.; Yang, R. T. *Langmuir* **2008,** *24*, 6159.

[5.35] Bett, J. A.; Kinoshita, K.; Stonehart, P. *J. Catal.* **1974,** *35*, 307.

[5.36] Chu, Y. F.; Ruckenstein, E. *Surf. Sci.* **1977,** *67*, 517.

[5.37] Baker, R. T. K.; Prestridge, E. B.; Garten, R. L. *J. Catal.* **1979,** *56*, 390.

[5.38] Yang, R. T. *Gas Separation by Adsorption Processes*; Imperial College Press: London, 1997; pp 108-123.

[5.39] Do, D. D. *Adsorption Analysis: Equilibria and Kinetics*; Imperial College Press: London, 1998; pp 521-561.

[5.40] Mitchell, P. C. H.; Ramirez-Cuesta, A. J.; Parker, S. F.; Tomkinson, J. *J. Mol. Struct.* **2003,** *651-653*, 781.

[5.41] Mitchell, P. C. H.; Ramirez-Cuesta, A. J.; Parker, S. F.; Tomkinson, J.; Thompsett, D. *J. Phys. Chem. B* **2003,** *107*, 6838.

[5.42] Ishikawa, Y.; Austin, L. G.; Brown, D. E.; Walker, Jr., P. L. Ortho-/Parahydrogen Conversion and Hydrogen-Deuterium Equilibration Over Carbon Surfaces. In *Chemistry and Physics of Carbon*; Walker, Jr., P. L., Thrower, P. A., Eds.; Marcel Dekker, Inc.: New York, 1975; Vol. 12, pp 39-108.

[5.43] McCabe, R. W.; Schmidt, L. D. *Proc. 7th Intern. Vac. Congr. and 3rd Intern. Conf. Solid Surfaces*; Vienna, Austria, 1977; Dobrozemsky, R., Rüdenauer, F., Viehböck, F. P., Breth, A., Eds.; p 1201.

[5.44] Bond Dissociation Energies, In *CRC Handbook of Chemistry and Physics*, 88th ed.; D. L. Lide, D. L., Ed.; CRC Press/Taylor & Francis: Boca Raton, FL, 2008; Internet Version.

[5.45] Chen, L.; Cooper, A. C.; Pez, G. P.; Cheng, H. *J. Phys. Chem. C* **2007,** *111*, 18995.

[5.46] Lin, Y.; Ding, F.; Yakobson, B. I. *Phys. Rev. B: Condens. Matter* **2008,** *78*, 041402.

[5.47] Michels, A.; De Graaff, W.; Wassenaar, T.; Levelt, J. M. H.; Louwerse, P. *Physica* **1959,** *25*, 25.

Chapter 6

Conclusions and Future Work

6.1 Conclusions and Key Findings of This Research

The objectives of this work were to (1) synthesize and characterize transition metal doped high surface area nanostructured carbons for hydrogen spillover and storage, (2) accurately measure hydrogen adsorption and spillover isotherms near ambient temperature, and (3) identify the mechanism and kinetics of hydrogen spillover on carbon-based nanomaterials with isotopic tracers to provide routes for optimization of spillover adsorbents. The following conclusions can be drawn from the results of this effort.

1. Enhanced capacity spillover adsorbents have been synthesized using ultrasound assisted solution impregnation and bridge building techniques between common catalytic materials and novel nanostructured carbons. The impregnation method generates a nanoparticle dispersion of nearly 40% on nanoporous and microporous carbons. Bridge-building techniques are patent-pending processes that can be applied to many spillover receptors and quickly extend the spillover behavior of new materials. Capacity enhancements of up to 70% over molecular hydrogen physisorption on carbons have been realized at 10 MPa and 298 K.

2. A highly accurate, volumetric adsorption apparatus has been constructed and validated internally and by the National Renewable Energy Laboratory (NREL). The instrument and technique is a cost-effective means of high throughput screening for hydrogen spillover adsorbents at ambient temperature. A heuristic for correction of helium adsorption on carbon-based nanomaterials was a critical development of the validation procedure. The apparatus reproduces literature capacity data for known materials spanning several orders of magnitude of capacity, from graphite to lanthanum nickel hydride. Kinetic data can be collected for adsorption and, unlike commercial low-pressure instruments, desorption to facilitate comparison of the rates for both processes. This new capability has directly led to the theory of different forward and reverse spillover mechanisms on carbon-based composites.
3. Isotopic tracer studies have been developed to evaluate forward and reverse spillover on carbon-based nanomaterials. A sequential dosing procedure has proven that hydrogen spillover proceeds at ambient temperature and follows a radial diffusion mechanism from the source particle. Equilibrium dosing procedures, building upon kinetic results obtained with the high-pressure volumetric system, have pointed toward a different mechanism for desorption, whereby a portion of the adsorbed species recombine before reaching the source particle. Recombination time constants have been estimated from differences in adsorption and desorption rates. Using kinetic results, a maximum reachable distance has been calculated for spillover on bridged composite nanostructured carbons. This information is key to optimizing the dispersion of nanoparticles on new materials to enhance capacity and improve kinetic response.

6.2 Proposed Future Studies

6.2.1 Enhancement of Spillover Adsorbent Properties

This work has demonstrated significant capacity gains for spillover adsorbents over traditional adsorbents that exhibit physisorption of hydrogen molecules. Nonetheless, there are additional opportunities for tailoring the receptor for further enhancement. The evidence of a maximum reachable distance in this study points to the need for optimization of the source density on the receptor. Higher dispersion and smaller particle size would reduce the diffusion distance and likely improve kinetics. This might also increase capacity, allowing atomic hydrogen to find additional adsorption sites that otherwise are too far from the source.

One method to achieve a higher dispersion of small metal particles is catalyzed gasification of carbon in the presence of transition metals. Platinum has been shown to channel in graphite at high temperature.[6.1,6.2] This process could be used to deposit a monolayer of platinum on the surface of pores in order to achieve high dispersion. A disadvantage would be the destruction of some porosity; however, new pores would be generated and could be tuned by specifying the tunneling particle size.

This work has demonstrated a bridge forming technique for producing composite adsorbents. The technique has tremendous promise in forming materials from newly developed nanostructured receptors and commercially available catalyst sources. The bridge precursor was a simple sugar; however, there has been evidence of catalytic enhancement due to bridges reported by other authors. Specifically, solutions of polyvinyl alcohol[6.3] and perylene[6.4-6.6] have been specified as potential bridge precursors. Grape must has been employed as a binder to form activated charcoal briquettes and

could be a candidate for bridges.[6.7] Optimization of the bridge precursor and composition could improve the diffusion path and limit the destruction of receptor porosity that should enhance both kinetics and capacity of the final composite.

6.2.2 Additional Characterization of Spillover

The surface of carbon-based adsorbents is populated by oxygen functionalities. The concentration and distribution of these species varies depending upon treatments given to the material.[6.8,6.9] Hydroxyl groups on the surface of a nickel on alumina hydrogenation catalyst have been identified at potential adsorption sites for atomic hydrogen.[6.10] Hydroxyls on the surface of silica have been shown to facilitate the spillover process.[6.11] A dedicated study on the capacity and catalytic kinetic effect of oxygen surface complexes would be a significant contribution to the development efforts for carbon-based adsorbents for hydrogen.

Kinetics of isotopic oxygen exchange are slower on metal supported catalysts doped with chlorine-containing precursors.[6.12,6.13] The primary spillover material, 6 wt% Pt/TC has not shown decreased capacity due to the hexachloroplatinate salt used to deposit platinum particles; however, the kinetic effect of using this precursor has not been studied in detail. Improvement of kinetics is desirable and such a study could point to the optimal synthesis route for hydrogen spillover adsorbents.

6.2.3 Novel Applications of Spillover Adsorbents

The work undertaken here has focused on a specific application of spillover adsorbents: hydrogen storage for on-board fuel cell applications. The general class of

adsorbents created in this work should have a broader range of application in the adsorption and catalysis community.

One potential area for application of spillover adsorbents is the catalyzed reduction of nitric oxides (NO_x).[6.14,6.15] Hydrogen has been observed to stabilize catalysts[6.16] and prevent catalyst poisoning by nitrates.[6.17] The presence of hydrogen also has been reported to activate oxygen into reactive oxygen species during selective catalytic reduction (SCR). Adsorbents exhibiting spillover at reaction conditions could be loaded with hydrogen by pretreatments to provide necessary concentrations during the reaction via reverse spillover.

6.3 Literature Cited

[6.1] Goethel, P. J.; Yang, R. T. *J. Catal.* **1988,** *114*, 46.

[6.2] Goethel, P. J.; Yang, R. T. *J. Catal.* **1986,** *101*, 342.

[6.3] Fujimoto, K.; Toyoshi, S. *Stud. Surf. Sci. Catal.* **1981,** *7A*, 235.

[6.4] Neikam, W. C.; Vannice, M. A. *J. Catal.* **1972,** *27*, 207.

[6.5] Vannice, M. A.; Neikam, W. C. *J. Catal.* **1971,** *20*, 260.

[6.6] Boudart, M.; Aldag, A. W.; Vannice, M. A. *J. Catal.* **1970,** *18*, 46.

[6.7] Deiana, A. C.; Granados, D. L.; Petkovic, L. M.; Sardella, M. F.; Silva, H. S. *Braz. J. Chem. Eng.* **2004,** *21*, 585.

[6.8] Contescu, A.; Contescu, C.; Putyera, K.; Schwarz, J. A. *Carbon* **1997,** *35*, 83.

[6.9] Jankowska, H.; Świątkowski, A.; Choma, J. *Active Carbon*; Ellis Horwood: New York, 1991; pp 75-106.

[6.9] Bianchi, D.; Gardes, G. E. E.; Pajonk, G. M.; Teichner, S. J. *J. Catal.* **1975,** *38*, 135.

[6.10] Cevallos Candau, J. F.; Conner, W. C. *J. Catal.* **1987,** *106*, 378.

[6.11] Abderrahim, H.; Duprez, D. In Catalysis: Theory to Practice, Proceedings of the 9th International Congress on Catalysis, Calgary, Alberta; Phillips, M. J., Ternan, M., Eds.; The Chemical Institute of Canada: Ottawa, 1988; p 1246.

[6.12] Abderrahim, H.; Duprez, D. *Stud. Surf. Sci. Catal.* **1986,** *30*, 359.

[6.13] Burch, R.; Coleman, M. D. *App. Catal., B* **1999,** *23*, 115.

[6.14] Frank, B.; Emig, G.; Renken, A. *App. Catal., B* **1998,** *19*, 45.

[6.15] Haneda, M.; Chiba, K.; Takahashi, A.; Sasaki, M.; Fujitani, T.; Hamada, H. *Catal. Lett.* **2007,** *118*, 159.

[6.16] Shimizu, K.; Shibata, J.; Satsuma, A. *J. Catal.* **2006,** *239*, 402.